FATIGUE OF THE TENSION-STIFFENING EFFECT IN REINFORCED CONCRETE

Vom Promotionsausschuss der
Technischen Universität Hamburg

zur Erlangung des akademischen Grades
Doktor-Ingenieur (Dr.-Ing.)

genehmigte Dissertation

von
Tomás Arana Villafán

aus
Sucre

2021

1. Gutachter: Prof. Dr. sc. techn. Viktor Sigrist
2. Gutachter: Prof. Dr.-Ing. Uwe Starossek

Tag der mündlichen Püfung: 09.04.2021

Foreword

The computational treatment of the bond between concrete and embedded reinforcing steel bars continues to be the subject of a debate among experts, even after many years of research. This is due to the complexity of the problem, as well as to the further development of construction methods and materials. In addition, with the focus on the assessment of existing structures, the expectations regarding the accuracy of predictions have also changed.

The dissertation presented by Tomás Arana Villafán deals with the bond action under fatigue loading and the influence of its degradation on the stiffness and the deformation capacity of tension chords and the shear resistance of girder webs. The investigations are based on a carefully conducted literature study as well as on tests on tensile elements under fatigue loading carried out at the TUHH. The Tension Chord Model and the method of Generalized Stress Fields serve as an uniform basis for theoretically addressing the issues.

The work is divided into six chapters: The introduction is followed by an overview on stochastically distributed actions and their computation for the example of (large) offshore structures. After that, a comprehensive discussion of the material properties of steel and concrete as well as of the bond behavior under static and repeated loading is presented. The main question of the thesis is pursued in the subsequent chapters. These start with the report on the tests with orthogonally reinforced tension members. Based on the results, the Tension Chord Model is extended for loading and unloading processes by adapting the corresponding design values and by introducing a linear damage function. Exemplarily, the findings are applied to the shear resistance of girder webs; the calculations are compared with experiments from the literature and good agreement is achieved. The work ends with a summary and conclusions.

This dissertation is an important contribution to the knowledge on the fatigue behavior of reinforced concrete structures. Tomás Arana Villafán critically reviews the assumptions made and the results found; in doing so, he points out deficiencies that still exist. Overall, he achieves results of high value for science and engineering practice. These represent a helpful basis for further research.

Lucerne (Switzerland), 2021
Prof. Dr. Viktor Sigrist

Summary

The deformation and carrying capacity of concrete structures depends on the existing bond between concrete and reinforcement. Due to the action of fatigue loads, the bond experiences a degradation process which subsequently modifies the mechanical behaviour of reinforced concrete. In order to quantify the effects of a bond fatigue, diverse tests on concrete chords were performed and evaluated in the present work. A main focus lay on the application of realistic random loads, derived from various sea spectra, since the load history has proven to decisively influence the fatigue behaviour of concrete and steel. Therefore, fatigue tests should reflect the totality of expected loads on a structural element. Additionally, the biaxial stress state around reinforcing bars was systematically varied with the aim of measuring the impact of transverse tension on bond.

The tests results reveal a progressive deterioration of the bond. In consequence, the axial stiffness of tension chords is reduced while the value of crack width after loading increases and the remaining crack width after unloading decreases. A transverse tension does not affect the response behaviour of the tested specimens. Also the ultimate carrying capacity is not negatively altered. However, a higher structural deformation capacity, caused by a weakening of the tension-stiffening effect, could be observed.

In addition, a sort of plastic-strain-accumulation effect in reinforcing bars could be registered. Although the applied loads did not exceed the yield strength f_{sy} of steel, the reinforcement in most of the tested specimens showed continuously growing plastic deformations. After discussing possible causes, a linear equation is proposed for a quantification of this effect. Further research is required in order to either confirm or refute the development of plastic strains in reinforcement under fatigue loading.

In a further step the nonlinear development of bond degradation is linearised and the Tension Chord Model [115] for static-monotonic loading modified for a mathematical description of the fatigue process. In the proposed model, the rigid-plastic character of bond stresses is kept. The value of bond stresses at serviceability level is linearly reduced depending on the experienced number of load cycles. The reduction is done following the decrease ratio of the tension-stiffening.

Based on the developed model, also a modification of the Generalised Stress Field Analysis [177] is proposed in order to quantify the inclination Θ_{fat} of compression struts in concrete beams with web reinforcement under fatigue loading. Results of tests published in the scientific literature reveal a significantly flatter inclination of Θ_{fat} as stipulated in design standards, which base on linear stress field analysis. The proposed modification delivers more accurate values of Θ_{fat} and enables a more favourable design of beams elements under fatigue.

Contents

Acknowledgements

Following doctoral thesis was developed mainly during my stay at the Institute of Concrete Structures at the Hamburg University of Technology. I wish to express my deepest gratitude to my supervisor, Prof. Dr. Viktor Sigrist, for the confidence shown to me and for his generous support in every step of this work. I also would like to pay my special regards to Prof. Dr.-Ing. Uwe Starossek for accepting to be the second examiner of this work and for permitting me to use the facilities of the Structural Analysis Institute for the realisation of the fatigue tests. Prof. Dr.-Ing. Rombach supported me repeatedly with valuable advice – I wish to show him my special gratitude. I would like to emphasize the invaluable assistance given by the staff of the Institute of Concrete Structures and of the Structural Analysis Institute: Harald Finger helped me solve numerous practical problems with the test configuration, Stefan Palm-Ziesenitz contributed considerably in the field of metrology, Axel Seils and Olaf Wittleben made the execution of the fatigue tests possible. I also thank Prof. Dr.-Ing. Hintze and his co-workers for facilitating the milling of longitudinal grooves on the reinforcement. I am deeply indebted to my wife and my children: Their infinite patience permitted me culminate this work. I deeply thank you.

Dresden, 2021
Tomás Arana Villafán

Notation

Roman capital letters

A_1	upper limit of the ferrite / cementite phase field
$A_{c,ef}$	effective concrete area
A_{ci}	idealised concrete area
A_{cn}	net concrete area
$A_{c,red}$	reduced cross sectional area
A_R	projected area of single rib
A_s	bar cross sectional area
$A_{s,fat}$	effective bar cross sectional area
A_{sz}	cross sectional area of reinforcement in z-direction
$\underline{B}$	damping matrix
C	constant
C_1	parameter
C_a	added mass coefficient
CC	consequence class
C_D	drag coefficient
C_{Ds}	drag coefficient for stationary flows
C_m	inertia coefficient
D	diameter, dimensionless damage
D_{equ}	real load-induced damage
D_{koll}	damage induced by $\Delta\sigma_{s,equ}$
EA	normal stiffness
E_{agg}	aggregate modulus of elasticity
E_c	concrete modulus of elasticity
$E_{c,fat}$	concrete modulus of elasticity under fatigue loading
E_{cm}	concrete secant modulus of elasticity
E_{c0m}	concrete tangent modulus of elasticity
E_i	idealised modulus of elasticity of uncracked concrete chord
E_{sm}	effective modulus of elasticity of tension chord
E_{sm0}	effective modulus of elasticity of tension chord at load beginning
F	force
$\underline{F}$	force matrix
F_{cr}	crack-inducing force
F_{hyd}	hydrodynamic force
F_{ins}	instationary force

F_{xV}	force component of stress field in x-direction
G	general failure function
G_f	dissipated energy per unit area
H	wave height, transfer function
HCF	high cycle fatigue
H_s	significant wave height
K	wave number, stress concentration range
$\underline{K}$	stiffness matrix
KC	Keulegan-Carpenter number
LCM	low cycle fatigue
M	bending moment
$\underline{M}$	mass matrix
N	normal force, number of loads
N_0	normal force range
N_f	total number of load cycles until failure
N_u	number of loads cycles that leads to fatigue failure
N^*	number of load cycles where inclination of Wöhler curve changes
P_m	post-tensioning force
Q_k	characteristic value of variable load action
$Q_{k;0.98}$	98% quantile of characteristic value of variable load action
QTF	quadratic transfer function
R	range, normal density function of resistance, response spectrum
RAO	response amplification factor
Re	Reynolds number
RC	reliability class
S	normal density function of load action, wave spectrum
$S_{c,a}$	relative amplitude compression strength
$S_{c,m}$	relative average compression strength
$S_{c,max}$	relative maximum compression strength
$S_{c,min}$	relative minimum compression strength
S_S	response spectrum
$S_ı$	sea spectrum
T	period
T_c	mean wave period
T_{cyc}	load period
T_{mg}	melting temperature of steel
T_t	transition temperature which leads to creep in steel
T_p	peak wave period
T_z	zero-up crossing period of wave
$T_{z,œ}$	zero-up crossing period of response
U_{cF}	specific fracture energy
V	shear force
V_{fat}	shear force under fatigue loading
$V_{R,c}$	shear resistance capacity of web concrete

$V_{R,sy}$	shear resistance capacity of web reinforcement
Y	yield function
Y_c	yield function of plain concrete
Y_{c1}	first yield limit of plain concrete
Y_{c2}	second yield limit of plain concrete
Y_s	response transfer function

Roman lower case letters

a	water acceleration, crack length
a_0, a_1, ..., a_n	Fourier coefficients, parameters
$\hat{a}$	amplitude
a_{sx}	lengthwise cross sectional area of reinforcement in x-direction
a_{sw}	lengthwise cross sectional area of web reinforcement
a_{sz}	lengthwise cross sectional area of reinforcement in z-direction
b	damping coefficient
b_0, b_1, ..., b_n	Fourier coefficients
b_{ffi_s}	parameter
$b_{ø}$	parameter
b_w	web width
c_0, c_1	constant values
c_{nom}	concrete cover
c_s	internal concrete cohesion
d	static height
d_w	water depth
f	frequency
f_c	uniaxial concrete compression strength
$f_{c,cube}$	uniaxial concrete compression strength tested on a cube
f_{ce}	concrete effective compression strength
$f_{c,fat}$	uniaxial fatigue strength of concrete
f_{ct}	concrete uniaxial tension strength
$f_{ct;0.05}$	5%-quantile of concrete uniaxial tension strength
$f_{ct;0.95}$	95%-quantile of concrete uniaxial tension strength
f_{load}	load frequency
f_R	bond index
f_{su}	steel uniaxial ultimate strength
f_{sy}	steel uniaxial yield strength
f_t	uniaxial tension strength
g	gravity constant
k	coefficient of f_{py}/f_{sy}, inclination of Wöhler curve
k_t	reduction factor
$k_ø$	factor for quantification of τ_{bU} and τ_{bR} in dependence of f_{ct}
k_u	displacement coefficient, coefficient of steel stress at cracked section by reloading and at first cracking

l_b	bond length
l_{by}	transmission length by yielding of reinforcement
m	exponent for Wöhler curve
m_a	added mass
m_0, m_2, m_4	statistical moments
m_{pl}	slope of $\varepsilon_{sm,pl} - n/N$-curve
m_{sm}	slope of $E_{sm} - n/N$-curve
m_{yy}	lengthwise bending moment
n	natural number, coefficient of E_s/E_c
n_{equ}	equivalent number of load cycles
n_x	axial membrane forces in x-direction
n_z	axial membrane forces in z-direction
$Ø_s$	reinforcing bar diameter
p	pressure, probability
p_0	atmospheric pressure
p_f	failure probability
p_{ins}	instationary pressure
p_r	radial compression
r_1, r_2	parameters of meridians
r_c	radius function
r_i	radius of inner concrete ring
r_o	radius of outer concrete ring
s_{rm}	average crack spacing
$s_{rm,max}$	maximum average crack spacing
$s_{rm,min}$	minimum average crack spacing
s_{r0}	maximum distance between cracks
u	mode value, velocity in x-direction
u_1	mode value in a reference period of 1 year
u_{50}	mode value in a reference period of 50 years
u_a	amplitude velocity of oscillating fluid
v	velocity in y-direction
w	velocity in z-direction
w_{cr}	crack width
$w_{cr,lim}$	limit value of crack width
w_{tr}	transverse crack width
w_u	crack width by which no force transmission is possible
x_{sR}	intersection point of steel stress distribution between unloading and reloading process
x_{sU}	intersection point of steel stress distribution between loading and unloading process
$\underline{x}$	deformation or motion matrix
$\underline{\dot{x}}$	velocity matrix
$\underline{\ddot{x}}$	acceleration matrix

$\underline{\dot{x}_r}$	velocity matrix of rigid body
$\underline{\ddot{x}_r}$	acceleration matrix of rigid body
z	lever arm of internal forces

Greek letters

α_1, α_2, α_3	parameters
α_b	inclination angle of stress resultant around reinforcing bar
$\alpha_{c,duc}$	ductility degree factor
α_e	$= E_s/E_c$
α_i	parameter
β_b	inclination angle between reinforcing bar and concrete wedge
$\beta_{c,fat}$	$= \varepsilon_{c,fat,da}/\varepsilon_{c,fat}$
β_{RC}	reliability index
β_1	mean direction of sea state
γ	shearing strain
γ_Q	safety factor for variable load action
$\gamma_{s,fat}$	material safety factor at fatigue limit state
γ_{Sd}	load safety factor at fatigue limit state
γ_{xz}	shearing strain in xz-plane
$\Delta\varepsilon_{s,el}$	elastic steel strain range
$\Delta\varepsilon_{s,pl}$	plastic steel strain range
$\Delta\varepsilon_{sm0}$	difference of average steel strain resulting from degradation of tension-stiffening
$\Delta\sigma_s$	normal stress range
$\Delta\sigma_{s0}$	$= N_0/A_s$
$\Delta\sigma_{s,equ}$	damage equivalent stress range
δ_d	factor for steel ductility
δ_s	slip between reinforcing bar and surrounding concrete
δ_{s0}	slip δ_s under static-monotonic loading
δ_{s1}	slip δ_s after one load cycle
δ_{sr}	residual slip
$\delta_{s,max}$	maximum bond slip
ϵ_1	principal strain
ϵ_3	principal strain
ϵ_c	concrete strain
ϵ_{c1}, ε_{c3}	concrete principal strains
ϵ_{c0}	uniaxial concrete compression strength at failure
$\epsilon_{c3,el}$	elastic component of concrete strain under fatigue
$\epsilon_{c3,t}$	time-dependent component of concrete strain under fatigue
$\epsilon_{c,fat}$	concrete strain under fatigue loading
$\epsilon_{c,fat,da}$	damage-induced strain under fatigue
ϵ_{cm}	average concrete strain
ϵ_{ct}	$= f_{ct}/E_c$

ϵ_{cu}	concrete failure strain
$\epsilon_{cu,fat}$	concrete ultimate fatigue strain
ϵ_{n}	phase angle
ϵ_{r}	remaining strain after unloading
ϵ_{sm}	average steel strain
$\epsilon_{sm,cal}$	calculated average steel strain
$\epsilon_{sm,mes}$	measured average steel strain
$\epsilon_{sm,ø}$	bond-dependent average steel strain
$\epsilon_{sm,pl}$	plastic part of average steel strain
$\epsilon_{s,max}$	maximal steel strain
ϵ_{smz}	average steel strain in z-direction
ϵ_{sr}	steel strain at at midpoint between cracks
ϵ_{sr0}	steel strain at cracked section
ϵ_{srx}	steel strain at cracked section in x-direction
ϵ_{srz}	steel strain at cracked section in z-direction
ϵ_{sy}	uniaxial steel yield strain
ϵ_{uf}	strain of flange of a composite bridge
ϵ_{x}	strain in x-direction
ϵ_{z}	strain in z-direction
ζ	water level function
ζ_{a}	wave amplitude, response amplitude
η_{D}	limit of cumulative damage ratio
η_{δ}	parameter for quantification of slip reversal
η_{TS}	tension-stiffening number
Θ	inclination angle
θ	relative roughness
Θ_{c}	Haigh-Westergaard-coordinate
Θ_{fat}	inclination of compression strut at fatigue limit state
$\Theta_{fat,cal}$	calculated inclination of compression strut at fatigue limit state
$\Theta_{fat,MC2010}$	inclination of compression strut at fatigue limit state according to Model Code 2010
$\Theta_{fat,mes}$	measured inclination of compression strut at fatigue limit state
$\Theta_{FB,stat}$	inclination of compression strut at ultimate limit state according to DIN Fachbericht 102
Θ_{max}	maximal inclination angle
Θ_{min}	minimal inclination angle
Θ_{ult}	inclination of compression strut at the ultimate limit state
Θ_{z}	yaw motion
κ_{b0}	bond strength according to Tension Chord Model
$\kappa_{c,fat}$	damage parameter
κ_{rsd}	calculation factor of residual bond strength
$\kappa_{t,fat}$	damage parameter
κ_{τ}	bond coefficient

λ	parameter for quantification of distance between cracks
λ_w	wave length
μ	mean value
μ_c	elastic Poisson's ratio
μ_G	mean value of G
$\mu_{H_{s,\text{œs}}}$	median value of significant stress in reinforcement
μ_R	mean value of R
μ_S	mean value of S
ν	Poisson's number
ξ	parameter
ξ_c	Haigh-Westergaard-coordinate
ρ_c	Haigh-Westergaard-coordinate
$\rho_{s,ef}$	effective geometrical reinforcement ratio
ρ_{sx}	geometrical reinforcement ratio in x-direction
ρ_{sz}	geometrical reinforcement ratio in z-direction
ρ_w	water density
σ	normal stress
σ_1	principal stress
σ_3	principal stress
σ_{br}	radial stress
$\sigma_{b\Phi}$	circumferential stress
σ_c	concrete normal stress
σ_{c1}	concrete principal stress
σ_{c3}	concrete principal stress
$\sigma_{c,D}$	real stress due to fatigue-induced damage of cross section
σ_{cx}	concrete normal stress in x-direction
σ_{cz}	concrete normal stress in z-direction
$\overline{\sigma_s}$	mean steel stress
$\sigma_{H_{s,\sigma_s}}$	standard deviation of significant stress in reinforcement
$\sigma_{s,max}$	maximal steel stress
σ_{sr}	steel stress at cracked section
σ_{sr0}	steel stress at cracked section immediately after crack formation
σ_{std}	standard deviation
σ_{sx}	steel stress in x-direction
σ_{sw}	steel stress in web reinforcement
σ_{sz}	steel stress in z-direction
σ_x	normal stress in x-direction
σ_z	normal stress in z-direction
τ	shear stress
τ_b	bond strength
τ_{bf}	frictional bond strength
$\tau_{b,0.1}$	bond stress at a slip of 0.1 mm
τ_{b0}	rigid-plastic bond strength for $\sigma_s < f_{sy}$
τ_{b1}	rigid-plastic bond strength for $\sigma_s \geq f_{sy}$

$\tau_{b,max}$	ultimate bond strength
τ_{bR}	rigid-plastic bond stress by reloading
τ_{bR1}	rigid-plastic bond stress by 1^{st} cycle of reloading
$\tau_{bR,rsd}$	residual rigid-plastic bond stress by reloading
τ_{bU}	rigid-plastic bond stress by unloading
τ_{bU1}	rigid-plastic bond stress by 1^{st} cycle of unloading
$\tau_{bU,rsd}$	residual rigid-plastic bond stress by unloading
τ_c	concrete shear stress
τ_{cxz}	concrete shear stress in the xz-plane
$\tau_{R,max}$	ultimate shear stress
τ_{xz}	shear stress in the xz-plane
Φ	potential function
Φ_b	conical shell expansion of bond stresses
ϕ_c	angle of internal friction of concrete
Φ_n	phase angle
Φ_s	potential function of diffracted wave
Φ_w	potential function of undisturbed wave
Φ_x	roll motion
Ψ_{KC}	modification factor for instationary flows
Ψ_y	pitch motion
ψ_0, ψ_1, ψ_2	combination factor
ω	circular frequency
ω_{sy}	mechanical reinforcement ratio
ω_p	circular peak frequency
ω_{py}	mechanical ratio of prestressing steel
ω_T	wave circular frequency

CHAPTER 1

Introduction

1.1 Context

The material behaviour of reinforcement as well as of concrete under fatigue loading has still not been sufficiently investigated. In most cases, the research of materials being subjected to fatigue loading only concentrates on the influence of specific parameters and on the derivation of empirical equations in order to estimate the service life of the tested specimens. This procedure is generally justified and widely accepted since robust but simple calculation models are rational and necessary in view of the complex and mostly non-linear mechanical behaviour of materials. Nevertheless, some important questions still remain unanswered.

A question concerns the deformation behaviour of steel and concrete under fatigue loading. It is commonly assumed that both materials practically behave linearly under fatigue loading. In case of the reinforcement, data about the development of strains under fatigue loading is virtually inexistent. Yet, the ribbed geometry of the reinforcement bars suggests a non-uniform stress distribution with a consequent stress concentration at the root of the ribs. As a result, a material plastification under service loads may be caused, leading to a hysteresis in the deformation response in the macro domain and to a different behaviour at the ultimate state. In case of the concrete, it is known that it exhibits increasing irreversible deformations under fatigue (uniaxial) loading. Thereby, the concrete stiffness constantly decreases. Such behaviour, which is important for the structural serviceability and the calculation of internal forces, has almost not been quantified.

The mechanical behaviour of reinforcement and of concrete at the ultimate limit state after being subjected to a significant fatigue loading is a further issue which has not yet been properly investigated. Some data in the literature suggests an unaltered load-bearing capacity in spite of a fatigue-induced damage. Nonetheless, the available data is scarce and a deeper research seems meaningful since practically all tests for the ultimate limit state are performed with "intact" materials, i.e. without a fatigue-induced damage. Real structures are expected to be reliable any time, even after having experienced a considerable amount of fatigue loading.

The biaxial fatigue behaviour of concrete is practically unknown.

The mechanical behaviour of the bond between concrete and embedded steel reinforcement is similar to the behaviour of the concrete. Since the bond properties are vital for the deformation capacity of structural members and for their serviceability, the bond degradation under fatigue deserves special attention. The majority of tests has focused on the static slip-force response of pull-out specimens under uniaxial loading and their

mathematical description. However, with regard to membrane members and to the web of beam elements, the biaxial bond behaviour has only been observed in a few publications. Also the ultimate bearing capacity of the bond after an extensive fatigue loading has obtained little attention yet.

A further question regards the test conditions for the fatigue behaviour. Although the sequence effect and the test frequency have proven to have a significant influence on the damage development of the concrete and even of the reinforcement, most fatigue tests are still performed with high test frequencies and with sinusoidal loads which considerably differ from reality. It seems necessary to develop representative loads (time-series, spectra) for test purposes in order to gain more realistic results.

At the structural level, the interaction between reinforcement and concrete in presence of membrane and shear forces as well as of moments is more complex. The same questions as described above are valid for structural elements. For example, the fatigue behaviour of beams under shear forces has only been investigated to a small extent. Adequate models for the fatigue-induced changes in the load-bearing mechanisms are rare and not well-grounded. Also plastic-hinge regions need to be clarified in their deformation capacity after experiencing fatigue loading. The stiffness reduction of the concrete may, on the other hand, lead to a different strain distribution in the compression zone of beam elements. Additionally, the load distribution of hyperstatic structures depends on the stiffness distribution of the whole system. As a result of the fatigue loading, the stiffness distribution may be affected and the load distribution at the ultimate limit state may be different.

1.2 Objective and Overview

Due to the substantial dependency of the structural behaviour on the bond between concrete and surrounding reinforcement, this work concentrates on the bond degradation under fatigue loading. The goal is the development of a simple but reliable model of the interaction between concrete and reinforcement in the fatigue range and its posterior application at the ultimate limit state. For this purpose, the Tension Chord Model of Sigrist [115] is taken as basis and shall be modified if necessary. With the help of tests performed on tension chords under different stress states and under realistic conditions regarding test frequency and load history, the bond and deformation behaviour of tension chords shall be adequately monitored and used for the development of a model.

A special emphasis shall be given to offshore concrete structures. Therefore, specimen dimensions, test configuration, and load history shall be derived from conditions present in offshore structures (low frequency, time-series from narrow-banded spectra). Ch. 2 describes, thus, the background of the safety concept of structures, the calculation of hydrodynamic loads, and the spectral fatigue analysis.

Ch. 3 gives an extensive overview of the state-of-the-art of the fatigue behaviour of reinforcement, concrete, and bond; it emphasizes important properties and depicts further research needs.

Ch. 4 discusses the Tension Chord Model. A brief description of the performed tests and of their results is given. Moreover, some considerations regarding the magnitude of

the effective concrete area $A_{c,ef}$ under fatigue are made. On the basis of the performed tests, a modification of the Tension Chord Model for fatigue is suggested.

Ch. 5 deals with the fatigue behaviour of beams in shear with a web reinforcement. Based on published data, the modified Tension Chord Model is used in order to adapt the Generalised Stress Field Analysis [177]. With that, the inclination of the compression strut in the web of a beam element may be accurately estimated. Due to the fatigue loading, the inclination of the compression strut decreases; this effect is considered by the modifications of the calculation models.

Finally, Ch. 6 gives a summary of the work and underlines the most important conclusions and open questions which may be taken into account in a future research.

CHAPTER 2

Analysis of Random Loads and Stresses for the Fatigue Check

2.1 Load Combinations and Required Reliability Index

The character of the majority of loads on structures is random. Loads may vary both in time and in space [66]. An accurate calculation is not possible and not reasonable despite the existence of numerous advanced calculation models. Especially the prediction of the future development of the expected loads is a challenging task. According to Haibach [74], load-time-functions are basically either deterministic or random. A deterministic value is determined mathematically and its trend in time is predictable. Furthermore, deterministic quantities are classified into periodic or non-periodic values. In contrast to them, random loads are describable only with statistical methods and their prediction is only possible on the basis of a probability analysis. They are classified into steady (stationary) and non-steady (non-stationary) random quantities. "Steady" implies, in this case, that the statistical properties like mean value or standard deviation are constant over the time. By non-steady random values they are variable over the time. Yet, some processes in nature exhibit steadiness only over a certain time interval and are therefore quasi-steady. An example of such a quasi-steady process is the sea state. Note that ergodicity is the principal requirement for a possible analysis of a steady random process (cf. Fig. 2.3a). Consequently, statistical methods become indispensable for the structural design. They allow the estimation of load values which have a predefined exceedance probability.

Table 2.1: Consequence classes (CC) according to DIN EN 1990 [39]

Consequence class (CC)	Attribute	Example
CC 3	Extreme consequences for human life, or extreme economic, social, or environmental consequences	Tribunes, public building with extreme consequences of failure (e.g. concert hall)
CC 2	Medium consequences for human life, or considerable economic, social, or environmental consequences	Residential or office building with medium consequences of failure (e.g. public office)
CC 1	Low consequences for human life, and little economic, social, or environmental consequences	Farm building without regular movement of people (e.g. barn, greenhouse)

Table 2.2: Stipulated reliability classes (RC) according to DIN EN 1990 [39]

Reliability class (RC)	Minimum value of β_{RC}	
	Reference period 1 year	Reference period 50 years
RC 3	5.2	4.3
RC 2	4.7	3.8
RC 1	4.2	3.3

In general, based on the high requirements of structures regarding their safety, serviceability, and durability, different limit states are defined in standards. They quantify a certain load level with requirements that have to be fulfilled. The most important, the ultimate limit state (ULS), defines different combinations of extreme load actions which a failure of structural elements is not allowed for. The ultimate limit state is associated with a failure probability which is stipulated by requirements of the civil society [166] and formulated in the actual standards. In DIN EN 1990 [39] the possible consequences of a structure failure are classified in the consequence classes (CC) 1 to 3 (cf. Tab. 2.1). Depending on the consequence class, DIN EN 1990 distinguishes the reliability classes (RC) 1 to 3 (Tab. 2.2). Reliability classes prescribe, on the other hand, obligatory values of the reliability index β_{RC} and a tolerable failure probability.

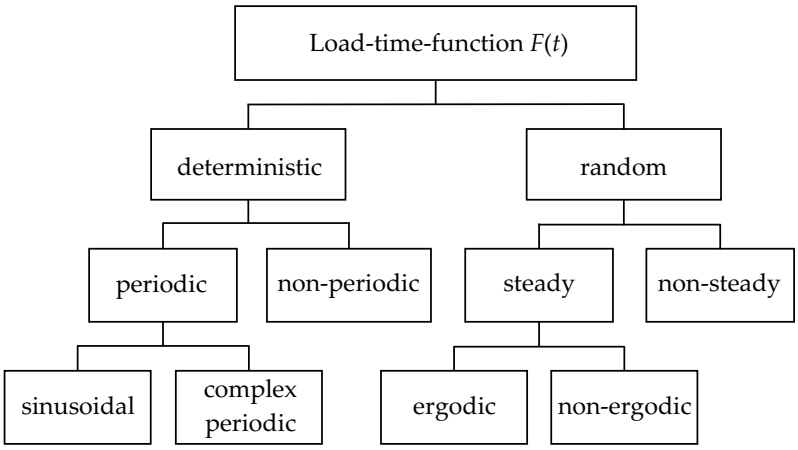

Figure 2.1: Classification of load-time-functions $F(t)$, redrawn from [74]

The probability of occurrence of every load may be described by a density function. Though, structures are subjected to numerous, often simultaneously acting loads. According to the central limiting value theorem, the sum of many independent variables exhibiting different density functions tends to approximate to the normal density function. Meanwhile, the product of many independent variables tends to approximate to a logarithmic density function (cf. [166], [146], [183]). Due to the unsteady character of loads it is common practice to quantify them by means of characteristic values Q_k which are derived from the load density functions and related to a given exceedance

probability in a reference time period. Characteristic values may be established as the median if the variation coefficient is low, or as a quantile if the variation coefficient is high, or as a nominal value for cases where the density function is unknown [66]. For building constructions, in a reference period of 1 year, permanent actions exhibit an exceedance probability of 100%. In contrast to them, variable actions have an exceedance probability of 1...5% (99% respectively 95% quantile). Abnormal actions are quantified with an exceedance probability of 0.01...10% for the same time period. Extreme values with low or high exceedance probabilities have to be estimated with the Gumbel or the Weibull density functions. Assuming a Gumbel density function and time-invariant values of mode u respectively standard deviation σ_{std}, the 98%-quantile $Q_{k;0.98}$ for a reference period of 1 year is [66]:

$$Q_{k;0.98} = u_1 - \frac{\sqrt{6}}{\pi} \ln(-\ln 0.98)\sigma_{std} = u_1 + 3.04\sigma_{std}, \tag{2.1}$$

with u_1 being the mode in a reference period of 1 year. For a reference period of 50 years, the mode results from [66]:

$$u_{50} = u_1 + \frac{\sqrt{6}}{\pi} \ln 50\sigma_{std} = u_1 + 3.05\sigma_{std}. \tag{2.2}$$

From Eq. 2.1 and 2.2 it becomes evident that the 98%-quantile related to 1 year practically corresponds to the 50-year-mode, i.e. the 98%-quantile has an exceedance probability of 2% in 1 year. However, the exceedance probability amounts 100% in a 50-year-period, leading to an exceedance occurrence of once every 50 years.

In the scope of semi-probabilistic safety methods and for reasons of simplification, all actions acting on a structure generally are assumed to follow the normal density function S, even though the logarithmic density function is the most appropriate [166]. Also the structural resistance, similarly, is simplified to a normal density function R. Since both are normal distributed, the failure function $G = R - S$ also obeys a normal density function. Values $G = R - S < 0$ means structural failure and the integral

$$p_f = \int_{-\infty}^{0} f_G \, dx = \Phi(-\beta_{RC}) \tag{2.3}$$

quantifies the failure probability p_f. The mean μ and standard deviation σ_{std} values of $G = R - S$ result from

$$\mu_G = \mu_R - \mu_S, \tag{2.4}$$

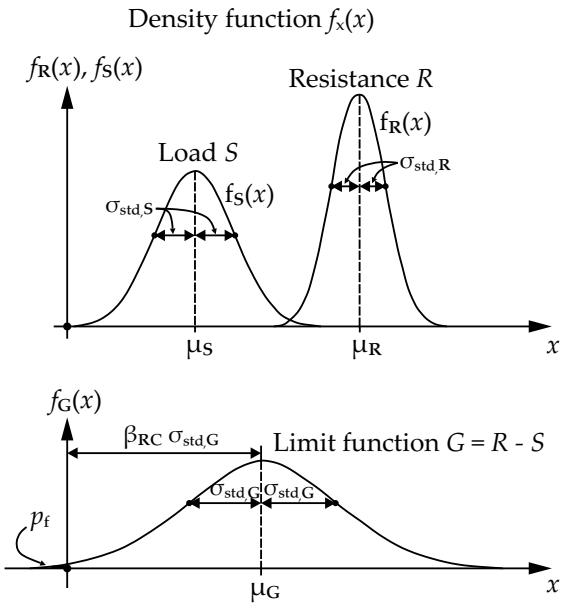

Figure 2.2: Reliability index β_{RC} and failure probability p_f, adapted from [58]

$$\sigma_{std,G} = \sqrt{\sigma_{std,R}^2 + \sigma_{std,S}^2}. \tag{2.5}$$

Per definition, the reliability index β_{RC} results from the division

$$\beta_{RC} = \frac{\mu_G}{\sigma_{std,G}} \tag{2.6}$$

and exposes the distance from the mode μ_G to the failure region $G < 0$ (Fig. 2.2). The larger β_{RC} is, the lower the failure probability p_f is. β_{RC} may be determined using tabled values Φ of the normal density function for a given failure probability p_f. For normal building structures the structural design is based on the reliability class 2 (RC 2) for a reference period of 50 years [39]. The minimum value of the reliability index in this case is $\beta_{RC} = 3.8$ (Tab. 2.2), which corresponds to a failure probability $p_f = 7.3 \cdot 10^{-5}$ in a reference period of 50 years. For a reference period of 1 year, DIN EN 1990 [39] demands $\beta_{RC} = 4.7$, which leads to a failure probability of $p_f = 1.3 \cdot 10^{-6}$. Other structures like bridges or offshore structures may require higher values of β_{RC}, depending on their complexity, the corresponding consequence class (CC), and the governing uncertainties. Bridges, for example, have to be designed for a reference period of 100 years [58].

The design value of a loading action results from the multiplication of the characteristic value Q_k of the load with a safety factor γ_Q. It is important to mention that β_{RC} does not contain the risk coming from a possible human error [39]. Human errors have to be dealt with other strategies [166].

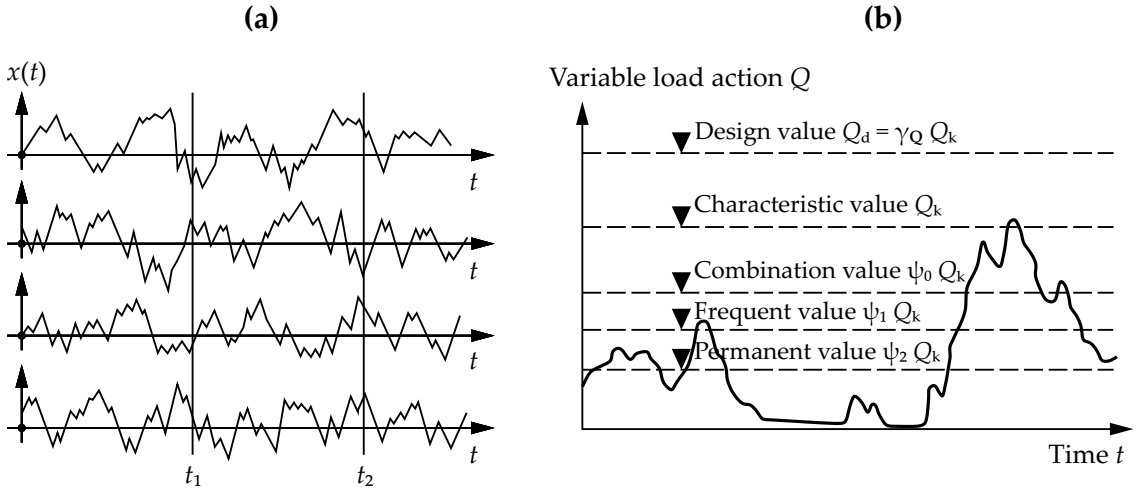

Figure 2.3: (a) Ergodic process of random values: Mean value and standard deviation are constant in the interval between t_1 and t_s, adopted from [74] (b) Representative values of a time-variable load action, adapted from [66]

The serviceability limit state (SLS) stipulates additional load combinations in order to guarantee structural functionality. Every load combination has an occurrence probability and also a reliability index β_{RC}. For normal building structures DIN EN 1990 [39] distinguishes between a permanent, a frequent, and a characteristic (rare) combination of actions. For bridges the not-frequent combination of actions is an additional combination that has to be taken into account. According to Grünberg [66], the characteristic combination of actions describes the limit of irreversible processes in a structural element. DIN 1055-100 [35], as precursor of the German DIN EN 1990 [39], assigns for this case a tolerable failure probability of $p_f = 1.0 \cdot 10^{-3}$ corresponding to $\beta_{RC} = 3.0$ (reference period 1 year) respectively $p_f = 5.0 \cdot 10^{-2}$ corresponding to $\beta_{RC} = 1.5$ (reference period 50 year). The frequent load combination involves a load level which is frequently reached, though with reversible effects on the structure. The permanent load combination corresponds to a load level which is not expected to be underrun. In case of bridge constructions, the characteristic load combination is expected to happen once in 50 years while the not-frequent combination of actions once in 1 year. The frequent combination of actions occurs once in a week [58]. The different load combinations are derived from the characteristic value of the corresponding loads. Each load, as long as it is variable, is multiplied with a combination factor ψ_i which takes into consideration the reduced probability of several variable characteristic loads acting at the same time [209].

For a verification of the structural resistance against a fatigue failure, in theory, the set of all experienced loads on a structure has to be considered. The fatigue life of materials, and for instance of structures, highly depends on the load characteristics like magnitude, sequence, frequency, etc. In most structures, yet, an accurate gathering of the expected future loads is not possible. In addition, the material and structural response under fatigue loading have still not been fully understood (cf. Ch. 3). At the same

time, available damage calculation models are simplified and fatigue test results show a considerable variability. Therefore, various abstract load models or load collectives in form of forces or stresses have been developed for different types of structures like road bridges, railway bridges, and cranes [15]. They represent a compromise and a simplification of real loads. Fatigue load models for bridges are usually applied on static calculation models. Dynamic effects of the structure are basically accounted for with dynamic coefficients [15]. However, this procedure neglects the effects of the load history. In the case of offshore wind energy converters, for which location-specific environmental loads in conjunction with the operational behaviour of the turbine are dominating, detailed simulations in the nonlinear time-domain have to be carried out considering different scenarios and the structural dynamic behaviour [59]. Similar requirements may be found by other complex structures. A structural verification for fatigue based on probabilistic methods and a reliability index β_{RC} is also possible, though very time-consuming [15]. Such procedure implies, however, a realistic damage calculation model.

The results of load measurements or of time-domain calculations usually are to be processed and filtered afterwards in order to perform a counting of the stresses (magnitude, number of cycles) [15].

2.2 Structural Response

In the scope of the Research Centre On- and Offshore Engineering Structures ("Bauwerke im und am Wasser") of the Hamburg University of Technology, a special emphasis was given to the fatigue loading and posterior response behaviour of offshore concrete structures. Such structures are subjected to environmental loads of great magnitude induced by waves, currents, wind, and ice. Moreover, they may experience a high number of load cycles. In future the number of offshore concrete structures will probably increase partially due to the growing proliferation of plants of renewable energy, and to the opening of new regions with promising extraction of crude materials. The global world trade demands further port infrastructure like for example floating ports [179]. Coastal regions with lack of disposable space for expanding, or with deep water, or difficult ground conditions are sometimes forced to develop unconventional infrastructure like floating airports or even floating bridges.

In the following section the derivation of fatigue loads and the response behaviour of offshore structures is discussed and showed using as example a concrete barge at the North Sea.

According to [130], the static analysis of structures implies the solution of the matrix equation

$$\underline{K}\underline{x} = \underline{F}. \tag{2.7}$$

Eq. 2.7 describes the equilibrium condition of structures which are not subjected to any acceleration. $\underline{K}$ is the stiffness matrix of the structure, $\underline{x}$ the deformation matrix, and $\underline{F}$ is the load matrix. Eq. 2.7 may also be non-linear. In case that the sum of all acting loads on the structure is not zero ($\sum_i F_i \neq 0$), an acceleration of the structure takes place and inertia

and damping forces are induced. The resulting linear motion equation becomes

$$\underline{M}\ddot{\underline{x}} + \underline{B}\dot{\underline{x}} + \underline{K}\underline{x} = \underline{F}, \tag{2.8}$$

where $\underline{M}$ is the mass matrix and $\underline{B}$ the damping matrix. $\ddot{\underline{x}}$ corresponds to the acceleration of the structure while $\dot{\underline{x}}$ is the velocity matrix. If the structural response is idealised as a rigid body motion, Eq. 2.8 may be solved for a mass point. Depending on the location of the different structural elements it is possible to derive subsequently the motion values at every point of the structure. Eq. 2.8 takes the form

$$\underline{K}\underline{x} = \underline{F} - \underline{M}\ddot{\underline{x}}_{\mathrm{r}} - \underline{B}\dot{\underline{x}}_{\mathrm{r}} \tag{2.9}$$

with $\ddot{\underline{x}}_{\mathrm{r}}$ and $\dot{\underline{x}}_{\mathrm{r}}$ being the acceleration respectively velocity of the rigid body motion. Eq. 2.9 has the form of Eq. 2.8 and implies that the load matrix $\underline{F}$ has to be modified by the motion values of the body in order to determine the structural stresses. Eq. 2.9 is usually employed in the analysis and design of floating structures.

Wave-induced loads, in most cases, belong to the load actions with the largest amplitudes on offshore structures and play, therefore, an important role. Following the classification given in [90], waves may be divided into

- waves generated by a floating structure or vessel which moves with a constant speed or oscillates,
- waves resulting from the interaction between wind and sea surface,
- waves generated by astronomic forces (tides),
- waves generated by earthquakes or submarine landslides (tsunamis), and
- free surface waves generated in fluids in partially filled tanks.

The free sea surface results from the state of equilibrium between the sea and the earth gravity [63]. Induced oscillations around the state of equilibrium constitute waves which propagate over the sea surface. According to [90], a sea is a train of waves driven by the prevailing local wind field of a certain fetch. The wind injects energy into the sea and leads to higher waves. An equilibrium state is achieved when the energy input equals the energy dissipation due to wave breaking and viscous effects [131]. The sea surface is irregular, the waves are short-crested, and the crests are sharp. In contrast to wind-induced waves, a swell is formed by waves propagating out of their origin area. Swells are wind-independent, may propagate over very long distances, and are more regular compared to the wind-induced sea state.

Basically, the irregular sea state may be described mathematically by superposition of simple elementary waves [63] like ring or plane waves with infinitely long wave crests. Harmonic plane waves are regular waves characterised by a wave length λ_{w}, a wave amplitude ζ_{a}, a wave height $H = 2\zeta_{\mathrm{a}}$, a wave period T_{w}, and the water depth d_{w} (Fig. 2.4b). They exhibit a sinusoidal course with small amplitudes ζ_{a}.

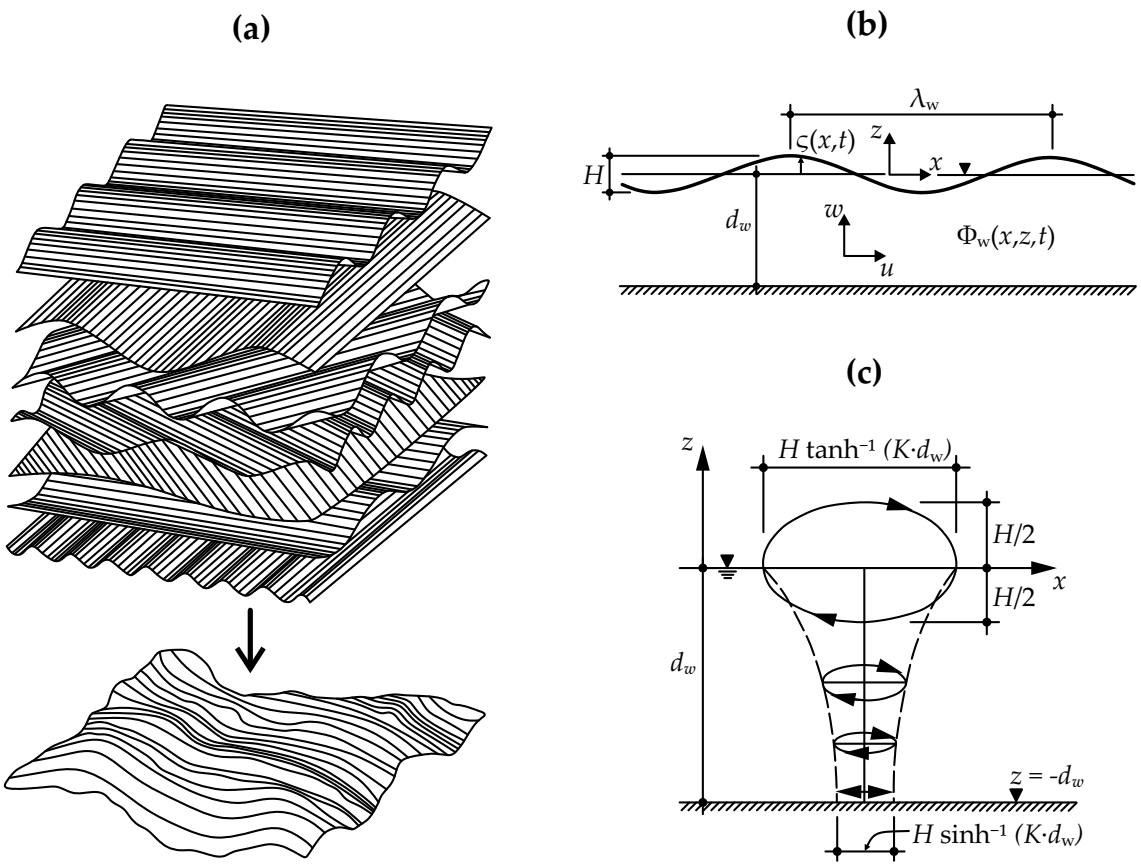

Figure 2.4: (a) Superposition principle of the sea state, adopted from [100], (b) Harmonic elementary sea wave, adapted from [100], (c) Orbital velocity distribution in a sea wave, adapted from [196]

Deep water waves are short. They are identified by the condition $d_w \geq 1/2\lambda_w$. Shallow water waves result if $1/20\lambda_w < d_w < 1/2\lambda_w$ and very shallow water waves correspond to $d_w \leq 1/20\lambda_w$ [196]. Some useful wave parameters are

- the wave number $k = \frac{2\pi}{\lambda_w}$,
- the wave steepness $\frac{H}{\lambda_w}$, and
- the circular wave frequency $\Omega = \frac{2\pi}{T_w}$.

In many practical cases, the viscous, nonlinear properties of water may be neglected so that it may be described as an ideal fluid. In this case, a potential function Φ_w is derived by which the velocities u, v, and w in the respective directions x, y, and z result from

$$u(x,y,z,t) = \frac{\partial \Phi_w(x,y,z,t)}{\partial x}, \tag{2.10}$$

$$v(x,y,z,t) = \frac{\partial \Phi_w(x,y,z,t)}{\partial y}, \tag{2.11}$$

$$w(x,y,z,t) = \frac{\partial \Phi_w(x,y,z,t)}{\partial z}. \tag{2.12}$$

The continuity equation

$$\frac{\partial u}{\partial x} + \frac{\partial v}{\partial y} + \frac{\partial w}{\partial z} = \frac{\partial^2 \Phi_w}{\partial x^2} + \frac{\partial^2 \Phi_w}{\partial y^2} + \frac{\partial^2 \Phi_w}{\partial z^2} = 0, \tag{2.13}$$

the kinematic boundary condition at seabed

$$w(z=\infty) = \frac{\partial^2 \Phi_w(z=\infty)}{\partial z^2} = 0, \tag{2.14}$$

the free surface kinematic boundary condition

$$w(z=\zeta) = \frac{\mathrm{d}\zeta}{\mathrm{d}t} = \frac{\partial \zeta}{\partial t} + \frac{\partial \zeta}{\partial x}\frac{\partial x}{\partial t} + \frac{\partial \zeta}{\partial y}\frac{\partial y}{\partial t} = \frac{\partial \zeta}{\partial t} + \frac{\partial \zeta}{\partial x}\frac{\partial \Phi_w}{\partial x} + \frac{\partial \zeta}{\partial y}\frac{\partial \Phi_w}{\partial y}, \tag{2.15}$$

and the free surface dynamic boundary condition for the pressure p at the sea surface being equal to the atmospheric pressure p_0

$$p(z=\zeta) = p_0 = \frac{\partial \Phi_w}{\partial t} + \frac{1}{2}\left[\left(\frac{\partial \Phi_w}{\partial x}\right)^2 + \left(\frac{\partial \Phi_w}{\partial y}\right)^2 + \left(\frac{\partial \Phi_w}{\partial z}\right)^2\right] \tag{2.16}$$

are further conditions to be fulfilled by the sought function Φ_w. Eq. 2.15 and 2.16 may be linearised [63]. With the parameters $c = \Omega/k_w$ and $k_w = 2\pi/\lambda_w = \Omega^2/g$, the following approach is applicable for deep-water waves:

$$\Phi_w = c\zeta_a \cos(\Omega t - k_w x)\, e^{k_w z}. \tag{2.17}$$

The Bernoulli equation for unstationary irrotational flows

$$\frac{\partial \Phi_w}{\partial t} + \frac{1}{2}\left(u^2 + v^2 + w^2\right) + \frac{p}{\rho_w} + gz = p_0 \tag{2.18}$$

may also be linearised, leading to

$$\frac{\partial \Phi_w}{\partial t} + \frac{p}{\rho_w} + gz = p_0. \tag{2.19}$$

After further derivations [90] the potential function Φ_w for shallow water becomes

$$\Phi_w = \frac{\zeta_a g}{\Omega} \frac{\cosh\left[k_w\left(d_w + z\right)\right]}{\cosh\left(k_w d_w\right)} \sin\left(k_w x - \Omega t\right). \tag{2.20}$$

The governing pressure for shallow water conditions results from the linearised Bernoulli equation (Eq. 2.19) and from the potential function Φ_w (Eq. 2.20):

$$p - p_0 = -\rho_w g z + \rho_w g \zeta_a \frac{\cosh\left[k_w\left(d_w + z\right)\right]}{\cosh\left(k_w d_w\right)} \cos\left(k_w x - \Omega t\right). \tag{2.21}$$

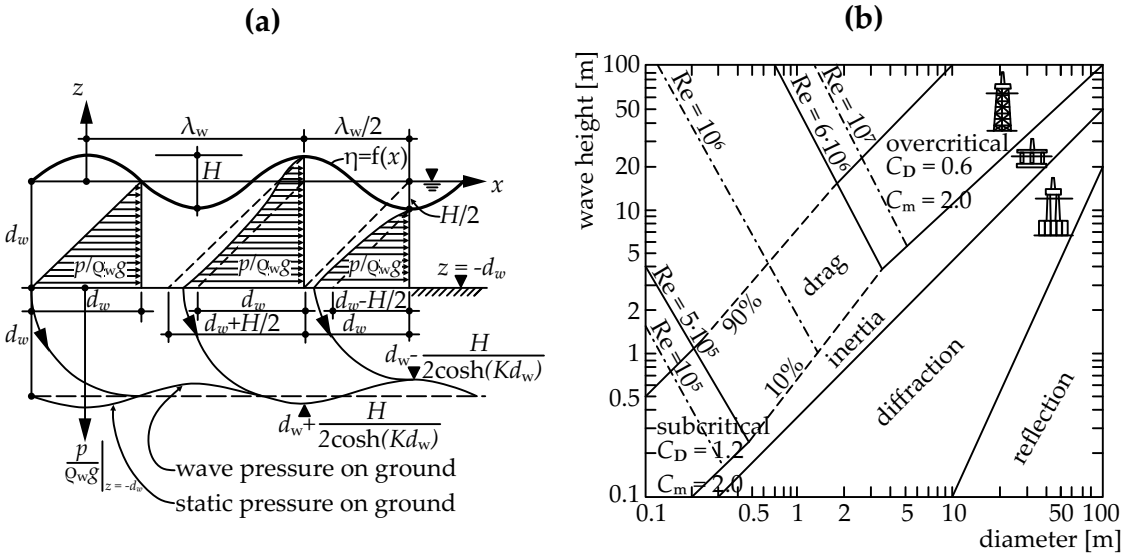

Figure 2.5: (a) Pressure field in an undisturbed wave, adopted from [196], (b) Governing wave force depending on wave height and structure diameter, adapted from [100]

For deep water the pressure distribution may be derived to following expression:

$$p - p_0 = -\rho_w g z + \rho_w g \zeta_a e^{k_w z} \cos\left(k_w x - \Omega t\right). \tag{2.22}$$

The first term in Eq. 2.21 and 2.22 describes the hydrostatic pressure, the second part the hydrodynamic pressure. Steep and nonlinear waves as well as second-order wave drift forces will not be mentioned in this work. Though, reference is made to literature

(e.g. [47], [129]). Nonlinear waves may however be design-relevant for offshore structures in the ultimate limit state (ULS).

The sea state has a random character. Also environmental loads due to wind or earthquake are characterised by their randomness. This means that the instantaneous values of a variable $f(x)$ cannot be predicted. Furthermore, the knowledge of a value $f(x = x_0)$ does not provide any information about other values $f_{x=x_n}$ $(n = 1, 2, 3, ...)$ [131]. A reasonable description and quantification of these environmental parameters is possible using statistical methods rather than determining the time history in a deterministic analysis. In spite of an apparently irregular behaviour, nevertheless, a statistical stationarity is visible in a sea state if the considered time period is not large. In fact, over a time frame of ca. 3 hours [43] the sea presents practically constant mean and standard deviation values of the water level $\zeta(t)$ and the corresponding probability density function obeys the Gaussian (normal) distribution [90]. The normal distribution of water level $\zeta(t)$ is a consequence of the central limit theorem (cf. 2.1). Further stationary parameters are the significant wave height H_s, the peak period T_p, the average zero-up crossing period T_z, and the mean direction β_ζ of the sea state [123]. The time frame mentioned above is referred as the short-term. The sea state may be described by a spectrum (Fig. 2.6a) which contains information about the frequency-dependent energy content of the real sea state. A probability analysis becomes thereby accessible, yet some information like the sequence of values, e.g. $\zeta(t)$, gets lost.

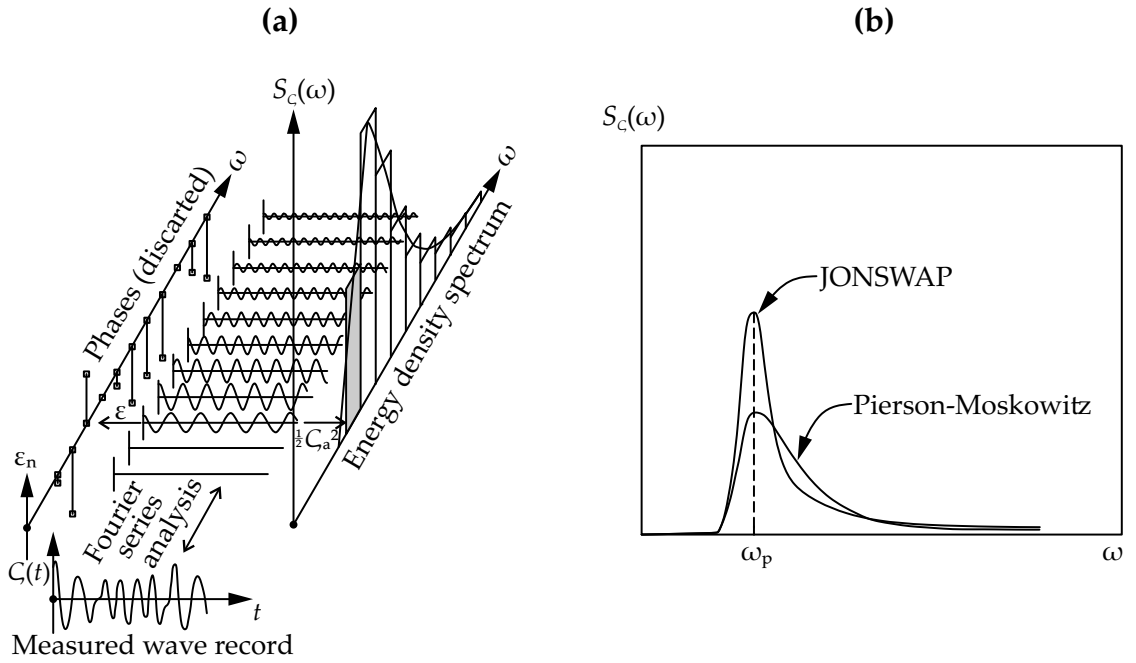

Figure 2.6: (a) Illustration of the superposition principle of waves in a spectrum, redrawn from [90], (b) Qualitative comparison between the Pierson-Moskowitz-spectrum and the JONSWAP-spectrum of the sea state.

The perhaps most useful property of linear waves is a linear superposition in order

to represent a real sea state [130]. Fig. 2.6a illustrates the superposition principle: Every discrete frequency bar f describes the frequency of a cosine function with a proper phase angle ϵ_n, which is naturally periodic and harmonic, and whose amplitude is dictated by the corresponding value $S_\zeta(f)$ of the spectrum. The basis for determining a spectrum of a time history is the periodicity of the signal $f(x)$. A random sea state may however be regarded as periodic by assuming a fictitious time period T which necessarily has to be long enough in order to reproduce the most relevant frequency range. Under this assumption, the signal $f(x)$ may be "represented by a series of sines and cosines which are harmonically related" [131]. This is called a Fourier analysis of $f(x)$.

$$f(x) = \frac{1}{2}a_0 + \sum_{n=1}^{\infty} \left[a_n \cos(nx) + b_n \sin(nx)\right]. \tag{2.23}$$

a_0, a_n, and b_n with $n = 1, 2, 3, ..., \infty$ are known as the Fourier-coefficients. They have to be determined by means of a Fourier-transformation of $f(x)$. The required number of Fourier-coefficients n depends on the sought accuracy. Integrating Eq. 2.23 in the limits 0 to 2π delivers the value of a_0:

$$a_0 = \frac{1}{\pi} \int_0^{2\pi} f(x) \mathrm{d}x. \tag{2.24}$$

By multiplying both sides of Eq. 2.23 with $\cos(qx)$, where $q = 1, 2, 3, ...$ and integrating again in the limits 0 to 2π one obtains the values of a_n for all $n = 1, 2, 3, ...$:

$$a_n = \frac{1}{\pi} \int_0^{2\pi} f(x) \cos(nx) \mathrm{d}x. \tag{2.25}$$

Similarly for the coefficients b_n after multiplying Eq. 2.23 with $\sin(qx)$:

$$b_n = \frac{1}{\pi} \int_0^{2\pi} f(x) \sin(nx) \mathrm{d}x. \tag{2.26}$$

Considering the corresponding circular frequency $\Omega_T = 2\pi/T$ of the fictitious period T of the signal $f(x)$, then $x = \Omega_T t = 2\pi/T t$ and $\mathrm{d}x = 2\pi/T \mathrm{d}t$. Eq. 2.24 to 2.26 may be then reshaped to

$$a_0 = \frac{2}{T} \int_0^{T} f(t) \mathrm{d}t, \tag{2.27}$$

$$a_n = \frac{2}{T} \int_0^T f(t) \cos(n\Omega_T t) \mathrm{d}t, \tag{2.28}$$

$$b_n = \frac{2}{T} \int_0^T f(t) \sin(n\Omega_T t) \mathrm{d}t. \tag{2.29}$$

Eq. 2.23 may also be rewritten as

$$f(t) = \frac{1}{2} \sum_{n=0}^{\infty} \left[c_n \cos(n\Omega_T t - \Phi_n) \right], \tag{2.30}$$

where

$$\frac{1}{2} c_n = \sqrt{a_n^2 + b_n^2}, \tag{2.31}$$

and

$$\tan \Phi_n = \frac{b_n}{a_n}. \tag{2.32}$$

The Discrete Fourier Transformation (DFT) is used for determining the spectrum of measured, discrete values of a signal $f(t)$. In this case it is essential, according to the sampling theorem, to select an adequate sampling period in order to record $f(t)$ correctly. For this purpose, a minimum sampling frequency is to be hold (Shannon sampling theorem). For more details, also relating to the Fast Fourier Transformation (FFT) for an effective calculation of the Fourier-coefficients of long time series, see [143].

For a sea state generally the amplitude spectrum $S_\zeta(\Omega)$ of the wave height is determined. Usual unidirectional spectra, which describe the sea state quiet good and which have been derived from extensive measurements, are the Pierson-Moskowitz (PM) spectrum and the JONSWAP-spectrum (Fig. 2.6b). The Pierson-Moskowitz spectrum follows the expression [43]

$$S_\zeta(\Omega) = \frac{5}{16} H_s^2 \frac{\Omega_p}{\Omega^5} e^{-\frac{5}{4} \frac{\Omega_p}{\Omega^4}}. \tag{2.33}$$

The wave height H for a concrete frequency value Ω is determined by

$$S_\zeta(\Omega)\mathrm{d}\Omega = \frac{1}{8}H^2(\Omega). \tag{2.34}$$

The spectral moments m_k of a wave spectrum contain valuable information about $\zeta(t)$.

$$m_\mathrm{k} = \int_0^\infty \Omega^k S_\zeta \Omega \mathrm{d}\Omega, \tag{2.35}$$

where $k = 1, 2, 3, ...$ The moment $m_{0\zeta}$ ($k = 0$) is identical with the root mean square σ_ζ of $\zeta(t)$:

$$\sigma_\zeta = \sqrt{m_{0\zeta}}. \tag{2.36}$$

The significant wave height H_s, defined as the average height of the highest one-third of all waves and approximately equal to the estimated highest wave of a sea state by the human eye [100], follows from

$$H_\mathrm{s} = 4\sqrt{m_{\mathrm{o}\zeta}}. \tag{2.37}$$

The significant wave height H_s is employed together with the zero-up crossing period T_z as representative parameters in order to define a sea state (cf. Eq. 2.33 and Eq. 2.44). The mean period T_z (cf. Fig. 2.7a) of the zero-up crossings results from

$$T_\mathrm{z} = \sqrt{\frac{m_{\mathrm{o}\zeta}}{m_{2\zeta}}}, \tag{2.38}$$

and the mean period T_c (cf. 2.7a) of the crests from

$$T_\mathrm{c} = \sqrt{\frac{m_{2\zeta}}{m_{4\zeta}}}. \tag{2.39}$$

If the spectrum is narrow-banded, i.e. it contains a narrow range of frequency, and the sea state presents no swell, the zero-up crossing frequency $f_\mathrm{z} = 1/T_\mathrm{z}$ equals the total number of crests per second [131]. Moreover, if the water surface elevation $\zeta(t)$ is normal distributed, then the wave amplitude statistics obey a Rayleigh-distribution [90]. The

(a)

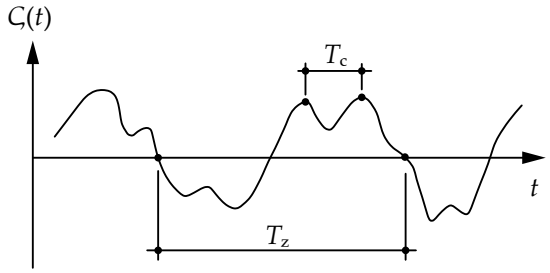

(b)

H_s [m]								
16.5								
15.0								
13.5						1		
12.0					8	12	10	
10.5				22	47	38	27	5
9.0			12	41	70	56	30	9
7.5		9	26	46	88	62	33	4
6.0		17	37	75	103	57	40	8
4.5	18	44	50	199	112	63	39	21
3.0	23	55	68	134	141	80	34	12
1.5	30	50	77	120	111	46	22	7
T_z [s]	4.0	5.0	6.0	7.0	8.0	9.0	10.0	11.0

Figure 2.7: (a) Definition of T_z and T_c, redrawn from [131], (b) Exemplary scatter-diagram.

probability density function for the distribution of an amplitude value $\hat{a}$ is

$$p(\hat{a}) = \frac{\hat{a}}{m_0} e^{-\frac{\hat{a}^2}{2m_0}} \tag{2.40}$$

and for the distribution of the range $R = 2\hat{a}$

$$p(R) = \frac{R}{4m_0} e^{-\frac{R^2}{8m_0}}. \tag{2.41}$$

The exceedance probability of a wave height H in a sea state characterised by a significant wave height H_s in the short-term is given by

$$p\left(H_w > H\right) = e^{-2\left(\frac{H}{H_s}\right)^2}. \tag{2.42}$$

The maximum wave height H_{max} in the short-term is pragmatically selected as the wave height exceeded on average once every 1000 (storm) waves [90]. This arbitrary convention is justified since about 3 hours are necessary for 1000 waves to pass by and after 3 hours the most unfavourable peak will have passed.

$$e^{-2\left(\frac{H_{max}}{H_s}\right)^2} = \frac{1}{1000}, \qquad H_{max} = 1.86 H_s. \tag{2.43}$$

For narrow-banded spectra, the peak period $T_p = 2\pi/\Omega_p$ is related to the zero-up

crossing period T_z [123].

$$T_p = 1.408 T_z. \tag{2.44}$$

For long-term analysis, so called scatter-diagrams are developed (Fig. 2.7b). They are in fact tables containing information about the number of sea states that have been registered with a given value of H_s and T_z at a certain location in an observation period. Such scatter-diagrams have also been developed for different regions worldwide [43] or may be gained for specific purposes from long-term measurements or simulations. With a scatter diagram it is possible to determine extreme-value statistics using unfavourable sea states (e.g. with an exceedance probability of 50 years) and then the highest expectable wave height (e.g. H_{max50}, cf. [59]). Such extreme-value analysis are important for structural design in the ultimate limit state.

In the scope of a fatigue design, floating structures are usually linearised. This procedure is valid since under service conditions the motions and loads remain in the linear range. Catenaring moorings may be neglected under certain conditions, other mooring types like tension legs may require to be accounted for. The floating structure is idealised as a rigid body which diverse hydrodynamic and non-hydrodynamic forces act on [63]. Hydrodynamic forces depend on the wave frequency, amplitude, water depth, structure geometry, and encounter angle between wave and structure.

Hydrostatic forces are a function of the water depth and act orthogonally to the submerged surface. Additionally, the hydrodynamic pressure field of the undisturbed wave (cf. Eq. 2.21, 2.22) generate an additional force on the structure which is known as the Froude-Kryloff force. The presence of a structure, though, obstructs the free wave propagation causing a diffraction of the wave and a further hydrodynamic pressure field whose surface integral is known as diffraction force. The consequence of these wave-induced forces is an oscillatory response motion of the structure which generates other, additional hydrodynamic pressure fields which, on the other hand, influence the acting forces (again). This interaction has to be solved iteratively, yet the linearisation of the system permits an usually good quality and suitability of the results [63].

There are cases where the interaction between hydrodynamic forces and response behaviour is significantly more intensive. Very large floating structures (VLFS) (cf. [3], [97]) are an example. Due to the size of the structure and its elasticity, the deformations resulting from experienced loads may reach dimensions which influence the hydrodynamic loads more extensively. Other nonlinear effects involve the field of flow-induced vibrations [127], [128].

Since the behaviour of floating structures is calculated using a linear approach, the superposition principle is valid. The motion of the structure, and for instance the loads on it, generally results from the superposition of the motion of the structure in still water and of the wave forces on the restrained structure [47] (Fig. 2.8).

Wave-induced forces and moments act on an (imaginary) restrained structure, i.e. it presents no motion response. As mentioned before, they are composed of the Froude-Kryloff and of diffraction forces. In case of fixed slender offshore structures, the diffraction

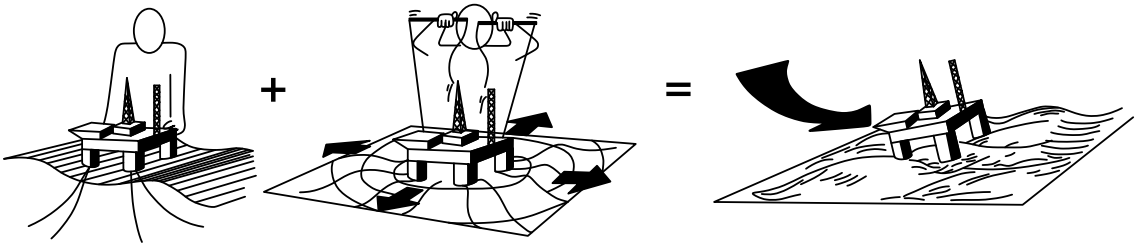

Figure 2.8: Superposition of wave excitation, added mass, damping, and restoring forces and moments, redrawn from [47]

force is not as pronounced as the nonlinear drag force which is caused by the viscosity properties of the fluid medium water (cf. [131]). Drag forces are calculated employing the Morison equation. Neglecting the drag – for large-volume structures with quotient of width respectively diameter D to wave length λ_w of $D/\lambda_w > 1/5$ [197] –, the Froude-Kryloff-force may be calculated by means of the potential function Φ_w of the undisturbed wave. Diffraction forces, on the other hand, may be estimated using a disturbance potential Φ_s which has to account for the boundary condition of the structure surface. The resulting potential function follows from the superposition [171]

$$\Phi = \Phi_w + \Phi_s. \tag{2.45}$$

In addition to the hydrostatic pressure, the hydrodynamic instationary pressure results from

$$p_{inst} = -\rho_w \frac{\partial \Phi}{\partial t} \tag{2.46}$$

and the unstationary forces on the structure from the surface integral

$$F_{inst} = -\int\limits_S \int p_{inst}\, \vec{n}\, dS = \rho_w \int\limits_S \int \frac{\partial \Phi}{\partial t}\, \vec{n}\, dS \tag{2.47}$$

with the instationary moments

$$M_{inst} = -\int\limits_S \int p_{inst} \left(\vec{n} \times \vec{r}\right) dS = \rho_w \int\limits_S \int \frac{\partial \Phi}{\partial t} \left(\vec{n} \times \vec{r}\right) dS. \tag{2.48}$$

The forced harmonic motion of a structure in still water induces additional hydro-

dynamic forces and moments. Commonly they are classified into a component that is proportional to the structure acceleration $\ddot{s}$ as an idealised rigid body and into a second component which depends on the velocity $\dot{s}$ of the structure [171].

$$F_{\mathrm{hyd}} = m_{\mathrm{a}}\ddot{s} + b\dot{s}. \tag{2.49}$$

m_{a} is an inertial coefficient which is denominated "added mass" or "hydrodynamic mass". It has the impact of an additional mass acting around the structure and describes the fluid inertia related to the acceleration of the rigid body [123]. The term $b\dot{s}$ is a damping force (potential damping) which acts on the contrary direction of the velocity vector $\dot{s}$ of the motion; b is called "damping coefficient". The damping force is the consequence of energy dissipation owing to ring waves induced by the oscillating body [123].

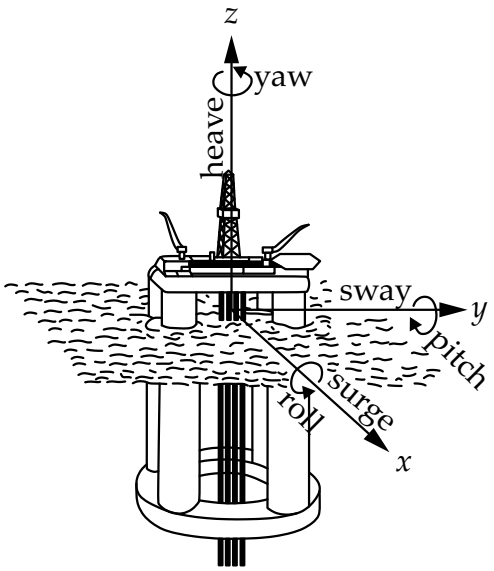

Figure 2.9: Definition of rigid-body-motion modes exemplified on a deep concrete floater, redrawn from [47]

Inertia, damping, and hydrostatic restoring forces are in equilibrium with wave loads according to the principle of d'Alembert. The linear equation of motion for one degree of freedom has the form

$$\left(m + m_{\mathrm{a}}\right)\ddot{s} + b\dot{s} + cs = F_{\mathrm{inst}}. \tag{2.50}$$

The equations of motion for all 6 degree of freedom (DoF) of a floating structure (surge in x-direction, sway in y-direction, heave in z-direction, roll Φ_{x} around the x-axis, pitch Ψ_{y} around the y-axis, and yaw Θ_{z} around the z-axis, cf. Fig. 2.9) result similarly to Eq. 2.50. The inertia, damping, and hydrostatic spring coefficients are different depending on the degree of freedom. Moreover, they are frequency-dependent. The equations of motion for

sway, heave, roll, pitch, and yaw are coupled while the influence of surge is negligible [171].

$$A_{11}\ddot{z} + A_{12}\dot{z} + A_{13}z + A_{14}\ddot{\Theta}_z + A_{15}\dot{\Theta}_z + A_{16}\Theta_z = F_{\text{inst},z} \tag{2.51}$$

$$A_{21}\ddot{z} + A_{22}\dot{z} + A_{23}z + A_{24}\ddot{\Theta}_z + A_{25}\dot{\Theta}_z + A_{26}\Theta_z = M_{\text{inst},\Theta_z} \tag{2.52}$$

$$A_{31}\ddot{y} + A_{32}\dot{y} + A_{33}y + A_{34}\ddot{\Psi}_y + A_{35}\dot{\Psi}_y + A_{36}\Psi_y + A_{37}\ddot{\Phi}_x + A_{38}\dot{\Phi}_x + A_{39}\Phi_x = F_{\text{inst},y} \tag{2.53}$$

$$A_{41}\ddot{y} + A_{42}\dot{y} + A_{43}y + A_{44}\ddot{\Psi}_y + A_{45}\dot{\Psi}_y + A_{46}\Psi_y + A_{47}\ddot{\Phi}_x + A_{48}\dot{\Phi}_x + A_{49}\Phi_x = M_{\text{inst},\Psi_y} \tag{2.54}$$

$$A_{51}\ddot{y} + A_{52}\dot{y} + A_{53}y + A_{54}\ddot{\Psi}_y + A_{55}\dot{\Psi}_y + A_{56}\Psi_y + A_{57}\ddot{\Phi}_x + A_{58}\dot{\Phi}_x + A_{59}\Phi_x = M_{\text{inst},\Phi_x}. \tag{2.55}$$

The coefficients $A_{33} = A_{39} = A_{43} = A_{49} = A_{53} = 0$ since the motions sway and yaw do not induce hydrostatic restoring forces.

The calculation of the potential coefficients and the solution of the equation of motion are carried out by means of numerical methods like the deterministic method (only for few cases), conformal maps, the integral equation method, and the finite element method (FEM) [123]. Moorings are eventually to be modeled, their behaviour may be either linear or non-linear and may have a decisive influence on the motion parameters.

Other environmental loads result from currents, wind, and ice. Fixed slender structures or slender members are rather drag-dominated while the inertia term is less pronounced. The Morison equation for oscillating, slender bodies delivers a line load [131]

$$f_{\text{Mor}} = \rho_w A a + C_a \rho_w (a - \ddot{s}) + \frac{1}{2} C_D D |u - \dot{s}| (u - \dot{s}), \tag{2.56}$$

with A being the cross sectional area of the member and D the (equivalent) diameter. The inertia term is composed of the Froude-Kryloff-force, which is proportional to the fluid acceleration a, and of the diffraction-induced added mass, which is expressed by the added mass coefficient C_a and is proportional to the relative acceleration between water a and body $\ddot{s}$. If the acceleration of the body is not taken into account, the term $1 + C_a$ is called inertia coefficient C_m.

$$C_m = 1 + C_a. \tag{2.57}$$

C_a depends on the body geometry and on the wave frequency. The drag loading is proportional to the square of the relative velocity $u - \dot{s}$ and is caused by a fluctuating pressure field at the lee side of the member which is a consequence of the viscosity-induced turbulence. The expression $|u - \dot{s}|\,(u - \dot{s})$ in Eq. 2.56 may become negative and acts like a damping drag force contrary to the direction of the actual oscillation of the body. The average drag force is described using the drag coefficient C_D. Again, C_D is a function of the body geometry. Moreover, the relative roughness ϑ of the body influences the total value of C_D since it determines the properties of the boundary layer at the interface body-fluid. For stationary flows like currents, the coefficient of inertial forces and viscosity-induced friction forces in a fluid, is expressed by a dimensionless number called Reynolds number Re [18]. Re quantifies the turbulence degree in a fluid and, indirectly, the resulting drag coefficient C_D of a slender member with an equivalent diameter D in a stationary flow with the velocity u and the kinematic viscosity ν. For water at 10°C, $\nu = 1.31 \cdot 10^{-6}$ m^2/s.

$$\mathrm{Re} = \frac{uD}{\nu}. \tag{2.58}$$

For high Re-numbers Re > 10^6, what practically is always the case in offshore structures, the C_D-coefficient for stationary flows (C_{DS}) may be determined depending on the relative roughness ϑ/D according to [43].

Unstationary flows, like in case of sea waves with a period T_w, are better described on the basis of another dimensionless number: The Keulegan-Carpenter number KC as the relation between drag forces over inertia forces [131]

$$\mathrm{KC} = \frac{u_a T_w}{D}, \tag{2.59}$$

where u_a is the amplitude velocity of the oscillating flow (or the oscillating body); in case of a wave, u_a corresponds to the maximal wave velocity. The value of the drag coefficient for stationary flows has to be modified via a factor ψ_{KC} which depends on the KC-number (cf. Fig. 2.10b) [43].

However, there are numerous additional forces of a nonlinear character [123]. They have to be accounted for, depending whether they are relevant or not. Fortunately, in the fatigue analysis of offshore structures, nonlinear forces are usually not indispensable like in the ultimate limit state.

1. Non-linear motion coupling,
2. finite motions,
3. nonlinear restoring forces,
4. steep waves,
5. nonlinear forces resulting from dynamic positioning,
6. slamming forces,

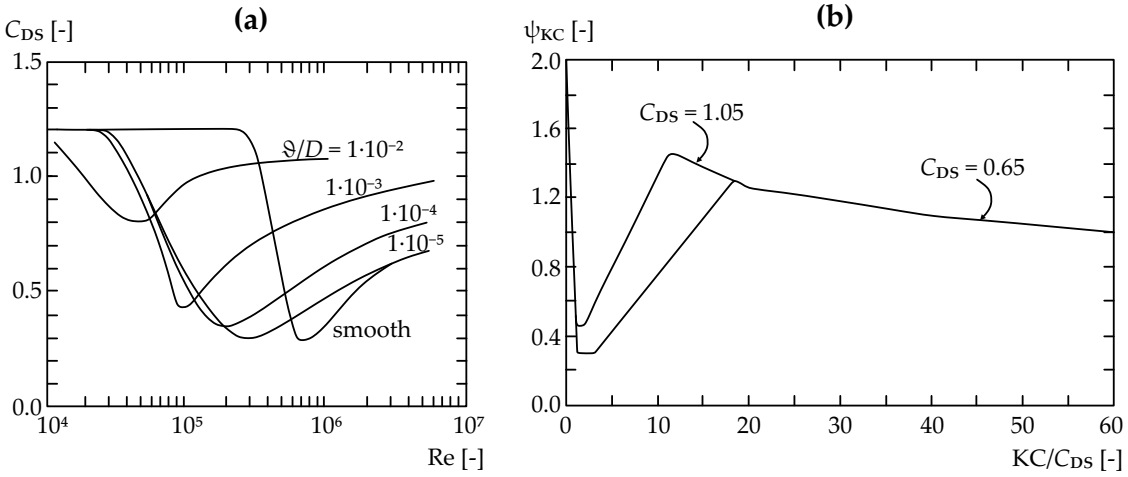

Figure 2.10: (a) C_{DS} coefficient for stationary flows as function of the Re-number and the relative roughness ϑ/D and (b) Increase factor Ψ_{KC} for unstationary flows as function of the KC-number, adapted from [43]

7. sloshing forces,
8. mooring forces, and
9. internal forces of the structure (like from drilling or storage components, machines, etc.).

On the basis of numerical methods the floating structure is modeled using panels which acting offshore loads are calculated for. The solution of the equations of motion is determined for a structure as an idealised rigid body. Both, the acting fluid pressures and the acceleration $\ddot{s}$ of the body and its velocity $\dot{s}$ are exported in a further step to a structural linear or nonlinear model in form of distributed loads (Fig. 2.11) – generally a finite element model – in order to calculate structural stresses or deformations and to perform a structural design. This procedure is known as the inertia relief method [67].

The floating body exhibits thereby a harmonic motion with the same wave frequency, a motion amplitude proportional to the wave amplitude, and a phase angle which describes the amplitude shift related to the wave amplitude. Therefore, the response amplitude may be expressed by means of a proportionality factor RAO(Ω) called response amplitude operator [63].

For the input signal of the water elevation surface $\zeta(t)$

$$\zeta(t) = \zeta_a \cos(\Omega t), \tag{2.60}$$

the response motion $s(t)$ follows from

$$s(t) = \mathrm{RAO}(\Omega)\zeta_a \cos(\Omega t). \tag{2.61}$$

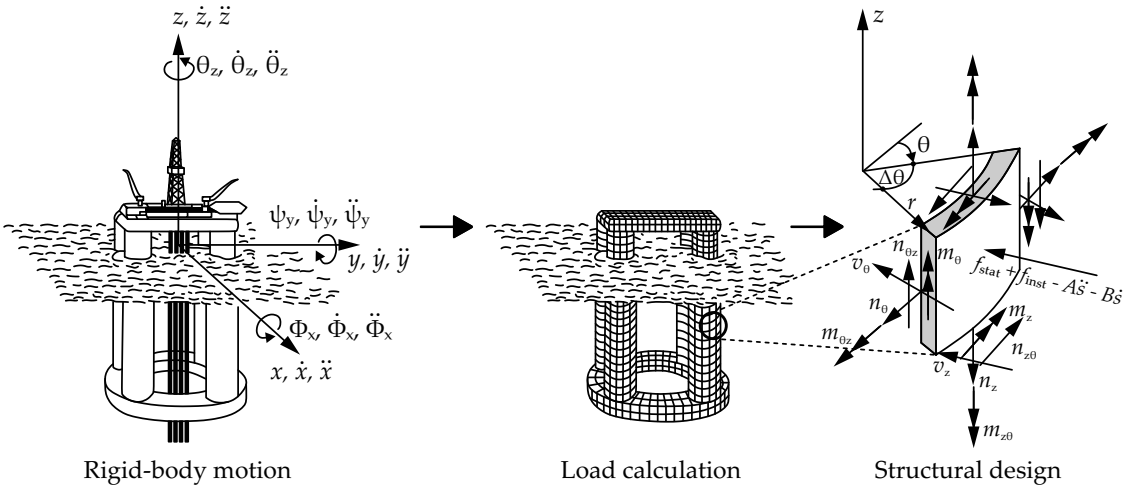

Figure 2.11: Overview of structural analysis and design of floating structures, partially adapted from [47]

Thus, making use of the superposition principle, the motion response of a rigid body in an irregular sea state, which is described by a frequency spectrum $S_\zeta(\Omega)$ (Eq. 2.33), may be expressed in the same matter by a response spectrum $S_s(\Omega)$. Such response spectrum has similar properties as the wave spectrum, e.g. the amplitude distribution of motions follows a Rayleigh-distribution. Also spectral moments of the motion response are calculable and a extreme-value analysis is possible. The spectral analysis in the frequency domain is based on the proportionality relation between input and output. In praxis however, the sea state spectrum $S_\zeta(\Omega)$ is defined in form of an energy (mean square) spectrum – the wave energy is proportional to the square of the water surface elevation $\zeta(t)$. The mean square values of oscillatory elements are proportional to their power [130]. Therefore, energy spectra are known as power density spectra with the unit [motion^{2}s]. The proportionality factor between input and output of power density spectra is denominated transfer function $Y_\zeta(\Omega)$ and the mathematical relation between both becomes quadratic (quadratic transfer function QTF).

$$S_s(\Omega) = [Y_s(\Omega)]^2 \, S_\zeta(\Omega). \tag{2.62}$$

Note again that a spectral analysis is valid for linear systems. In presence of nonlinear loads and effects other calculation methods should be employed if a linearisation is not permissible. Nevertheless, the spectral analysis is a useful tool for fatigue design since loads and motion of a floating structure under serviceability conditions are predominantly linear.

The main task in the frequency domain analysis consists in determining the transfer function $[Y_s(\Omega)]^2$ for all six spatial motions. The usual procedure is to discretise the sea frequency range of the sea state spectrum into at least 33 frequency classes (0.2 ... 1.80

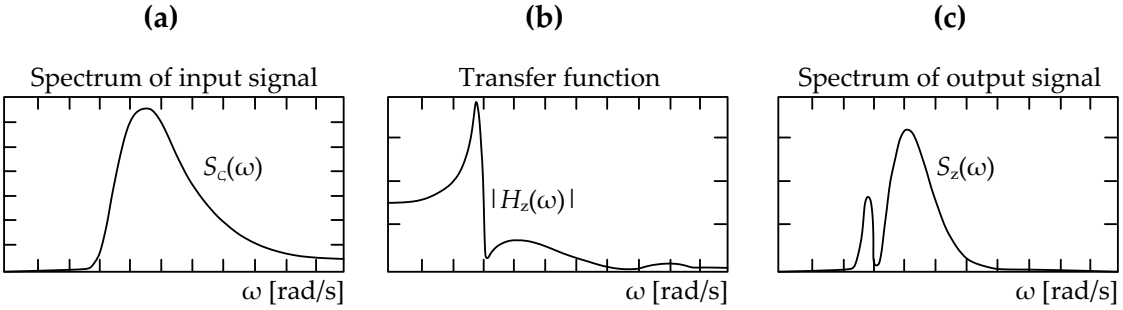

Figure 2.12: (a) Qualitative spectrum of sea state, (b) Transfer function for heave motion of a floating structure, and (c) Response spectrum of heave motion, adapted from [27]

rad/s at 0.05 rad/s increment) and into 12 directions (in case of a directional spectrum) [67]. In a next step, for each frequency (and direction) value a unity harmonic wave, i.e. a wave with the amplitude 1.0, is modeled and the resulting response behaviour of the structure is determined by solving the linearised motion equations either deterministically or numerically. The squared quotient between response amplitude $s_a(\Omega)$ and wave amplitude $\zeta_a(\Omega)$ (in this case equal to one since unity wave) is the value of the transfer function for the frequency Ω (and the direction β_ζ). $s_a(\Omega)$ may also represent an acceleration or a velocity. This procedure is done for all frequency (and direction) values.

$$[Y_s(\Omega)]^2 = \left[\frac{s_a(\Omega)}{\zeta_a(\Omega)}\right]^2 \tag{2.63}$$

In an additional step, the same calculation method is applied for determining the transfer function of the resulting internal forces and stresses of the structure. After calculating the rigid-body motion for a unity wave and circular frequency Ω (and direction β_ζ), the motion values s, $\dot{s}$, and $\ddot{s}$ are exported together with the hydrodynamic loads to a structural design model (generally a FEM-model). Using this model the resulting structural behaviour in form of stresses and deformations is calculated considering the equilibrium of forces with all load actions, including the inertia and damping forces (inertia relief method). In this way, the value of e.g. the transfer function $\left[Y_{m_{yy}}(\Omega)\right]^2$ for the bending moment of the extern hull of an offshore concrete platform may be determined.

$$\left[Y_{m_{yy}}(\Omega)\right]^2 = \left[\frac{m_{yy}(\Omega)}{\zeta_a(\Omega)}\right]^2, \tag{2.64}$$

with $m_{yy,a}$ being the amplitude of the bending moment m_{yy} at a certain location of the extern hull. Similarly, the transfer function of all other internal forces and moments may be established (cf. Fig. 2.11). Again, with transfer functions of internal forces or stresses $[Y_{xxx}(\Omega)]^2$ it is possible to obtain the corresponding spectrum for a given sea state. Since

the amplitude distribution of a narrow-banded spectrum obeys a Rayleigh-distribution, an extreme-value analysis of internal forces resp. stresses becomes consequently possible. Additionally, also the corresponding spectral moments may be calculated and, with them, additional parameters like the standard deviation or the zero-up crossing period T_z. For example, the stress $\sigma_p(t)$ in a prestressing tendon of an offshore concrete structure like a floating quay or a drilling platform has following zero-up crossing period T_{z,σ_p}:

$$T_{z,\sigma_p} = \sqrt{\frac{m_{0,\sigma_p}}{m_{2,\sigma_p}}}. \tag{2.65}$$

Special attention is thus mandatory in the fatigue verification of structural elements since the zero-up crossing period of the stress $\sigma_p(t)$ in the tendon may probably differ from the zero-up crossing period of the wave, i.e. $T_{z,\sigma_p} \neq T_z$. The average number n_{waves} of waves in a sea state of the duration t_{sea} results from

$$n_{waves} = \frac{t_{sea}}{T_z}. \tag{2.66}$$

The corresponding number n_{σ_p} of induced stress cycles in the analysed tendon in a sea state is

$$n_{\sigma_p} = \frac{t_{sea}}{T_{z,\sigma_p}}. \tag{2.67}$$

In case $T_{z,\sigma_p} < T_z$, then $n_{\sigma_p} > n_{wave}$ and, in consequence, the number of stress cycles in the tendon is higher than the number of waves.

The fatigue design has necessarily to take into account the totality of loads experienced by a structural element. In regard to the long-term distribution of sea states, the response spectra of the investigated internal forces or stresses have to be determined for all combinations of the scatter-diagram. For details concerning broad-band spectra see [131]. In the scope of a fatigue analysis, the response spectra may be transformed into time-series of internal forces or stresses according following exemplary equation for the stress σ_p in a tendon.

$$\sigma_p(t) = \sigma_{pm} + \sum_{n=0}^{n=N} \sqrt{2 S_{\sigma_p}(\Delta\Omega_n)\,\Delta\Omega_n} \cos\left(\Omega t + \epsilon_n(\Omega)\right), \tag{2.68}$$

with σ_{pm} representing the average pre-stressing value in the tendon and N as the total number of frequency discretisations. The phase angles ϵ_n are to be selected randomly. Afterwards, one may use adequate counting methods in order to classify the calculated structural internal forces or stresses, determine their magnitude, and the corresponding number of cycles which are required for the fatigue analysis.

An extensive overview and description of the diverse counting procedures is given in [99]. A practical algorithm for performing a rainflow counting has been published in [193] and rewritten in python™ in Appendix A.

An exemplary calculation is performed with a floating structure of pre-stressed concrete based on the data published in [134]. The Seadeck platform was a pontoon-shaped floating structure which was modularly conceived (Fig.2.14). It was the prototype for a large scale development of plants for desalination, chemical processing, oil and gas production or as temporary storage facilities. Also an use as floating support, as vessel or even as part of floating airports, bridges or tunnels is thinkable and promising in regard to costs, robustness, durability, and dynamic behaviour (cf. [87], [53], [142], [150], [159], [28], [186], [202]).

A concrete B45 (today equivalent to C35/45) with an uniaxial compression cylinder strength of f_c = 35.0 MPa was employed in the construction of the platform. The reinforcement was of the type BSt 420/500 with f_{sy} = 420 MPa while the prestressing steel was St 1570/1770 with f_{py} = 1570 MPa. The Seadeck platform was prestressed in the longitudinal direction as well as in the transversal and moreover in the vertical direction so that no concrete cracking was expected even at the ultimate limit state. This is an important requirement of floating concrete structures since both, bouyancy and hydrostatic stiffness, may be negatively affected in case of cracking if no other provisions have been taken in order to guarantee the structural tightness. The total mass amounted ca. 3,444 t and the concrete volume was ca. 1,329 m^3. The height of the pontoon was 6.0 m, the breadth 20.0 m, and the length of a module 61.45 m. With a draught of 2.86 m, Seadeck had acceptable stability properties with a favourable hydrostatic stiffness-matrix. The recalculation of wave and hydrodynamic loads together with the response motion of the structure was performed for this example with the simulation software ANSYS AQWA™ (Fig. 2.15a). The water depth was chosen with 30.0 m, the considered frequency range was set between 0.10...2.40 rad/s, and the directions of the sea states were taken to 0°, 45°, and 90°. Moorings were neglected. In Fig. 2.16a the calculated response amplitude operator (RAO) for the pitch motion in a 0°-sea state is exemplary plotted.

After concluding the hydrodynamic and motional analysis the results were exported to ANSYS APDL™ for the calculation of internal forces (Fig. 2.15b). The structural model was composed of shell elements. Transfer functions for selected locations of interest for the fatigue design of the structure were evaluated for different internal forces (Fig. 2.16b). Finally, through multiplication of the transfer function with the governing sea spectrum, the response spectra of internal forces were obtained. They may be transformed into time series (Fig. 2.17) for a subsequent rainflow counting and a fatigue verification.

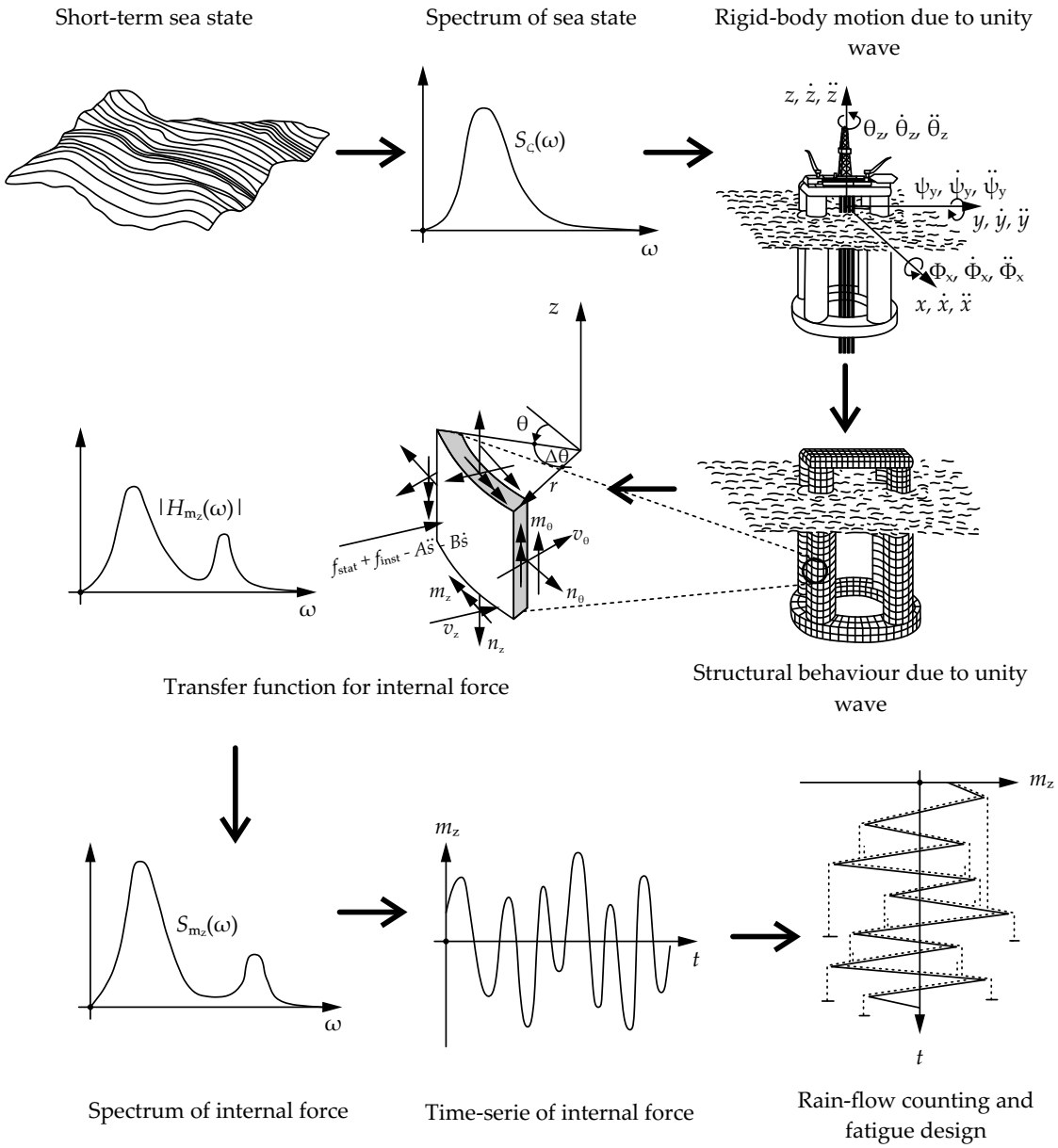

Figure 2.13: Overview of spectral fatigue analysis for a sea state in the short-term, partially adapted from [47]

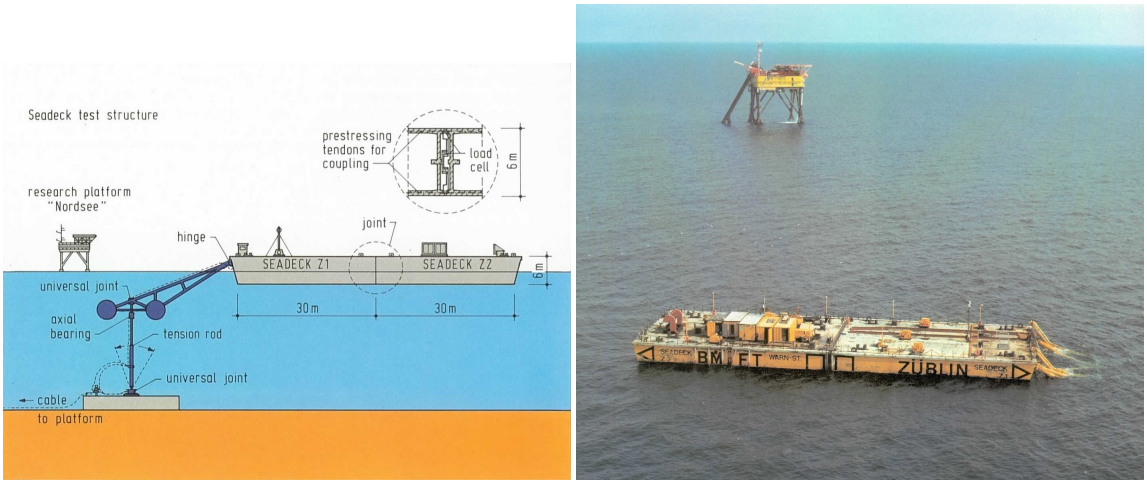

Figure 2.14: Left: Overview of the Seadeck platform, Right: Seadeck platform in the North Sea [134]

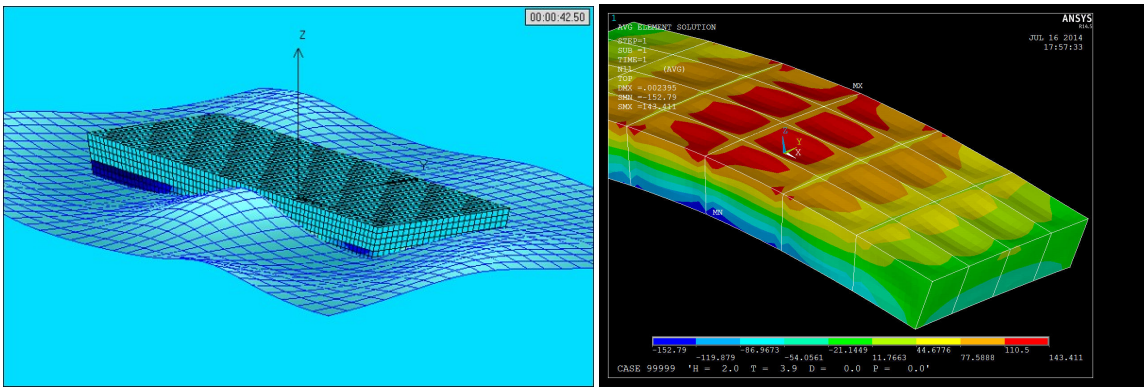

Figure 2.15: Left: Overview of hydrodynamic analysis of the Seadeck platform, Right: Calculation of membrane forces n_x of Seadeck using the FEM-method

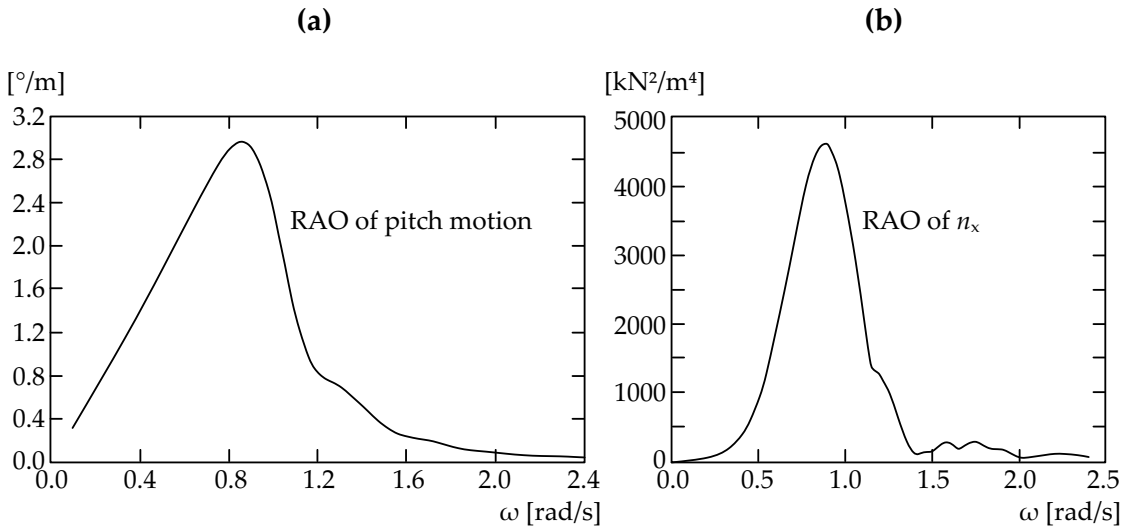

Figure 2.16: (a) Response amplitude operator (RAO) for pitch motion in a 0°-sea state, (b) Response amplitude operator (RAO) for membrane force n_x at the top side of the concrete platform

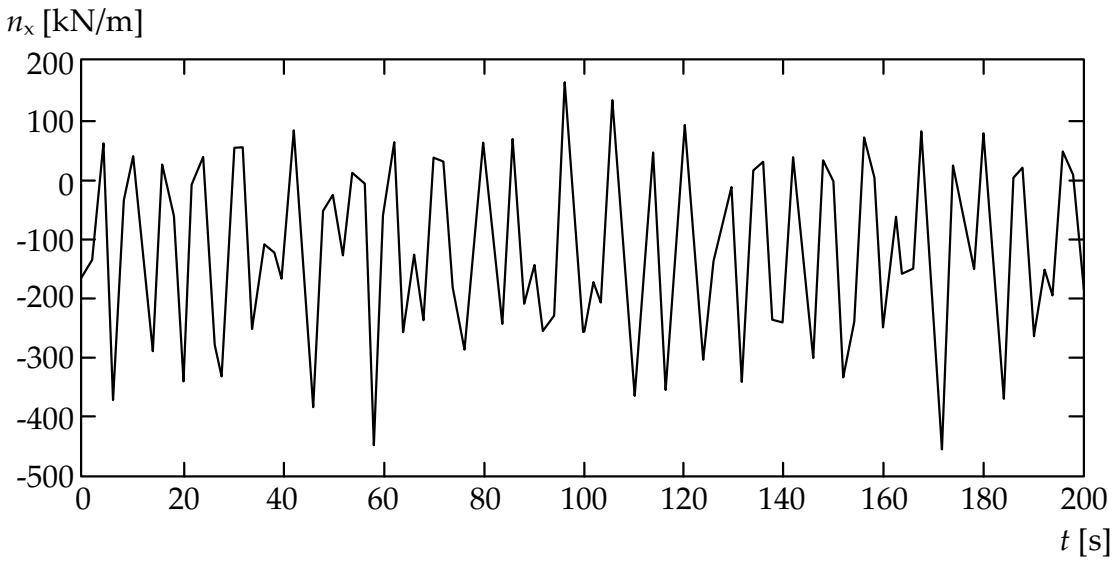

Figure 2.17: Time-series of membrane force n_x at top side of the concrete platform for a given sea spectrum

CHAPTER 3

Material Behaviour

3.1 Reinforcement

3.1.1 Reinforcement Behaviour under Static Loading

Steel may be considered as isotropic for most design calculations in civil engineering. A high tensile strength together with a high ductility – both greatly dependent on the chemical composition, the heat treatment, production technique, and service temperature – are the principal properties which may be used to complement the negligible tensile strength of concrete. Reinforced concrete is a very effective composite material that exhibits sufficient ductility if a reasonable structural design is provided.

An important simplification is the assumption of homogeneously distributed stresses at the cross section of reinforcing bars. In fact, stress concentrations, which are located especially at the rib roots, are not accounted for. A further essential assumption corresponds to the stress direction. Accordingly, steel reinforcement experiences only uniaxial stresses in the longitudinal axis. Multiaxial stress states, like those present in the dowel effect in cracked slab structures, are practically disregarded.

Pull-out tests of reinforcement steel are mostly strain-controlled with minor strain rates of approximately 0.02 ‰/s.

Steel belongs to the crystalline materials, being an alloy of iron and carbon, whereas the carbon content is limited by definition up to 2.06%. Higher carbon contents produce another microstructure and the final material is known as cast iron. The idealised internal structure of steel is composed by crystals where iron and carbon atoms, present as an interstitial solid solution, are arranged in geometric defined units called elementary cells. Similar to other metals, iron and steel exhibit a so called polymorphism – a property that describes the change of the elementary cell depending on temperature, surrounding pressure, and concentration. The most important polymorph transformation is that of face-centred cubic iron (austenite) into body-centred cubic iron (ferrite) [169]. Based on the idealised structure of steel and the currently accepted physical material models, the theoretical steel strength may reach a value of 21,000 MPa. Real materials, though, have a considerably lower strength with values which are lower by a factor of 10^2 [172].

The presence of multidimensional lattice defects is considered responsible for the difference between real and idealised material behaviour. Among others, principally dislocations (one-dimensional), and crystal boundaries (two-dimensional) affect the theoretical steel strength [172]. Dislocations may be present in form of edge or screw dislocations. According to [89], the normal dislocation density in metal materials after solidification

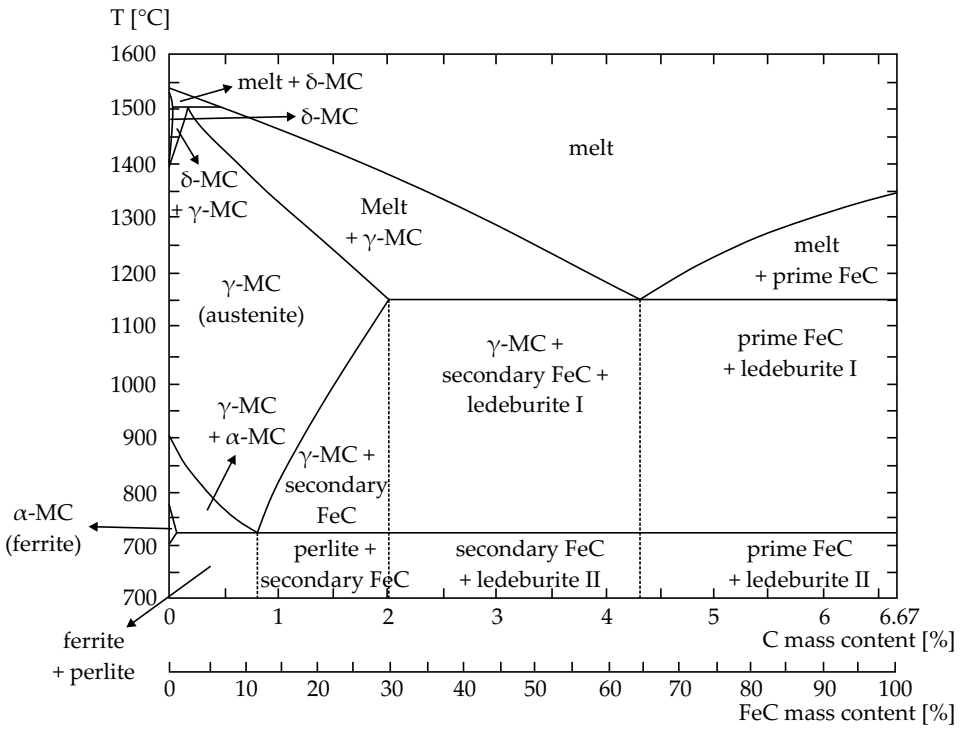

Figure 3.1: Phase diagram of iron and carbon [89]

amounts $10^7/\text{cm}^2$. This value may increase up to $10^{12}/\text{cm}^2$ due to the development of plastic deformations.

Materials experience deformations under the action of forces. In principle, forces activate inner bonding attractive or repulsive stresses between atoms and deviate them from their equilibrium position, enlarging or reducing their corresponding distances. As long as the acting forces do not exceed a critical local value, a local material rupture or the induction of sliding motions (plastic deformations) is not expected. The atoms return to their original equilibrium position and the induced material deformation reverts fully (elastic deformation) [89]. In case of unalloyed steel under one-dimensional stress states and ambient temperature, tensile forces that exceed a certain critical value cause a sliding of crystals along crystallographic planes (sliding planes) in determined crystallographic directions (slip directions) [169]. A crystallographic plane with its corresponding slip direction defines a crystal system. Shear stresses are, therefore, the principal slip parameter [12]. The sliding capacity of crystals is a function of the elementary cells which exhibit various lattice planes depending on the plane direction. Hence, the plasticity of steel is locally a rather anisotropic property [12]. Following the sphere model of atoms, sliding motions are generally activated along those lattice planes which posses the highest packing density of atoms since the required shear stresses in this direction are a minimum. Face-centred cubic elementary cells (e.g. austenite steel) have 12 crystal systems while a hexagonal closed packed elementary cell (e.g. graphite) has only one – a reason for

the poor plasticity of materials with hexagonal closed packed elementary cells. Body-centred cubic elementary cells (e.g. ferrite steel) have, in contrast, theoretically 48 crystal systems. However, not every one may be considered as equivalent to the others. Hence, the plasticity of body-centred cubic materials resides between face-centred cubic and hexagonal closed packed materials [89].

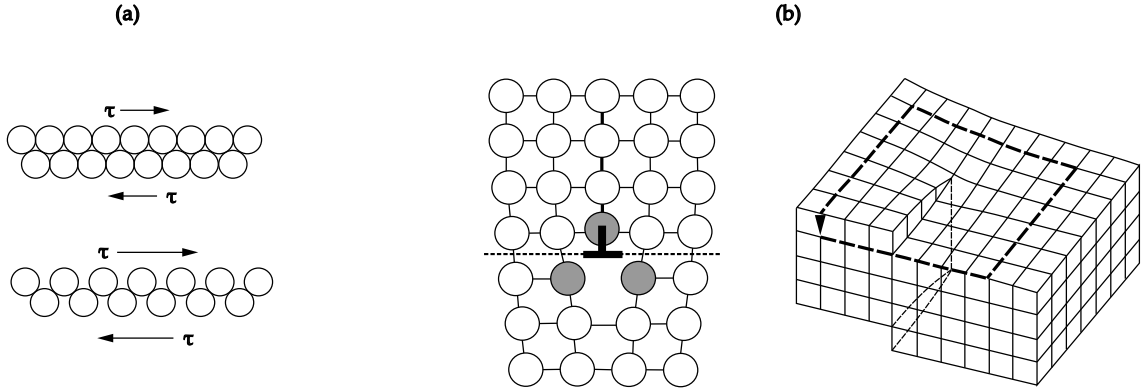

Figure 3.2: (a) Sphere model of dislocation slips [12], (b) Model for an edge dislocation (left) and a screw dislocation, redrawn from [12]

Dislocations inside the crystal lattice structure are described as carrier of plastic deformations [22]. Their formation is induced mainly by diverse crystallographic restrains during crystallisation and the presence of other phases. Dislocations are one-dimensional lattice defects, show interaction effects with other dislocations, and may experience slip motions under the action of forces or temperature. In [22], the elementary processes for dislocation motions are extensive described:

- Slip of edge and screw dislocations,
- reciprocal slicing of edge and screw dislocations,
- cross slipping of screw dislocations, and
- climbing of edge dislocations.

An important phenomenon is the creation of further lattice defects like dipoles, lattice vacancies, and new dislocations owing to plastic deformations. As a consequence, an increasing number of obstacles for the additional dislocation motion emerges and further forces are required for overcoming them. Thus, the material exhibits a strain hardening which is also a function of the deformation rate. A higher deformation rate causes the material to have a lower time lapse to activate the necessary mechanisms for inducing inner slip motions [22]. This leads to a higher material strength.

Reinforcement steel is classified under the unalloyed steel class [33]. In accordance with [38], the percental amount of accompanying elements like manganese, nickel, chrome, molybdenum, silicon, aluminium, and others is strictly limited to comparably low values. Carbon does not exceed a 0.22% content. These elements generally lead to a strength increase in different degrees, however, with a simultaneous loss of ductility (exception:

nickel). Therefore, the reduction or restriction of other metallic, or non-metallic elements causes reinforcement steel to be (more) adequate for welding, possessing also an acceptable ductility capacity [89]. Moreover, alloy elements lead in many cases to a creation of mixed crystals, and for instance, of further obstacles for the dislocation motion (strength increase). This process is usually subjected to a ductility decrease, though. In compliance with [36] and [33], the adopted manufacturing processes are listed below:

- Hot-rolled steel without post-treatment. The molten steel flows into a rising permanent mould, being moulded to a slab [89]. Following this step, the ribbed bar shape is achieved by hot rolling the still hot or reheatet steel slab (approx. 1100°C) into the desired shape [91]. The steel properties depend only on the steel chemical composition. In many cases, carbide-forming alloy elements with an overall content percentage of <0.12% like vanadium, titan, and boron, are added to the steel melt, leading to the formation of a fine-grained microstructure which results from the presence of nucleus-inducing carbides [33].
- Hot-rolled steel with a post-heat-treatment. The heat treatment consists on hardening and tempering the steel during the rolling process [33]. High strength and hardness values are obtained first due a rapid cooling of the austenite steel (γ-steel) generally in water, resulting in a difussionless microstructural transformation where carbon atoms are forced-dissolved in a body-centred cubic ferrite steel (α-steel). The obtained microstructure is a highly strained body-centred tetragonal one, known as martensite, which exhibits significant strength and hardness values, yet a very brittle bahaviour. The martensite distribution over the steel is, depending on the hardening process and the temperature gradient, not uniform and is especially concentrated on the ribbed surface area of the reinforcement (surface-hardening). In a further step, the steel is tempered, i.e. it is subjected to a heat treatment beneath the so called A_1-temperature [89], which lets, depending on temperature and time, to a certain diffusion of carbon atoms and a partial reduction of hardness combined with an increase of ductility. The reinforcement presents, thus, a normal-strength ductile core and a comparatively hard surface. This has the clear advantage of an increased resistance against wear resulting from the friction with the surrounding concrete under fatigue loading, yet with a more susceptible behaviour against notches [199], and a consequently lower fatigue strength. Also the induced surface-hardening leads to residual stresses inside the reinforcement bars – a fact that may further reduce the fatigue strength.
- Hot-rolled steel, then cold-hammered. After the hot-rolling process the steel bar is subsequently subjected to a stretch forming with up to 10% plastic strains [154] without any heat addition. As a consequence, the crystal dislocation intensity is considerably increased, which leads to a more abundant mutual impediment between crystal dislocations and to an aggravation of the crystal sliding motion [89]. Finally, a so called strain hardening occurs, revealed in form of an strength increase with an undesired ductility loss.
- Cold-formed steel. The reinforcement bars are manufactured by cold-rolling the

steel slab.

It is worth mentioning that rolling processes cause a stretching of the steel grains whereby the steel loses its isotropic properties [89].

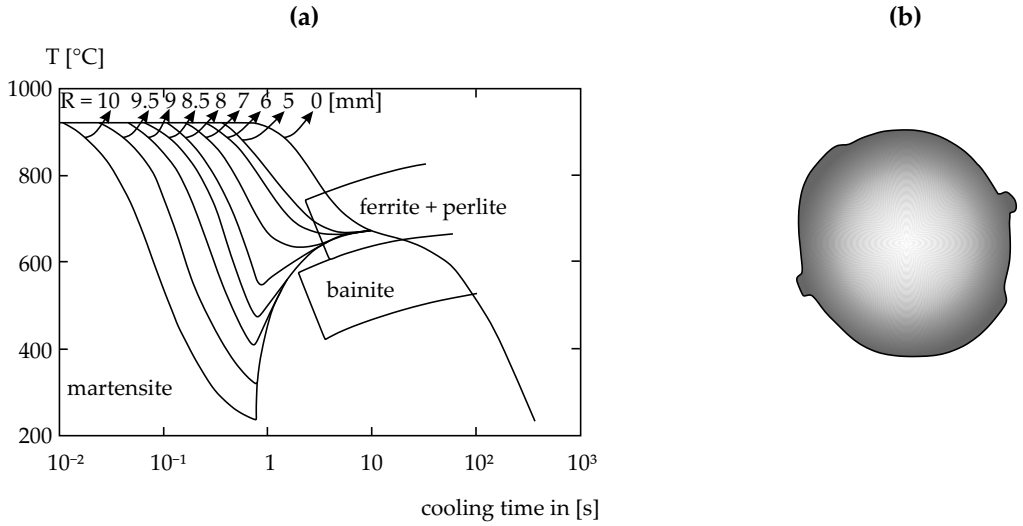

Figure 3.3: (a) Time-temperature-transformation (TTT) diagram of hot-rolled reinforcement steel with a post-heat-treatment, redrawn from [154]; (b) Reinforcement cross section: Hard surface and ductile core, redrawn from [33]

A detailed description of the mechanical behaviour of reinforcement steel under static, monotonically increasing, practically one-axial loading is given in [2]. Until reaching the so called yield strength f_{sy} the reinforcement steel behaves linear-elastically. Reinforcement steel that has been subject of hot-rolling or heat treatment processes presents a yield plateau immediate after exceeding the yield strength. At this stage, which begins as soon as the steel strain achieves a value of ca. ϵ_{sy} = 2.5‰ and that corresponds nowadays to an average stress of ca. f_{sy} = 550 MPa, several dislocation motions are induced and the reinforcement steel exhibits under strain-controlled load conditions a nearly constant strain increment by a virtually constant nominal stress (yield strength). The yield plateau is completed after yielding is distributed over the entire bar length [178], which occurs by average steel strains of 15...25‰. The steel deformations are already irreversible; after unloading only the elastic part may be reversed. Following the yield plateau, a so called strain hardening occurs under increasing strains, i.e. a nonlinear stress increment is required in order to increase the average strains until reaching the nominal ultimate tension strength f_{su}. A volume variation does not take place; consequently, a transverse bar contraction is observed, and the sectional area decreases [116]. By determining the nominal stresses by means of the coefficient of force and initial section area, a material softening may be noticed. By further increasing strains the steel stress declines until failure. Hereby, an intense local lateral bar contraction takes place which extends over a length twice the bar diameter [116]. If the real stress in this contraction region is calculated, it may be observed that the stress increases locally until finally a material failure happens.

Other than hot-rolled steel, cold-formed reinforcement steel does not present such a yield plateau since dislocation motions have already been activated during manufacturing and the transition from elastic to plastic deformations is steady. According to a general agreement, the yield strength is defined as the strength which corresponds to a remaining strain of $\epsilon_{sy} = 2.0‰$ after unloading [178].

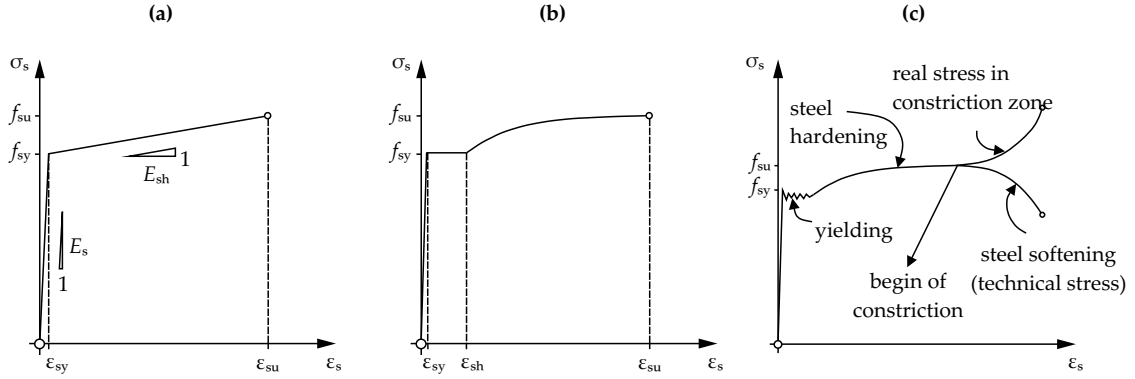

Figure 3.4: (a) Idealised bilinear stress-strain curve of reinforcement steel according to [2]; (b) Idealised stress-strain curve of reinforcement steel with nonlinear hardening according to [2]; (c) Stress-strain curve of reinforcement steel with technical softening and real stress in constriction zone

The (ductile) failure of reinforcement steel in the material plane proceeds in 3 stages [89]:

1. Tensile stresses lead initially to elastic strains without producing any damage.
2. By greater becoming stresses, manganese sulphide are segregated from the steel microstructure, forming local defects where microcontractions originate as consequence of raised stresses.
3. Microcavities result from the above mentioned defects, weakening the inner structure and leading to stress concentrations which ultimately cause a material separation.

3.1.2 Reinforcement Behaviour under Fatigue Loading

Fatigue loading produces changes in the steel microstructure. Following stages [169] may be observed:

1. (Micro)plastic deformations.
2. Crack formation.
3. Uncritical crack growth.
4. Critical crack growth and material failure.

Precisely microplastic deformations lead to microstructural changes and are described as principal damage-inducing parameter in the fatigue of metal materials [169], [25]. In the stage of a fatigue-induced (micro)crack formation, a series of property changes can

be observed (e.g. increase of the electrical resistance, heat conductivity reduction, other damping values). In the following uncritical crack growth, no distinctive changes are noticed for the load capacity. As soon as a critical (macro)crack growth rate is achieved, additional changes become apparent. A fatigue fracture may only occur if a part of the loading stress are tensile stresses; pure compression stresses do not lead to fatigue [31].

The stress-strain-diagrams under cyclic respectively fatigue loading are known to form hysteresis figures whose area integral provides a value of the performed work by the mechanical system and of the dissipated energy. Microstructural inner friction and microdamaging processes, which lead to irreversible (micro)plastic deformations, result in irrecoverable, released heat energy. Even stresses far under the yield strength that are in the order of the so called fatigue endurance limit may induce local microplastic, irreversible deformations which cumulate with every load cycle [25], [102]. Courtney [31] speaks in this context about an "inhomogeneous plastic flow occurring (usually) at a microscopic level". Depending on the loading character beyond the yield strength f_{sy} (constant stress amplitude or constant strain amplitudes), the stress-strain-hysteresis do not remain constant, but indicate rather the development of an either cyclic stress hardening, or a stress softening, or a mixed behaviour of both [169]. In the case of reinforcement steel, which is characterised by showing so called Lüders deformation ligaments [178], there is a transition from stress softening to stress hardening [169].

Under the action of fatigue loading the dislocation motions concentrate on persistent slip bands [25], developing geometric band extrusions and intrusions which modify the surface topography of the material, being precursors of a crack formation [169]. Persistent slip bands may be transcrystalline or even intercrystalline [25]. The term *persistent slip bands* connotes their stability on the surface, even after polishing [122]. Fatigue cracks appear mostly on the outer material surface at the location of material defects like vacancies, inclusions, inhomogeneities, scrapes, etc. The growth of extrusions and intrusions on the surface is intensified. As a result, macro slip bands (protrusions) are forged, producing a notch effect which leads to (multiaxial) stress concentrations [169] that may exceed the material strength [89]. In the case of brittle, non-metal inclusions like manganese sulphides, these may also aggravate the above mentioned inner notch effect. This represents a further argument for requiring a strict restriction of impurities in reinforcement steel. The fatigue crack initiation in most cases originates at the external surface [31].

Following the stage of crack formation, several microcracks merge gradually. Finally, a principal macrocrack emerges and grows [102]. The growth path of microcracks is in most cases transgranular since grain boundaries represent a greater restraint for the slip motion [164]. In case of unalloyed steel, fatigue cracks develop at the beginning on the material surface in the direction of maximal shear stresses. Subsequently, it expands orthogonally to the direction of maximal tension stresses. The crack surfaces are characterised for exhibiting wavelike bands (striations) located perpendicular to the crack direction of propagation. The distances between striations are, however, not a measure of the crack growth per load cycle [31]. The crack growth rate depends primarily on the material ability to resist a crack growth and not on the material surface conditions [164]. Growth and form of striations have been proven to depend on the load intensity, and for instance, on the load history [164]. Due to the fact that fatigue stresses are usually considerably

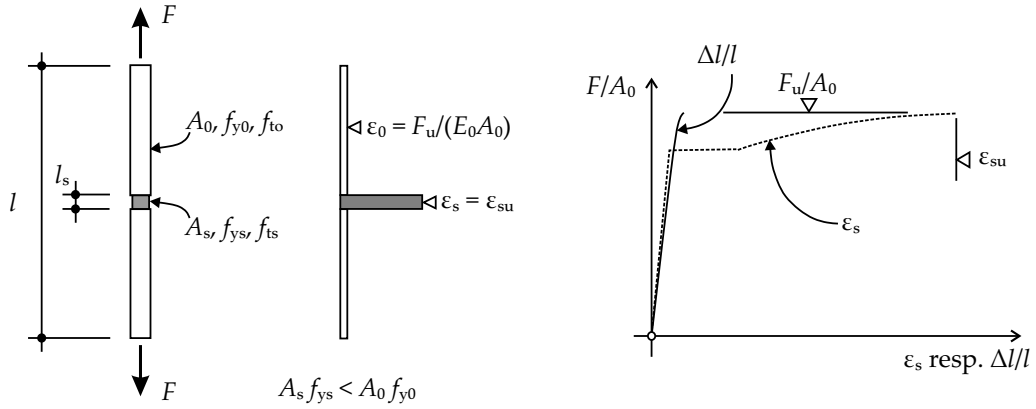

Figure 3.5: Load-deformation-behaviour of a reinforcement bar with local disturbance zone, redrawn from [178]

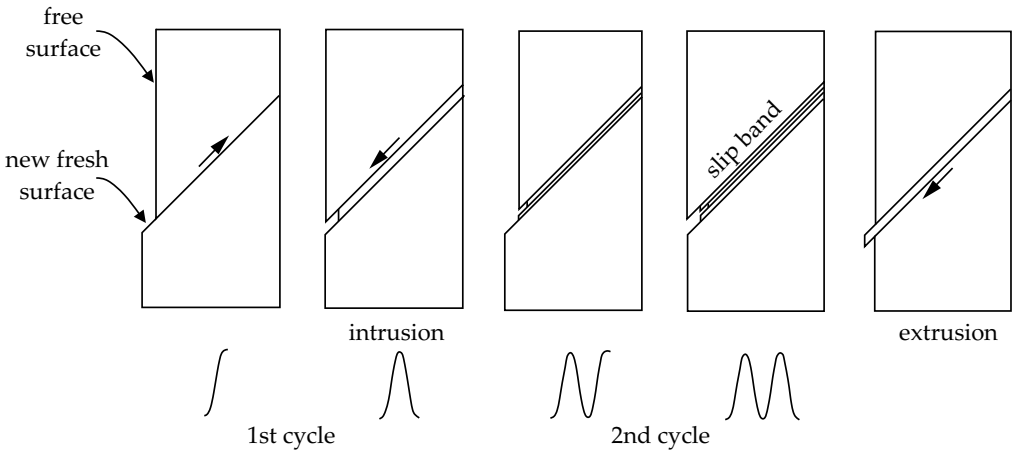

Figure 3.6: Crack nucleation due to cycle slip, redrawn from [164]

below the yield strength, the (multiaxial) stress conditions and the crack propagation may be described by means of linear-elastic fracture mechanics [169]. For a more detailed description of the developed processes inside the material see [164].

In the final fatigue stage, the growth rate of a fatigue crack increases. Due to the caused material separation the effective stress-carrying area is reduced and the structural element, in this case the reinforcement bar, may no be capable to bear the applied (service) load. Consequently, the reinforcement bar ruptures, being this final failure rather a ductile (static) one [56]. The logical consequence of this process is that the ultimate structural safety is no longer given as soon as the fatigue crack reduces considerably the structural area of the reinforcing bar. This may be the case at the ultimate limit state since structural design is performed based on intact structural dimensions and calculations models developed for quasi static loading conditions without a previous fatigue loading. The fact that usually a sufficient structural safety is achieved in praxis may be a result of the applied statistical safety concept, generous strength provisions, and conservative (simplified)

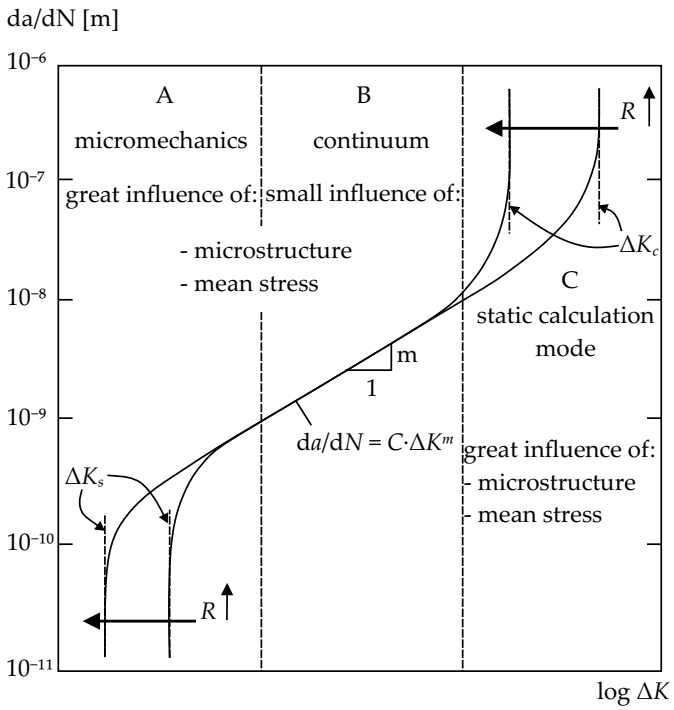

Figure 3.7: Development of crack propagation: Crack growth per load cycle da/dN as function of the stress concentration range ΔK , redrawn from [169]

loading models. Performed tests in the context of this work, where tension elements of reinforced concrete have been subjected to an intense fatigue loading without reaching a fatigue failure, have been tested afterwards statically (see Ch. 4.2.1).

The fatigue damage D in reinforcement steel is quantified via a reduction of the bar cross section area A_s. Owing to fatigue induced cracks, the bar cross section area is effectively reduced, taking a value

$$A_{s,fat} = A_s(1 - D), \tag{3.1}$$

with $0.0 \leq D \leq 1.0$. Assuming a constant loading force range $N_0 = \Delta\sigma_{s0} A_s$, the stress range in the damaged reinforcement becomes under consideration of Eq. (3.1) [112]:

$$\Delta\sigma_s = \frac{\Delta\sigma_{s0}}{1 - D}. \tag{3.2}$$

Assuming a linear proportionality between the derivation of the fatigue damage D after a number N of cycles with constant loading ranges and $\Delta\sigma_s^m$, a proportionality constant c_0

is introduced.

$$\frac{\mathrm{d}D}{\mathrm{d}N} \propto \Delta\sigma_{\mathrm{s}}^{m} \Longleftrightarrow \frac{\mathrm{d}D}{\mathrm{d}N} = c_0 \Delta\sigma_{\mathrm{s}}^{m}. \tag{3.3}$$

Using Eq. (3.2) in Eq. (3.3)

$$\frac{\mathrm{d}D}{\mathrm{d}N} = \frac{c_0 \Delta\sigma_{\mathrm{s0}}^{m}}{(1-D)^{m}}. \tag{3.4}$$

After integration of Eq. (3.4) one obtains

$$-\frac{(1-D)^{m+1}}{m+1} = N c_0 \Delta\sigma_{\mathrm{s0}}^{m} + c_1, \tag{3.5}$$

being c_1 another constant. With the boundary conditions $D(N = 0) \equiv 0.0$ in Eq. (3.5) (no load – no damage)

$$c_1 = -\frac{1}{m+1}, \tag{3.6}$$

and $D(N = N_{\mathrm{u}}) \equiv 1.0$ in Eq. (3.5) and (3.6), i.e. fatigue failure is achieved after reaching a maximal number N_{u} of bearable load cycles

$$N_{\mathrm{u}} = \frac{1}{c_0 (m+1) \Delta\sigma_{\mathrm{s0}}^{m}}. \tag{3.7}$$

Eq. (3.5) may be rewritten in the form

$$D(N) = 1 - \left(1 - \frac{N}{N_{\mathrm{u}}}\right)^{\frac{1}{m+1}}. \tag{3.8}$$

The proportionality assumption taken in Eq. (3.3) leads to a nonlinear development of the fatigue damage D with a sharp increase for values $D > 0.8$. According to [112], for constant inclination values m of the Wöhler curve (cf. Tab. 3.1) the superposition principle is valid for D and a fatigue failure is obtained by

$$\sum_{\mathrm{i}} \frac{N_{\mathrm{i}}}{N_{\mathrm{u}}} = 1.0 \tag{3.9}$$

Aggressive environmental conditions, as this is the case for offshore structures, as well as corrosion of the reinforcement may affect the stages of crack formation and growth

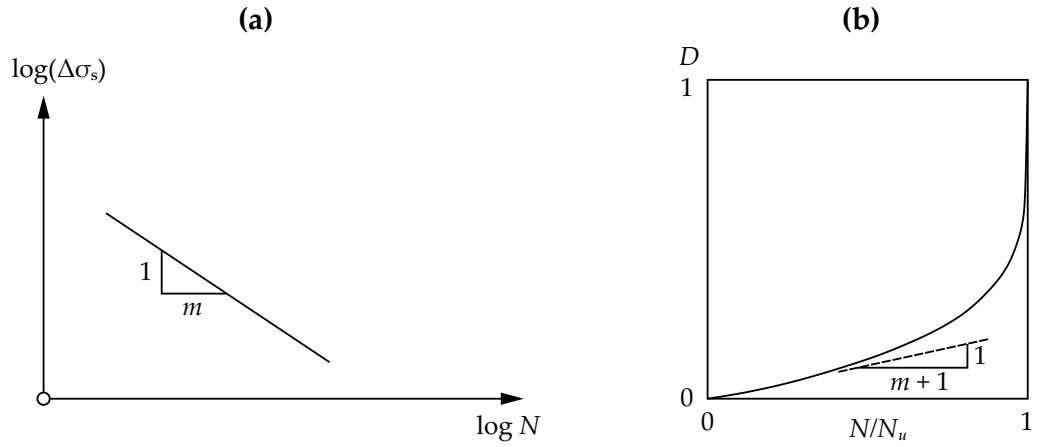

Figure 3.8: (a) Wöhler curve with constant inclination; (b) and fatigue damage development of reinforcement as function of the load cycles, redrawn from [112]

considerably [199], [164].

The research of the fatigue behaviour of steel reinforcement for engineering purposes, like for other materials, focuses principally on the fatigue strength, i.e. the material capacity of carrying service stresses for a certain number of cycles under diverse conditions. Information concerning the deformation behaviour during and as a consequence of a fatigue loading is practically inexistent.

For the sake of practicable design calculations, diverse influencing parameters are not accounted for in fatigue verification analyses. The most important identified parameter in single-level fatigue tests with sinusoidal stress curves is the stress variation range $\Delta\sigma_s$ [102], [15]. Only this parameter is considered in most standards of reinforced concrete. One exception may be found in [42] where the reinforcement steel fatigue strength also depends on the exposure class. The yield strength f_{sy} does not have a relevant significance [149]. In [133] the bending radius of curved reinforcing bars, as well as the fact whether the reinforcement has been welded or not, are also considered through different inclination values of the Wöhler curve.

Most research on the fatigue behaviour of steel reinforcement also bases on single-level fatigue tests with sinusoidal stress curves as described in [37]. According to [151], at present such fatigue tests are performed with a maximal stress of $\sigma_{s,max}$ = 300 MPa and test frequencies of 10...20 Hz respectively 60...140 Hz. These comparatively high test frequencies are somehow necessary in order to obtain reasonable test durations. In [111] and [102] is reported that test frequencies up to 150 Hz do not have any impact on the fatigue strength of reinforcement. Courtney [31] affirms that the fatigue response of metals may be considered as frequency-independent as long as the test frequency does not exceed 200 Hz. However, Schott [169] indicates that tests with high load frequencies produce a temperature rise in the specimens, resulting in a lower fatigue performance. In this case, test specimens should be cooled regularly while testing.

According to [209] and [15], fatigue tests of reinforcement are basically performed at straight, free reinforcing bars or at straight, in concrete embedded bars. The majority of

available test results have been obtained employing free reinforcing bars since, on the one hand, these are more economical and simpler to handle; on the other hand, it is mostly accepted that fatigue tests on free bar specimens are more unfavourable and, for instance, more conservative. Reports like [120] seem to confirm this fact. Zilch [209] mentions that free reinforcement bars always fail at the weakest location, beginning at the ribs root. Due to the bond between reinforcement and surrounding concrete, the steel stresses are not constant, but maximal – in static, monotonically tested samples – at crack locations. Since the probability that the weakest bar section coincides with the crack location is relatively low, it is logical to conclude that free reinforcement bars are more prone to experience a fatigue failure. Though, it is also possible that embedded bars rupture earlier due to the friction experienced by means of a cyclic slip motion (fretting corrosion) between concrete and steel [102]. Furthermore, the bond strength may be significantly weakened due to fatigue loading (bond fatigue) while the reinforcement develops residual stresses (cf. Ch. 3.3.2).

Actually, the fatigue design of steel reinforcement in standards is done using Wöhler curves derived from single level tests in double logarithmic scale. Based on a sufficient number of stress-controlled tests, by which the stress range $\Delta\sigma_s$ is hold constant and the number of load cycles until failure is registered, a statistical analysis follows in order to determine the 5%-quantile value for each $\Delta\sigma_s$ [151], [15]. Hereby, a Gauss probability distribution is assumed. Danielewicz [32] points out that the design fatigue strength of reinforcement is 40...70% lower than its mean value, being the phenomenon of the fretting corrosion the principal reason for it. According to [14], fretting corrosion is a local corrosion process on metal surfaces as a result of friction without outer heat input. Through (cyclic) friction a local notch develops – it is an initiation point for a fatigue crack. For a mathematical description of the Wöhler curves of reinforcement the linear approach (in logarithmic scale) made by Basquin has become the most accepted [102]:

$$N\Delta\sigma_s^k = C, \tag{3.10}$$

with k as the inclination of the Wöhler curve, N as the number of load cycles till failure, and $\Delta\sigma_s$ as the stress range. C is a constant. The defined Wöhler curves in standards like [133] reflect the actual state-of-the-art of fatigue of reinforcing steel [15]. By $N = N^*$, the inclination of the Wöhler curve changes and becomes flatter. The inclination values for k_i depend on the bar diameter, the environment, and whether the reinforcing bar has been bent or welded. However, even tests performed on straight, free reinforcement bar specimens reveal a great scatter depending on the manufacturer or the producing country [32]. Moreover, test values for a number $N > 10^7$ of load cycles are scarce. Newly, Heeke [76] has conducted single-level tests on both, free reinforcing steel bars and in concreted casted bars, achieving a number of load cycles $N = 10^7$. His results show that the design Wöhler curves in [133] are conservative. Moreover, the fatigue strength of embedded specimens is 13% higher than free reinforcing bars.

Based on the simple but practicable cumulative damage hypothesis of Miner-Palmgren and on the Wöhler curves of reinforcement it is possible to calculate the damage-equivalent

Table 3.1: Parameters of Wöhler curves for reinforcement steel embedded in concrete [51]

	N^*	Stress exponent		$\Delta\sigma_{Rsk}$ [MPa]	
		k_1	k_2	at N^* cycles	at 10^8 cycles
Straight and bent bars $D \geq 25\varnothing_s$					
$\varnothing_s \leq 16$ mm	10^6	5	9	210	125
$\varnothing_s \geq 16$ mm	10^6	5	9	160	95
Bent bars $D \leq 25\varnothing_s$	10^6	5	9	(*)	(*)
Welded bars including tack					
Welding and butt joints	10^7	3	5	50	30
Mechanical connectors	10^7	3	5	65	40
Marine environment(**)	10^7	3	5	65	40

(*) Equal to values of $\varnothing_s \leq 16$ mm multiplied with $\xi = 0.35 + 0.026D/\varnothing_s$
(**) Values according [24]

stress range $\Delta\sigma_{s,equ}$ which, by definition, causes the same damage as a real given random loading. Yet, it is important to mention that the concept of damage-equivalent stress ranges is valid as long as it may be assumed that the load history and the randomness character of loads are negligible. After analysing a stress-time-series $\sigma_s(t)$ using an appropriate counting method, a classification of the calculated stress ranges $\Delta\sigma_s$ and mean stresses $\overline{\sigma_s}$ with the corresponding number of load cycles n may be determined by means of a Markov-matrix. Each couple $\Delta\sigma_{s,i}$-n_i induces a material damage and may be estimated separately. Following [32], the damage D_{koll} induced by a real sequence of stresses may be the same as D_{equ}, induced by a damage-equivalent stress range $\Delta\sigma_s$ with a number of

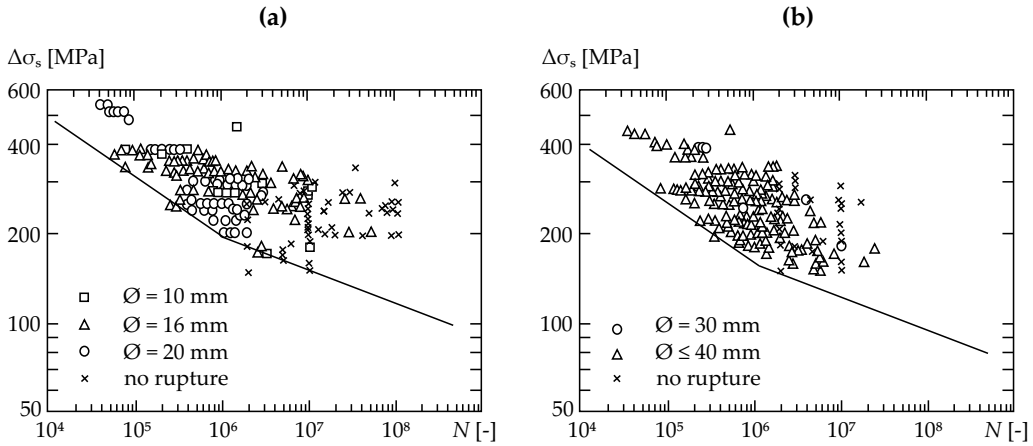

Figure 3.9: Comparison of Wöhler curve of straight reinforcement bars according DIN 1045-1 with test values for (a) $\varnothing_s \leq 28$ mm and (b) $\varnothing_s \geq 28$ mm according to [77]

cycles n_{equ}.

$$D_{\text{koll}} = \frac{n_{\text{equ}}}{N(\Delta\sigma_{\text{s}})}. \tag{3.11}$$

Eq. 3.10 is satisfied by every pair of values of the Wöhler curve and the damage-equivalent stress range $\Delta\sigma_{\text{s,equ}}$. Based on it:

$$N(\Delta\sigma_{\text{s,equ}}) = \frac{\Delta\sigma_{\text{Rsk}}^{k} N(\Delta\sigma_{\text{Rsk}})}{\Delta\sigma_{\text{s,equ}}^{k}}. \tag{3.12}$$

Combining Eq. 3.11 and 3.12 one obtains

$$D_{\text{koll}} = \frac{n_{\text{equ}}\Delta\sigma_{\text{s,equ}}^{k}}{N(\Delta\sigma_{\text{Rsk}})\Delta\sigma_{\text{Rsk}}^{k}} \tag{3.13}$$

And by choosing $n_{\text{equ}} = N(\Delta\sigma_{\text{Rsk}})$, the induced material damage is equal to

$$D_{\text{koll}} = \frac{\Delta\sigma_{\text{s,equ}}^{k}}{\Delta\sigma_{\text{Rsk}}^{k}}. \tag{3.14}$$

For design purposes, according to the concept of partial safety factors, it is appropriate to reshape Eq. 3.14 into

$$D_{\text{knoll}} \leq D_{\text{u}} = 1.0 \Rightarrow \gamma_{\text{Sd}}\Delta\sigma_{\text{s,equ}} \leq \frac{\Delta\sigma_{\text{Rsk}}(N^{*})}{\gamma_{\text{s,fat}}}, \tag{3.15}$$

where γ_{Sd} and $\gamma_{\text{s,fat}}$ are partial safety factors and N^{*} is an arbitrary selected number. Usually, $N^{*} = 10^{6}$. The boundary between low-cycle-fatigue (LCF) with stresses $\sigma_{\text{s}} \geq f_{\text{sy}}$, and high-cycle-fatigue (HCF) with $\sigma_{\text{s}} < f_{\text{sy}}$ lies approximately by $N = 10^{3}$ load cycles, where the plastic strain ranges are almost equal to the elastic strain ranges $\Delta\epsilon_{\text{s,pl}} \approx \Delta\epsilon_{\text{s,el}}$ [31].

Though, the linear cumulative damage hypothesis of Miner-Palmgren has to be taken with care since it may not be accurately enough. In fact, according to Frost et al. [56], the damage accumulation in metals is nonlinear and depends on the load history. In two-level step tests, where the first load step is higher than the following, the crack growth rate is reported to decelerate and the fatigue life to increase; otherwise, by an inverse order of load steps, the crack growth rate is reported to be higher. The reason may be found in different microstructural damage processes, different interactions with residual stresses and plasticised regions which should not be simply added. In [56] is also reported that the steel endurance under random fatigue loading may be shorter.

The reinforcement steel surface is a further important parameter [102], [48]. The ribs on the surface, which are generated by means of (hot or cold) rolling with the finality of increasing and ensuring the bond by interlocking, may present different forms and are basically unfavourable for the fatigue strength. The reason is the induced notch effect which leads to stress concentrations and, for instance, to a higher risk of developing fatigue cracks. The notch effect is further intensified due to the force transfer between reinforcement and concrete since the bond-interlocking also generates multiaxial stress states on the ribs [102]. Sharp changes of geometry increase the present notch effect. Observed fatigue cracks mostly initiate at the rib roots where the stress concentrations are maximal. However, the statistical scatter of test results is high [48]. Schijve [164] reports among other things that inhomogeneous plastic deformations, like those induced by notches, may cause residual stresses in the material, leading to increasing mean stress values and a higher risk of fatigue failure. Hence, it is essential that ribs roots are rounded in order to reduce any notch effect. According to [102], the interlock ribs should not cross the longitudinal steel bar ribs since this produces unfavourable multiaxial stress states. For this reasons, reinforcement ribs are crescent-shaped [40].

Generally, the metal fatigue strength is also enhanced with increasing yield strength [89]. This applies to smooth reinforcing bars (which practically are not employed anymore). The fatigue behaviour in ribbed bars, though, is rather dominated by the induced notch effect of the ribs [102]. Likewise, any applied curvatures on the reinforcement bars may reduce the fatigue performance significantly due to the developed plasticising of the outer side and the internal stresses on the inner side [102]. Bending radii should therefore not fall below a certain limit that is stipulated in corresponding standards.

Another imperative factor of the fatigue strength is corrosion of the reinforcement. In [102], based on literature, the pitting corrosion is mentioned as the most dangerous type of corrosion: Apart from a reduced sectional area, the (sharp) corrosion front represents a notch which leads, again, to fatigue-supporting stress concentrations. Reinforcement steel that is exposed to seawater is thus especially vulnerable [111], [149]. Price et al. [149] reports of structural members of reinforced concrete tested under sea water. Correspondingly, two forms of fatigue crack initiation may be observed: Under high stress ranges $\Delta\sigma_s$ and load frequencies the crack initiates at rib intersection points, leading to a shorter fatigue life; otherwise, under low stress ranges $\Delta\sigma_s$ and load frequencies, pitting corrosion of the reinforcement occurs at primary cracks, being the starting point for a fatigue crack. In [81] is reported that seawater-corrosion of reinforcement in structural beams may extend the fatigue life thanks to a "blunting of initiated cracks", but corrosion also leads to a reduction of the reinforcement sectional area, facilitating the growth of present fatigue cracks. On the basis of fatigue tests carried out on reinforcement bars under corrosive conditions, Weirich [199] concludes that reinforcing bars with diameters $\varnothing_s \leq 16$ mm have a pronounced steeper Wöhler curve, leading to a weaker fatigue strength. He also suggests a modification of the design Wöhler curves in standards for the case of corroded reinforcement. Furthermore, the experienced mean stress $\overline{\sigma_s}$ exhibits an influence on the fatigue strength.

In [111] the role of the mean stress $\overline{\sigma_s}$ may be determined by means of a modified Goodman diagram and is not as pronounced as the stress range $\Delta\sigma_s$. Nevertheless,

the value of $\overline{\sigma_s}$ in fatigue tests should always be indicated for the purpose of better comparability with other results. According to [48], [102], and [111] the reinforcement shows a so called size effect: Higher size values cause the fatigue strength to decrease since the probability of occurrence of defects is connected to the value of the bar diameter. Reinforcing bars with low diameter values present also a finer microstructure. Welding also affects the fatigue behaviour negatively. In [89], primarily the brittle heat-affected zone (of unalloyed steel) is made responsible for the reduction of fatigue strength together with frequent surface irregularities due to welding – both hard to avoid in the construction practice. Therefore, the Wöhler curves for welded reinforcement steel is more adverse in design standards. Even in highly dynamic loaded structures like bridges or offshore structures, the use of welding on reinforcement is prohibited.

The selected way for fatigue analysis bases on the statistical analysis of a great number of test specimens with different varying parameters. Generally, the scatter of results of fatigue tests is high [50]. However, there is practically no data about the fatigue behaviour of reinforcement under variable amplitude loading or even random loading. Following the descriptions given in [164], where general results from variable amplitude tests are presented and discussed, the cumulative damage is a nonlinear function which depends on the load history. This also implies that the linear damage function may not always be safe. Since reinforcement steel exhibits a rich number of notches (ribs), the observations found in [164] may also apply to reinforcement steel. Schott [169] reports likewise of diverse fatigue tests with varying amplitudes, i.e. with different sequential load arrangements, from other authors and concludes that the fatigue behaviour of metals is considerably dependent on the load history. Therefore, a correct prediction of the fatigue life of metals is also only possible if mathematical models are able to account for the effects of different load sequences.

Table 3.2: Stress analysis feature scales in metal fatigue [148]

Scale [mm]	Stress analysis feature
10^{-1}	Large plastic strains
1	Elastic-plastic field
10	Stress intensity factor
100	Component or specimen

Schijve [164] declares that no macroplastic strains are visible during and due to a fatigue loading. Although the fatigue process is connected to microplastic material deformation, there is practically no reports in scientific literature about macroplastic strains, i.e. over a visible segment length. Christ [26], [25], however, reports about cubic body-centered metals with pronounced Lüders-band-spreading (reinforcement steel belongs to this category). Accordingly, a phenomenon that he calls "cyclic creep" (which is misleading since steel creep appears only by high temperatures above 30% of the melting temperature [89]) may be observed. Test samples under stress-controlled, cyclic, linear-elastic fatigue loading experience according to this a time-dependent increase of the average strains. The

carbon and nitrogen contents have showed to be responsible by causing an increase of slip dislocations regions which, on the one hand, produce strain-hardened regions that are compensated by further plastic deformations. On this way, the test sample is characterised by an inhomogeneous distribution of elastic- and plastic-deformed regions, e.g. in the vicinity of notches [56], where residual stresses may be induced, quickly exceeding the yield strength f_{sy}. Milella [122] declares that the observed plastic deformation during the fatigue process may be found only on the metal surface, stretched over a region of the size order of a few metal grains. In the macroscale, in contrast, the steel is supposed to exhibit a linear-elastic behaviour.

3.2 Concrete

3.2.1 Concrete Uniaxial Compression Behaviour under Static Loading

Concrete is actually the most used construction material worldwide. It is not only economical; concrete also exhibits a usual high durability and is, by a correct manufacturing, deployable even in very adverse environmental conditions. As the principal components of concrete are hardened cement paste (as a result of the hydratation of water with cement) and concrete aggregates, it is expectable that these influence, among others, the mechanical properties of concrete. The water-cement-ratio plays for example a significant role in the compression strength development.

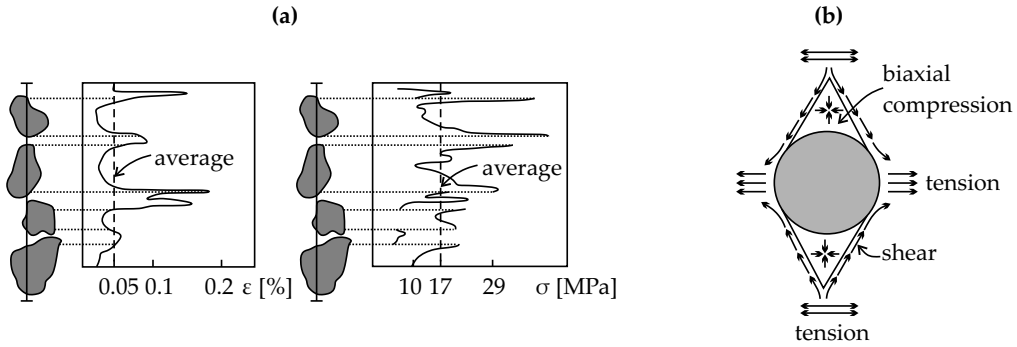

Figure 3.10: (a) Transmission of compression forces in concrete, redrawn from [44]; (b) Interface stresses between aggregate and cement paste, redrawn from [44]

Rogge [157] describes the stress distribution inside a concrete body. Accordingly, load stresses are transmitted mainly by the irregularly distributed aggregates. This leads to different stress deflections, resulting in tension stresses between cement paste and aggregates which is a source of microcracks and cause for the initiation point of a microstructure weakening under compression as well as tension loads. Moreover, the aggregates are substantially stiffer and volume-stabler than the cement paste and obstruct its plastic shrinkage [16]. The interface between cement paste and aggregates is fundamental for the overall concrete strength. It represents the weakest link in concrete since the adherence strength has been proven to be lower than the cement tension strength. Among others, especially the aggregate type, its surface properties, the cement tension strength, and environment moisture are the principal parameters which govern the cement-aggregate

adherence strength [44]. Following [44], the adherence strength is characterised by the components

- Mechanical adhesion (indentation) due to the aggregate roughness,
- adhesion owing to capillary forces,
- adhesion forces resulting from chemical reactions between cement and aggregates.

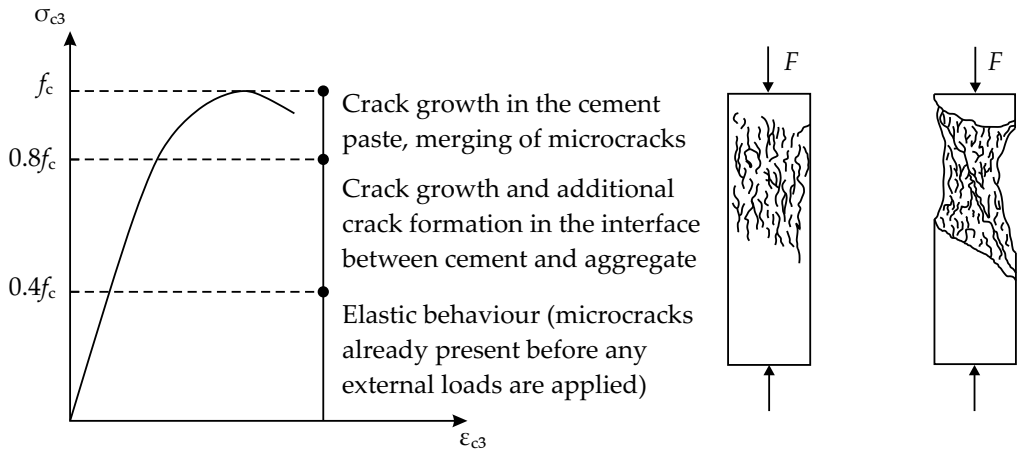

Figure 3.11: Phases of the stress-strain response under uniaxial compression (left), test specimen short before failure (middle), and fracture pattern, redrawn from [124]

Under uniaxial stress states the resulting internal tension stresses increase with growing load stresses. After [57], concrete behaves linearly under unixial stress loading for $\sigma_{c3} \leq 0.3 f_c$ with $\epsilon_{c1} = \epsilon_{c2} = -\nu\epsilon_{c3}$ and a Poisson's ratio value $\nu = 0.16$. However, in [16] values are specified between $\nu = 0.15...0.25$ for the concrete in the serviceability load range, while $\nu \approx 0.5$ for $\sigma_{c3} = f_c$, and $\nu > 0.5$ for $\epsilon_{c3} > \epsilon_{cu}$ (volume dilatation). By stress values of $\sigma_{c3} \approx 0.4 f_c$ the microcracks, present at the interface between aggregates and cement paste and which already originate before any extern load is applied, begin to expand. By $\sigma_{c3} \approx 0.8 f_c$ they cross the cement paste phase, nearly parallel to the main load direction and the deformation behaviour becomes highly nonlinear [16]. The uniaxial concrete tension strength may be reached and the concrete element fails showing a high volume dilatancy $\epsilon_{c1} + \epsilon_{c2} + \epsilon_{c3} \geq 0$ [157], [57]. The specimen deformation does not concentrate on a single cross sectional area; it rather exhibits a fracture process zone where the concrete is split into individual lamellas which become unstable and begin to shear off when $\sigma_{c3} = f_c$ [116]. The concrete presents afterwards – under a strain-controlled test – a softening behaviour which depends on the test facility configuration [178]. The fact that the concrete does not fails suddenly is due to the friction and indentation forces between the lamellas [116].

In the pre-peak span $\epsilon_{c3} \leq \epsilon_{cu}$, the compressive stress-strain constitutive equation may be approximated by a parabola with [92]

$$\sigma_{c3} = \frac{(\epsilon_{c3}^2 + 2\epsilon_{c3}\epsilon_{cu})}{\epsilon_{cu}^2} f_c, \tag{3.16}$$

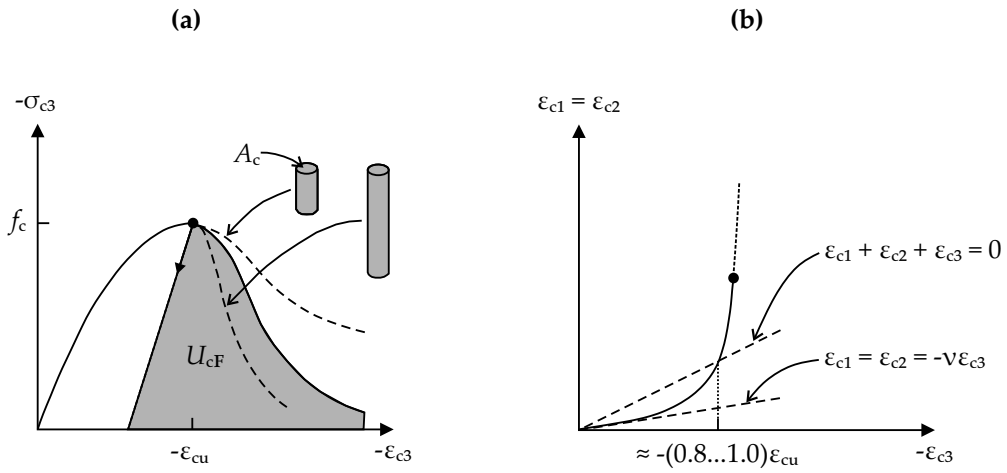

Figure 3.12: (a) Stress-strain response under uniaxial compression and influence of specimen length on strain-softening [92]; (b) Axial and lateral strains in a compression-tested cylinder [92]

where ϵ_{cu} is the concrete strain at $\sigma_{c3} = f_c$. For normal-strength concrete, $\epsilon_{cu} \approx 2.0‰$; for high-strength concretes the values of ϵ_{cu} may increase [92].

By definition, the concrete Young's modulus of elasticity may be defined either as the tangent inclination of the compressive stress-strain-curve (E_{c0m}) or as a secant inclination E_{cm} between the values $\sigma_{c3} = 0$ and $\sigma_{c3} = 0.4f_c$ [16]. E_{c0m} as well as E_{cm} are determined by the stiffness of the aggregates and the cement paste. Also the water-cement-ratio and the hydration grade play a role [16]. Nevertheless, for normal-strength concrete, the aggregate stiffness may present the weightiest influence. Also the highest variability, since e.g. sandstone-based aggregates have $E_{agg} = 10000$ MPa, while basalt-based aggregates may show values of $E_{agg} = 90000$ MPa [16]; both are thereby stiffer than the cement paste. On the other side, light-weight aggregates tend to be less stiffer than the cement paste. Consequently, the Young's modulus of elasticity is the result of an intricate interaction between cement paste and aggregates, moisture grade and concrete age; further the experienced load history, even if only in the elastic range, may affect E_{c0m} resp. E_{cm} decisively, see Ch. 3.2.4.

In strain-controlled tests the concrete, subjected to uniaxial compression, exhibits a softening behaviour for values $\epsilon_{c3} > \epsilon_{cu}$. It has been demonstrated, though, that this property reflects, in fact, rather the system performance; for instance, it is not an intrinsic material behaviour [175] and may be described using concepts of fracture mechanics. Larger test specimens show e.g. a steeper decrease than short ones. The dissipated energy in the fracture process zone (the area as shown in Fig. 3.16) is strongly dependent on the specimen size and is further known as the specific fracture energy U_{cF} per unit volume. Its value can only be derived from test results since a valid accepted mathematical model has not been found yet [92]. Nevertheless, due to the approximate size of the fracture process zone of twice the cylinder diameter, the values of U_{cF} oscillate between $U_{cF} = 60...160$

kJ/m^3 [175].

It has been observed that microcracks in concrete grow, even until failure, if the concrete is put under high constant uniaxial compression forces for a long time [154]. The creep strength is therefore defined as the compression strength which theoretically may be achieved, in this case from the concrete, infinitely long. Its value takes about 80% from the 28-day-compression-strength f_c. Yet, the creep strength depends also highly on the point of time when compression loads are applied. The main reason may be found in the hydration process of concrete: By sufficient moisture the (young) concrete tends to continue hydrating – a process that increases its strength. Simultaneously, it also loses strength due to the mentioned microcracking.

It is worth mentioning that both uniaxial compression and tension strength generally decrease with increasing specimen size (size effect). According to [192], this phenomena expresses the higher probability of occurrence of material defects the bigger the specimen volume is. Further important factors are listed in [124].

3.2.2 Concrete Uniaxial Tension Behaviour under Static Loading

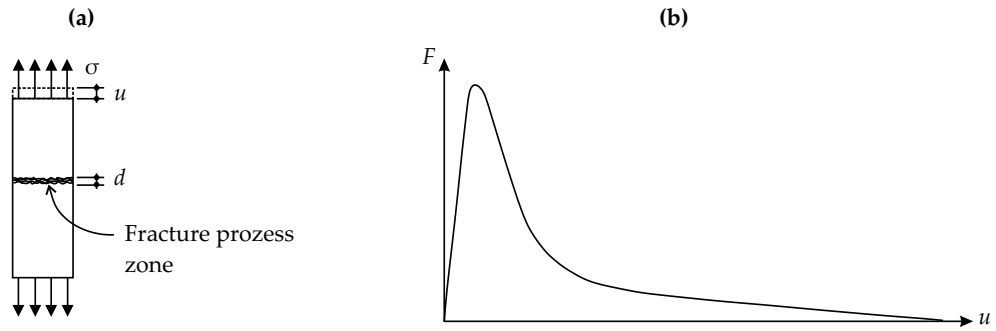

Figure 3.13: (a) Tension test with fracture prozess zone; (b) force-elongation-diagram (right), redrawn from [94]

Owing to the hydration process and the different properties between cement paste and aggregates, the concrete manifests numerous microcracks that are irregularly distributed and especially concentrated at the interface aggregate-cement paste. Uniaxial tension tests with uniformly distributed stresses show firstly a linear-elastic behaviour of the concrete specimens. Beginning with a tension stress $\sigma_{c3} = 0.7 f_{ct}$, the present microcracks start to expand preferably orthogonally to the main stress direction [16]. Regions with local material defects or notches cause stress concentrations and lead to the formation of fracture process zones which are characterised by numerous growing microcracks. A limited stress transmission in this zone is possible, but it decreases with increasing crack width. In force-controlled tests the specimen fails as soon as $\sigma_{c3} = f_{ct}$. Strain-controlled tests permit however a further specimen elongation with simultaneously sinking test loads, i.e. the concrete exhibits, again, a softening behaviour. It has been observed that at this point the specimen deformations concentrate predominately in the fracture process zone. With increasing elongation the crack width expands while the remaining specimen sections are gradually unloaded – the applied force decreases –, behave linear-elastically,

and return to their original shape.

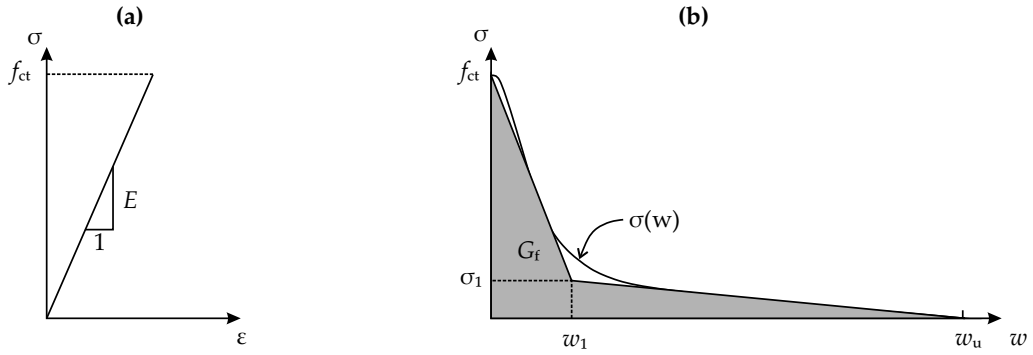

Figure 3.14: (a) Elastic behaviour outside of fracture prozess zone; (b) Softening behaviour in fracture prozess zone with assumed bilinear trend, redrawn from [94]

The most established model for describing the crack formation and crack growth in concrete under tension stresses has been proposed by Hillerborg et al. based on fracture mechanics [80]. Accordingly, a crack propagates as soon as the stress at the crack tip reaches the value $\sigma_{c3} = f_{ct}$. Afterwards, the crack opening becomes greater, though the stress transmission does not fall to zero, but decreases with increasing crack width until $w_{cr} = w_u$ (Fig. 3.15). By $w_{cr} = w_u$ the crack width is sufficiently wide so that no stress transmission is possible. The crack region, where $w_{cr} < w_u$, is characterised by either yield ranges or damage zones with the presence of many microcracks [94] with remaining material ligaments which permit a certain stress transmission. As the crack propagation dissipates energy due to the formation of new surfaces, the amount of dissipated energy per unit crack area G_f for an assumed linear variation of σ_c with w_{cr} is calculated with

$$G_f = \int_0^{w_u} \sigma_c dw = \frac{1}{2} f_{ct} w_u. \tag{3.17}$$

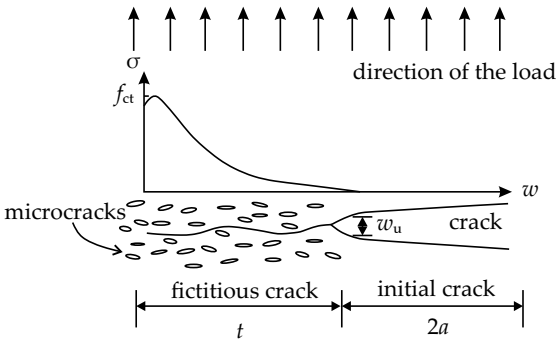

Figure 3.15: Hillerborg's fictitious crack model, redrawn from [192]

Hillerborg et al. [80] estimates values of $G_f/f_{ct} = 0.005...0.010$ mm for normal concrete,

thus for w_u, assuming a linear trend, he suggests

$$w_u = 2\frac{G_f}{f_{ct}}, \tag{3.18}$$

where $w_u = 0.01...0.02$ mm. More detailed values and models may be found in [94].

For many design purposes, the uniaxial tension strength of concrete may be estimated by means of the uniaxial compression strength. According to Fehsenfeld [49]:

$$f_{ct} \approx 0.3 f_c^{\frac{2}{3}}. \tag{3.19}$$

3.2.3 Concrete Multiaxial Behaviour under Static Loading

Biaxial tensile strength tests of concrete are not standardised. The tests may be performed on plates, on cylinders, as well as on cubes. Nevertheless, they all are laborious and not trivial [192]. Practically, the biaxial tensile strength of concrete is equal to the uniaxial tensile strength [114]. A statistical evaluation conducted in [107] and based on published results reveals an increase of tensile strength of approximately 5% in relation to f_{ct} for a stress ratio of $\sigma_{c2}/\sigma_{c1} = 0.25$ and a decrease of tensile strength of 2% for $\sigma_{c2}/\sigma_{c1} = 1.00$. Schröder [170], however, reports that the biaxial tensile strength by $\sigma_{c2}/\sigma_{c1} = 1.00$ is reduced with growing values of the uniaxial compression strength f_c. Also the deformation capacity of concrete specimens under biaxial tension has been observed to decrease with increasing σ_{c2}/σ_{c1}-rates. Though, the number of performed tests does not permit an overall generalisation.

Similar to the concrete mechanical behaviour under uniaxial tension, the response behaviour under biaxial tension depends on the test facility and the specimen properties [170]. Likewise, a major number of parameters like aggregate size, water-cement-ratio, concrete strength, strain velocity, etc. have been found to influence the biaxial tensile behaviour significantly. It is, thus, difficult to determine a proper value for the biaxial tension strength of the concrete. Considering that the concrete behaviour under tension exhibits a great variability due e.g. the environmental conditions, the post-treatment, and the present residual stresses, it seems appropriate to assume a constant strength under biaxial tension states.

Kupfer [105] performed biaxial load tests on concrete slabs for different stress configurations: Tension-tension, compression-compression, and compression-tension. Through the use of brush bearing platens he was able to apply uniform stress conditions and to avoid, on the same time, strain restrain effects on the load application zones of the concrete specimens. For compression-compression stress states with $\sigma_{c2}/\sigma_{c1} = -1.00/-1.00$ he noticed an increase of the compression strength f_c by a factor of 16%. After the formation of numerable microcracks the specimen failure occurred owing to an approximately 30° diagonal macrocrack. A similar behaviour was observed for compression-tension stress states as long as $\sigma_{c1} \leq 1/15|\sigma_{c2}|$ ($\sigma_{c1} \geq 0 \geq \sigma_{c2}$), otherwise the main cracks were perpendicular to the tension stress. However, the achieved compression strength f_c was considerably

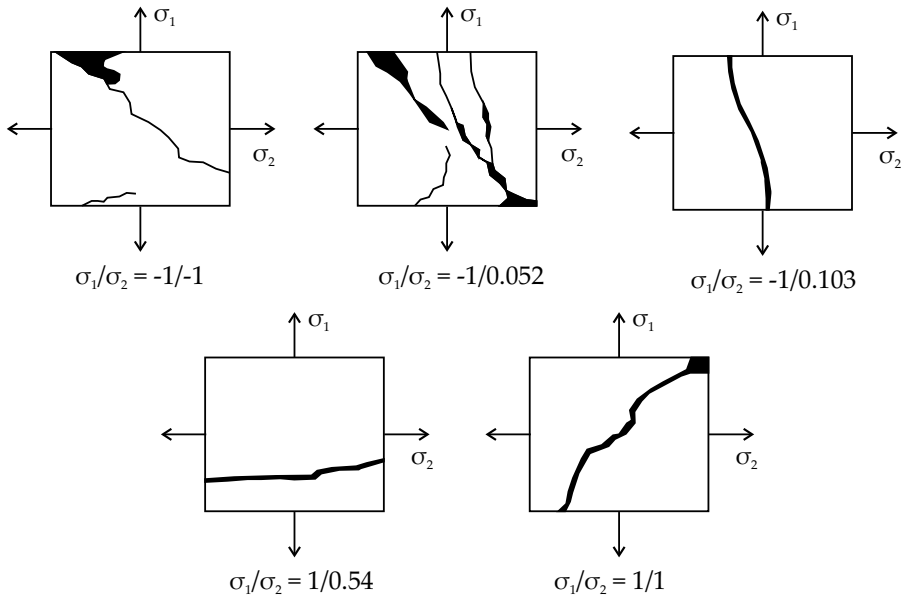

Figure 3.16: Failure modes of tested slabs under biaxial stress states, redrawn from [105]

reduced depending on the value of the transverse tensile stress. Additionally, the deformation behaviour of concrete was also extremely affected under compression-tension stress states since the presence of tensile stresses leads to a brittleness rise. The maximal strength increase of 27% was found by a ratio $\sigma_{c2}/\sigma_{c1} = -1.00/-0.50$ [104]. The measured $\sigma_c - \epsilon_c$–curves (Fig. 3.18) contain information about the modified concrete ductility in dependence of the biaxial stress state; also the Young's modulus of elasticity E_c and the elastic Poisson's ratio μ_c may be obtained. Kupfer's results show, like in uniaxial concrete tests, a decreasing ductility with growing concrete strength f_c [104].

The mechanical concrete behaviour under triaxial stress states depends on the applied stress ratio. Also the concrete composition and the porosity degree play an important role [192]. The inner structure, however, experiences in a more or less degree tension stresses similarly to specimens under unixial stresses. According to [157], tested concrete cylinders under triaxial compression present a positive lateral strain owing to the Poisson's ratio if the transverse compression loads are not high. As a result, the specimen failure in this case is a consequence of transverse tension stresses between matrix and aggregates, exactly as under unixial compression and exhibiting almost the same phases of tightening and linear-elastic course, then a phase of stable cracking, a phase of volume dilatancy closed to the curve peak, and finally a softening post-peak phase [192]. Are the lateral compression loads high, then a more elevate concrete ductility and a greater distribution of microcracks over the specimen height may be noticed. Under nearly hydrostatic stress states ($\sigma_{c3} \approx \sigma_{c2} \approx \sigma_{c1} \leq 0$), practically no failure is observed. After the concrete inner pores collapse due to compression, a material hardening without any material softening may be registered [157]. Only very elevate load values produce a failure: Compact test specimens are crushed while slender test cylinders experience a diagonal fracture surface

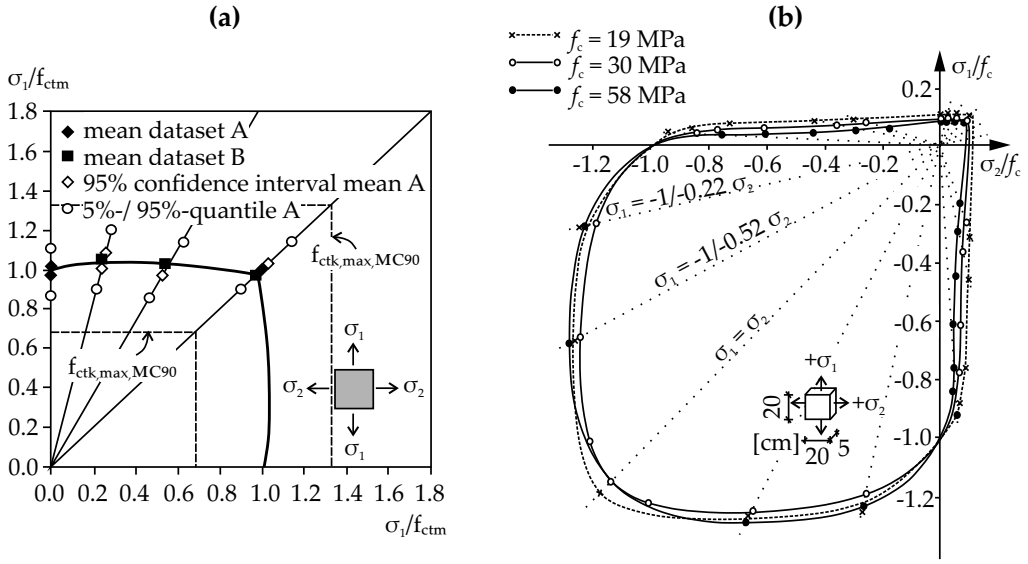

Figure 3.17: (a) Statistical data analysis of biaxial tension behaviour of concrete, redrawn from [107]; (b) Biaxial concrete strength in the $\sigma_{c1} - \sigma_{c2}$-plane, redrawn from [104]

of about 25...35° and hence a shear failure. Furthermore, the concrete strength f_c was identified as an influencing parameter since lower values of f_c cause the test specimens to suffer a crush failure rather than a shearing. Under multiaxial stress states the failure mode is not unambiguous [157] and in many cases it is defined based on the formation of macrocracks, leading to a prominent increase of transverse strains and to a volume dilatation. The transition between a brittle and ductile concrete mechanical behaviour is known as *softening-hardening transition* [192]. Torrenti [192] classifies the concrete failure in form of growing microcracking together with a material collapse, material softening, and porosity increase as Mode I. On the other hand, Mode II corresponds to a failure in form

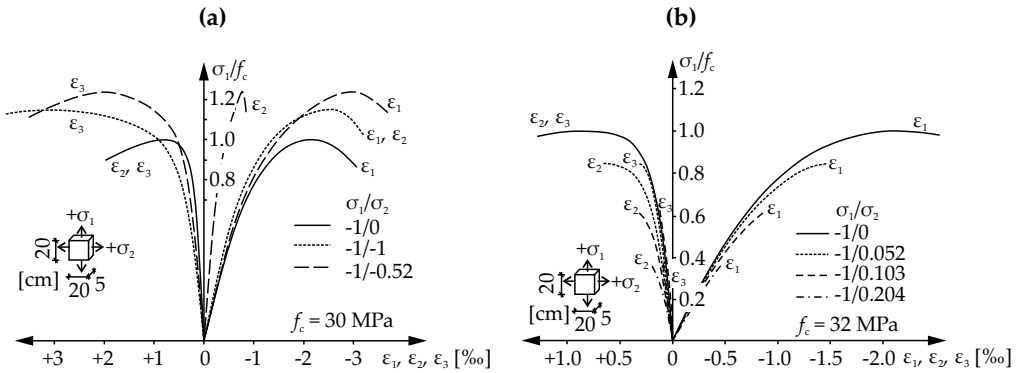

Figure 3.18: (a) Stress-strain relationships of concrete under biaxial compression; (b) Stress-strain relationships of concrete under combined compression and tension, redrawn from [105]

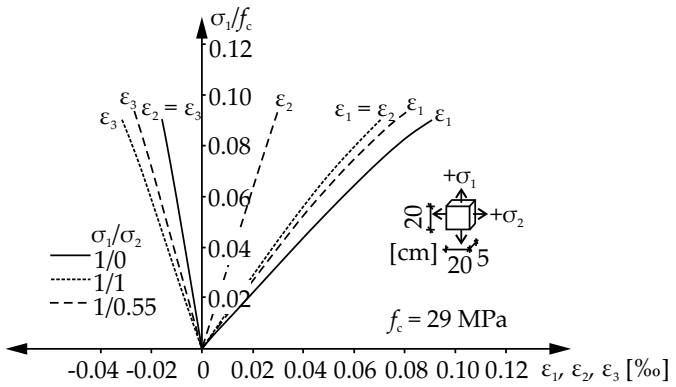

Figure 3.19: Stress-strain relationships of concrete under biaxial tension, redrawn from [105]

of microcracking combined with shear bands.

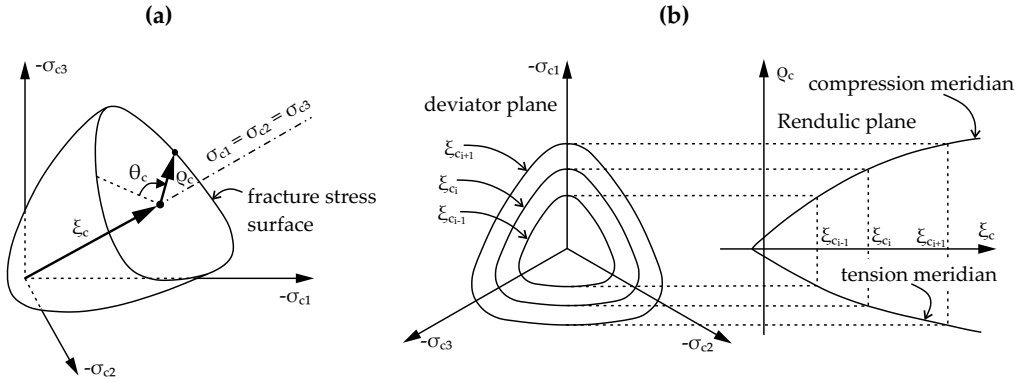

Figure 3.20: (a) Fracture stress surface of concrete with Haigh-Westeergard coordinates, redrawn from [157]; (b) Deviator plane (left) and Rendulic plane (right) of concrete, redrawn from [185]

Rogge [157] classifies the different available calculation models of the mechanical behaviour of concrete into those according to the classical failure theory, where materials are considered isotropic, and those which base on fracture mechanics. In general, the mechanical behaviour of concrete under monotonic static loading is characterised by a nonlinear curve behaviour due to existing and growing microcracks resulting from increasing loads. However, un- and reloading processes are substantially more complicate to describe and calculate. One of the main difficulties is the mathematical modeling of the memory capacity of concrete [157] since it is evident that properties of the experienced load history like deformation values may decisively affect the actual mechanical answer (see Ch. 3.2.4).

The general Mohr-Coulomb fracture-stress-hypothesis corresponds to the classical failure theories and is frequently employed owing to its simple mathematical background – a linear equation [114] – with an acceptable degree of accuracy. Shear failure is an usual failure mode of concrete. Though, the resulting shear stresses τ_c at the fracture surface

are strongly governed by the corresponding active normal σ_c stresses. Therefore, the general calculation model of Mohr-Coulomb, similar to the behaviour of soil, describes the ultimate shear stress τ_c as a function of normal stresses and of internal cohesion. According to [114], the Mohr-Coulomb failure model is inadequate for a numerical implementation due to the discontinuous curve progress.

$$|\tau_c| = c - \sigma_c \tan \varphi_c. \tag{3.20}$$

Equation (3.20) leads to an uniaxial tension strength of

$$f_t = c \cot \varphi_c. \tag{3.21}$$

A stress state with $0 < \sigma_c < f_t$ provides an alternative equation for the uniaxial tension strength with

$$f_t = c \cot \varphi_c = \frac{1}{2}(\sigma_{c1} + \sigma_{c3}) + \frac{1}{2}\frac{\sigma_{c1} - \sigma_{c3}}{\sin \varphi_c}. \tag{3.22}$$

Reshaping equation 3.22 leads to an expression of the general Mohr-Coulomb yield criterion under principal stresses:

$$Y = \sigma_{c1}(1 + \sin \varphi_c) - \sigma_{c3}(1 - \sin \varphi_c) - 2c \cos \varphi_c = 0. \tag{3.23}$$

With $\sigma_{c1} = 0$ and $\sigma_{c3} = -f_c$, one obtains for the uniaxial compression strength:

$$f_c = \frac{2c \cos \varphi_c}{1 - \sin \varphi_c}, \tag{3.24}$$

and with $\sigma_{c1} = f_t$ and $\sigma_{c3} = 0$ for the uniaxial tension strength:

$$f_t = \frac{2c \cos \varphi_c}{1 + \sin \varphi_c}. \tag{3.25}$$

According to [157], the calculation model of Mohr-Coulomb is valid as long as the applied stress are not excessively high. Marti [114] neglects the strength increase under biaxial compression-compression but seeks to appropriately model the reduced concrete strength under compression-tension. For the inclination of the failure curve in the $\sigma_c - \tau_c$-plane he suggests $\tan \varphi_c = 3/4$ ($\varphi_c \approx 37°$), a test-based value which is appropriate for not too high hydrostatic compression values but which leads to an unacceptable tension strength. Inserting $\tan \varphi_c = 3/4$ into equation (3.24) one obtains $c = 0.25 f_c$. This value together with $\tan \varphi_c = 3/4$ in equation 3.25 leads to $f_t = 0.25 f_c$. However, tests deliver a

value of $f_t = 0.10 f_c$ [114], [178]. For this reason, a modification turns mandatory which is known as the modified Coulomb yield criterion [112] with $f_t = f_{ct}$.

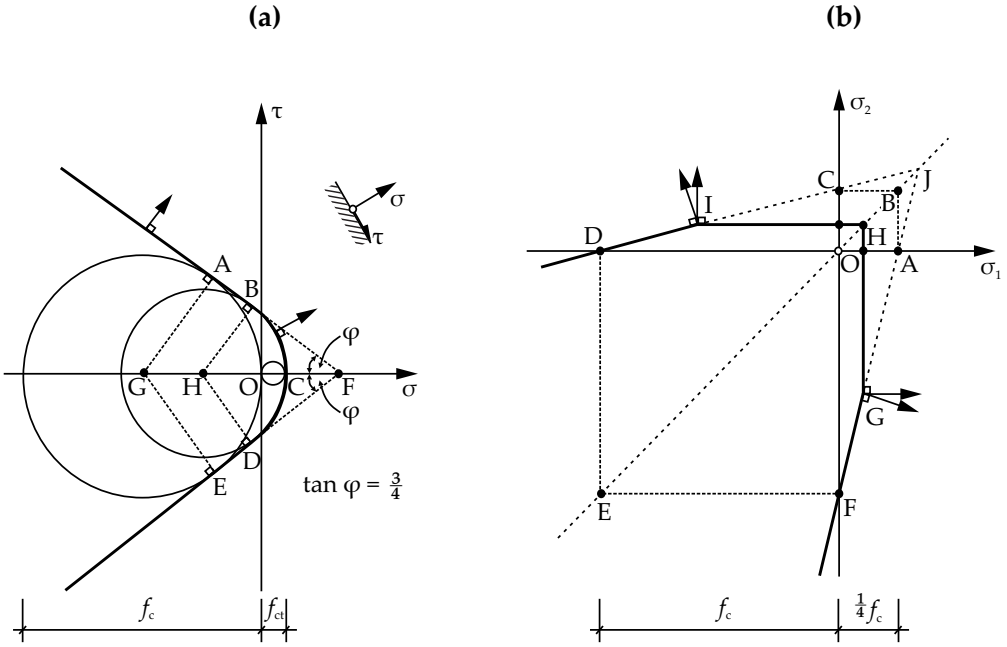

Figure 3.21: Modified Coulomb yield criterion of concrete, redrawn from [114]

Further calculation models are discussed in [157] and [185]. Specially the model developed by Willam and Warnke [201] is considered appropriate for a numerical implementation with the finite element method since it presents no geometrical discontinuities but continuously differentiable surfaces. However, both models are quiet complicate to deal with due to the many parameters which have to be derived.

Willam and Warnke [201] developed a simplified 3-parameter model with a conical failure surface and a non-circular base section in the principal stress state. The model leads to an acceptable agreement with test data in the lower compression regime. For higher compression values it shows however, in accordance to the authors, appreciable errors. A further refinement results in a 5-parameter model, where principal meridians are described as parabolas instead of straight lines, connected by an ellipsoidal surface. In the deviatoric plane, the failure curve is defined as ellipse in a section between $\theta_c = 0°$ and $\theta_c = 60°$ and then mirrored to the remaining sections. It is rather triangular for low compression values while it becomes more circular for higher compression values. For the sake of a stable numerical implementation, special attention was given to the smoothness criterion (continuous surfaces and varying tangents) as well to convexity (no reflexion points). In sum, the model after [201] follows an "elastic, perfectly plastic material formulation in compressions and an elastic, perfectly brittle behaviour under tension".

The mathematical definition of the failure surface of concrete under multiaxial stress states may be expressed by means of a three-dimensional stress space with the principal

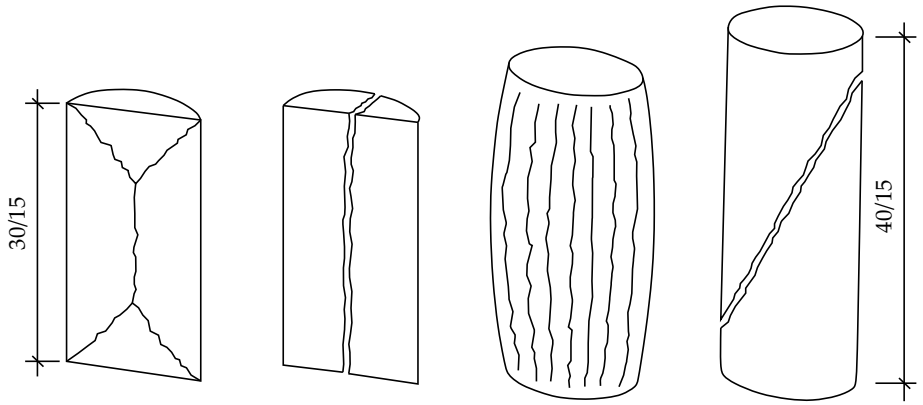

Figure 3.22: Observed failure mechanisms at encased concrete cylinders with h/D = 30/15 cm and at a drilled concrete cylinder with h/D = 40/15 cm, redrawn from [157]

stresses $\sigma_{c1}, \sigma_{c2}, \sigma_{c3}$, or using the octahedron stresses σ_{c0}, τ_{c0} with the Lode angle θ_c, or also the Haigh-Westergaard cylindrical coordinates ξ_c, ρ_c, θ_c, where ξ_c describes the hydrostatic axis, ρ_c the deviatoric plane perpendicular to ξ_c and θ_c corresponds to the Lode angle with

$$\xi_c = \frac{1}{\sqrt{3}}\sigma_{cI} = \frac{1}{\sqrt{3}}(\sigma_{c1} + \sigma_{c2} + \sigma_{c3}), \tag{3.26}$$

$$\rho_c = \sqrt{2s_{cII}} = \frac{1}{\sqrt{3}}[(\sigma_{c1} - \sigma_{c2})^2 + (\sigma_{c2} - \sigma_{c3})^2 + (\sigma_{c3} - \sigma_{c1})^2]^{\frac{1}{2}}, \tag{3.27}$$

$$\cos\theta_c = \frac{2\sigma_{c1} - \sigma_{c2} - \sigma_{c3}}{\sqrt{6}\rho_c}. \tag{3.28}$$

The failure surface of the 5-parameter model after [201] is described using the Haigh-Westergaard cylindrical coordinates

$$Y(\xi_c, \rho_c, \theta_c) = \frac{1}{r_c(\xi_c, \rho_c, \theta_c)}\frac{\rho_c}{\sqrt{5}f_c}, \tag{3.29}$$

with the radius function r_c in the deviatoric plane

$$r_c(\xi_c, \theta_c) = \frac{2r_2(r_2^2 - r_1^2)\cos\theta_c + r_2(2r_1 - r_2)\sqrt{4(r_2^2 - r_1^2)\cos^2\theta_c + 5r_1 - 4r_1r_2}}{4(r_2^2 - r_1^2)\cos^2\theta_c + (r_2 - 2r_1)^2}. \tag{3.30}$$

The principal meridians are parabolas whose parameters are to be quantified based on

determined tests.

$$r_1(\xi_c, \theta_c) = a_0 + a_1 \frac{\xi_c}{f_c} + a_2 \left(\frac{\xi_c}{f_c}\right)^2 \tag{3.31}$$

$$r_2(\xi_c, \theta_c) = b_0 + b_1 \frac{\xi_c}{f_c} + b_2 \left(\frac{\xi_c}{f_c}\right)^2 \tag{3.32}$$

Rogge [157] combines the models of Willam and Warnke [201]: Ellipses describe the deviatoric plane while the meridians follow the concept of Ottosen. The failure surface is defined in sections, what at first increases the number of parameters to be determined. According to the author, the model exhibits a better adaptability for numerical purposes.

Speck [185] analyses the material behaviour of high-strength concrete under multiaxial stress states. The interesting results published in [185] reflect that the multiaxial stress state has a significant lower influence on the mechanical performance of high-strength concrete compared to normal-strength concrete. Accordingly, the biaxial strength is practically equal to the uniaxial strength f_c. However, through the application of fibres, the high-strength concrete attains a similar ductility as normal-strength concrete.

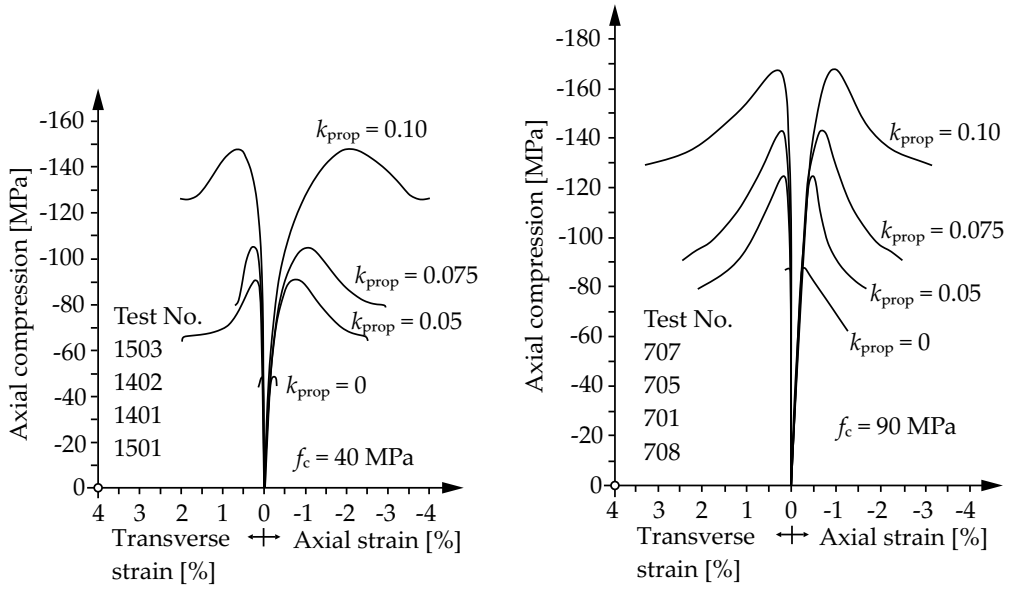

Figure 3.23: Measured stress-strain-curves of concrete cylinders under axial compression σ_{c1} and transverse compression $\sigma_{c3} = k_{prop}\sigma_{c1}$, redrawn from [157]

3.2.4 Concrete Uniaxial Behaviour under Fatigue Compression Loading

Fatigue loading of concrete structures has usually a random character. Nonetheless, the concrete fatigue bahaviour has been examined mostly using dynamic, sinusoidal-curved, and uniaxial loads with a constant and generally high frequency. In doing so, maximal and

minimal load values are related to the static uniaxial concrete strength f_c. According to [137], the relative maximum (compression) stress $S_{c,max} = \sigma_{c,max}/f_c$, the relative minimum (compression) stress $S_{c,min} = \sigma_{c,min}/f_c$, the relative average (compression) stress $S_{c,m} = \sigma_{c,m}/f_c$, and finally the relative amplitude stress $S_{c,a} = \sigma_{c,a}/f_c$ respective the relative stress range $\Delta S_c = \Delta\sigma_c/f_c$ are employed for the load description. However, the use of f_c is not standarised, but should be determined on test specimens with equal characteristics (dimensions, manufacturing, storage, preparation, age) than those destined for fatigue tests [137]. For this reason, the comparison of result data from different documented fatigue tests turns to be difficult due to variable test conditions (specimen size, load characteristics, etc.) [137]. Investigations of the concrete fatigue behaviour under biaxial or triaxial stress states are almost inexistent.

Since a high number of load cycles has to be achieved during testing, which implies a long test period, at first a maximum number of load cycles is commonly defined depending on a favoured (and technically feasible) test frequency. If the test specimen does not fail afterwards, then it is categorised as one without fatigue rupture (run-out) [137].

The comprehension of the fatigue behaviour of concrete has shown to be a complex and challenging task. Additionally to the complicate mechanisms of crack formation and crack growth in such a heterogeneous and brittle material like concrete, numerous influencing parameters, which interact with each other and whose quantitative significance in the fatigue process has not been fully detected yet, have been identified. A comprehensive description of the fatigue process in concrete is still lacking. In consequence, many (actual) sources in literature report about tests done in order to determine the governing parameters of the concrete fatigue behaviour for engineering purposes (e.g. [207], [82]).

The concrete fatigue process is the result of growing (micro)cracks which gradually weak the internal concrete structure, producing in this way a significant stiffness loss. Never-loaded concrete already shows the presence of microcracks between aggregates and cement paste as outcome of the restraining effect of aggregates on the shrinkage deformation of the cement paste [102], [15]. After unloading of a concrete specimen, which has previously been loaded in the elastic region, the deformations of aggregate and cement paste are (partially) reversed. Yet, according to [82], the deformation reversal of the aggregates is less pronounced than by the cement paste. In consequence, tension stresses between aggregate and cement paste are induced transversally to the main load direction at a certain degree by each load cycle, leading to a growth of the already existing microcracks in the interface layer between aggregate and cement paste. The further crack growth until failure of the specimen constitutes the fatigue process of concrete. In [111] it is reported that also the water-cement ratio in concrete plays a dominant role in the fatigue crack development.

Oneschkow [137] observes that most reported tests of concrete in the compression range have focused only on the achievable number of load cycles and the effect of numerous parameters. The development of axial as well as of transverse strains of the specimen have usually not been subject of interest, although they may provide valuable information about the damage process. Test specimens that experience uniaxial, sinusoidal loads in the compression range exhibit a nonlinear increase of strains over time and relative number of load cycles. This is one fundamental difference to the fatigue damage process that

occurs in steel [15]. The development of strains over the relative number of load cycles is described in the literature as an S-shaped curve which may be divided into the 3 typical phases [85], [15], [17]

- Initial phase: Rapid, nonlinear strain increase associated with an increment of microcracking, from 0% to approx. 10% of total life.
- Growth phase: Nearly linear strain increase, stable crack growth, from 10% to approx. 80% of total life.
- Failure phase: Again rapid, nonlinear strain increase and unstable crack growth until specimen rupture, from approx. 80% to 100% of total life.

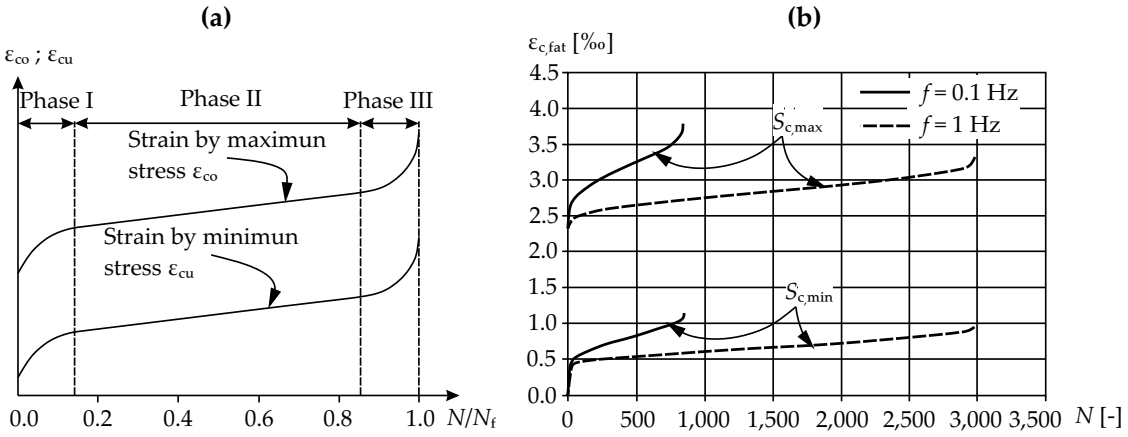

Figure 3.24: (a) Strain development of concrete under fatigue loading, redrawn from [137], (b) Strain development of high-strength concrete under different load frequencies, redrawn from [137]

Uniaxial fatigue tests in the compression range carried out in [85] reveal the typical S-shaped development of concrete strains. Fatigue-induced strains are irreversible [82]. An important finding obtained from carefully performed strain measurements is the value of the ultimate fatigue strain $\epsilon_{cu,fat}$. For normal-strength concrete C50/60 tested with a frequency of 1.0 Hz respective 10.0 Hz the ultimate fatigue strain oscillates between $\epsilon_{cu,fat} = -2.97 ... -4.55‰$ with a mean value of $\overline{\epsilon_{cu,fat}} = -3.55‰$ while the mean value of the ultimate strain of equal specimens tested statically coincidentally was the same: $\overline{\epsilon_{cu}} = -3.55‰$. In [137] (for high-strength concrete) and in [85], [82] (for normal-strength concrete) the ultimate fatigue strain $\epsilon_{cu,fat}$ does not exceed the ultimate static strain ϵ_{cu}, a fact which refutes the calculation model of Pfanner [144] and confirms the so called Envelop-model [75]. Furthermore, temperature changes in test specimens were recorded during the test process in [85]. It has been found out that high test frequencies lead to a temperature increase. For example, specimens tested with $S_{c,max} = 0.60$ at 1.0 Hz presented a surface temperature of 31°C; at 10.0 Hz the surface temperature was 69°C. In accordance with the authors, a high temperature increase may be responsible for the measured lower

strain values in specimens subjected to higher load frequencies and should be taken into account while interpreting fatigue test data. Creep effects are also considered to play a certain role in the strain development depending on the load frequency. Is the stress-strain-curve plotted for each load cycle, then, according to [83], the curve curvature changes from concave to convex, indicating a near fatigue failure.

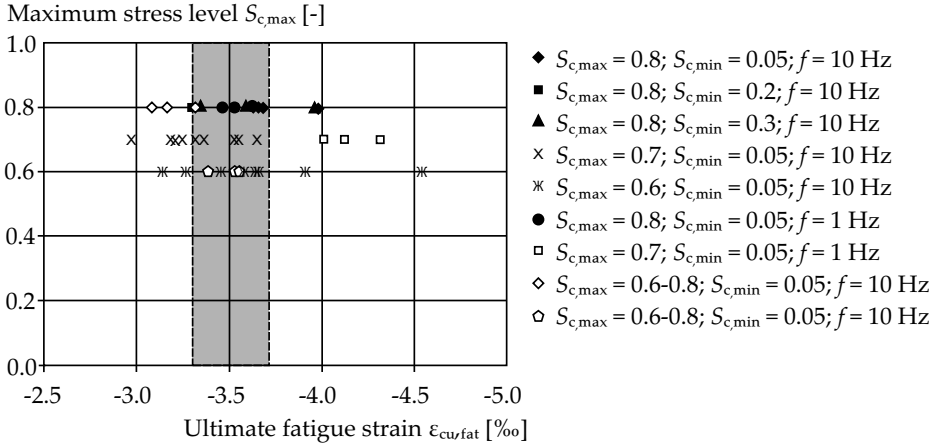

Figure 3.25: Fatigue strain of concrete at failure vs. stress level, redrawn from [85]

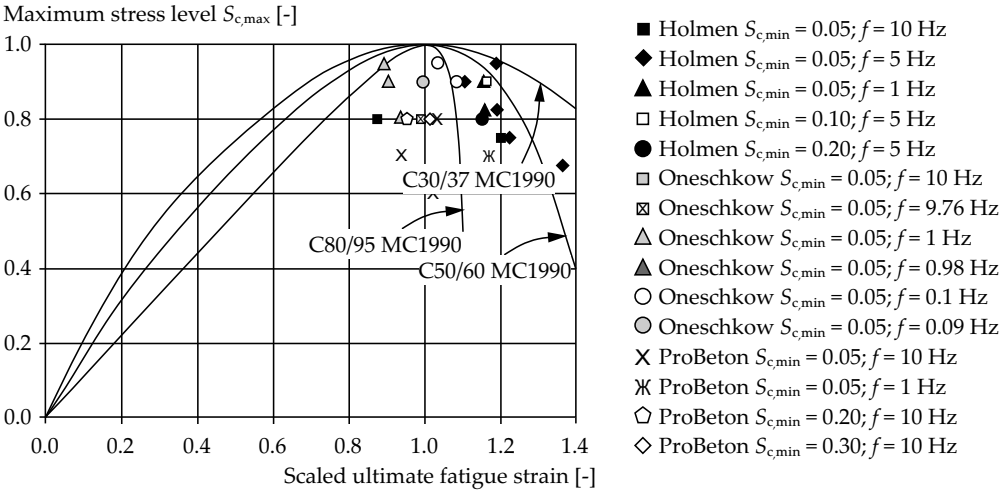

Figure 3.26: Fatigue strain of concrete at failure vs. static strain, redrawn from [85]

Breitenbücher et al. [20] divides the total (uniaxial) concrete strain $\epsilon_{c,fat}$ due to the fatigue process into a damage strain $\epsilon_{c,fat,da}$ and a plastic part $\epsilon_{c,pl}$ with

$$\epsilon_{c,fat} = \epsilon_{c,fat,da} + \epsilon_{c,pl}. \tag{3.33}$$

Based on published data he derives a constant value for the ratio $\beta_{c,fat}$ between $\epsilon_{c,fat}$ and $\epsilon_{c,fat,da}$, independently of the number of load cycles:

$$\beta_{c,fat} = \frac{\epsilon_{c,fat,da}}{\epsilon_{c,fat}} = 0.35. \tag{3.34}$$

The Envelope-concept states that the static stress-strain-curve of concrete constitutes an envelope which may not be trespassed by the growing strains due to a fatigue process [75].

The concrete modulus of elasticity E_c is repeatedly reported to change under fatigue loading. This is a logical consequence of the strain increase owing to the dependence of E_c on ϵ_c and the growth of micro-cracks in the concrete [82]. Experimental reports [83] show a consequent, nonlinear decrease of the secant modulus of elasticity over the relative number of load cycles. As a result, the test specimen becomes softer, a property which, applied on concrete structural members, leads to a permanent internal stress redistribution which is usually favourable [72]. Damaged regions withdraw themselves from the load transfer and more intact regions are forced to carry higher loads. According to [85] and [158], this significant stiffness degradation may be interpreted as fatigue damage. The stiffness degradation is, hence, supposed to be a consequence of increasing fatigue-induced cracks in concrete [72]. Holmen [83] determines the modulus of elasticity in sinusoidal, constant amplitude tests by means of maximal and minimal values

$$E_c = \frac{\sigma_{c,max} - \sigma_{c,min}}{\epsilon_{c1,max} - \epsilon_{c1,min}}. \tag{3.35}$$

Due to fatigue loading, E_c decreases in [83] until it approaches a value equal to 60% of the statical value, a development which seems to be independent of the test frequency. In general, the decrease of the concrete modulus of elasticity has wide consequences for structures exposed to dynamic loading and whose eigenfrequency behavior is strongly influenced by E_c. Since e.g. offshore wave loading is mostly low-frequent ($\approx$ 0.1 Hz), reduced E_c-values are more unfavourable due to the consequent decrease of the structural eigenfrequency. In any case, the behaviour of E_c under fatigue loading should be considered in structural design. The reduction of E_c under variable-amplitude loads is less pronounced than under constant-amplitude loads [83].

Measurements done by von der Haar [72] with ultrasonic pulse revealed that the pulse velocity is reduced with the number of applied load cycles N. Thus, this method may be employed indirectly for the capture of fatigue damage in concrete. His tests, conducted with the stress levels $S_{c,max} = 0.80$ and $S_{c,min} = 0.05$, expose a reduction of E_c up to 80...85% of its initial value. By tests with $S_{c,max} = 0.60$ and $S_{c,min} = 0.05$ the reduction was of approximately 34%, i.e. E_c kept only 66% of its initial value. Tests performed with different load frequencies (constant amplitude loading) showed no influence on the final degradation of E_c; solely the curve gradient is altered. In [20] the value of E_c after 600,000 load cycles with $S_{c,max}/S_{c,min} = 0.675/0.10$ oscillates between 100% and 60% of its statical

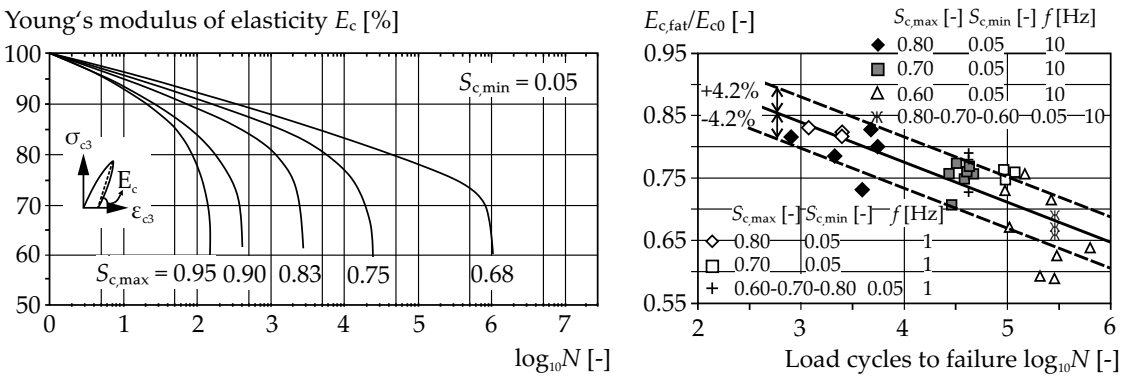

Figure 3.27: (a) Reduction of modulus of elasticity in dependence of the number of load cycles, redrawn from [83]; (b) Reduction of modulus of elasticity before failure, redrawn from [72]

original value.

Breitenbücher et al. [20] reports of changes of the concrete fracture energy g_c. Compared to the stiffness degradation, a significant decrease of the fracture energy is observable. In his performed tests with $S_{c,max}/S_{c,min}$ = 0.675/0.10 and N = 0, the fracture energy amounts g_c = 63.8 kJ/m³, while it decreases to g_c = 36.8 kJ/m³ after N = 25,500,000 load cycles.

The stiffness degradation for isotropic materials is usually described by a linear damage model. In [60] the basic assumptions are derived on the basis of a concrete chord subjected to a vast number of tension stresses. Owing to the experienced progressive fatigue damage in form of cracks, the sectional area A_c of the concrete concrete is reduced to an effective area $A_{c,red}$. Since the applied force F exhibits the same magnitude, then the concrete stresses are affected accordingly:

$$F = \sigma_c A_c = \sigma_{c,D} A_{c,red}, \tag{3.36}$$

where σ_c corresponds to the primary nominal stress and $\sigma_{c,D}$ to the augmented concrete stress due to $A_{c,red}$. The damage variable D is introduced with

$$D = 1 - \frac{A_{c,red}}{A_c}. \tag{3.37}$$

For $A_{c,red} = A_c$, then D = 0, i.e. no damage is present. By $A_{c,red}$ = 0, then D = 1, which implies failure. Eq. 3.37 inserted into Eq. 3.36:

$$\sigma_c = (1 - D)\sigma_{c,D}. \tag{3.38}$$

Considering only linear-elastic material behaviour, then the stress in a chord under

fatigue loading becomes

$$\sigma_c = (1 - D)\sigma_{c,D} = (1 - D)E_c\epsilon_{c,fat}. \tag{3.39}$$

Setting

$$E_{c,D} = (1 - D)E_c, \tag{3.40}$$

it becomes evident that the concrete modulus of elasticity decreases in the same proportion of the concrete damage D. Since the applied fatigue loads are held with unmodified magnitude and E_c degrades, the concrete strains are consequently forced to grow. Yet, concrete is an anisotropic material that develops cracks under low tension stresses. Nonetheless, the linear damage model permits a first evaluation of the nonlinear damage development.

In [85] low load frequencies are suspected to intensify the effects of concrete creep since the effective load duration is directly proportional to creep. Accordingly, high load frequencies rather disturb creep processes and, for instance, the specimen deformations are smaller. Oneschkow [137] and Schneider et al. [167] attribute the higher fatigue resistance of concrete under loads with high frequency to the related higher rate of loading. Both, concrete compression strength f_c and tension strength f_{ct}, have been proven to show a significant increase under high load rates [51]. Tests conduced in [82] show almost no influence of the load frequency f_{load} on $\epsilon_{cu,fat}$ as well as on the number of cycles to failure N as long as 0.01 Hz $\leq f_{cyc} \leq$ 1.0 Hz. Higher values of f_{load} seem to cause a decrease of $\epsilon_{cu,fat}$ but a significant increase of N. Hsu [84] follows the approach

$$NT_{cyc} = \text{constant}, \tag{3.41}$$

with N being the number of cycles (by constant amplitude) until failure and T_{cyc} the load period. Based on published test data, he derives four-parametric Wöhler-curves which account, besides $S_{c,max}$, $S_{c,min}$, and N, also for the load frequency f_{cyc}.

Regarding the number of load cycles to failure, the results published in [85] and [208] evidence a strong dependence on the load history, a property known as sequence effect. In [85], multi-step uniaxial fatigue tests in the compression range with $S_{c,min} = 0.05$ and a load frequency of 10.0 Hz, the fatigue life of the tested specimens was 5 times higher for the decreasing load step configuration. An increasing load configuration, in contrast, results in a lower number of load cycles until failure.

In general, under a constant value $S_{c,min}$, the number of load cycles until failure is higher, the smaller $S_{c,max}$ is [137]. Both parameter, $S_{c,min}$ as well as $S_{c,max}$, and hence the mean stress $S_{c,m}$, are of decisive importance [21], [15].

Leeuwen has performed extensive fatigue uniaxial tests of concrete under compression [106]. 130 constant-amplitude tests, ca. 100 program loading tests, and ca. 150 variable-amplitude tests, all under water, which fulfills an important requirement concerning the

Table 3.3: Damage sum of multiple step fatigue tests [85]

$S_{c,max1}$ = 0.80		$S_{c,max2}$ = 0.70		$S_{c,max3}$ = 0.60		
N_1	N_1/N_{f1}	N_2	N_2/N_{f2}	N_3	N_3/N_{f3}	$\sum N_i/N_{fi}$
1,000	0.38	11,000	0.29	267,305	1.14	1.81
1,000	0.38	11,000	0.29	191,314	0.82	1.48
1,000	0.38	11,000	0.29	123,665	0.53	1.20
					D_{avg} =	1.49

$S_{c,max1}$ = 0.60		$S_{c,max2}$ = 0.70		$S_{c,max3}$ = 0.80		
N_1	N_1/N_{f1}	N_2	N_2/N_{f2}	N_3	N_3/N_{f3}	$\sum N_i/N_{fi}$
30,000	0.13	11,000	0.29	1,167	0.45	0.87
30,000	0.13	11,000	0.29	1,357	0.52	0.94
30,000	0.13	11,000	0.29	968	0.37	0.79
					D_{avg} =	0.86

fatigue of concrete in offshore conditions. The test frequency was hold constant at 6.0 Hz and every test configuration was repeated several times in order to quantify the statistical variation. In fact, the experimental scatter was considerable. The author recognizes furthermore that the real load character in most structures is random and time-variable; hence, it is to be treated by stochastic methods. The derivation of Wöhler-curves for the concrete based on constant-amplitude, sinusoidal tests with frequencies, which normally are higher than the governing load frequencies in offshore structures, may not be directly applicable. The employment of damage assessment models is a possible way in order to simplify and approximately calculate the load induced damage. According to [106], the Miner's rule, which adopts "hypothetical units" for the damage description, has become widely accepted, even though it is not accurate and has not been sufficiently verified for real, random loads. Miner's rule provides a connection between the damage caused by real loading and the results of simple constant-amplitude tests, provided that tests conditions are equal to those of the real structure [106] – this point is rarely considered in praxis. On the other hand, fracture mechanics have not been capable to deliver a usable and simple model for the calculation of the degree of damage [106]. Leeuwen's most important finding is that the damage D calculated by means of Miner's rule presents a logarithmic-normal distribution. In case of variable-amplitude tests generated using different spectra, where the test specimens experienced a fatigue failure, the calculated damage with Miner's rule and Wöhler-curves of concrete was less than one – although the tests experiences a fatigue fracture. Additionally, the occurred fatigue damage due to variable-amplitude loading was found to be more pronounced than under constant-amplitude loads but strongly depended on the applied loading program, especially on the load history.

Following the results of [83], it becomes evident that Miner's rule cannot predict the nonlinear fatigue damage behaviour of concrete. Tests carried out by Holmen [83] reveal difficulties faced when measuring the concrete strains employing strain gauges. He tested

numerous concrete cylinders under uniaxial loads both statically and under fatigue loading with either constant amplitudes (sinusoidal load shape) or randomly. The developed random loads represented a stationary narrow-band Gaussian process with, in this case, a constant frequency of 5.0 Hz. The probability distribution of peaks corresponded to a Rayleigh distribution, i.e. the generated random loads were an attempt to have the same statistical nature of forces experienced under offshore conditions in the short term (cf. Ch. 2.2). However, some limitations were required in order to facilitate the test implementation (e.g. constant sequence level amplitudes). The load generation resulted from a computer program. The tests revealed that low frequency values lead to a lower fatigue resistance while a high rate of loading increases the concrete strength – a fact found out by many other researchers. An important finding at tests carried out with constant amplitude loading or with constant average load value was a logarithmic normal distribution of the fatigue life. Nonlinear Wöhler-curves were derived and Holmen [83] and Cornelissen [30] evidenced the same scatter in the concrete fatigue life as in static uniaxial compressive strength. Concerning the strain development, and depending on whether the test duration was short or long, the strain increase rate was faster the longer the test duration was. Also interesting is the fact that the test frequency shows to be less influential on the strain development than on fatigue life. Holmen [83] describes the concrete strain consisting of an elastic component $\epsilon_{c3,el}$, related to the specimen endurance, and of a time-dependent component $\epsilon_{c3,t}$ which is independent of the concrete endurance but having a similar deformation behaviour than creep.

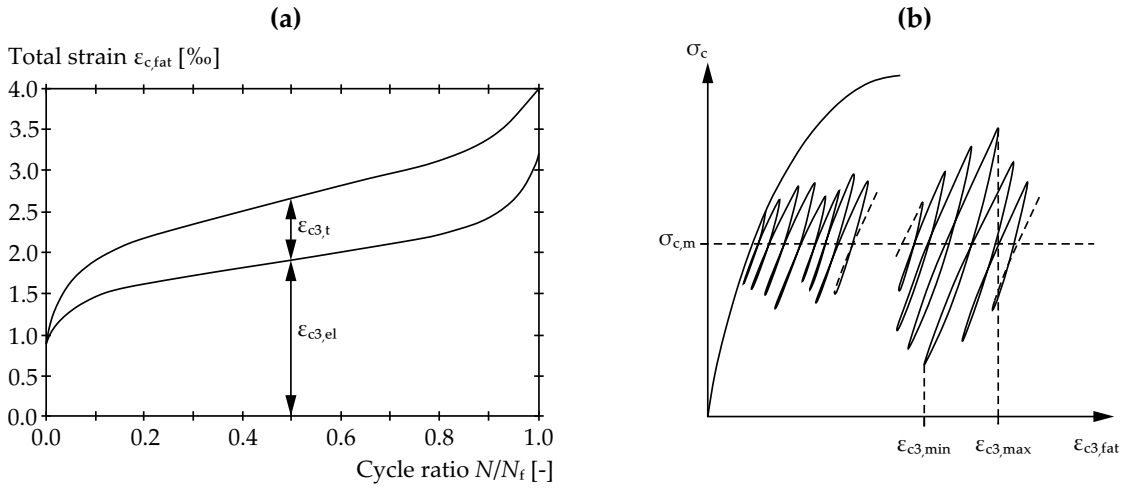

Figure 3.28: (a) Total strain components in long duration tests according to and redrawn from [83]; (b) Longitudinal concrete strain under random fatigue loading, redrawn from [83]

Holmen [83] established a mathematical equation for $\epsilon_{c3,t}$ with $S_{c,max} = 0.675$, and $S_{c,min} = 0.05$ and sought to scale it for other values of $S_{c,max}$.

Questions regarding the remaining concrete compressive strength after an imposed fatigue loading were also analised on the run-out test specimens by Holmen [83]. A reduction of f_c may logically be expected since the damage caused by fatigue loads leads

to a raise of internal cracks which may weak the concrete strength, depending of course on the perpetrated damage. However, Holmen [83] found out an increase of f_c of up to 8% after the specimens were subjected to fatigue loads with e.g. 12 million cycles. This knowledge leads to an important conclusion: Fatigue loading does not deteriorate the concrete statical strength at the ultimate limit state. The concrete "only" becomes softer, as it may be appreciated based on the development of E_c. Also in [82] only a light variation of f_c after the application of fatigue loads is reported.

Two-stage constant-amplitude tests with $S_{c,max1} = 0.90$ and $S_{c,max2} = 0.75$, both with $S_{c,min} = 0.05$, were also performed by Holmen [83]. Two sequence arragements were considered: Series I began with the higher stress level loads while Series II began with the lower stresses. As a result, the fatigue failure of the tests of Series I occurred at a calculated linear damage of $D < 1.0$ according Miner's rule; by Series II D achieved values higher than unity, i.e. $D > 1.0$. Holmen deduces herefrom a not sufficient accuracy of the linear cumulative damage hypothesis like Miner's rule. The so called sequence effect has a considerable role on the fatigue life of concrete. Likewise, the strain development rate of Series I was higher than Series II. Interestingly, the strain value $\epsilon_{cu,fat}$ at failure was almost unchanged for both Series, suggesting a constant, universal valid value of $\epsilon_{cu,fat}$. Hilsdorf [79] reports as well of self-performed two-stage fatigue tests and comes to the same conclusions regarding the sequence effects.

Variable-amplitude tests reported by Holmen [83] with a constant frequency of 5.0 Hz and a Rayleigh distribution of peaks have been analised statistically. The calculated linear damage after Miner's rule shows a logarithmic normal distribution. The average value was in all cases lower than unity: $D < 1.0$. This observation is also confirmed by Waagaard in [195]. Run-out specimens were subsequently tested at the ultimate limit state with the result that the static compressive concrete strength f_c was 7.0% higher than in pure static cases, similar to the specimen tested under constant-amplitude loads. Tests carried out by Cornelissen [30] with uniaxial, random compressive loading under variation of the load distribution (normal, Rayleigh), mean value, standard deviation, and type of spectrum (single peak, double peak, broad band) show similar results with $D < 1.0$ according to Miner's rule. The test scatter with a broad band spectrum is naturally higher; nevertheless, Cornelissen concludes than the use of Miner's rule is practicable provided that a counting method filters the small-range stress out which seem to lead to very favourable results.

Oh [135] analyses the fatigue life of concrete beam specimens under variable amplitude loading. The applied load configuration consisted of different constant-amplitude loads with increasing or decreasing sequences. After confirming the inapplicability of the linear Miner's rule on concrete under variable-amplitude loading, he derives a nonlinear damage accumulation function which is intended to account for the sequence-effect of concrete. The three stages of fatigue damage D are described by a cubic polynomial of the type

$$D = a_1 \left(\frac{N}{N_F}\right)^3 + a_2 \left(\frac{N}{N_F}\right)^2 + a_3 \left(\frac{N}{N_F}\right), \tag{3.42}$$

with N/N_F being the ratio of the actual number of stress cycles N to the total number of

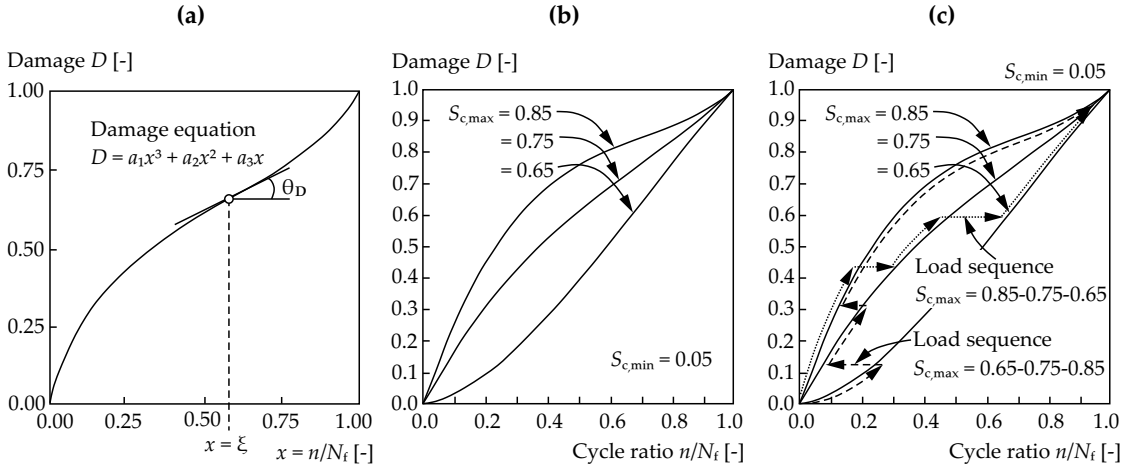

Figure 3.29: (a) Definition of nonlinear damage curve due to fatigue loading; (b) Fatigue damage curve for different stress levels; (c) Damage fatigue accumulation due to 3-stage fatigue loading with different sequences, redrawn from [135]

stress cycles until failure N_F, and a_1, a_2, a_3 being constants which depend on the load level. They may be derived by means of following conditions, setting $x = N/N_F$:

1.

$$D\,(x = 1) = 1, \tag{3.43}$$

2.

$$\frac{\mathrm{d}D}{\mathrm{d}x}\,(x = x_0) = \tan\theta_D, \tag{3.44}$$

3.

$$\frac{\mathrm{d}^2D}{\mathrm{d}x^2}\,(x = x_0) = 0. \tag{3.45}$$

x_0 indicates the so called inflexion point of the damage curve with a curvature change while θ_D represents the curve inclination at x_0. Following the test results of Holmen [83], Oh determines a constant value $x_0 = 0.7$ for the inflexion point. In contrast, θ_D is a function of the load levels $S_{c,max}$ and $S_{c,min}$. For example, for $S_{c,max} = 0.675$ and $S_{c,min} = 0.05$, the inclination becomes $\theta_D = 47.7°$; for $S_{c,max} = 0.75$ and $S_{c,min} = 0.05$, $\theta_D = 35.8°$. The cumulative damage calculation for different constant-amplitude amplitude sequences is done calculating first the damage D_1 resulting from the load sequence 1 with Eq. 3.42. For load sequence 2, an equivalent relative number of load cycles N_2/N_{F2} is then determined from the damage D_1 produced by load sequence 1 by solving Eq. 3.42 with $D = D_1$. Summing afterwards the relative number of load cycles of load sequence 2 to the already determined equivalent relative number of load cycles, then the total damage caused

by both load sequences may be calculated. This step may be repeated for a third load sequence (cf. Fig. 3.29). The damage caused by the load sequences 1 and 2 is converted into an equivalent relative number of load cycles N_3/N_{F3} that is added then to the actual relative number of load cycles of load sequence 3. Finally, the total fatigue damage is calculated.

The curing conditions of concrete as well as the degree of hardening are also considered to be important for the fatigue performance.

Another parameter, the time-related shape of loads, is reported to have certain influence on the concrete fatigue [83].

Hohberg [82] affirms that the water content in concrete is the most important parameter in the fatigue process.

Park [140] assumes the validity of the Envelope-concept. Based on test results of other researchers and simplified stress-strain-hysteresis with an assumed common intersection point situated on the third quadrant of the stress-strain-diagram, he develops a number of nonlinear equations capable to estimate the strain increase and the stiffness degradation of concrete. Yet, the assumption of a common intersection point of all hysteresis loops has not been confirmed by other researchers.

Heek [75] introduces the concept of a ductility-degree factor $\alpha_{c,duc}$. Based on published test data he notices a constant ratio between elastic and plastic concrete strains inside of the analised stress-strain-hysteresis. Therefore, he concludes that the ratio between dissipated energy due to fatigue damage and total applied energy should also be constant (damage invariance). Accordingly, the dissipated energy in the fatigue process may be estimated by means of the constant ratio mentioned before, provided the Envelope-concept is valid. The calculated deformation energy per unit area is then set in relation to the corresponding elastic deformation energy – this is the ductility-degree factor $\alpha_{c,duc}$, with values between 0 (low ductility) and 1.0 (very ductile). With help of $\alpha_{c,duc}$ and considering the load frequency by modifying the concrete strength (high load frequencies enlarge f_c and f_{ct}), Heek develops Wöhler-curves that are supposed to be valid for both, plain concrete and steel fibre concrete, taking the applied load frequency (constant amplitude loads) into account.

Energy-based calculation models base on the hypothesis that the area under a static stress-strain-curve represents the (whole) required energy for the failure of a concrete specimen. However, as a result of the fatigue process, the stress-strain-curve is altered (irreversible strains, stiffness loss); therefore, the required (rest)-energy for failure is expected to be reduced. If it is possible to accurately estimate the dissipated energy during the fatigue process, then it should be possible to estimate the remaining fatigue life [82].

Lately, Pfanner [144] has published a damage calculation model for concrete under uniaxial compression as well as under uniaxial tensile stresses. The model uses energy-based concepts for estimating the remaining fatigue life of concrete. Comparison calculations performed by [60] and [98] seem to confirm its applicability. Basically, the (complex) Pfanner-model assumes the invariance of the required energy for achieving failure. The achieved strain $\epsilon_{c,fat}$ during a fatigue loading is calculated previous determination of the generated damage D which results from the energy-invariance-condition and an assumed concrete constitutive material equation. The strain development depends hereby only

on the number of cycles and it follows a nonlinear trend that results from superposition of three equations: The first equation accounts for the creep-similar concrete behaviour at begin of the fatigue process. The second equation describes the linear accumulation of micro-cracks while the last equation considers an abrupt strain increase at the failure stage. Pfanner's model makes damping effects in the material responsible for the major part of energy dissipation; this is taken into account together with further corrections taken from test results found in the available literature. With these values, estimations of the remaining fatigue life and concrete strength are accessible. A detailed mathematical derivation of Pfanner's model is not intended here, comprehensive information may be found in [144] and [60].

However, Pfanner's model is criticised by Oneschkow [137]. Accordingly, the partially large fatigue-induced strains, which may extend beyond ϵ_{cu} and which are predicted by Pfanner's model, have not been completely confirmed, especially in specimens of high-strength concrete. Actually, Pfanner's model requires an accurate description of the softening concrete behaviour; yet this is, according to [178], not an inherent material property but rather depends on the specimen dimensions. Pfanner's model also may predict a remaining concrete strength which is lower than the static strength f_c. Though, diverse authors report that the remaining concrete strength after fatigue loading, basically, is not affected.

As claimed by [102], [111], no fatigue endurance limit for concrete has been established.

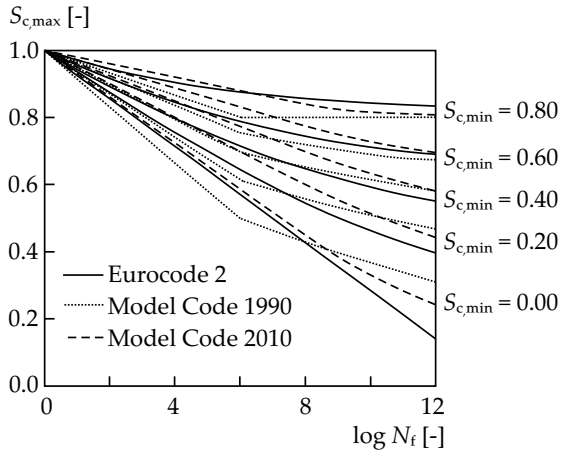

Figure 3.30: Wöhler-curves of concrete under uniaxial compression loading, redrawn from [138]

The actual design standards [132], [24], [51] for concrete compression fatigue base all on Wöhler-curves and on a fatigue strength $f_{cd,fat}$ [138]. Accordingly, the fatigue design is part of the ultimate limit state of structures and requires a stringent reliability. Therefore, the design value of the material strength is provided with partial safety factors comparable with the ultimate limit state. The variability of test results is taken into account by means of a design value for the concrete compression strength. The Wöhler-curves in the standards correspond therefore to average values and are no quantiles. The lower

value of $f_{cd,fat}$ compared to f_{cd} is due to a believed more brittle concrete behaviour under fatigue loads and should be adjusted to actual more favourable test findings. Miner's rule is still used owing to the lack of more practicable alternatives even though the already mentioned sequence-effect of concrete may lead to unsafe results. The influence of the load frequency is globally taken into account through a parameter ($\beta_{c,sus}(t,t_0)$ or $k_1\alpha_{cc}$) for high permanent loads and deviations of the verified load frequencies [139]. The DNV standard for offshore concrete structures [42] also employs the linear Miner's rule but limits the achievable cumulative damage according the location of structural element.

$$D = \sum_{i=1}^{k} \frac{n_i}{N_i} \leq \eta_D, \tag{3.46}$$

with η_D according Tab. 3.4.

Table 3.4: Limit of cumulative damage ratio according to DNV standard [42]

	No access for inspection or repair	Below or in the splash-zone	Above the splash-zone
$\eta_D[-]$	0.33	0.50	1.00

In accordance with the RILEM Committee [111], the value of η_D depends on the loading parameters like governing frequencies and randomness characteristics. Based on [208], the Model Code 2010 [51], in the Level IV of approximation for the fatigue design, stipulates that values $\eta_D \leq 1.0$ may be necessary for decreasing stress levels. For increasing stress levels, $\eta_D = 1.0$ is a conservative assumption. A nonlinear accumulation rule of damage according to [192] may have following shape:

$$D = \sum_{i=1}^{k} \left(\frac{n_i}{N_i}\right)^{\alpha_i} = 1.0, \tag{3.47}$$

with α_i depending on the load sequence. However, Eq. 3.47 is not applicable under random loading.

The DNV standard [42] is probably the unique standard which also takes the effects of water into account. It differentiates whether the structure is in contact with seawater – like in offshore-structures – or not. The presence of water has shown to have a considerable negative influence on the fatigue resistance [30]. According to reports and test results cited in [195], concrete structures under water may be subjected to an usually significant hydrostatic water pressure and experience reversed fatigue loading. Under these conditions, a water-pumping-effect has been observed. It describes the process of water being pumped out of concrete cracks by reversed loads, causing cracks to open and close periodically. This water-pumping-effect generates overpressures inside the cracks [182] and this phenomenon is considered responsible for the measured lower fatigue strength of concrete under water.

Banerjee et al. [11] reports of tests with prestressed concrete beams performed under both conditions, in air and seawater, the latter however without a noteworthy water pressure. Since prestressed concrete structures are usually designed to be under compression at the serviceability limit state – consequently the experienced stress ranges by the tendons are small and cracks are permitted only in accidental or extreme load situations–, the tests emphasise partial prestressed conditions. The governing load frequency was chosen to f = 0.17 Hz in accordance to the dominating wave frequency in the North Sea. It was expected that two damage processes were set in motion:

1. Concrete damage due to water pumping effects in cracks, leading to a loss of prestressing force and eventually to a fatigue failure of the concrete in the compression range.
2. Corrosion fatigue in tendons as a result of the contact with sea water in the cracks.

While the beams tested in air failed at the main flexural cracks, the beams tested under sea water conditions showed salt deposits in cracks as well as reduction of the crack opening range and beam deflection. An erosion of crack surfaces could not be observed. According to Barnejee et al.[11], this may be due to the low load frequency which impeded an effective damaging through the pumping effect. The reported tests, however, did not exhibit any significant pressure in the surrounding sea water. A corrosion process was observed only in the ducts of the tendons. A reduction of the fatigue life could not be confirmed.

A British research project investigated the fatigue performance of concrete and reinforced concrete members under offshore conditions between 1980 and 1990. In numerous tests of specimens under the presence of sea water and with low, wave-similar load frequencies, it could be confirmed that sea water caused a shorter fatigue life of the specimens. Sea water accelerates corrosion processes in reinforcement and, provided that low load frequencies and a long test duration were given, the fatigue strength was considerably lower [176]. A partial blocking of the crack surfaces was also observed which, according to the author's opinion, may be considered favourable for reducing the stress range in the reinforcement. However, for high load frequencies, an erosion of the crack surfaces was noticeable. Yet, results published in [81] show the contrary: Similar fatigue life of beams tested in seawater than those tested in air and even a higher fatigue life provided the stress range is limited to $\Delta\sigma_s \leq 250$ MPa. The cause for it is believed to be the accumulated salt deposits in the cracks which increase the beam stiffness and reduces its deflections. The stiffness increase due to a crack sealing through salt deposits is called "cyclic stiffening" [141]. Price et al. [149] reports, based on a literature review, that a water pumping process happens in concrete cracks of underwater structural members subjected to dynamic loading with a consequent erosion of crack surfaces, an increase of crack widths, and a stress redistribution within the member. This observation is confirmed by [141].

3.2.5 Concrete Uniaxial Behaviour under Fatigue Tension Loading

Similar to the tension strength under monotonic statical loading, the fatigue behaviour of concrete under tension stresses exhibits a considerable scatter [29]. In addition, the test

procedure is complicate and susceptible to errors or inaccurate results. Cornelissen [29] mentions concentric tensile tests which may be performed force-controlled or deformation-controlled. The main advantage of this sort of tests is a quasi-uniform stress distribution. Bending tests are also popular since they are simpler to execute than concentric tests. Though, the generated stress gradient in the cross sections as well as along the test beams leads to different results as in concentric tensile tests. Another test procedure are splitting tests. They are also simple to perform but present, apart from an inhomogeneous stress distribution, biaxial stress states which may influence the results. A detailed review of influencing parameters may be found in [96].

Results of concentric tests and bending tests published in [29] reveal a strong dependency of damage on the load magnitude and moisture content. The fatigue process under tension stresses is attributed to the raise of microcracks and deformations caused by creep effects which are dominant by low-magnitude loads or low load frequency values whereas crack growth is more important by high-magnitude loads [29]. According to this source, the static tension strength is not affected by the action of fatigue loads. After evaluating own fatigue splitting tests, Tepfers [189] concludes that the inhomogeneous stress distribution of his test specimens has no influence on the results, which contradicts the opinion of Cornelissen [29], and develops Wöhler-curves for plain concrete under (splitting)-tension. Kessler-Kramer [96] notes, however, that the results greatly depend on the test procedure.

A convenient parameter to analyse and quantify the fatigue process under tension loading and its softening behaviour is the stress-strain-curve [155]. Displacement-controlled tests in the tension region found in [155] reveal a steady stiffness decrease, an increase of irreversible deformations and of the deformation rate with every load cycle. Further tests are reported where the test specimens were subject of low compression stresses after being loaded with tensile stresses. The decrease of stiffness seems to be more pronounced while the increase of deformation rate is less accentuated. Yet, are the lower stress amplitudes $\sigma_{c,min}$ high compression stresses, then the increase of deformation rate is again more elevated. The cracking regions expand and their internal crack surfaces progressively become hart to fit. Under compression stresses the specimens are reported to gain some stiffness probably due to certain interlock or frictional effects which permit a low amount of force transmission. The principal finding in [155] is the confirmation of an unique envelope-curve, independent on load history, that is valid for displacement-controlled fatigue tension. The test results of Kessler-Kramer [96] are very similar. Among others, they show a considerable change of the fracture energy of concrete with increasing number of load cycles.

According to [29], test data of concentric tests with alternating loads in compression and tension regions are rare. Based on self-performed tests, Cornelissen [29], [30] found out that the fatigue life is dramatically reduced by alternating compression-tension loads. Stress reversals seems to be more damaging for tensile fatigue failure than for compressive fatigue failure.

Following approaches of continuum damage mechanics, in [125] an interesting nonlinear model is given for the determination of damage under tension fatigue. The maximum tensile strain is chosen as main parameter for quantifying the damage progress. Assuming

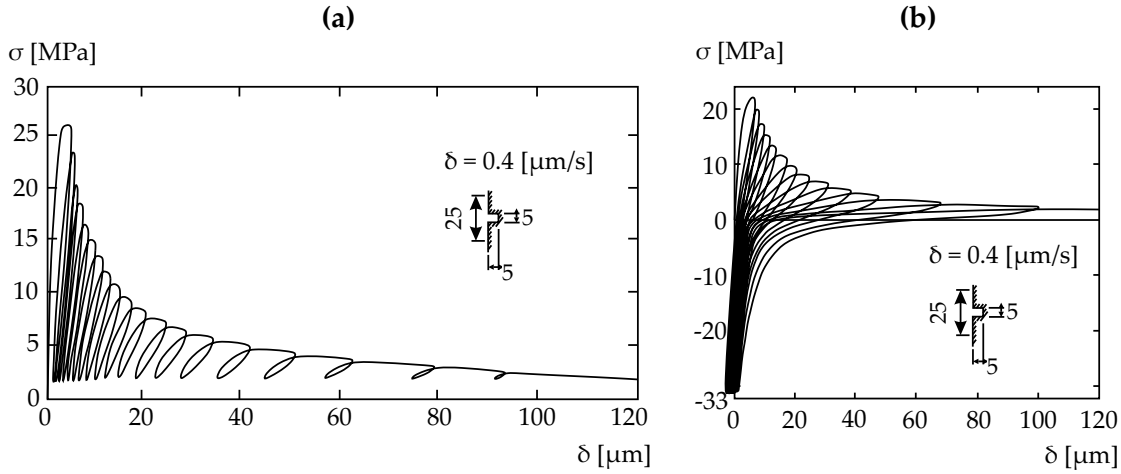

Figure 3.31: (a) and (b) Stress-deformation curves (deformation-controlled) of concrete under cyclic tensile loading, redrawn from [155]

a S-shaped strain development over the load cycles, following equation is suggested for the damage evolution under only pure tension loading:

$$D = \alpha_0 S_{c,max}^2 + \alpha_1 S_{c,max} S_{c,min} + \alpha_2 \left(S_{c,max} - S_{c,min} \right). \tag{3.48}$$

$S_{c,max} = \sigma_{c,max}/f_{ct}$, $S_{c,min} = \sigma_{c,min}/f_{ct}$, and f_{ct} is the concrete statical uniaxial tensile strength. α_0, α_1, and α_2 are different depending on the actual relative load cycle and have to be derived from tests.

Note that actual standards like [132], [51] do not consider aspects neither of tension fatigue nor of compression-tension fatigue of concrete.

3.2.6 Concrete Multiaxial Behaviour under Fatigue Loading

Holmen [83] observes, based on published test data in the literature, that a lateral pressure strongly influences the concrete resistance against uniaxial fatigue loads. Accordingly, a lateral pressure raises the fatigue life, an effect comparable to the static compression strength increase under simultaneous lateral compression stresses.

Concerning the fatigue performance of concrete under biaxial stress states there are almost no available research results. Especially stress regions under compression with simultaneous lateral tension are frequently found in practice like in beams experiencing shear and torsion or in discontinuity regions of slab structures. It may be expected that the fatigue resistance in this case is considerably reduced the higher lateral tension stresses are. However, the difficult test procedure and the lack of reliable calculation models for the fatigue response of concrete under uniaxial loading are presumably the main reason for the almost nonexistence of usable data.

In [188] is a report of tests carried out on hollow cylindrical concrete specimens subjected

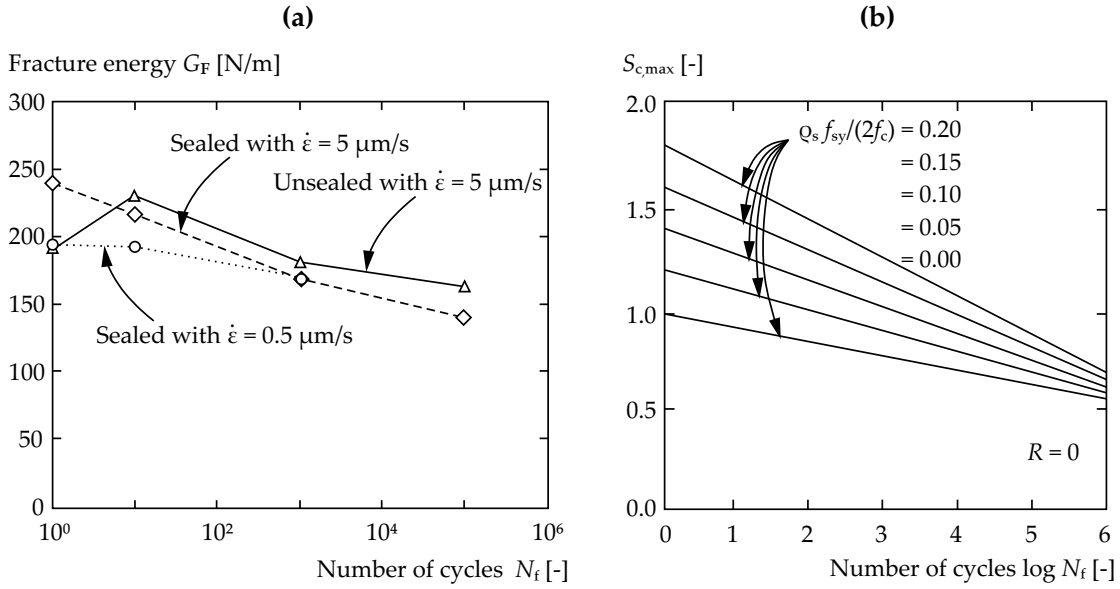

Figure 3.32: (a) Development of fracture energy under fatigue loading (strain-controlled) with different strain rates and seal conditions, redrawn from [96]; (b) Increase of fatigue compression strength as function of a passive confinement with the yield strength f_{sy} and a reinforcement ration $\rho_s = A_s/A_c$, redrawn from [192]

uniquely to torsional fatigue loading. Torsional moments cause shear stresses which, in terms of principal stresses, may practically be considered as a biaxial stress state composed of compression and lateral tension stresses. According to [188], the fatigue induced damage is governed by a single crack and its corresponding growth. The torsional stiffness is found to decrease constantly while the axial strains increase. Similarly to uniaxial fatigue loads, the Envelope-concept seems to be applicable too.

According to [192], the presence of lateral compression enhances the fatigue performance of concrete, comparable to the effects on the statical strength. A lateral compression may be applied directly in form of loads or passively in form of a confinement.

Günberg et al. [65] presents a model developed by Göhlmann in [60] for the fatigue response of concrete under multiaxial loading. The model is energy-based, follows the hypothesis of Pfanner [144], and uses the analysis concept of [102] and [24]. The three-dimensional concrete constitutive equation of [201] is employed and complemented with two new so called damage-parameters: $\kappa_{t,fat}$ for the tension meridian and $\kappa_{c,fat}$ for the compression meridian. Göhlmann's model has also the possibility to account for multi-stage, constant-amplitude loading and includes elements of [135]. The value of dissipated energy, fatigue-induced damage, and the strain development together with the stiffness degradation are calculated iteratively. The corresponding numerical implementation in a finite-element-program enables afterwards the structural analysis of critical regions like towers of wind energy converters. It should be stated, though, that Göhlmann's model partially bases on assumptions owing to the lack of material parameters. Moreover, the

data base, which this models is based on, is not sufficient for a wide generalization and more experimental data is urgently required. Finally, Pfanner's model, which constitutes the core of Göhlmann's model, is still not sufficiently verified. In fact, Pfanner's model is considered controversial e.g. by [137]. The bottom line is that more test results of the biaxial and multiaxial fatigue behaviour of concrete are necessary.

3.3 Bond

3.3.1 Bond Behaviour under Static Loading

The purpose of the embedded reinforcement in concrete is to carry structural tension forces which result from stresses that exceed the modest tensile strength of concrete. In structural regions, where the stress resultant is higher than the concrete tensile strength, the concrete cracks and a subsequent internal stress redistribution occurs until a new admissible equilibrium state is reached. After cracking the steel reinforcement carries the tensile forces – ideally only in longitudinal direction – and transfers them partially into the concrete in form of bond stresses, inducing in this way a new internal stress and equilibrium state in the vicinity of a crack. Therefore, the bond properties play an important role in terms of a required anchorage length or overlap length. Likewise, crack behaviour, stiffness, and deformation capacity of structural members are directly related to the bond properties. The interaction between reinforcement and concrete is given principally due to an interlocking-effect between bar ribs and concrete and to other, less relevant force-transfer mechanisms.

An extensive overview over the bond behaviour and the most important parameters may be found in [190]. Bond stresses between reinforcement and concrete are described as shear stresses τ_b at the reinforcement-concrete-interface. Orthogonally to τ_b, radial stresses σ_{br} are generated which originate radial compression on the surrounding concrete [152]. This factor enhances the concrete strength at the bond interface. Both, bond and radial stresses, result from a transformation of coordinates; the principal stress, basically present at the slope of the ribs, is inclined with an angle α_b of approximately 53...64° [156] towards the reinforcing bar at the maximum bond stress τ_{bu} and it decreases depending on the location along the bar and on the load magnitude. Goto [62] points out, that the inclination angle α_b of internal cracks lies between 45...80°, most of which show an inclination of 60°. Fehsenfeld [49] proposes values for α_b which are summarised in Tab. 3.5. The expansion of radial stresses causes circumferential stresses $\sigma_{b\phi}$ in the surrounding concrete and superpose to other existing, global stresses from e.g. bending moments and normal forces in a structural element. As a result of the interlocking-effect of the ribs, the concrete located at the rib slopes experiences an enormous compression at the ultimate limit state which leads to inhomogeneous distributed stresses and a partial local plastification of the concrete. An induced multiaxial stress state in this region permits a higher concrete strength than f_c [118]. It also enhances the friction between concrete and steel [62], increasing the bond performance. Rehm [152] reports that the achievable local stress in the concrete teeth may reach values $\sigma_c \approx 16 f_{c,cube}$.

A simple mathematical model consists of bond stresses τ_b uniformly distributed along reinforcement bars, where bond stresses τ_b are activated as soon as there is a slip δ_s (a

Table 3.5: Values of inclination angle α_b of the interlocking forces between concrete and reinforcement as function of the loading degree and the concrete cover c_{nom} [49]. SLS is the serviceability load state, ULS the ultimate load state

$Ø_s$ [mm]	SLS - steel linear-elastic - crack widths thin		ULS - steel plasticises - crack widths thick
	$c_{nom}/Ø_s < 3$	$c_{nom}/Ø_s \geq 3$	
< 25	35...45°	30...35°	45°
≥ 25	30°	-	45°

deformation difference) between reinforcement and surrounding concrete. δ_s results from the irreversible deformation of the concrete around the steel bar in form of radial cracks and compressive strains at the corbels of a reinforcing bar, and constitutes for instance an average value of the concrete behaviour [49]. Thus, the $\tau_b - \delta_s$-curve constitutes a kind of pseudo material equation [109] which describes the mechanical bond behaviour similar to the stress-strain-relationship of materials. Nonetheless, it is not a material equation in terms of continuum mechanics due to the strong dependence on the test set-up [86]. The bond stress τ_b has to be considered as a nominal bond stress [49]. $\tau_b - \delta_s$-curves are determined in diverse pull-out tests with a reinforcement bar embedded in concrete with an effective bond length of $2Ø_s...5Ø_s$. In older tests, bond lengths between $5Ø_s...15Ø_s$ and sometimes even of $20Ø_s$ have been used. In fact, in [119] it is reported that under a bond length $\leq 10Ø_s$ the bond stress distribution is nearly constant. The bond length employed for the determination of $\tau_b - \delta_s$-curves is considered as an infinitesimal bond element that is independent of other influencing factors; however, numerous other parameters do play an additional role in the $\tau_b - \delta_s$-curves [2]. Therefore, the $\tau_b - \delta_s$-curves are not universal valid [86].

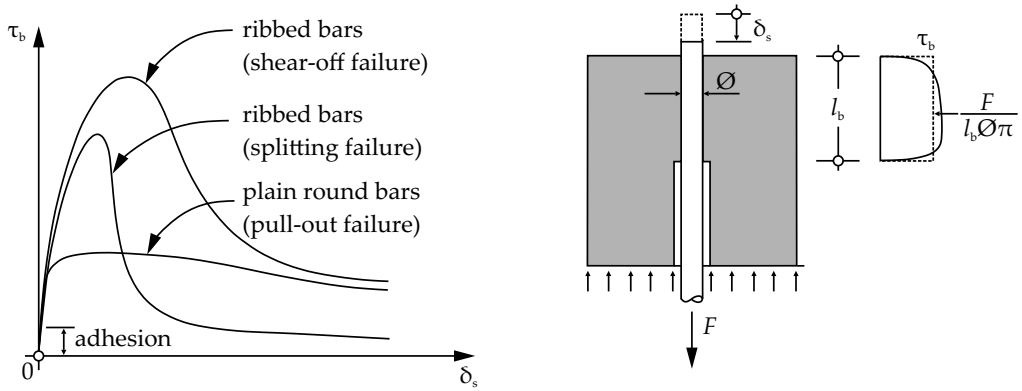

Figure 3.33: Qualitative bond-slip-behaviour and pull-out test with bond stress distribution, redrawn from [2]

The stress and strain distribution in the reinforcement and surrounding concrete may approximately be described through a differential equation that has been derived in

[152]. It was developed for uniformly, symmetrically reinforced and loaded concrete chords based on equilibrium equations and a linear-elastic, uniaxial material behaviour. It considers an infinitesimal reinforced concrete chord under tension forces. Taking into account a circular steel bar area $A_s = \pi/4 \varnothing_s^2$ in a simplified scheme and the bond stress τ_b being uniformly distributed around the steel bar, the equilibrium equations for reinforcement and concrete are set separately. With $n = E_s/E_c$ and $\rho = A_s/A_c$ it follows

$$\frac{d\sigma_s}{dx} = \frac{\pi \varnothing_s}{A_s}\tau_b = -\frac{4}{\varnothing_s}\tau_b, \tag{3.49}$$

$$\frac{d\sigma_c}{dx} = -\frac{\pi \varnothing_s}{A_c(1-\rho)}\tau_b = \frac{4\rho}{\varnothing_s(1-\rho)}\tau_b. \tag{3.50}$$

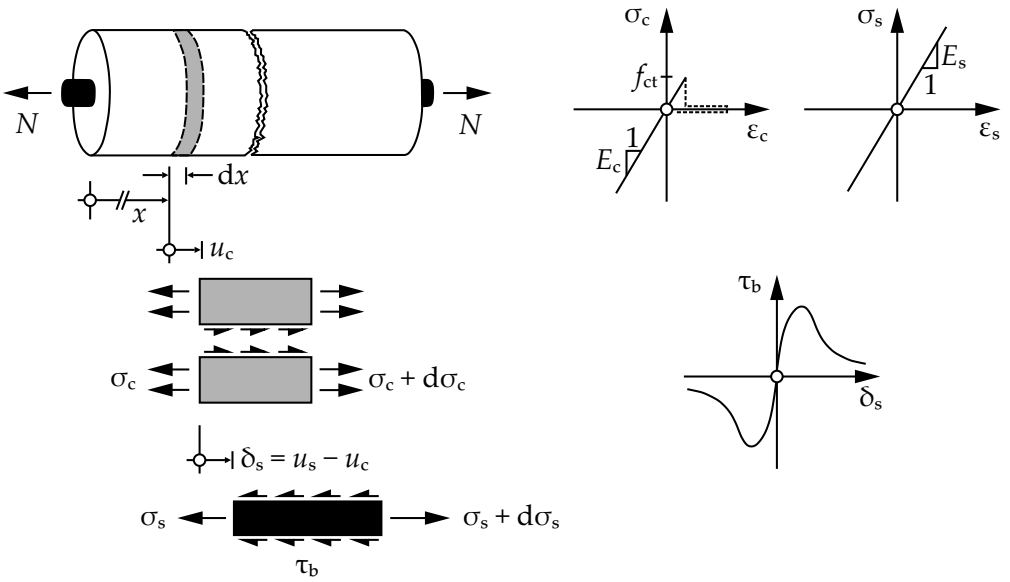

Figure 3.34: Derivation of differential equation of bond at a reinforced concrete chord, definition of the slip δ_s, and linear-elastic material equations, redrawn from [2]

Per definition, the slip between reinforcement and concrete is defined as difference of the (longitudinal) deformation u of both.

$$\delta_s = u_s - u_c \tag{3.51}$$

As mentioned before, the differential equation of bond bases on linear-elastic material behaviour: $\sigma_s = E_s \epsilon_{sy}$ for reinforcement and $\sigma_c = E_c \epsilon_c$ for the concrete around it. With the

kinematic equations

$$\frac{\mathrm{d}u_\mathrm{s}}{\mathrm{d}x} = \epsilon_\mathrm{sy}, \tag{3.52}$$

$$\frac{\mathrm{d}u_\mathrm{c}}{\mathrm{d}x} = \epsilon_\mathrm{c}, \tag{3.53}$$

it follows for Eq. 3.51, after derivation after x,

$$\frac{\mathrm{d}\delta_\mathrm{s}}{\mathrm{d}x} = \epsilon_\mathrm{sy} - \epsilon_\mathrm{c} = \frac{1}{E_\mathrm{s}}(\sigma_\mathrm{s} - n\sigma_\mathrm{c}). \tag{3.54}$$

After a second derivation after x and taking Eq. 3.49 and 3.50 into account:

$$\frac{\mathrm{d}^2\delta_\mathrm{s}}{\mathrm{d}x^2} = \frac{1}{E_\mathrm{s}}\left(\frac{\mathrm{d}\sigma_\mathrm{s}}{\mathrm{d}x} - n\frac{\mathrm{d}\sigma_\mathrm{c}}{\mathrm{d}x}\right) = \frac{1+\rho(n-1)}{1-\rho}\frac{4}{E_\mathrm{s}\varnothing_\mathrm{s}}\tau_\mathrm{b}, \tag{3.55}$$

where the bond stress is a function of the slip, i.e. $\tau_\mathrm{b} = \tau_\mathrm{b}(\delta_\mathrm{s})$. Eq. 3.55 can be analytically solved only for some simple cases of $\tau_\mathrm{b}(\delta_\mathrm{s})$, like those described in [152] and [118]. Other solutions may be obtained using numerical calculation methods; a numerical procedure is given in [2].

If a reinforced concrete chord is subjected to a normal force gradient $\mathrm{d}N/\mathrm{d}x = q_\mathrm{n}$ – this may be the case e.g. in tension chords of beams under bending loading –, the differential bond equation needs to account for q_n. Alvarez [2] assumes tacitly that q_n is carried only by the concrete around the reinforcement

$$\frac{\mathrm{d}\sigma_\mathrm{c}}{\mathrm{d}x} = \frac{\rho}{(1-\rho)A_\mathrm{s}}q_\mathrm{n} - \frac{4\rho}{\varnothing_\mathrm{s}(1-\rho)}\tau_\mathrm{b}. \tag{3.56}$$

$$\frac{\mathrm{d}^2\delta_\mathrm{s}}{\mathrm{d}x^2} = \ldots = \frac{1+\rho(n-1)}{1-\rho}\frac{4}{E_\mathrm{s}\varnothing_\mathrm{s}}\tau_\mathrm{b} + \frac{n\rho}{(1-\rho)E_\mathrm{s}A_\mathrm{s}}. \tag{3.57}$$

The simplified model conception that is used for deriving the differential equation of bond assumes a fictitious concrete area A_c where the tensile stresses, resulting from the load transfer of the reinforcement into concrete, are uniformly distributed. However, A_c is difficult to quantify [152]; the concrete strains may be up to 0.1...0.2‰. At this point, different empirical equations have become most accepted [163]. In [23] there is a well-founded mathematical derivation of A_c for bending members (cf. Ch. 4.2.3). Further sources concerning the estimation of A_c are given in [190].

The bond constitutive equation consists of four stages that are summarised in [190]. In

case of a tension chord being monotonically loaded until failure, these are:

- Stage 1: Uncracked concrete. No slip between reinforcement and concrete occurs and a certain force transmission is achieved through chemical adhesion and micromechanical interaction.
- Stage 2: First cracking. The reinforcement carries tension forces at the crack surfaces and introduces them into the concrete. The consequent slip between reinforcement and concrete activates bond forces resulting mainly from the interlocking action of the bar ribs. Transverse microcracks – responsible for the slip together with deformation of the pressed concrete – arise at the ribs tips [62]. There is a nearly linear relation between bond stress τ_b and slip δ_s.
- Stage 3: nonlinear $\tau_b - \delta_s$-relation until the ultimate bond stress τ_{bu} is reached. The ultimate bond stress τ_{bu} is defined by the shear strength capacity of the concrete corbels. Transverse microcracks (microcracks are cracks that do not reach the concrete surface [9]) increase in depth and width, sometimes even crossing primary surface cracks or growing to the surface in form of secondary cracks [62], while the circumferential stresses $\sigma_{b\phi}$ around a reinforcing bar also increase, causing the surrounding concrete to a deform in radial direction. If $\sigma_{b\phi} > f_{ct}$, the so called splitting cracking along a reinforcing bar takes place which may provoke an early bond failure. Thereby, a certain release of the splitting action is observed which is caused by the radial contraction of the reinforcement. This effect reduces the bond stresses and is connected with a further considerable increase of slip δ_s [49].
- Stage 4: Descending branch of the $\tau_b - \delta_s$-curve, depending on the type of failure (pull-out-failure, splitting-failure). In case of a pull-out-failure, the remaining bond stresses are principally friction forces between the sheared-off concrete corbels and the surrounding concrete. By a splitting failure the longitudinal cracking grows until the bond strength is completely reduced.

It is important to mention that the $\tau_b - \delta_s$-curve only describes the local bond behaviour of a bar segment whose length often amounts $2Ø_s...5Ø_s$ since lower length values do not really alter the measured bond stresses [156]. Because the force transfer is enabled mainly by the bar ribs, it is recommendable that the bond length for test purposes amounts at least the rib spacing [152]. Though, low values of the bond length in tests inevitably result in a greater scatter owing to the concrete composition [156] and side effects. The structural behaviour of a reinforced tension chord, however, is characterised by a redistribution of bond stresses at the ultimate limit state, so that a local bond failure does not necessarily leads to a structural failure.

After unloading there is a remaining restrain and the reinforcement still experiences tension stresses, especially in the uncracked sections [62]. Cracked sections do not completely close. Goto [62] assumes that this effect is caused by a plastic deformation of concrete at the ribs.

Thanks to a longstanding research on the bond behaviour, numerous relevant parameters have been identified [190], [109]. Results of a few selected sources are discussed in the following section owing to the abundance of published works.

Table 3.6: Influencing parameters on mechanical bond behaviour [109]

Parameters			
Reinforcement	Concrete	Load	Test specimen
Diameter	Concrete strength	Longitudinal stress	Specimen shape
Bar cross section	Concrete manufacturing	Transverse stress	Specimen size
Rib geometry	Composition	Pulsating load	Bond length
Surface shape	Material behaviour	Alternating load	Cast direction
Final design	Consolidation	Load range	Bond region
Corrosion	Young's modulus of elasticity	Long-term load	Reinforcement confinement
Ductility		Load history	
Tensional strength		Load velocity	Concrete cover
		Load frequency	Bar inclination
		Temperature	Points of measurement
		Radiation	

The first essential parameter is the concrete tensile strength f_{ct} and, hence, the concrete uniaxial compression strength f_c [118]. Based on numerous pull-out tests, Martin et al. [119] concludes that the influence of the concrete strength may be described by

$$\tau_{b,0.1} = b f_{c,cube}^{c}. \tag{3.58}$$

$\tau_{b,0.1}$ denotes the achieved bond strength by a slip value of $\delta_s = 0.1$ mm. The constant c depends on the bond index f_R and exhibits values between $c = 1.0...1.2$ for ribbed bars while for plain round bars the values are $c < 1.0$. For bar diameters $Ø_s = 16...32$ mm and a bond index $f_R = 0.065...0.090$, the bond strength may be calculated by

$$\tau_{b,0.1} = f_{c,cube}^{c}, \tag{3.59}$$

with $c > 1.0$ [119].

A further significant parameter is the bond index f_R [49]. Defined as the coefficient between the projected area A_R of a single rib and the skin surface of the reinforcing bar $\pi Ø s_R$ (s_R is the rib spacing) between two ribs, the bond index summarises geometric properties of the bar ribs. According to [118], the circumferential stresses σ_{br} increase with growing f_R. The bond strength may be significantly enhanced with increasing values of f_R, which results in short crack spacings and thus in thin crack widths in structural members. However, high f_R-values also multiply the risk of splitting cracks [119]. Hence, it turns to be mandatory to find a balance between serviceability, safety, practicability, and economic feasibility. Since the rib geometry is crucial for the industrial reinforcement production, it was necessary to fix the requirements for minimal values of f_R considering the effects on splitting of the concrete cover, bond degradation under fatigue loading,

ductility properties, and safety. An interesting overview of this iterative process is given in [109]. The German standard DIN 488-1 [36] determines minimal values depending on the bar diameter; for $Ø_s$ = 11.0...40.0mm, the minimal bond index amounts f_R = 0.056. Small ribs result in a slip decrease [152] as a consequence of a reduced deformation of the concrete corbels. Additionally, in order to avoid notching effects and a limited fatigue performance of the reinforcement, it is important that rib roots are sufficiently rounded out [152].

Likewise, the cast direction of the concrete has proven to decisively influence the bond strength. Bars which lie horizontally have a considerable lower bond stress. Vertically casted reinforcing bars show a bond strength twice as high as in horizontally casted bars [119]. According to [152], one reason for this effect is the settling of the freshly mixed concrete. In this way, pores arise beneath the reinforcement and the effective bond area is reduced. Furthermore, the gap between reinforcement and concrete disturbs the restrain effect on concrete and the subsequently multiaxial stress state, reducing in this way the achievable strength.

The thickness of the concrete cover c_{nom} is also a decisive parameter for the failure mechanism of bond. The induced circumferential stresses σ_{br} behave at first linear-elastically. The maximal achievable tensile stress $\sigma_{br,max}$, though, is considerably higher than the uniaxial tensile strength f_{ct} due to the governing restrain. An average value has been found to $\sigma_{br,m} \approx f_{ct}$ [118]. If the ribs are higher than 0.5 mm and the rib spacing ≥ 2 mm, then the shear-off failure occurs at slip values of approx. 10% of the rib spacing [152]. In case of a splitting failure, Eligehausen et al. [45] concludes, based on measurements of the transverse strain of the concrete surrounding the reinforcement, that the (local) splitting-crack-formation does not lead to an abrupt bond change or loss. Bond stresses may be redistributed and still be transfered until new splitting cracks arise or the concrete cover is lost.

Actually, the transferability of pull-out-tests, which are performed with relatively thick concrete specimens, and the resultant bond-slip-relationships to reinforced structural members with usually thin concrete covers is questionable. Fehsenfeld [49] demonstrates that concrete covers which are as thick as the bar diameter $Ø_s$ are normally not sufficient for avoiding a splitting failure. Schenkel [162] and also Fehsenfeld [49] analise the force transfer processes and their limits with conventional concrete covers. By means of a linear-elastic model Schenkel calculates the ultimate circumferential capacity of the concrete ring surrounding the reinforcement. As soon as $\sigma_{b\phi} = f_{ct}$, radial cracks arise beginning from the inner edge, i.e. the concrete-reinforcement-interface, and a circumferential stress transfer becomes limited or even impossible. In consequence, a stress redistribution occurs, enlarging the effective load radius from r_i to r_{ct} (Fig. 3.36). r_i corresponds to the radius of a reinforcing bar while r_{ct} is the radius to the point where radial cracks end. Since $r_i < r_{ct}$, the resulting circumferential stresses after cracking are lower which allows a further load increase. Based on a linear-elastic material behaviour,

$$\sigma_{b\phi} = \frac{r_i r_{ct} p_{ri}}{r_o^2 - r_{ct}^2} \left(1 + \frac{r_o^2}{r}\right), \tag{3.60}$$

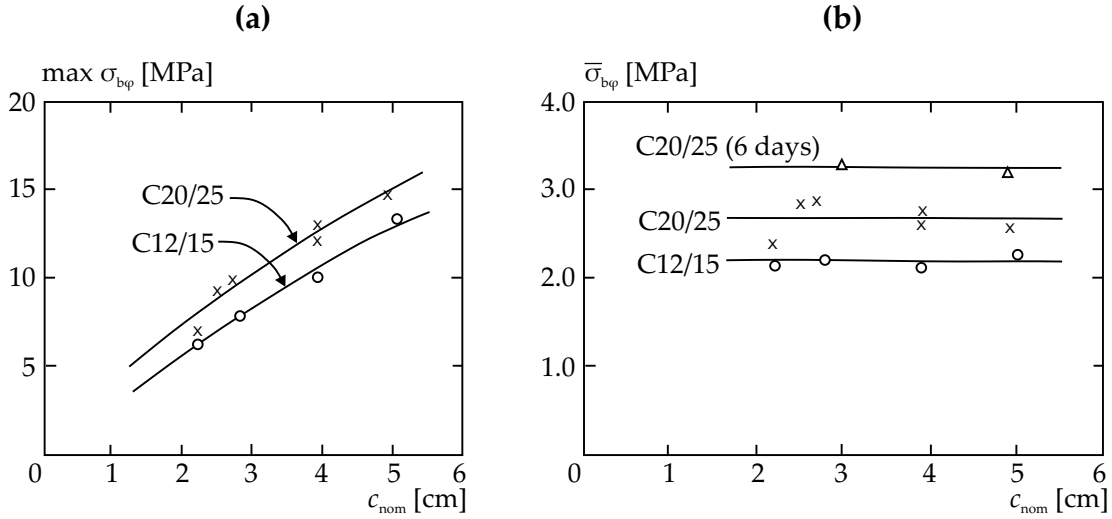

Figure 3.35: Maximal and average circumferential stresses in dependence of concrete cover and characteristic concrete strength, redrawn from [118]

with p_{ri} being the ideally uniformly distributed radial pressure coming from bond action between concrete and reinforcement, and r_o the outer radius of the concrete body surrounding the reinforcement. If the inclination α_b of the interlocking-force is known, p_{ri} is calculated by (see [49])

$$p_{ri} = \tau_b \tan \alpha_b. \tag{3.61}$$

Failure is expected when $\sigma_{b\phi} = f_{ct}$, i.e. (compare [162])

$$\frac{p_{ri}}{f_{ct}} = \frac{r_{ct}}{r_i} \frac{r_o^2 - r_{ct}^2}{r_o^2 + r_{ct}^2}. \tag{3.62}$$

The ultimate circumferential capacity is found by differentiating Eq. 3.62 after r_{ct} and setting it equal to zero. According to Schenkel

$$\frac{p_{ri}}{f_{ct}} = 0.3 \frac{r_o}{r_i}. \tag{3.63}$$

Eq. 3.63 represents the lower capacity limit in terms of the plasticity theory. The upper limit is found when either the whole concrete ring around the bar plasticises or the ultimate circumferential strain ϵ_{ctu} is reached. Assuming an uniaxial rigid-linear material equation for concrete under tension and a linear equation for compression, Schenkel determines

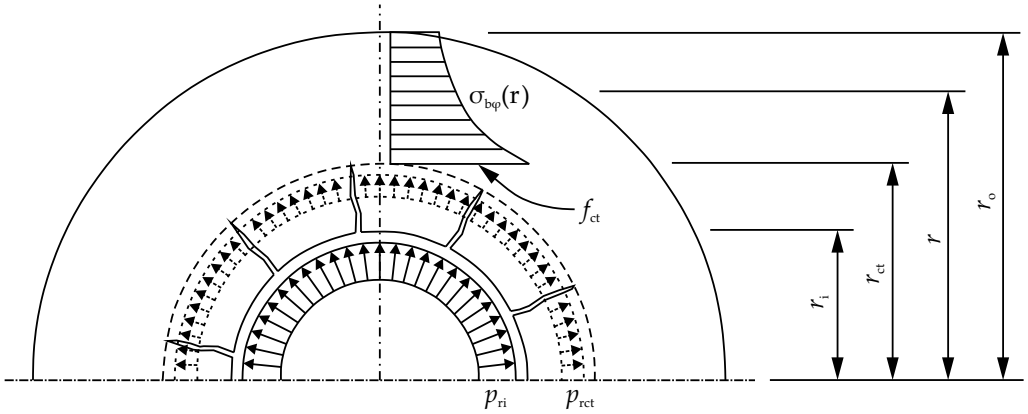

Figure 3.36: Radial cracks and subsequent load redistribution around reinforcing bar, redrawn from [162]

the upper capacity limit in case that the concrete completely plasticises with

$$\frac{p_{ri}}{f_{ct}} = \frac{r_o}{r_i} - 1. \tag{3.64}$$

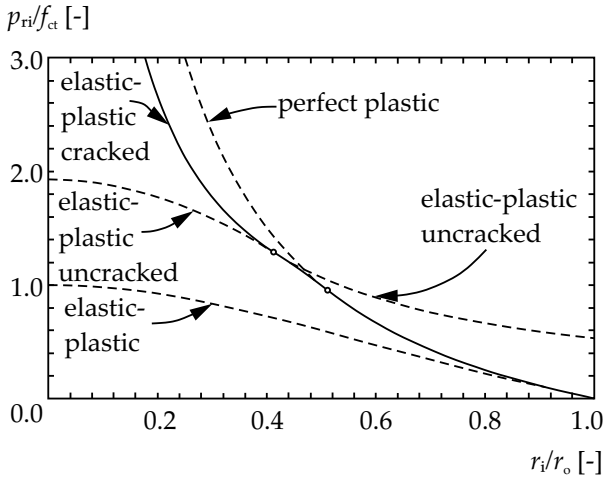

Figure 3.37: Ultimate circumferential capacity as function of calculation model and tension chord geometry, redrawn from [162]

Yet, Schenkel points out that the expected ultimate capacity lies between both limits. In reality, a cracked region with radial cracks is present in the surrounding concrete ring, followed by a region where concrete partially plasticises. Finally, a region with elastic behaviour follows the latter one (Fig. 3.37).

Fehsenfeld [49] comes to similar results. Though, additionally, based on a concrete-wedge-model (see Fig. 3.38), she takes the effects of a radial bar contraction into account by locally modifying the wedge radius r_{ci} not only in accordance to the radial deformation

of the concrete ring around the bar, but also to the radial (Poisson's) contraction of the reinforcement. Introducing β_b as the inclination angle between reinforcement and concrete wedge along two ribs with values $\beta_b = 3...12°$, she obtains (cf. Fig.3.38):

$$\delta r_{ci}(x) = \delta_s(x) \tan \beta_b - \frac{1}{2} \nu \epsilon_{sy} \varnothing_s. \tag{3.65}$$

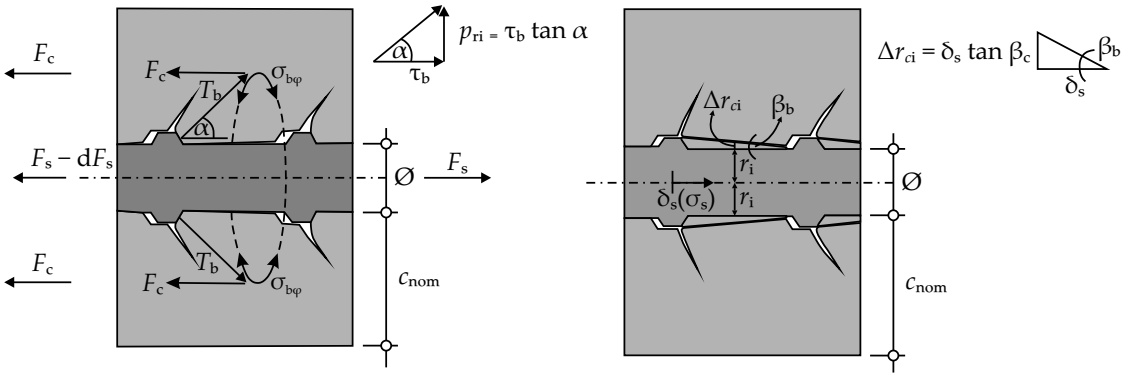

Figure 3.38: Bond model after Fehsenfeld [49]: Bond forces T_b due to interlocking action of ribs (left); increase of the internal radius r_i due to the slip δ_s, redrawn from [49]

After loading and unloading, if radial cracks have emerged, then a remaining stress state follows from the calculation model of Schenkel. Accordingly, after unloading, the concrete in the direct vicinity of the reinforcement experiences circumferential compression and with increasing distance the compression turns to tension.

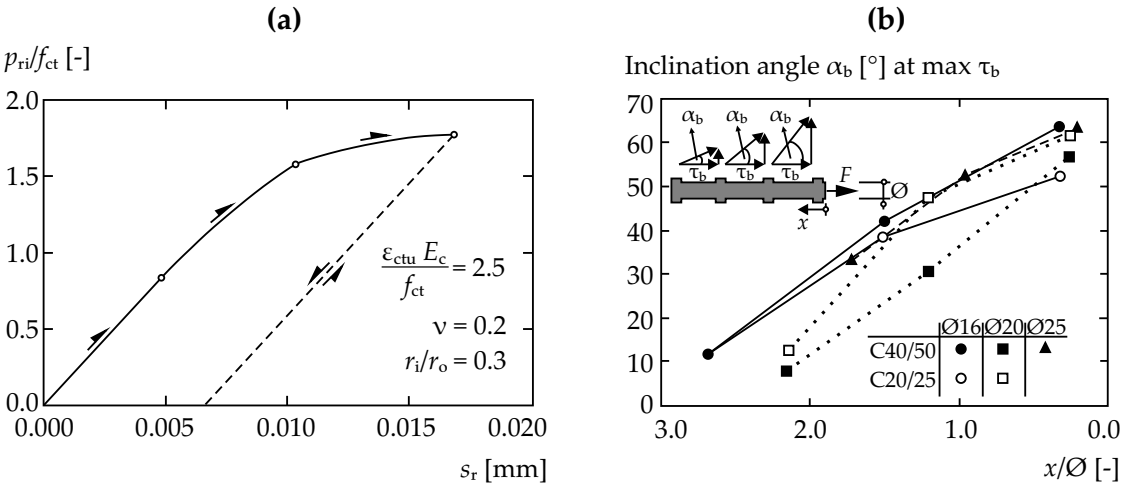

Figure 3.39: (a) Load-deformation-diagram of a concrete ring under cyclic loading, redrawn from [162]; (b) Inclination angle α_b of interlocking bond forces as function of distance to a crack, redrawn from [156]

Finally, the load history affects greatly the mechanical behaviour of bond. This aspect is discussed in the next section.

The ductility properties of reinforced concrete members are dictated by the plastic deformation capacity of steel. With it, the bond behaviour plays an important role since only an optimal interaction of reinforcement and concrete may guaranty the ductility requirements for a safe structural design and structural response. A high bond strength does not permit the reinforcement between two principal cracks to develop its complete deformation capacity [190] although the crack spacing is smaller.

The global stress state surrounding the reinforcing bar is also of great importance. The force transfer between reinforcement and concrete depends principally on the mechanical properties of concrete. Since the mechanical performance of concrete is sensitive to the governing stress state, in the same matter the bond behaviour highly depends on the surrounding stress state orthogonally to the length axis of a reinforcing bar. Especially tensile forces have proven to be considerably unfavourable by increasing the risk of concrete splitting [156] with a simultaneous reduction of the induced multiaxial compression in the concrete around the reinforcement and of the bond strength τ_{bu}.

Reinforcing bars being subjected to transverse tensile forces are found in reinforced concrete vessels, tanks, slabs, and bridges, among others [86], [109].

Tests carried out by Idda [86] on this topic reveal a general decline of bond properties because of the presence of transverse tensile forces. He tested reinforced tension chords under transverse tensile forces which were implemented as a function of the crack width $w_{cr0,l}$ along the bar length axis. Thereby he varied different parameters like bar diameter, concrete strength, rib geometry of the bars, bond length, and induced crack widths $w_{cr0,l}$. Values of $w_{cr0,l}$ = 0.0 mm (no transverse tensile forces), $w_{cr0,l}$ = 0.25...0.50 mm for the serviceability limit state and $w_{cr0,l}$ = 0.75...1.50 mm for the ultimate limit state were chosen for the longitudinal cracks. Under the action of longitudinal forces, there is a slip between reinforcement and concrete with a subsequent force transfer and the origin of circumferential stresses. Different than in tests without transverse tension, Idda was able to quantify an additional increase $\Delta w_{cr0,l}$ of the longitudinal crack $w_{cr0,l}$. The effect of the bar diameter was more appreciable the smaller the bar diameter was; otherwise, a transverse reinforcement displayed an enhancement of the bond.

The abundance of relevant parameters makes an universal mathematic approach for the description of the bond difficult. For that reason, characteristic values of the bond strength may be modified in actual standards according to the governing parameters (cast direction, concrete strength, stress state orthogonally to the bar, presence of a transverse reinforcement) for the design of anchorages and overlaps.

3.3.2 Bond Behaviour under Fatigue Loading

If a reinforcing bar embedded in concrete is subjected to high-cycle fatigue loading with stresses beneath the yield strength, then the slip δ_s between both reinforcement and concrete increases gradually. In consequence, thicker cracks, greater deformations, and a stiffness loss in structural members may be observed. The phenomenon is caused by a bond softening [8] or degradation under the action of dynamic loads and is known as bond fatigue, a phenomena which is directly connected to the concrete fatigue behaviour [15].

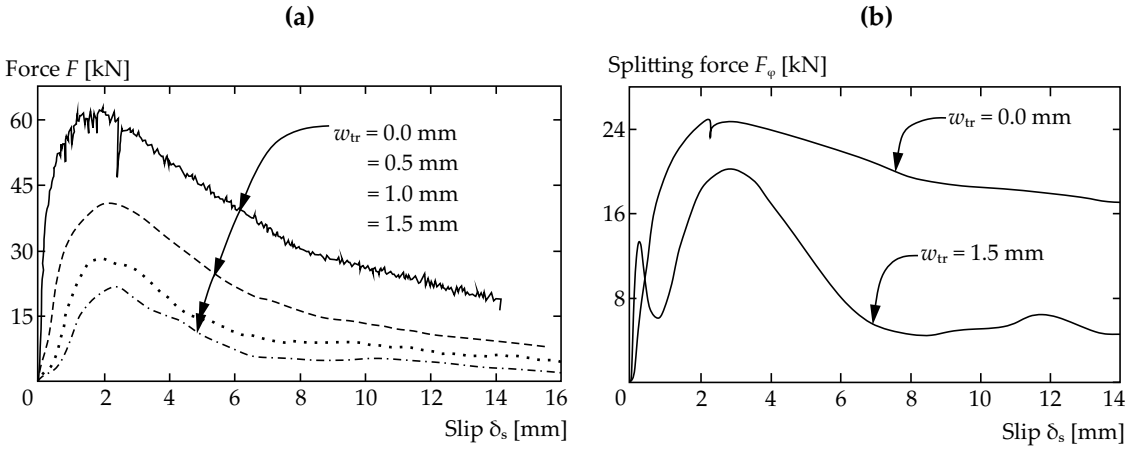

Figure 3.40: (a) Force-slip-curve for different values of a transverse crack w_{tr} and a bar diameter $Ø_s$ = 16 mm, redrawn from [86]; (b) Splitting force F_Φ for different values of a transverse crack w_{tr}, a bond length l_b = 100 mm, and a bar diameter $Ø_s$ = 16 mm, redrawn from [86]

Through the alternating bond action the concrete around a reinforcing bar is subjected to fatigue loading: Alternating tensile stresses at the tip of radial cracks combined with alternating circumferential (splitting) tensile stresses and alternating multiaxial compressions stresses at the concrete corbels. The resulting expansion of internal cracks and the progressive crushing of the concrete under the bar ribs [8], [88] lead to a notable progressive stiffness reduction in the concrete and a consequent slip increase. The tension-stiffening effect is also reduced [15]. This process is, similarly to other fatigue mechanisms, irreversible. Finally, a pull-out failure is possible by bond stresses $\tau_b < \tau_{bu}$ [6], if the concrete cover is adequate; otherwise, a splitting failure is more probable [9].

Rehm [153] observes a strong increase of slip in bond specimens under constant-amplitude fatigue loading with a bond length $l_b = 3Ø_s$ and a concrete cover $c_{nom} = 5Ø_s$. He also notices a relation between slip development, maximum applied load, and the existing bond length l_b respectively. The slip value after N constant load cycles is expressed with

$$\delta_{sn} = \delta_{s0}\,(1 + k_n)\,, \tag{3.66}$$

where δ_{s0} represents the static monotonic slip achieved under the applied maximum load. The displacement coefficient k_n is described empirically with $k_n = (1+n)^{0.107} - 1$.

Based on own tests, Rehm [153] also derives Wöhler curves for the prediction of bond fatigue as a function of the number of load cycles and the present stress degree τ_b/τ_{bu}, showing a similar development to the fatigue behaviour of concrete. Additionally, he carries ultimate tests on specimens which did not fail after 10^6 load cycles in order to quantify the remaining bond strength. This is of a remarkable importance for the reliability of the ultimate load of existing structures. Rehm notices that τ_{bu} does not experience any

reduction but it even increases by 5% compared to the static value (Fig. 3.41). He presumes that the reason for a slip increase under fatigue loading lies on the creep and relaxation behaviour of concrete under the bar ribs. Yet, in [88] it is reported that high-cyclic fatigue loading with stress ranges $\Delta\sigma_s \geq 0.4 f_{sy}$ may lead to a 50%-reduction of τ_{bu}. Also Balázs [8] reports of reduced values of τ_{bu} after fatigue loading. An extensive and precise study carried out by Oh [136] comes, however, to the conclusion that a previous fatigue loading does not affect the ultimate bond strength τ_{bu} as long as no fatigue failure occurs.

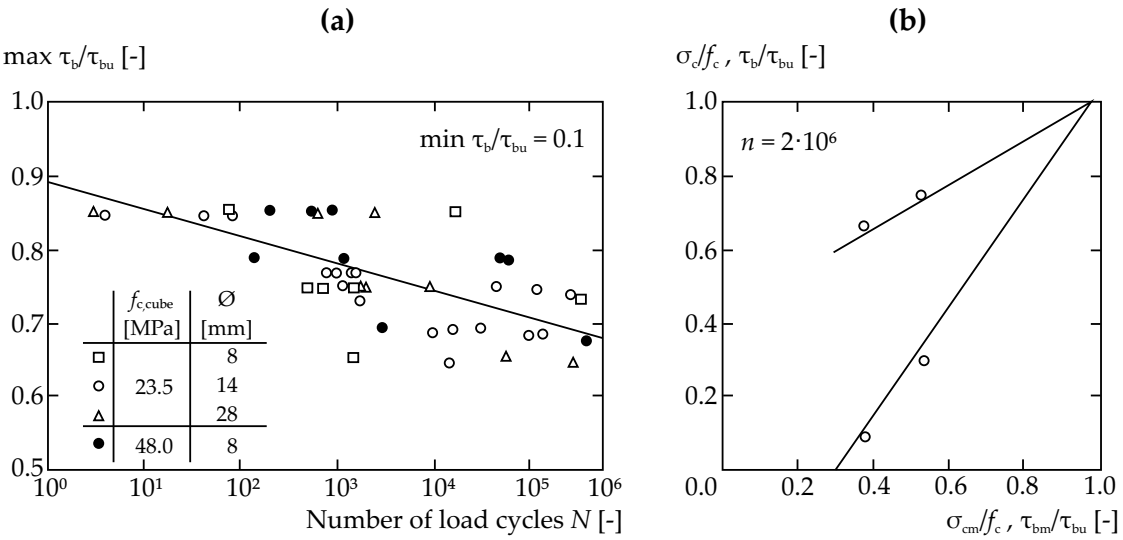

Figure 3.41: (a) Wöhler-curve of bond under constant-amplitude loading, redrawn from [153]; (b) Smith-diagram of concrete under compression fatigue loading compared to results of bond fatigue tests (right), redrawn from [153]

Eligehausen et al. [46] analyses the bond behaviour of bond specimens with $l_b = 5Ø_s$ under low-rate cyclic loading, reaching stresses beyond the linear-elastic limit. He notes that the maximum static bond strength is proportional to the square root of the concrete tensile strength, i.e. $\tau_{bu} \propto \sqrt{f_{ct}}$. Furthermore, the static monotonic $\tau_b - \delta_s$-curve constitutes a sort of envelop curve since the final $\tau_b - \delta_s$-curve of bond specimens that have been subjected to low-rate cyclic loading is always located inside the envelop. By means of a damage parameter with values 0...1.0, Eligehausen estimates a reduced $\tau_b - \delta_s$-curve based on the envelop-curve.

Balázs [6], [8] presents additional conclusions based on own force-controlled tests performed also with $l_b = 3Ø_s$ and $c_{nom} = 5Ø_s$. Likewise, he observes a relation between slip increase and bond length l_b as well as the chosen load parameters. Balázs reports that the slip increase rate is not constant. After a short beginning phase with relatively high slip increase rates another phase follows with a constant and stable slip increase rate. As soon as the specimens reach a slip value which corresponds to the maximum bond strength in static monotonic tests $\delta_s(\tau_{bu})$, the slip increase rate raises significantly and a pull-out failure occurs rapidly. Due to the established nonlinear slip development, the fatigue life determination with Miner's rule is reported to be inaccurate.

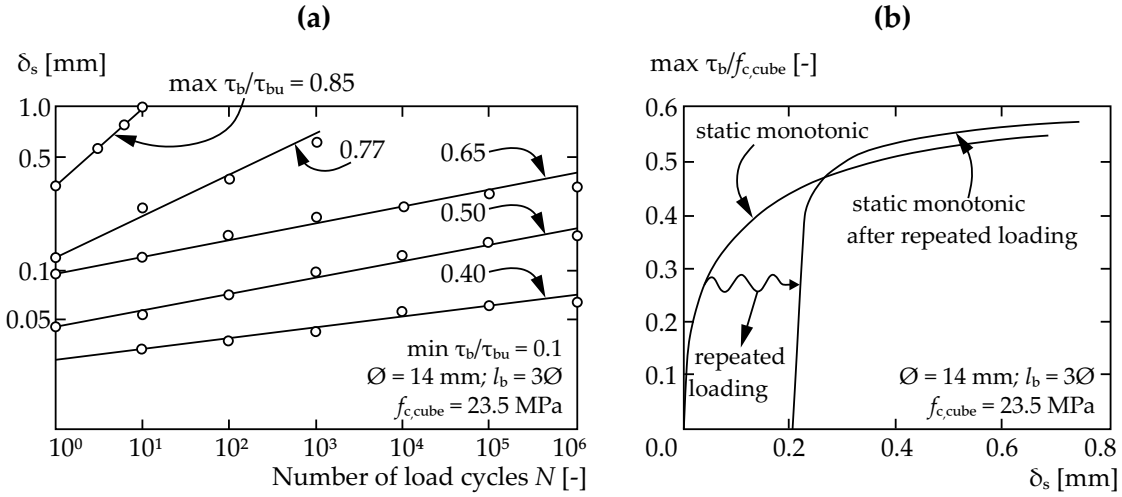

Figure 3.42: (a) Slip development as function of load cycles, redrawn from [153]; (b) Bond performance after repeated loading (right), redrawn from [153]

The developed damage in bond fatigue processes has also been monitored using the acoustic emission technique [9].

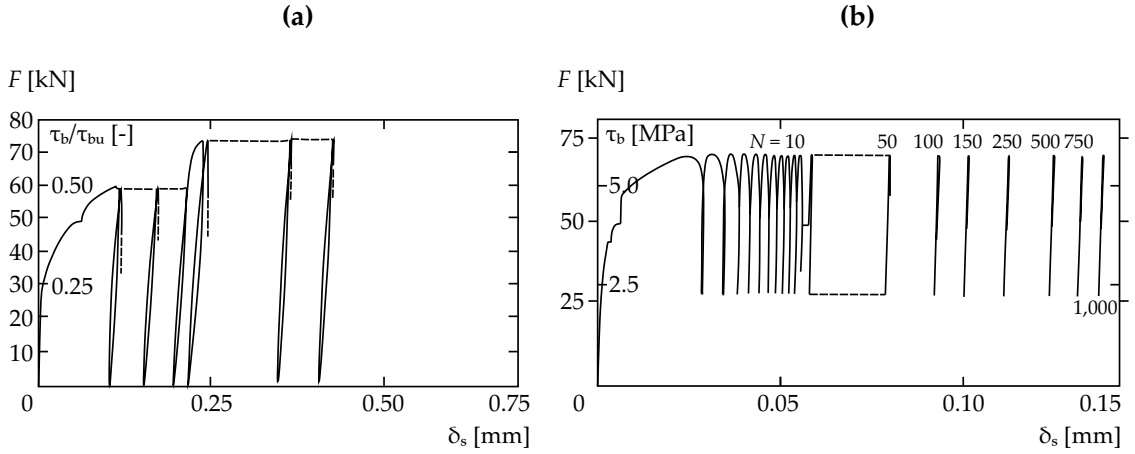

Figure 3.43: Slip development between reinforcement and concrete under repeated loading with (a) f_c = 20 MPa, $Ø_s$ = 16 mm, and $l_b = 6Ø_s$; (b) respectively $l_b = 12Ø_s$, redrawn from [6]

Based on the described slip development, Balázs proposes a mathematical model in order to predict the remaining fatigue life of specimens under constant-amplitude fatigue loading. Assuming that the inflexion points of the slip development and the constant rate of slip increase are known, the maximal number of load cycles until failure may be estimated. Results of tests performed in order to analyse the effects of load history on the slip development are reproduced in Fig. 3.44. Especially the bond length l_b is important

for the measurement of bond stress redistributions. As expected, the slip increase is at first higher on the loaded specimen side; however, with growing number of cycles, it shifts progressively to the unloaded side.

In the case of reversed loading, Balázs [8] reports that immediate after unloading a residual slip remains. By loading the reinforcing bar in the opposite direction, negative bond stresses are activated, firstly only in form of friction stresses, which is mainly due to the lacking interlock effect as a consequence of the concrete crushing under the bar ribs. As soon as a the slip value that corresponds to the deteriorate concrete under the ribs is overcome, the bond stresses increase again and a new residual slip results after unloading again. This loop is repeated whereupon the slip δ_s consistently increases. The induced damage under reversed loading is reported to be four times higher than else; though, it highly depends on the load history.

By bond specimens that experience random loads, Balázs [10] reports that the slip considerably increases only if the present load exceeds the previous highest load level. Lower load levels are reported to be practically irrelevant. The slip increase under constant-amplitude loading (the amplitude value is not reported) is faster than under random loads.

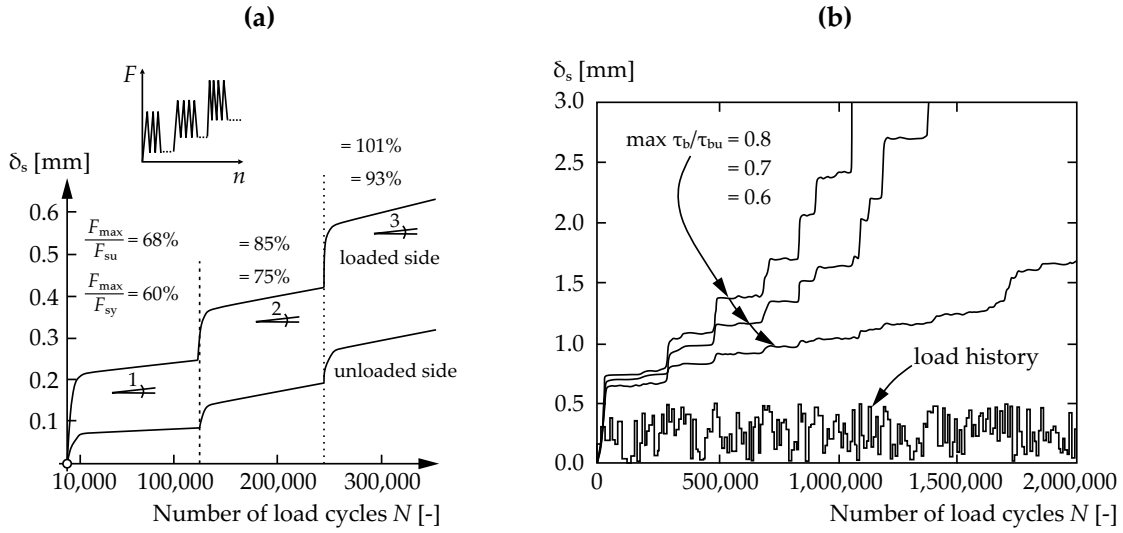

Figure 3.44: (a) Slip development under multi-level loading with f_c = 20 MPa, $Ø_s$ = 16 mm, and l_b = 12$Ø_s$, redrawn from [6]; (b) Slip development under random loading with f_c = 30 MPa, $Ø_s$ = 16 mm, and l_b = 5$Ø_s$, redrawn from [10]

The emphasis of the study performed by Oh [136] was the derivation of realistic $\tau_b - \delta_s$-curves for bond specimens in the ultimate limit state previous being under action of fatigue loads. As mentioned before, no reduction of τ_{bu} was observed. His research program consisted of bond specimens with $l_b = 2Ø_s$ and $c_{nom} \approx 4Ø_s$. The bar diameter was $Ø_s$ = 16.0 mm, the yield strength f_{sy} = 421.0 MPa, and the concrete uniaxial compression strength f_c = 37.0 MPa. The applied fatigue loads were constant-amplitude loads with a frequency f = 2.0 Hz. After reaching a determined number of load cycles, the specimens were tested in the ultimate state, slip-controlled with a rate of 0.3 mm/min, if no previous

fatigue failure took place. The three selected load levels were $\tau_b/\tau_{bu} = 0.45; 0.60; 0.75$; the chosen number of load cycles was $N = 0; 10^1; 10^2; 10^3; 10^4; 10^5$. The static monotonic tests reveal a good agreement with the $\tau_b - \delta_s$-curve of the Model Code 1990 [24]. The ultimate bond strength is given by

$$\tau_{bu} = 2.5 f_c^{0.6}, \tag{3.67}$$

and the static monotonic $\tau_b - \delta_s$-curve until τ_{bu} is expressed for the described tests results by

$$\tau_b = \tau_{bu} \left(\frac{\delta_s}{\delta_{sp1}} \right)^{0.32}, \tag{3.68}$$

with $\delta_{sp1} = 1.04$ mm. Oh also reports that the gap between residual slip (after unloading) and the following slip increase becomes smaller with a growing number of load cycles. Failure is assumed as soon as $\delta_s = \delta_s(\tau_{bu})$. For the slip development δ_s after N load cycles, he suggests

$$\delta_{sn} = \delta_{s1} N^{b_{\delta_s}}, \tag{3.69}$$

where δ_{s1} is the slip after the first load cycle, which may be calculated with the equation for the static monotonic $\tau_b - \delta_s$-curve of Model Code. From his experimental results, Oh provides $b_{\delta_s} = 0.071...0.114$. The residual slip δ_{sr} after N load cycles is calculated by Oh with

$$\delta_{srn} = \delta_{sr1} N^{b_{\delta_{sr}}}, \tag{3.70}$$

with $b_{\delta_{sr}} \equiv b_{\delta_s}$, and δ_{sr1} as the residual slip after the first load cycle

$$\delta_{sr1} = \delta_{s1} \left[2 \frac{\tau_b}{\tau_{bu}} - \left(\frac{\tau_b}{\tau_{bu}} \right)^2 \right]. \tag{3.71}$$

The $\tau_b - \delta_s$-curve after N load cycles is expressed by Oh with

$$\tau_b(n) = \tau_{bu} \left(\frac{\delta_s - \delta_{sr}}{\delta_{s1} N^b} \right)^{\alpha_n}, \tag{3.72}$$

$$\alpha_n = \frac{\alpha_n(n = 1)}{n^{0.092 \frac{\tau_b}{\tau_{bu}}}}. \tag{3.73}$$

For the results presented in his paper, Oh derives $\alpha_n\,(n=1) = 0.3234$. Finally, he describes the maximal number of load cycles until a fatigue failure with

$$N_f = \left(\frac{\tau_{bu}}{\tau_b}\right)^{\frac{1}{\alpha_n (n=1) b \delta_s}} . \tag{3.74}$$

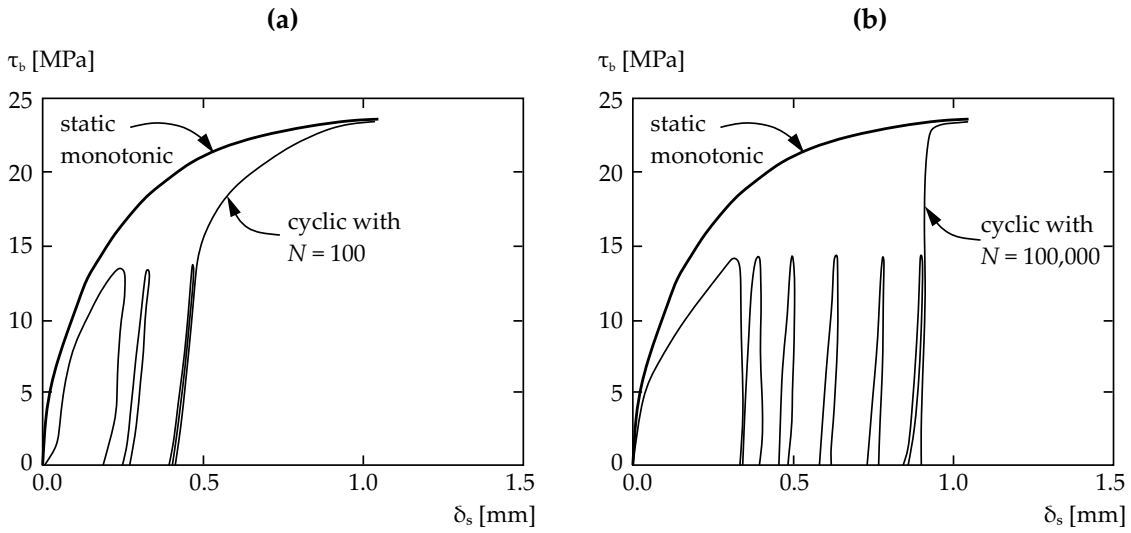

Figure 3.45: Comparison between $\tau_b - \delta_s$-curve of a static-monotonic loaded bond specimen and a cyclic and afterwards until failure loaded bond specimen with $n = 100$ cycles (left), and $n = 100{,}000$ cycles (right), redrawn from [136]

Another calculation model for estimating the induced damage as well as the resulting bond envelope curve after a fatigue loading is briefly described in [147].

Rteil et al. [161] analyses the bond performance of anchorages in reinforced concrete beams. The importance of such tests lies on their closeness to real structural members. Here, it may be observed that weak concrete covers may split, lowering the effective bond-carrying surface. The ultimate capacity of anchorages may be, therefore, negatively affected. Also interesting are the results concerning the bond stress redistribution along the anchorage which were measured with the help of strain gauges applied on the reinforcement. Increasing number of load cycles reduce the bond stress at the loaded end while the unloaded one experiences rising bond stresses (Fig. 3.46).

In the German Eurocode 2 [52] the bond degradation due to fatigue action is indirectly taken into account [15]. Bond stresses in the reinforcement are reduced by means of a simple factor k_t for the design of crack widths; anchorages and splices are verified by limiting the admissible bond stresses and stipulating robust construction rules. The standard for concrete offshore structures DNV-OS-C502 [42] is perhaps the onliest one which prescribes rules for the (direct) fatigue design of anchorages with a certain bond

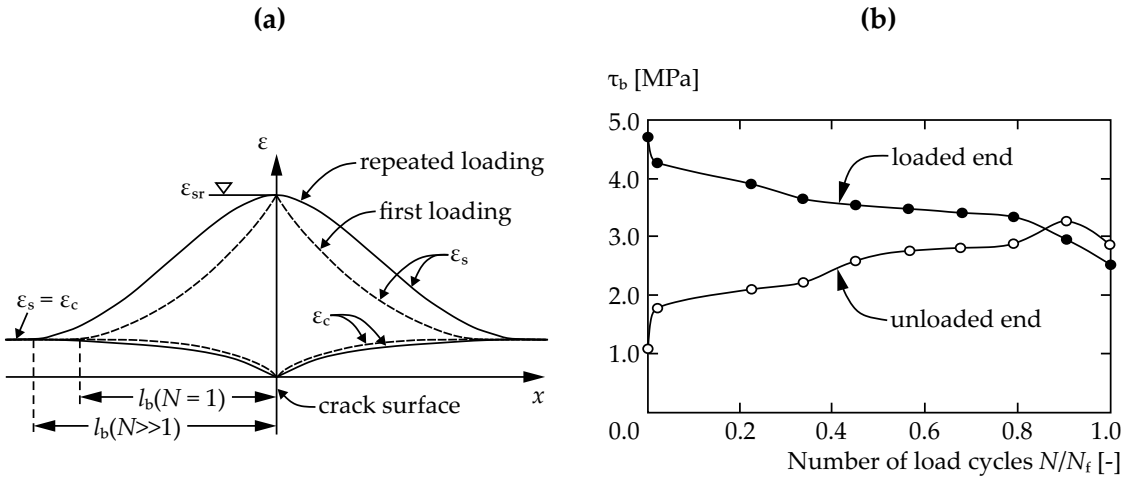

Figure 3.46: Stress redistribution in reinforcement as a consequence of repeated loading: (a) Qualitative, redrawn from [15]; (b) In anchorages, redrawn from [161]

length l_b:

$$\log N_f = C_1 \left(\frac{1 - \frac{\tau_{b,max}}{\tau_{bu}}}{1 - \frac{\tau_{b,min}}{\tau_{bu}}} \right). \tag{3.75}$$

C_1 depends on the proximity of sea water. DNV-OS-C502 prescribes $C_1 = 12.0$ for structures without being in contact with sea water. $C_1 = 10.0$ is valid if for structures in sea water with loads only in one direction while $C_1 = 8.0$ is required for structures in sea water and under reversed loading. For design purposes of anchorages the bond stress is assumed to be uniform distributed. The bond length of anchorages is determined by

$$\tau_{b,max} = \frac{\varnothing_s \sigma_{s,max}}{4 l_b}, \tag{3.76}$$

$$\tau_{b,min} = \frac{\varnothing_s \sigma_{s,min}}{4 l_b}. \tag{3.77}$$

The stress state surrounding the reinforcement is an essential parameter of the bond performance. Especially transverse tensile stresses may cause cracking and a weaker bond capacity. This process is more accentuated under fatigue loading. Lindorf [109], [110] carried out a meticulous study with bond specimens where $l_b = 10\varnothing_s$ in order to quantify the influence of transverse cracks on the slip development under repeated loading. As expected, the slip increase is higher, the greater the width of transverse cracks is. Since a fatigue failure of bond in form of a pull-out failure with a provided sufficient bond length

l_b and concrete cover c_{nom} is difficult to reproduce in tests under serviceability loads, Lindorf defines a slip-based failure criterion. Accordingly, a slip increase of $\Delta\delta_s$ = 0.1 mm is considered as bond fatigue failure since it would lead to an unacceptable crack width increase in real structural members, facilitating corrosion processes and affecting the serviceability in general. Based on this failure concept and on own test results, Wöhler curves have been developed by Lindorf. By converting the (average) bond stresses τ_b into equivalent steel bar stresses σ_s it becomes possible to evaluate the fatigue performance of bond by means of the reinforcement stress at the crack surface. Eq. 3.66 is confirmed by Lindorf, yet the factor k_n has proven to be dependent on the transverse crack width w_{tr}, applied stress range $\Delta\sigma_s$, and concrete strength f_c.

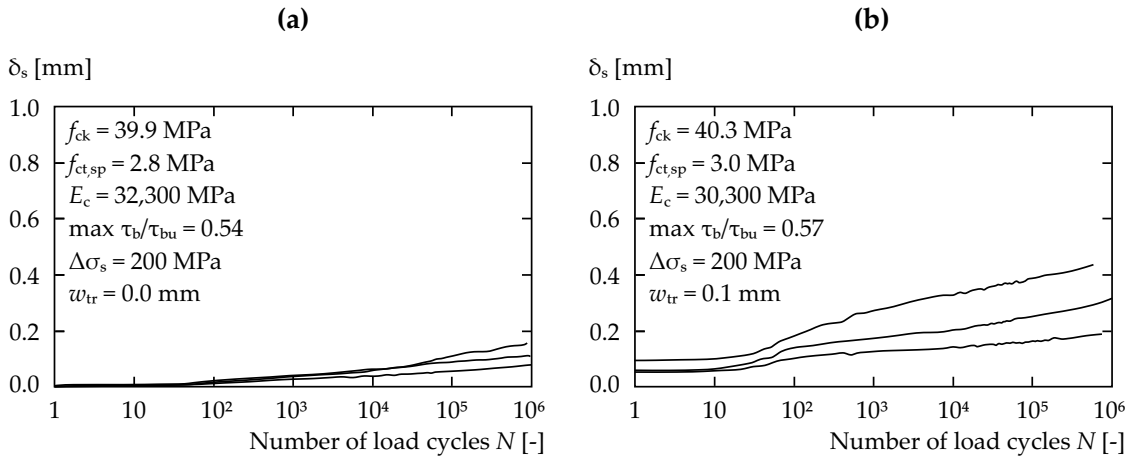

Figure 3.47: Slip development between reinforcement and concrete under transverse cracks w_{tr} and fatigue loading: (a) w_{tr} = 0.0 mm; (b) w_{tr} = 0.1 mm, redrawn from [109]

3.3.3 Tension Chord Modell

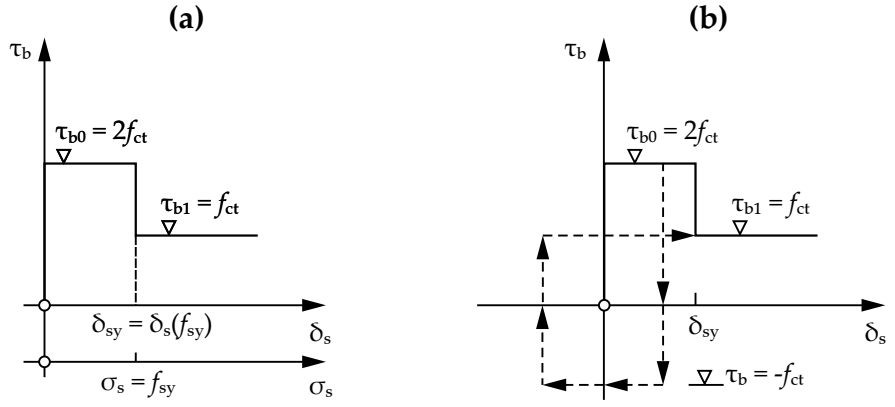

Figure 3.48: (a) Rigid-plastic $\tau_b - \delta_s$-curve for static monotonic loading, adapted from [178]. (b) Modification for unloading and reloading processes, adapted from [103]

The Tension Chord Model (TCM), developed first by Sigrist [178], [115], represents a simplified model of the $\tau_b - \delta_s$-curve (Fig. 3.48). It was originally postulated for a simplified but very effective calculation of the deformation capacity of tension members.

Based on a rigid-plastic $\tau_b - \delta_s$-curve, the bond stress τ_b remains constant as long as the reinforcement stress is in the elastic state, i.e. the slip between reinforcement and concrete is short. As soon as the reinforcement yields, a process that induces large deformation and slip values, the bond stress is then considerably reduced. τ_b remains constant in the plastic state of the reinforcement, yet with a lower value.

In principle, the Tension Chord Model evades the complex interaction between force equilibrium and displacement relations [2], expressed by the differential equation of the bond (Eq. 3.55). Thus, a (numerical) integration of Eq. 3.55, which is very laborious, is no longer necessary. Beginning with the reinforcement stress in cracked sectional areas, the stress distribution along the reinforcing bar and, consequently, the longitudinal stress in the concrete, may be quickly calculated by means of the constant bond stress τ_b. For practical purposes, this means that the bond stress τ_b becomes a (direct) function of the reinforcement stress while the slip characteristic may be neglected. Depending on the governing constitutive equations of reinforcement and concrete, the deformation behaviour of a beam element may be estimated.

The Tension Chord Model has been further developed and applied in cases concerning minimum reinforcement and crack limitation [2], [117], [49], mechanical behaviour of reinforced concrete slabs [92], serviceability of structural members [23], fatigue behaviour of prestressed tension members [57], stress field analysis of beams [177], unloading and reloading processes [103], and others. In particular the modification suggested by Koppitz et al. [103] in Fig. 3.48 may be further developed for general questions regarding the fatigue behaviour of reinforced concrete.

CHAPTER 4

Tension-Stiffening under Fatigue Loading

4.1 Tension-Stiffening Effect in Reinforced Concrete

According to [7], [54], the average strain difference between a bonded and an unbonded reinforcing bar originates from the so called tension-stiffening effect of the surrounding concrete. Tension-stiffening, therefore, results from the interaction between reinforcement and concrete by means of bond stresses at a member level. Principally, it describes the average deformation and load transfer behaviour of reinforced tension members. The tension-stiffening effect is a macroscopic property of the reinforced concrete [54].

A reinforced tension chord, which is subjected to an uniaxial static-monotonic tensile force, behaves initially linear-elastically with a stiffness corresponding to the idealised cross section values A_{ci} of the chord, where both, concrete and reinforcement, participate in the inner load transfer in accordance to the ratio of their respective extensional stiffness. No bond stresses between reinforcement and concrete are activated since both materials exhibit the same strain and, consequently, no slip (rigid bond). As soon as the concrete stress exceeds the governing tensile strength f_{ct}, the concrete cracks – in case of a load-controlled process instantaneously – and a crack, which crosses the effective cross sectional area of the chord, is formed. The whole tensile force is carried by the reinforcement at the cracked cross section and the longitudinal stiffness of the cross section is limited to the stiffness of the reinforcement [19]. Thereby, the steel strain increases substantially whereas the concrete is unloaded at the crack surface. The produced strain difference between both, steel and concrete, leads to a slip between them and activates bond stresses which, beginning with the cracked cross section, induce longitudinal tensile stresses on a (fictive) surrounding effective concrete area $A_{c,ef}$ (cf. [70]). The tensile stress in the reinforcement is gradually reduced while the effective concrete area $A_{c,ef}$ experiences a gradual increment of tensile stresses which act stiffness-enhancing and not as a strengthening factor [54]. When the gradually growing tensile stress in the effective concrete area $A_{c,ef}$ equals f_{ct}, a new crack is produced again. This process is repeated until the concrete tensile strength is nowhere exceeded [49].

The non-linear tension-stiffening effect plays an important role in the practical estimation of member deformations, crack widths, and deformation capacity. Since the structural behaviour of reinforced concrete is often simplified into the interaction of strut and ties [116], [113], the average behaviour of the ties is essential for the structural design according to the theory of plastic limit analysis. One of the most effective finite-element-calculation methods for structures is the smeared-reinforcement-modelling [160], [19], [121]. It consists in the smeared distribution of reinforcement in finite elements. The reinforcement is

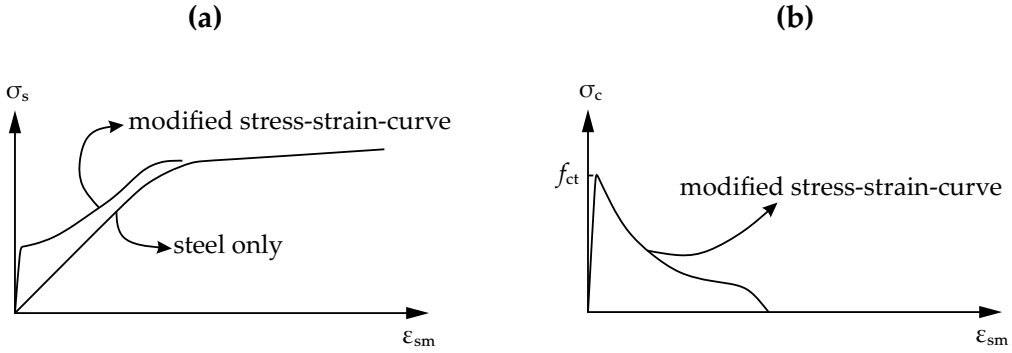

Figure 4.1: Calculation models for the tension-stiffening-effect, adapted from [121]: (a) Modification of the $\sigma_s - \epsilon_s$-curve of the reinforcement, (b) Modification of the $\sigma_c - \epsilon_c$-curve of the concrete.

not modelled discretely and for instance no bond elements are required. Concrete and steel elements are rigidly coupled at the element nodes [121]. The finite elements are assumed to follow the average stress-strain-curve $\sigma_s - \epsilon_{sm}$ of the idealised concrete chord for a calculation of deformations in the direction of the reinforcing bars. The $\sigma_s - \epsilon_{sm}$-curve results from the constitutive equation of reinforcement combined with the stiffening effect of the surrounding concrete. In the praxis, a modification of the stress-strain-behaviour of concrete has proven to be suitable for beam structures [19], but not for thick-walled concrete structures since usually the predicted deformations are too small compared to real values [187]. Moreover, additional considerations are required for cases where the applied tensile load is not parallel to the reinforcement.

Another computational method for taking the tension-stiffening effect of concrete into account consists in assigning a residual strength to the concrete after cracking. In this way, the concrete is capable to still carry a limited tensile load, an effect which also acts stiffness-enhancing. The mentioned model originates from the observation that a certain transfer of tensile loads in plain concrete is possible in case of very small crack widths, but it declines with greater cracks (tension-softening) [54]. However, the use of models based on tension-softening may lead to considerable numerical problems as well as to a dependence of the results on the employed mesh size [121].

The quantification of the tension-stiffening effect has led to numerous calculation models in the past. An overview is given for example in [68]. The emphasis lies mainly on the estimation of the average reinforcement strain ϵ_{sm} which is most relevant for the calculation of crack widths. Based on equilibrium considerations between cracked cross section and midpoint of two (principal) cracks, following equation must be fulfilled (cf. [209]):

$$E_s A_s \epsilon_{sr} = E_s A_s \epsilon_{sr0} + E_c A_{cn} \epsilon_{ct}, \tag{4.1}$$

with ϵ_{sr} being the steel strain at the cracked cross section and ϵ_{sr0} the steel strain

between two cracks; $A_{cn} = A_c - A_s$ is the net concrete cross sectional area and $\epsilon_{ct} = f_{ct}/E_c$. Reshaping Eq. 4.1 yields to

$$E_s A_s(\epsilon_{sr} - \epsilon_{sr0}) = E_s A_s \Delta\epsilon_{sr} = E_c A_{cn} \epsilon_{ct}. \tag{4.2}$$

Equilibrium may be postulated at every cross section, therefore

$$\Delta\epsilon_{sr}(x) = \epsilon_{sr} - \epsilon_s(x) \tag{4.3}$$

.

corresponds to the difference between cracked cross section and steel strain at x. The average steel strain between two cracks with a crack space s_r is expressed as follows (cf. [209]):

$$\epsilon_{sm} = \frac{1}{s_r}\int_0^{s_r} \epsilon_s(x)\mathrm{d}x = \frac{1}{s_r}\int_0^{s_r} \left(\epsilon_{sr} - \Delta\epsilon_{sr}(x)\right). \tag{4.4}$$

Introducing the parameter β_t, the average steel strain finally becomes

$$\epsilon_{sm} = \epsilon_{sr} - \beta_t\left(\epsilon_{sr} - \epsilon_{sr0}\right). \tag{4.5}$$

Eq. 4.5 is valid in the German Eurocode 2 [78] and $\beta_t = 0.6$ is to be used in case of short-term loading while $\beta_t = 0.4$ is assumed for long-term and repeated loading. Crack formation degree and concrete effective tensile strength are the main parameters which determine, apart from reinforcement degree, the stiffness of a reinforced concrete chord [108], [68]. The $\sigma_s - \epsilon_{sm}$-curve in [78] is divided into 3 stages (Fig. 4.2a). A possible degradation of the tension-stiffening effect due to bond creep or repeated loading is globally taken into account with the parameter β_t.

1. Uncracked stage with $0 < \sigma_s \leq \beta_t\sigma_{sr}$:
   $\epsilon_{sm} = \epsilon_{s0}$
   The steel strain is constant over the tension chord and equal to the concrete strains. The extensional stiffness of a chord corresponds to the sum of both, the stiffness of reinforcement and concrete. The crack process is initiated as soon as $\sigma_s = \sigma_{sr}$ and it is completed when $\sigma_s \approx 1.3\sigma_{sr}$.
2. Cracked stage with $\beta_t\sigma_{sr} < \sigma_s \leq f_{sy}$:
   $\epsilon_{sm} = \epsilon_s - \beta_t(\epsilon_{sr} - \epsilon_{sr0})$
   The crack formation stage is (normally) completed before the reinforcements yields. ϵ_{sr} corresponds to the steel strain at the crack surface. The inclination of the $\sigma_s - \epsilon_{sm}$-curve is equal to the reinforcement and the tension-stiffening produces a reduction of the overall elongation with $\Delta\epsilon_{sr} = \beta_t(\epsilon_{sr} - \epsilon_{sr0})$. In accordance with Model Code

2010 [51], $\Delta\epsilon_{sr} = \beta\sigma_{sr}/E_s$ with $\sigma_{sr} = f_{ct}/\rho_{s,ef}\left(1+\alpha_e\rho_{s,ef}\right)$ and $\beta = \beta_t$. Unloading processes are not described in the mentioned standard.

3. Yielding of the reinforcement stage with $f_{sy} < \sigma_s \leq f_{su}$:
   $\epsilon_{sm} = \epsilon_{sy} - \beta_t(\epsilon_{sr} - \epsilon_{sr0}) + \delta_d\left(1 - \frac{\sigma_{sr}}{f_{sy}}\right)\left(\epsilon_s - \epsilon_{sy}\right)$
   δ_d accounts for the influence of the steel ductility. For high-ductile steel $\delta_d = 0.8$, for normal-ductile steel $\delta_d = 0.6$.

For practical purposes, a modification of the Young's modulus of elasticity of reinforcement may be used for describing the stiffness of a concrete chord. According to [209],

$$E_{sm} = \frac{\sigma_s}{\epsilon_{sm}}. \tag{4.6}$$

The influence of shrinkage leads to residual stresses inside of a reinforced concrete member. In fact, induced tensile stresses in concrete cause an effective reduction of the force required for cracking [181], [49] since the induced concrete contraction is impeded by the reinforcement, producing in this way tensile stresses in the concrete.

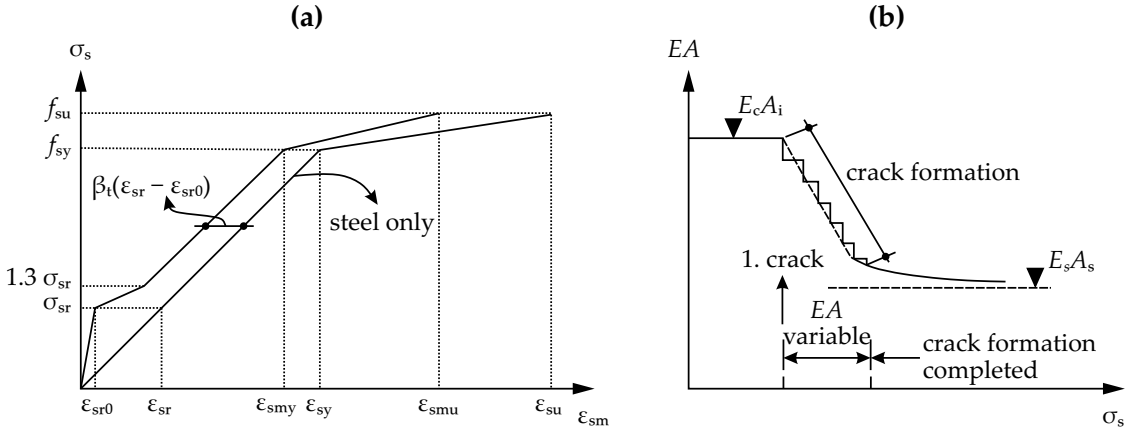

Figure 4.2: (a) Modification of $\sigma_s - \epsilon_s$-curve of reinforcement according to [78], (b) Development of the elongation stiffness as function of stresses in reinforcement, redrawn from [108].

Supported by theoretical considerations and experimental data, Kolleger [101] analyses the contribution of the tension-stiffening effect in cases where the direction of the principal (tensile) stress does not coincide with the axis of the reinforcement. For this purpose, Kolleger evaluates tests carried out on reinforced concrete slabs under different biaxial load configurations. He concludes that the tension-stiffening effect does not depend on the angle between principal stress and principal concrete strain. Tension-stiffening acts always in direction of the reinforcement. This fact plays an important role in the structural design of reinforced concrete slabs.

Under the action of constant loads – they induce creep of the bond action – and repeated

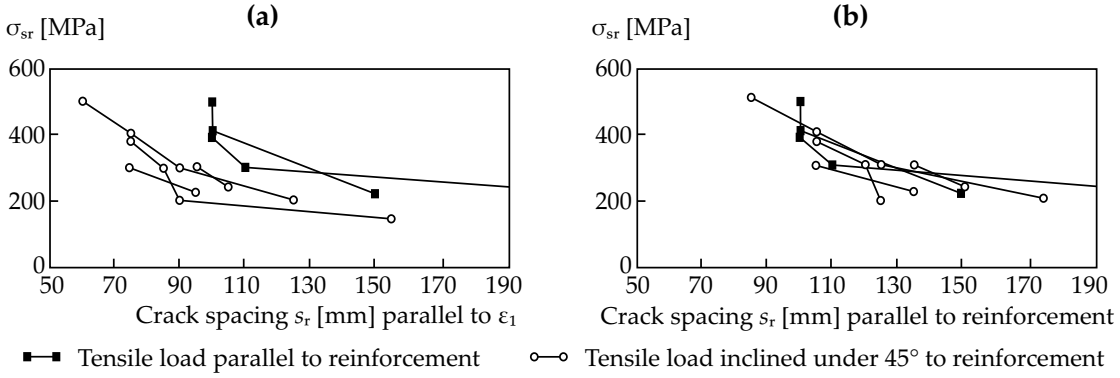

Figure 4.3: Measured crack width in slabs as function of tensile load direction, redrawn from [101]: Crack width measured (a) In the principal-strain direction (ϵ_1) and (b) In direction of the reinforcement

loads the tension-stiffening effect is gradually weakened depending principally on the load degree [108]. After unloading and reloading the stiffness of a chord is affected. Leonhardt [108] argues that the stiffness loss by high reinforcement degrees and during the stabilised crack formation phase is small compared to the more prominent stiffness reduction by low reinforcement degrees and during the crack formation phase. He also quantifies the degradation of the tension-stiffening effect of concrete under repeated loading to 33 ... 50% in relation to the behaviour at the first loading.

A long-term sustained loading has also been reported to reduce notably the tension-stiffening contribution of concrete around reinforcing bars, in part due to creep effects at the steel-concrete-interface (bond creep). Representative for the research in this topic is e.g. Albrecht et al. [1], where also a significant and quick weakening of the concrete tensile strength f_{ct} in the first 24 hours after load begin is described. Based on these effects, Albrecht et al. develops a calculation model for the reinforced concrete flange of composite bridges under consideration of the induced restrain in the steel web and possible internal stress redistributions in the bridge.

Sippel [181] reports of remaining deformations when a reinforced tension chord has previously been loaded and subsequently unloaded. He assumes a constant "unloading-stiffness" during a repeated loading process and develops a model for the calculation of deformation and crack width under repeated loading. The first cracking is assumed to form when the uniaxial concrete stress reaches the 5%-quantile value of the concrete tensile strength, i.e. $\sigma_c = f_{ct;0.05}$. The cracking process is assumed to conclude when σ_c equals the 95%-quantile of f_{ct}. The effective concrete area $A_{c,ef}$ follows the geometric approaches of Model Code 1990 [24] whereas the concrete modulus of elasticity E_c under repeated loading obeys the equations suggested by Park [140], where $E_c = E_c(N)$ exhibits a reduction, in addition to the number of load cycles, in dependence of the experienced maximal values of strain $\epsilon_{c,max}$ and stress $\sigma_{c,max}$. Though, as mentioned in Ch. 3.2.4, Park's equations could no be confirmed by other researchers.

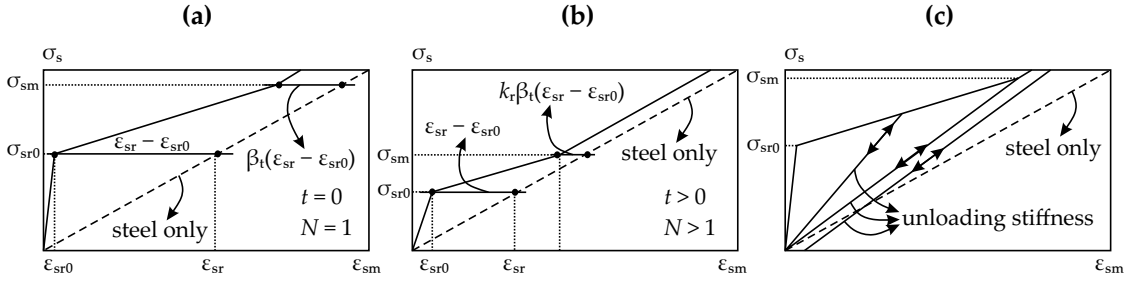

Figure 4.4: Tension-stiffening behaviour of a reinforced concrete chord according to Sippel [181]: (a) Static-monotonic loading, (b) Weakening due to repeated loading, (c) Development of the unloading paths in dependence of the number of load cycles.

Günther [68], [69], [70], [71] performed various tests at reinforced concrete chords with both, static monotonic and repeated loading – the last one in the elastic region –, and analysed the resulting effects on bond behaviour and tension-stiffening. The steel reinforcement was made from austenitic steel and steel strains were measured employing strain gauges situated in milled grooves whereas the slip between reinforcement and concrete was recorded with a magnet, which was located on the reinforcement, and a hall effect sensor in the concrete. As expected, due to the weakening of the bond behaviour, the measured values of ϵ_{sm} showed an increase during a certain number of load cycles depending on the load degree. A sort of stabilisation afterwards is reported and the $\sigma_s - \epsilon_{sm}$-hystereses exhibit a nearly constant area, where loading and unloading paths become practically equal. Also the remaining strain after unloading stabilises and becomes constant with a value $\epsilon_r = 0.2‰$ [71], whereas in the tension chord residual stresses emerge with the concrete being under compression and the reinforcement experiencing tensile stresses [69] (cf. Fig. 4.5c). After applying 1,000 ... 26,000 load cycles the tensile load was increased beyond the value used during the cyclic loading. Günther [68] assumes that growing internal cracks, as consequence of the repeated loading, are the cause for the observed bond degradation. He also reports of a reduction of the maximal bond stress by a factor of 10 ... 40%, depending on the concrete strength. Günther's results show furthermore a practically linear distribution of bond stresses along the reinforcement, similar to those predicted by the Tension-Chord-Model of Sigrist [115]. According to [71], the stress in reinforcement immediate after cracking amounts

$$\sigma_{sr} = \frac{f_{ct}}{\rho_{s,ef}}. \tag{4.7}$$

The average steel strain ϵ_{sm} under static monotonic loading follows the relation

$$\epsilon_{sm} = \frac{\sigma_s}{E_s}\sqrt{1-\left(\frac{\sigma_{sr}}{\sigma_s}\right)^2}, \tag{4.8}$$

with σ_{sr} according to Eq. 4.7. For a reinforced concrete chord being subjected to ca. 5,000 load cycles respective to a long-term loading (6 months) he assumes for the tension-stiffening degradation $\Delta\epsilon_{sm0}$ (cf. Fig. 4.5a):

$$\epsilon_{sm} = \frac{\sigma_{s,max}}{E_s}\left[\sqrt{1-\left(\frac{\sigma_{sr}}{\sigma_{s,max}}\right)^5} - \sqrt{1-\left(\frac{\sigma_{sr}}{\sigma_{s,max}}\right)^2}\right], \tag{4.9}$$

where $\sigma_{s,max}$ represents the maximal steel stress at the cracked cross section under repeated loading (sinusoidal tension loading).

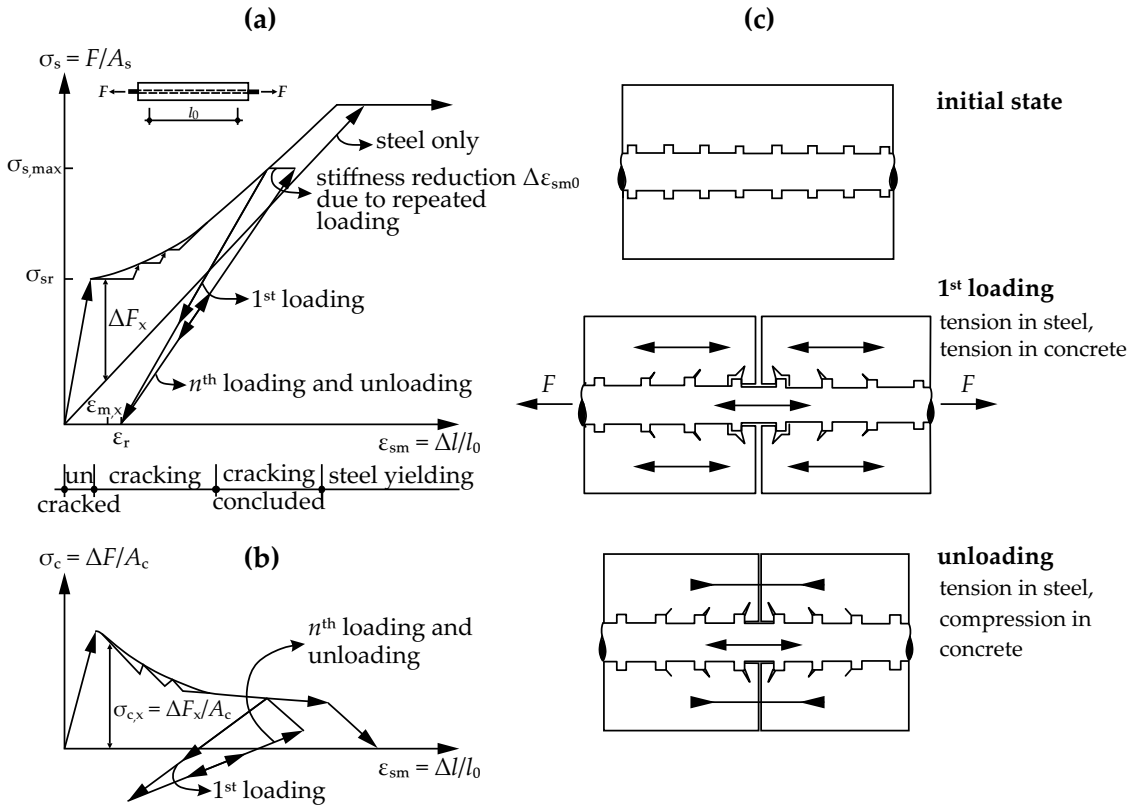

Figure 4.5: Tension-stiffening behaviour of a concrete chord according to Günther [68]: (a) $\sigma_s - \epsilon_{sm}$-curve under loading and unloading, (b) $\sigma_c - \epsilon_{sm}$-curve under loading and unloading, (c) (Residual) Stress in reinforcement and concrete after loading (unloading).

Gómez Navarro demands in [61] that the real behaviour of structures, in this case e.g.

composite bridges, which results from alternating service loads, has to be taken into account in a structural design. In large-scale tests of composite beams under loading and subsequent unloading processes he realises residual strains at the upper flange of the steel web and a definitely different and stiffer unloading path than the loading path. Considering the moment-strain-curve $M - \epsilon_{uf}$, the unloading path cuts the "state II-curve" of monotonic-static loading and the area below enclosed between the unloading path and the "state II-curve" is called by the author the "negative tension-stiffening" effect. A repeated loading and renewed unloading process is then assumed to follow the first unloading path.

Zanuy [205], [204], [206], [203], based on experimental data of Günther [68], [69], [70], [71] examines the behaviour of concrete tension chords under repeated loading. He focuses especially on the induced tension-stiffening degradation and quantifies the observed so called "negative tension-stiffening" by [61]. Finally, design models are presented for the estimation of crack width and remaining strains after unloading. Long-term effects such as sustained loading or repeated loading may be accounted for in a simple manner through a shifting of the $\sigma_s - \epsilon_{sm}$-curve in direction of the stress-strain-curve of the "naked" reinforcement.

Increasing number of load cycles cause a slip increase between steel and concrete, an effect which may be regarded as a sort of bond-stiffness degradation. By unloading processes, negative bond stresses are activated through a slip recovery of the reinforcement, leading in consequence to a prestressing effect where the concrete around the reinforcing bar is compressed and the reinforcing bar is restrained from deforming back, remaining thereby under tension stress. Hence, cracks are not completely closed after unloading. Zanuy refers in [204] also to further mechanisms like friction forces between aggregates at the crack surface and seeks to take them into account in the calculation of remaining deformations. The $\tau_b - \delta_s$-behaviour under repeated loading conforms the most relevant parameter (cf. Fig. 4.6), though. Apart from assuming a similar constitutive equation than Sippel [181] for the bond stress under repeated loads, Zanuy additionally assumes a constant value for the negative bond stress $\tau_b = \tau_{bf}$, defined as frictional bond stress, during a slip-reversal process. A complete slip reversal is achieved only after the governing load falls below a limit; then, according to Zanuy, negative bond stresses are activated along the whole reinforcement. Otherwise, the slip reversal may be expected only at a certain length which is denominated transfer length. By means of a numerical model a parametric study is presented and threshold values for the development of crack width are derived.

Zanuy also seems to be the first author who presumes a sort of fatigue effect of the effective concrete area $A_{c,ef}$ around the reinforcement. In [204] an evolution equation for $A_{c,ef}$ is presented as function of published Wöhler-curves of concrete in tension and compression-tension.

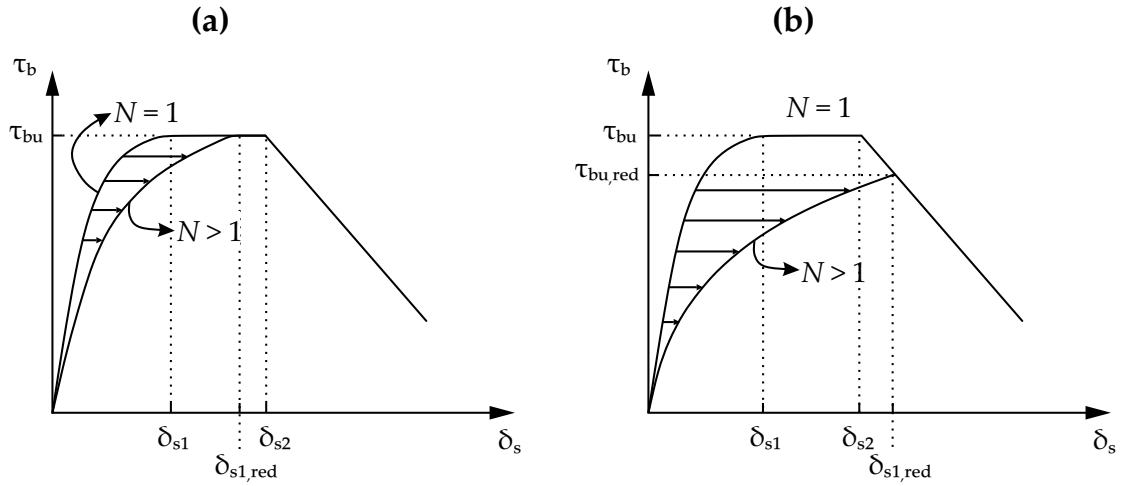

Figure 4.6: Idealised $\tau_b - \delta_s$-curve under repeated loads with $N > 1$ according to Zanuy [204]: (a) No bond strength degradation and (b) With bond strength degradation

4.2 Tension-Stiffening Effect Modelled with the Tension Chord Model

4.2.1 Experimental Results

Fatigue tests on concrete chords were performed at the Hamburg University of Technology (Technische Universität Hamburg, TUHH) with the intention to quantify the effects of bond degradation. Apart from the evolution of crack width, the experimental program pursued the objective of monitoring remaining deformations after unloading and the gradual increase of deformation as consequence of fatigue loading. Moreover, the effects of bond degradation on the deformation capacity were likewise quantified. The extensive experimental report may be found in [4].

Two parameters were given special attention: The stress state around the reinforcing bar and the load history. A focus lay on structural elements of offshore concrete structures (slabs, shells), following the main research topic of the Research Centre On- and Offshore Engineering Structures ("FSP Bauwerke im und am Wasser"). For this purpose, the tested specimens were slabs with dimensions 750 mm × 300 mm × 114 mm. In longitudinal direction they were centrally reinforced with a single ripped steel bar B500B according to DIN 488 [36] of a nominal diameter $Ø_s$ = 20 mm (main reinforcement). All employed steel bars belonged to the same charge. The obtained yield strength was f_{sy} = 545 MPa at ϵ_{sy} = 2.73‰, the ultimate strength was f_{su} = 645 MPa at ϵ_{su} = 91.0‰. Fracture of the reinforcement was recorded at ϵ_{fr} = 195.0‰ and the Young's modulus of elasticity amounted E_s = 201.0 GPa (cf. Tab. 4.1). Transversally the reinforcement consisted of 6 threaded rods B500B according to [34] with $Ø_s$ = 14 mm. They were used in order to induce tensile stresses orthogonally to the main reinforcement as well as cracking along it, reproducing on this way an adverse, yet realistic stress state which may appear on slabs, shells, and, to a limited extent, on beams (e.g. stirrup reinforcement for shear forces).

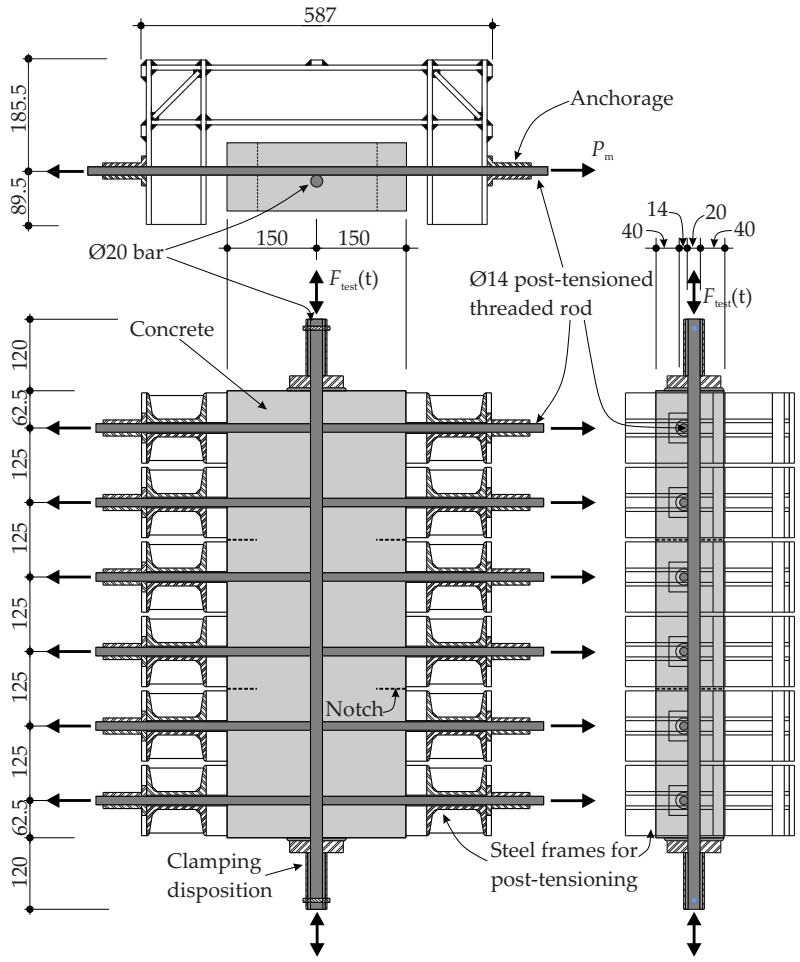

Figure 4.7: Layout and view of test specimen with post-tensioning steel frames, dimensions in [mm]

The desired tensile stresses were applied through a limited post-tensioning of the transverse reinforcement. For this aim, steel frame elements were welded, prepared, and located at the free ends of the transverse reinforcement, without coming in contact with the concrete chord (Fig. 4.7). The transverse reinforcement was then anchored on both sides of the steel frame elements. The detailed description of the post-tensioning arrangement and determination of the post-tensioning forces may be found in [4]. The anchorage forces were therefore transmitted to the steel frames, avoiding compressions forces on the concrete. Though, the induced positive strains on the transverse reinforcement led to a transmission of tensile forces into the concrete chord by means of bond stresses. 3 levels of post-tensioning were applied:

1. No transverse tension.
2. Transverse tension induced – longitudinal crack w_{cr} = 0.2 mm.

3. Transverse tension induced – longitudinal crack w_{cr} = 0.3 mm.

Table 4.1: Determined main properties of reinforcement

Property	Nominal value acc. to DIN 488-1 [36]	Mean experimental value
Bar diameter $Ø_s$ [mm]	20.0	19.01 (rib root) 21.47 (with ribs)
Bar cross section A_s [cm^2]	3.14	2.91
Yielding strength f_{sy} [MPa]	500	549
Ultimate strength f_{su} [MPa]	525	645
f_{su}/f_{sy} [-]	1.08	1.18
Yielding strain ϵ_{sy} [‰]	2.50	2.73
Ultimate strain ϵ_{su} [‰]	50.0	91.0
Fracture strain $\epsilon_{s,fr}$ [‰]	no specifications	195.0
Young's modulus of elasticity E_s [GPa]	no specifications	201.0

For general effects of cracks and transverse tensile stresses on bond see Ch. 3.3.2. The performed load program and the consequent crack formation in the concrete chord proved to have only a little effect on the post-tensioning, which was monitored constantly during the tests.

The concrete uniaxial compression strength at both, the beginning and the end of the experimental program, was ca. f_c = 55.0 MPa while the uniaxial tensile strength was f_{ct} = 4.0 MPa and the secant modulus of elasticity E_c = 35.0 GPa (cf. Tab. 4.2). All specimens were cast in vertical position (good bond properties for the main reinforcement, cf. [52]) and stored under testing conditions (dry, at 20°C). The first specimen was tested at a concrete age of 109 days, the last one at 307 days. Altogether, 22 specimens were tested.

For the sake of a better monitoring, the concrete specimens were supplied with notches at 1/3 and 2/3 of the element length in order to cause stress concentrations and a subsequent crack formation. The main reinforcement bar was milled longitudinally and provided with a groove of 6.5 mm × 2.5 mm at the location of the longitudinal rib, where the bond action is practically absent. In the middle segment 5 strain gauges were applied with the aim of measuring the steel strain distribution between cracks under the selected test parameters (Fig. 4.9). The general arrangement of strain gauges was performed carefully, guaranteeing a minimum distortion of the bond properties (cf. [173], [174], [68]). The strain gauges delivered valuable information during the stages of crack formation, fatigue loading, and ultimate loading up to a strain value of ≈ 3.0‰. In most cases where $\epsilon_s > 3.0$‰ the strain gauges failed.

Additionally, mechanical displacement transducers were also applied on the concrete chord (Fig. 4.9). They had the finality of monitoring the development of crack width, longitudinally and transversally, and average deformations. Difficulties faced with clamp-

Table 4.2: Determined main concrete properties in fatigue tests

Property	Concrete age in [days]	
	109	307
Density ρ_c [t/m³]	2.35	2.34
Cylinder compression strentgh f_c [MPa]	55.30	53.8
Tension strentgh f_{ct} [MPa]	3.97	4.17
Splitting tensile strentgh $f_{ct,sp}$ [MPa]	3.97	4.17
Secant modulus E_c [GPa]	34.70	35.51

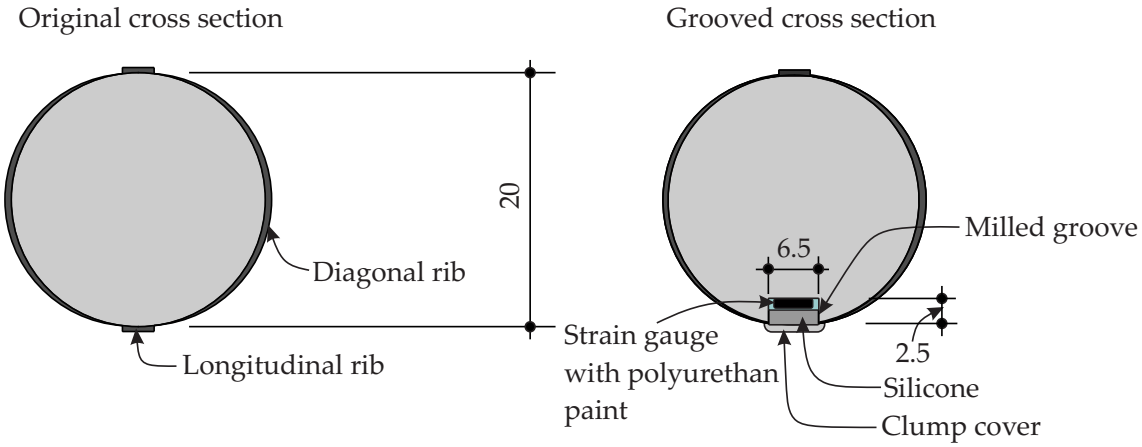

Figure 4.8: Grooved reinforcing bar with strain gauges, dimensions in [mm]

ing of the test specimens and the recording of the average steel strain ϵ_{sm} in the ultimate state are described in the experimental report [4]. ϵ_{sm} was determined using the delivered results of the displacement transducers and additionally also using values of the strain gauges.

Some specimens were tested only under quasi-static load conditions; however, the majority was tested later under fatigue and finally ultimate load conditions. The load stages were:

1. Displacement-controlled: Tension load up to ca. 90 kN for crack formation.
2. Unloading.
3. Where required: Post-tensioning of transverse reinforcement and crack formation along the main reinforcement bar.
4. Displacement-controlled: Ultimate tension test.

The testing of the specimens St4-w0.2 and St5-w0.3 was, differing from the other specimens, force-controlled.

The test pattern of the dynamically tested specimens is listed below.

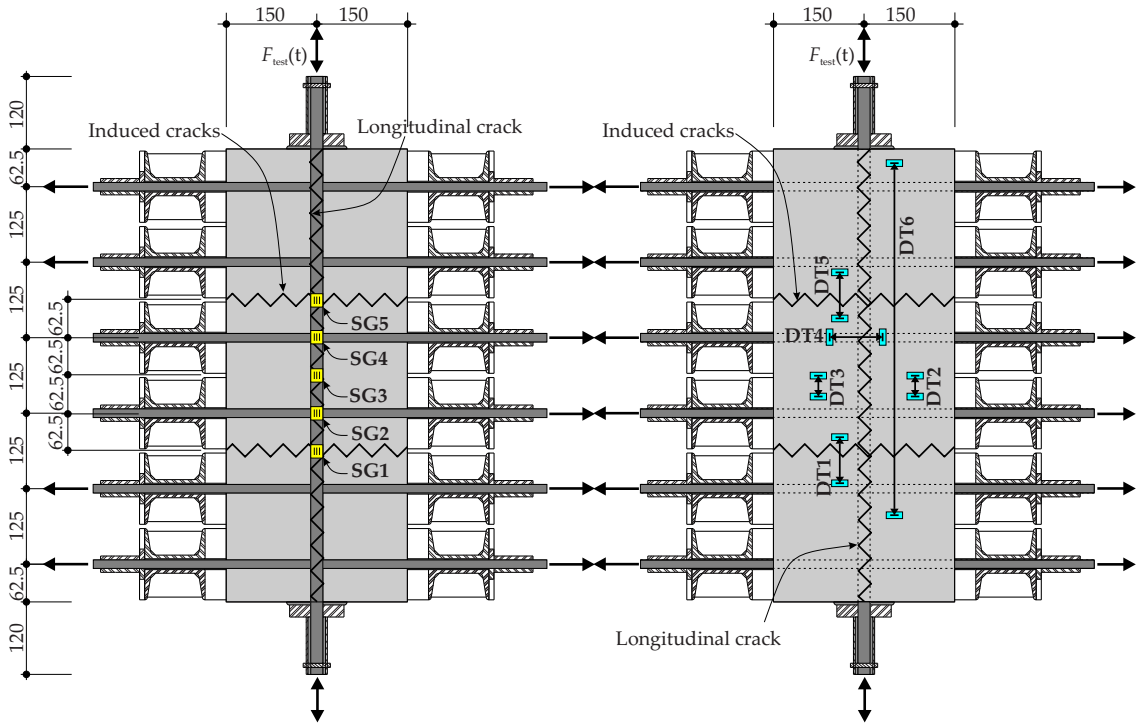

Figure 4.9: Layout of test specimen with strain gauges SG (left) and displacement transducers DT (right), dimensions in [mm]

1. Displacement-controlled: Tension load up to ca. 90 kN for crack formation.
2. Unloading.
3. Where required: Post-tensioning of transverse reinforcement and crack formation along the main reinforcement bar.
4. Force-controlled: Fatigue loading according to load file.
5. Displacement-controlled: Ultimate tension test if specimens experiences no previous fatigue failure.

Since the fatigue behaviour of both, concrete and bond, are highly non-linear and irreversible, the load history is crucial in order to understand the property changes of stiffness, deformation behaviour, remaining deformation, and fatigue life (cf. Ch. 3.2.4 and Ch. 3.3.2). Offshore structures – and also other similar engineering structures which experience diverse types of random loads – may suffer a material degradation depending strongly on the experienced loads. An estimation of fatigue life and, if at all stipulated on design standards, effects of the fatigue process on a structure (serviceability, ultimate load bearing capacity) base, above all, on simple experiments with mostly uniaxial sinusoidal load configuration. It becomes clear that the real and predominantly complex structural behaviour is not examined accurately. However, an analysis of the structural behaviour under the whole load history is problematic, not only because the de facto loads are per se

unknown. Their random character makes the evaluation of experimental results extremely difficult so that the determination of universally valid constitutive material equations becomes practically impossible.

A thinkable method consists on the generation of realistic and at the same time representative load series [31] that obey certain characteristic parameters. Such representative loads, in order to obtain useful representative results, must cover the totality of expected loads during the operating life of a structure.

Service and extreme loads exhibit usually a statistical character (Fig. 2.3b). In case of offshore structures, where hydrodynamic loads (especially waves) constitute the governing loads, it may be distinguished between short-term (3 hours) and long-term loads (cf. Ch. 2.2). The random nature of waves in the short-term may be mathematically formulated in the frequency domain through a spectrum that is commonly characterised by the significant wave height H_s and the zero-up-crossing period T_z. Using the inverse Fourier-transformation it is possible to convert a spectrum of wave height into a time series. Assuming waves of 1st order – under service and fatigue conditions a legitimate assumption – the resulting hydrodynamic loads exerted on a structure lead to a linear response of the form (cf. Ch. 2.2)

$$R(\omega) = S(\omega)H(\omega), \tag{4.10}$$

with ω being the frequency, $R(\omega)$ the response spectrum (stress resultants, motions), $S(\omega)$ the wave spectrum, and $H(\omega)$ the so called transfer function. $H(\omega)$ may be determined by means of an analysis of the structure response to a sufficient number of discrete wave frequencies. Moreover, $H(\omega)$ is a function of the structure properties which means that it has to be calculated for every structural member separately. At this point, a constant value $H(\omega) = 1.0$ was selected as a type of universal transfer function for the experimental program. In consequence, the load response spectrum had the same form as the wave spectrum.

The long-term wave behaviour results from the sum of all short-term sea states (cf. Ch. 2.2). A scatter-diagram matrix contains the information about the statistical distribution of the expected sea states, yet not about their sequential arrangement. The rough North Sea region is one of the best documented regarding wave data owing to numerous offshore structures placed in it and the intense shipping traffic. The scatter-diagram provided in [43] with a probability density function (logarithmic distribution) of short-term sea states of the North Sea and the resulting characteristic statistical values such as median and standard deviation was taken as basis for the definition of the test loads. Since $H(\omega) = 1.0$, the long-term load distribution also obeys a logarithmic distribution.

The median value was set as the theoretical load, estimated based on the Tension Chord Model, for the quasi-permanent combination of actions which produces a crack of the width $w_{cr,lim} = 0.2$ mm. This value has not to be exceeded in the permanent combination of actions (cf. [66]) in compliance with Model Code 2010 [51]. The DNV standard [42] is in this regard even more restrictive, though. The median value of the long-term distribution of significant stresses was chosen to $\mu_{H_{s,\sigma_s}} = 250$ MPa and the standard deviation followed

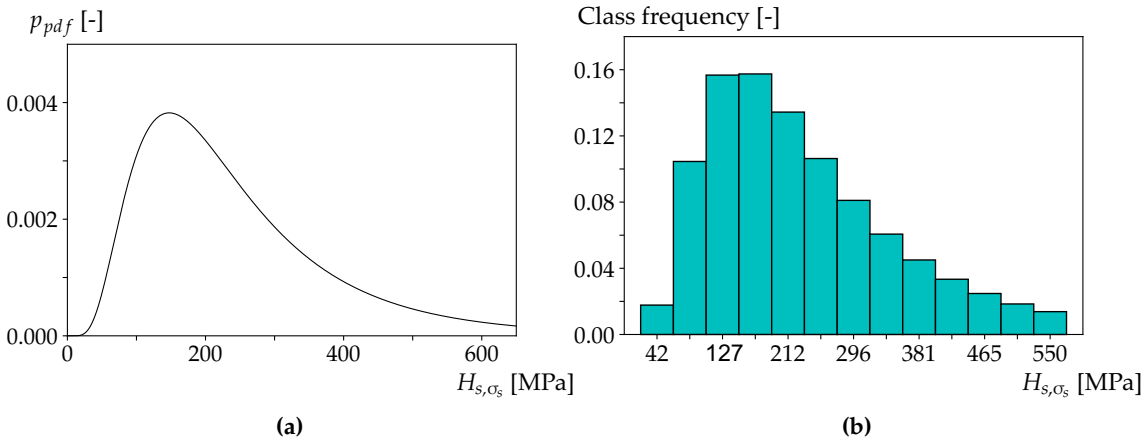

Figure 4.10: Long-term distribution of (a) Significant reinforcement stress ranges and (b) Discretisation into 13 corresponding short-term load spectra

with $\sigma_{H_{s,\sigma_s}}$ = 162.5 MPa from the condition of a constant variance value between load and wave long-term distribution.

In a further step the gained long-term distribution of loads was discretised into 13 short-term load spectra. As a result of the met assumptions, every load spectrum is narrow-banded with a Rayleigh-distribution of load ranges. Using the randomness generator of python™, load ranges that result from the long-term distribution (cf. Tab. 4.3) were generated in order to build time-series of stresses. The resulting load amplitudes were increased by a constant value corresponding to the admissible value of the quasi-permanent combination of loads. Mean value and standard deviation of the 13 generated stress time series are listed in Tab. 4.4.

Table 4.3: Probability of occurrence and time span of chosen time series of significant stress range of reinforcement

Nr.	H_{s,σ_s} [MPa]	p_{prob} [-]	t_{class} [hrs]	Nr.	H_{s,σ_s} [MPa]	p_{prob} [-]	t_{class} [hrs]	Nr.	H_{s,σ_s} [MPa]	p_{prob} [-]	t_{class} [hrs]
1	42.31	0.02	2.59	6	253.86	0.11	15.48	11	465.41	0.02	3.61
2	84.62	0.10	15.22	7	296.17	0.08	11.80	12	507.72	0.02	2.69
3	126.93	0.16	22.82	8	338.48	0.06	8.83	13	550.00	0.01	2.01
4	169.24	0.16	22.93	9	380.79	0.05	6.56				
5	211.55	0.13	19.57	10	423.10	0.03	4.86				

The main frequency content of the North Sea wave spectra lies between 0.05...0.30 Hz [43]. In order to achieve at least $N = 10^6$ load cycles with such relatively low frequencies – offshore structures may experience even $N \geq 10^8$ load cycles –, a considerable amount of time is necessary for testing the specimen. Furthermore, the employed testing rig was not able to simulate arbitrary load frequencies. Since the load frequency has proven to be an important influencing parameter in fatigue tests (cf. Ch. 3.2.4), yet long test durations are very impractical, a reasonable compromise regarding the load frequency had to be

made. According to Hohberg [82], the fatigue life of concrete under uniaxial compression seems to be to a greater or lesser extent constant for load frequencies ≤ 1.0 Hz. Higher frequencies lead to a higher fatigue life (cf. Ch. 3.2.4). Because the fatigue performance of bond relies on the concrete fatigue behaviour, a similar dependency for load frequencies ≤ 1.0 Hz may be assumed. In this way, a constant time interval of 0.5 sec between the generated stress peaks was established which corresponds to cycle interval of 1.0 sec and a fictive frequency of 1.0 Hz.

Table 4.4: Mean value and standard deviation of chosen time series of stress ranges in reinforcement

Nr.	$\overline{H_{\sigma_s}}$ [MPa]	$\sigma_{H_{\sigma_s}}$ [MPa]	Nr.	$\overline{H_{\sigma_s}}$ [MPa]	$\sigma_{H_{\sigma_s}}$ [MPa]	Nr.	$\overline{H_{\sigma_s}}$ [MPa]	$\sigma_{H_{\sigma_s}}$ [MPa]
1	24.91	10.58	6	149.44	63.46	11	273.97	116.35
2	49.81	21.15	7	174.35	74.04	12	298.88	126.92
3	74.72	31.73	8	199.25	84.62	13	323.79	137.50
4	99.63	42.31	9	224.16	95.19			
5	124.53	52.88	10	249.07	105.77			

Hence, the whole frequency content of the load spectra could not be implemented. The statistical distribution of peaks, mean value, and an acceptable low frequency ≤ 1.0 Hz, however, were held. Every test took ca. 6 days until $N = 10^6$ fictive peaks were achieved and the percentage duration of every time series followed from the probability of occurrence of every sea state in the long-term distribution (Tab. 4.3).

All stress time series from the 13 generated load spectra were combined in 3 different sequences (cf. Fig. 4.12), creating 3 different load histories that were finally used in the performed tests:

1. Series Pe: Begin with spectrum with the lowest stress values, then an increasing arrangement.
2. Series Pb: Begin with spectrum with the higher stress values, then a decreasing arrangement.
3. Series Pm: Higher stress values in the middle of all sequences, remaining spectra randomly arranged.

A subsequent rain-flow counting for the 3 final load histories was carried out with the algorithm provided in [193], defining 11 classes. The results may be found in [4].

In the uncracked state the concrete chord exhibits a stiffness which results from the combined interaction between reinforcement and concrete. Both materials interact in a degree corresponding to their respective stiffnesses. Their strains are equal and no bond stresses are activated. The idealised cross section A_i with

$$A_i = nA_s + A_c(1 - \rho_{s,ef}) \tag{4.11}$$

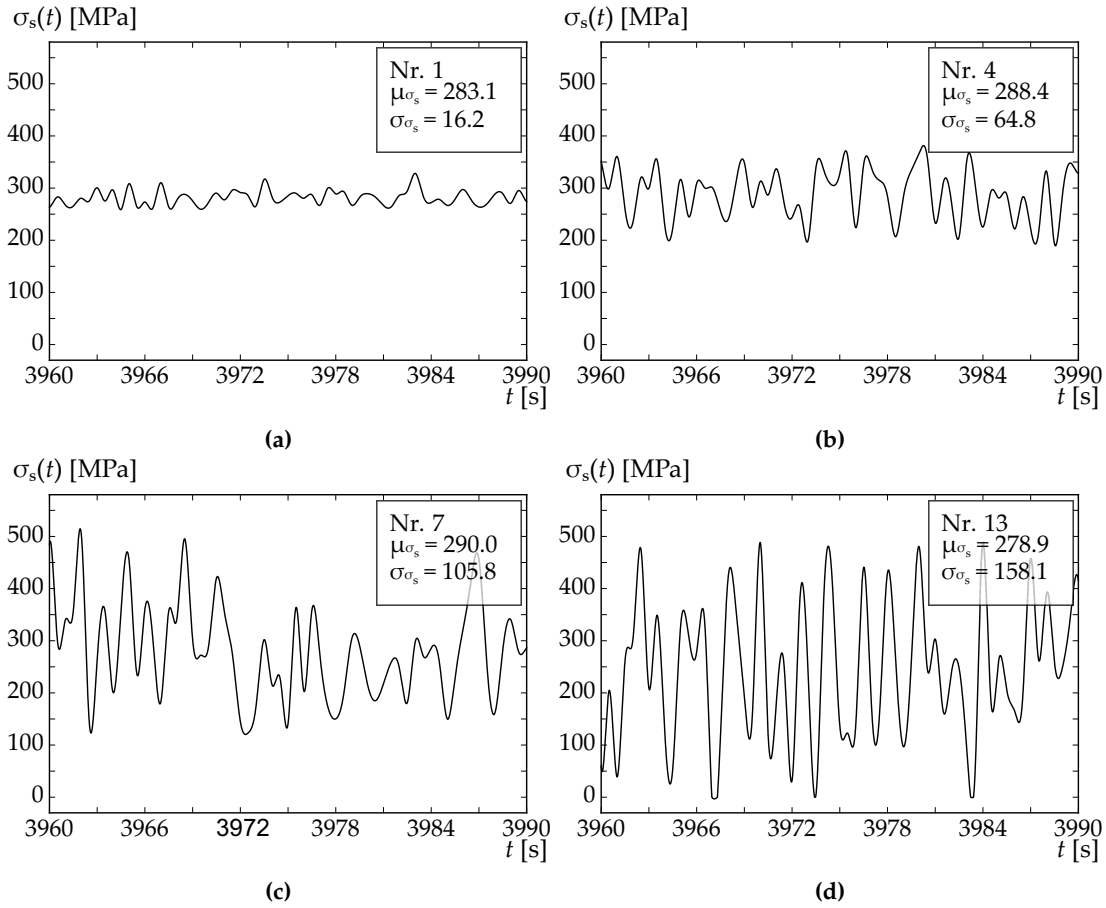

Figure 4.11: Extract of stress time series: (a) Nr. 1, (b) Nr. 4, (c) Nr. 7, (d) Nr. 13

is higher than the single net concrete area $A_c(1 - \rho_{s,ef})$. Based on the condition of equal strains in both, steel and concrete, it is possible to derive an equivalent idealised modulus of elasticity E_i for the uncracked concrete chord:

$$E_i = E_c \left[1 + \rho_{s,ef}(n-1)\right]. \tag{4.12}$$

As soon as the tension strength f_{ct} is reached, cracking of the concrete is expected. Yet, as mentioned in [49], the cracking occurs practically under lower loads than those predicted using the tensile strength f_{ct}. This is presumably the result of restraint stresses due to the effect of shrinkage which leads to tensile stresses in the concrete and simultaneously to compressions stresses in the reinforcement.

At first, the tests were static-monotonically loaded (strain-controlled) up to $F \approx 90...100$ kN until the expected principal cracks became visible. Afterwards the tests were unloaded and, depending on the planed test configuration, a post-tensioning force was applied in order to achieve transversal tension stresses and a transverse crack. As expected, the

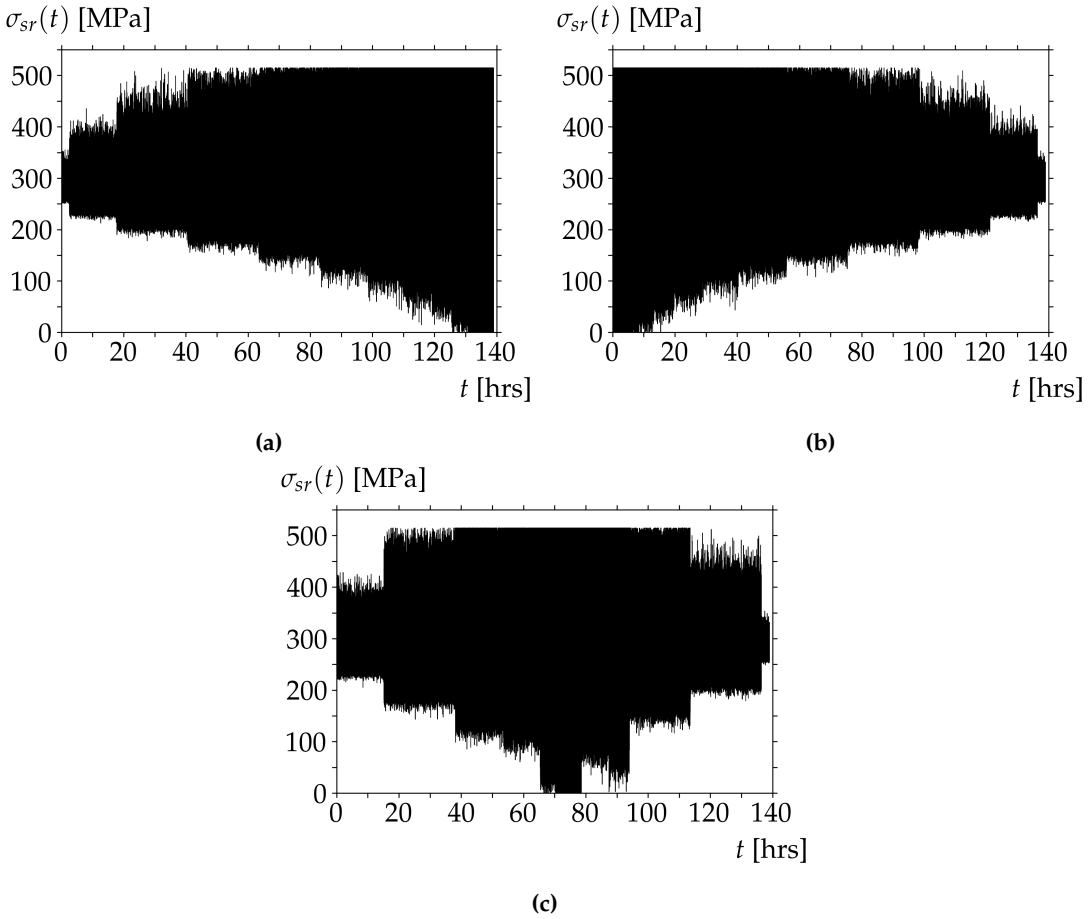

Figure 4.12: Overview of the overall stress time series: (a) Pe, (b) Pb, (c) Pm

concrete cracking lead to a slip δ_s between reinforcement and concrete, activating bond stresses along the interface steel-concrete. Following the equilibrium equations (cf. Ch. 3.3), the (idealised) constant bond stresses according to the Tension Chord Model may be estimated by

$$\frac{d\sigma_s}{dx} = \frac{4}{\varnothing_s}\tau_{b0}. \tag{4.13}$$

The steel strains result from the material constitutive equation in the elastic state. For the performed tests, an average rigid-plastic bond stress of

$$\tau_{b0} \approx 0.6 f_{ct} \tag{4.14}$$

may be derived for steel stresses in the elastic range, based on the ϵ_s-values of the strain

gauges between a cracked section and the next SG-location. Although the test specimens were cast in the vertical direction and meticulous compacted, the achieved average bond stress value τ_{b0} is less than half the value derived by [178], were $\tau_{b0} = 2f_{ct}$. Presumably the lower value of the used concrete cover in the experiments compared to the data employed by Sigrist in [178] and the weighty effect of shrinkage may be considered as the cause for the deviation.

After completing the unloading process the reinforcement presents positive strain values $\epsilon_s > 0$ which evidences tension stresses. At the cracked cross section the steel strain is not zero perhaps due to the roughness of the crack lips and the fact that cracking does not exactly occurs at the location of the strain gauge. Also worth of mentioning is that the steel strain ϵ_s and, for instance, the steel stress σ_s in the midpoint between the principal cracks also is $\epsilon_s > 0$, other than mathematically described by Alvarez [2] and Koppitz [103], who assume that the reinforcement does not exhibit any strain after unloading in the midpoint between cracks for $s_{rm} = s_{r0} = s_{rm,max}$ or a reduced value for $s_{rm} = 1/2 s_{r0} = s_{rm,min}$. The remaining stress σ_s in the midpoint of principal cracks is higher than at the cracked section after unloading and seems to obey a similar response than the wedge slip of post-tensioning systems. Thereby, the stress reduction at the cracked section causes a more or less linear distribution of stresses until the unloading line crosses the ascending first-loading-line. The induced compression stresses in the concrete may be neglected since the compression strains, which are non-linearly distributed, may be expected to be small. In fact, the unloading model of Muttoni and Fernández Ruiz [126] reveals a better agreement with the results of the tests.

During a fatigue test, a load redistribution is observed: Steel strains ϵ_s in the section between the principal cracks tend to increase, an effect which is produced by a degradation of the induced bond stresses at the interface between reinforcement and concrete. This already becomes apparent after a few load cycles. At the same time, the slope of the $\sigma_{sr} - \epsilon_{sm}$-curve decreases after every reloading act and approaches progressively the slope of the "naked" reinforcement.

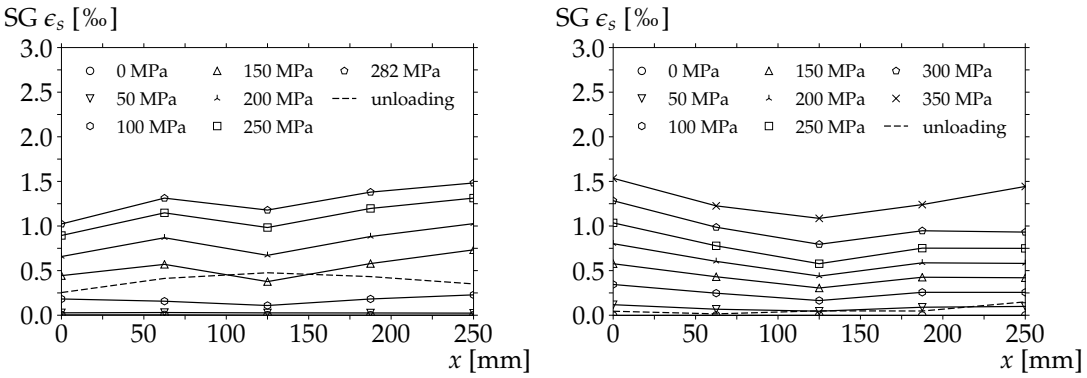

Figure 4.13: Overview of strain distribution of reinforcement during static first loading and after unloading: (a) Specimen St4-w0.2, (b) Specimen Dy1-Pe-w0

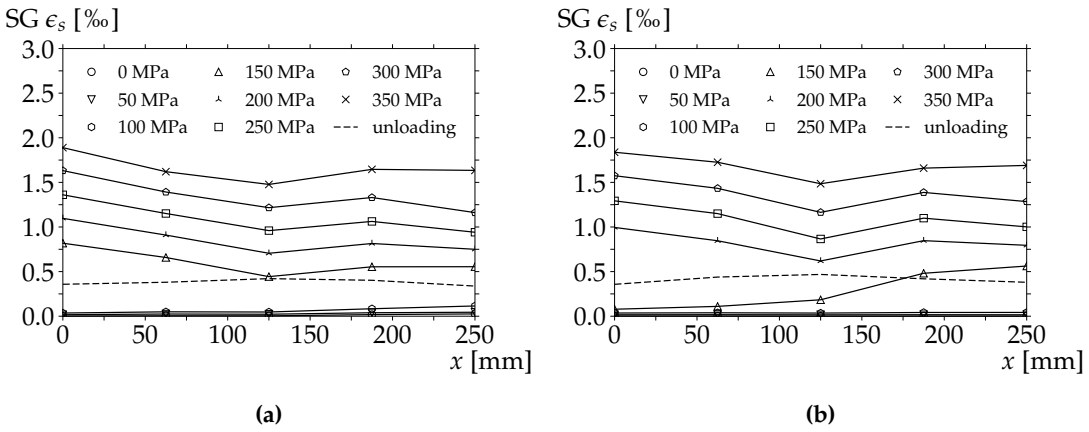

Figure 4.14: Overview of strain distribution of reinforcement during static first loading and after unloading: (a) Specimen Dy7-Pb-w0.2, (b) Specimen Dy9-Pm-w0.2

Additionally, the value of remaining steel strains, if the loading force gets close to zero, also decreases after a few cycles. In this way the restraint of reinforcement after unloading is weakened. The negative bond stresses, induced in unloading processes, degrade under fatigue loading, confirming the trend postulated by Koppitz in [103].

During the first load cycles, the structural modulus of elasticity E_{sm} in the reloading processes presents values which are higher than E_s. The steeper slope of the $\sigma_{sr} - \epsilon_{sm}$-curve results from the bond between reinforcement and concrete and partially from the produced compression stresses in the concrete. However, the progressive bond degradation leads to an also progressive decrease of E_{sm}. In consequence, a flattening of the $\sigma_{sr} - \epsilon_{sm}$-curve becomes visible, getting closer to the slope of the $\sigma_{sr} - \epsilon_s$-curve of the reinforcement – depending on the existing bond. In reality, the bond fatigue does not occur simultaneously at every place of the tension chord; it rather advances beginning at the cracked sections

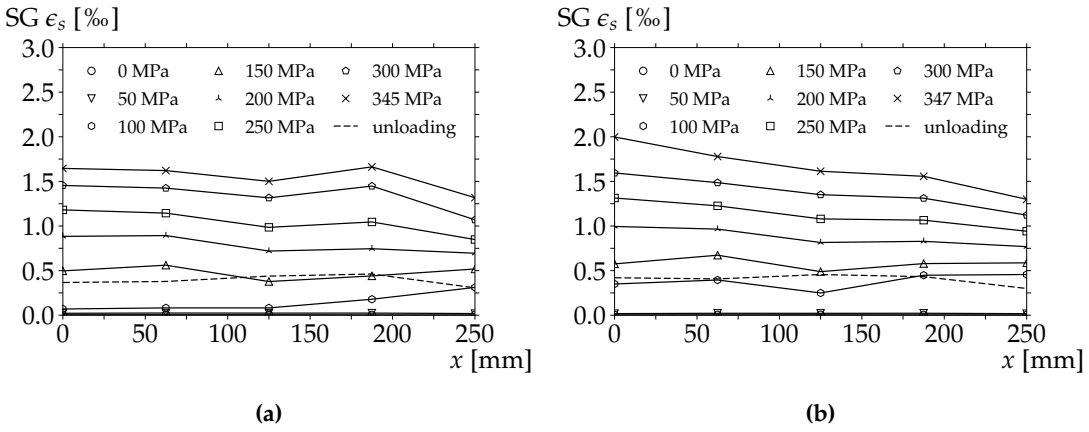

Figure 4.15: Overview of strain distribution of reinforcement during static first loading and after unloading: (a) Specimen Dy12-Pe-w0.2, (b) Specimen Dy15-Pb-w0.3

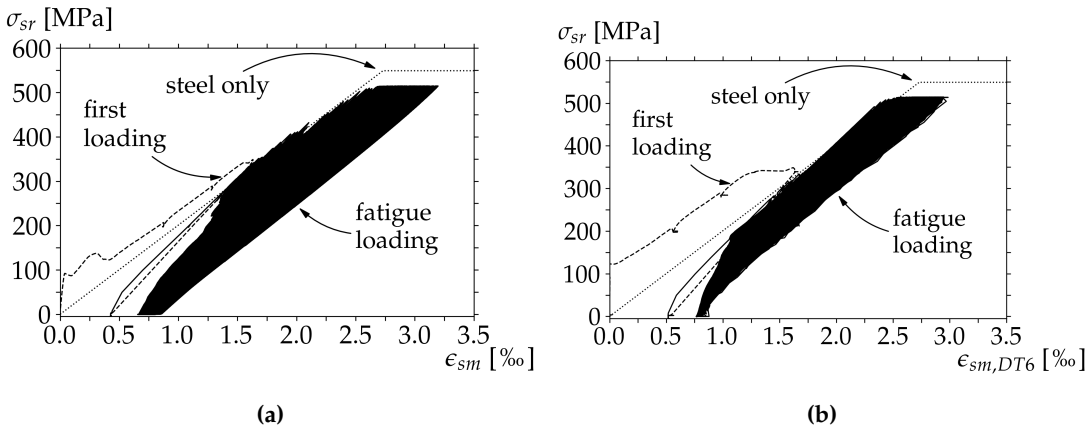

(a) **(b)**

Figure 4.16: $\sigma_{sr} - \epsilon_{sm}$-curve under first loading and subsequent fatigue loading of specimen Dy2-Pe-w0: (a) ϵ_{sm} calculated based on strain gauges (SG), (b) ϵ_{sm} calculated based on displacement transducer (DT)

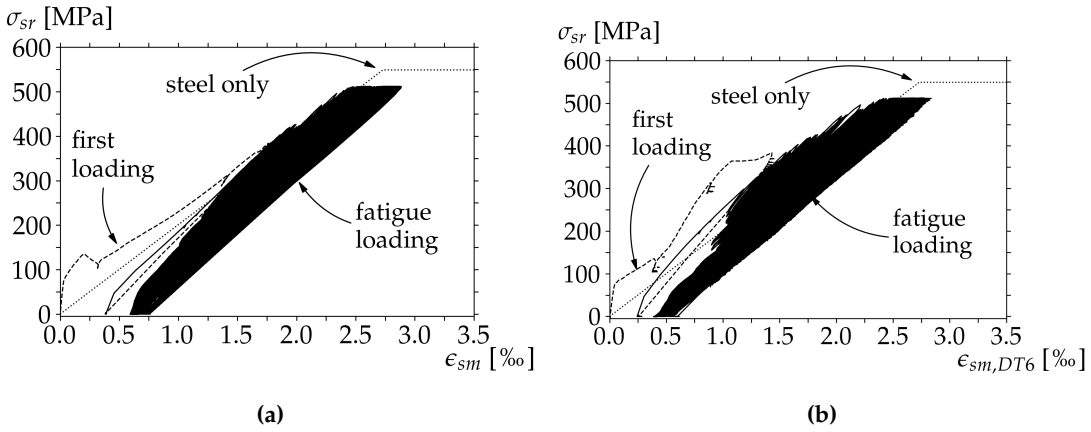

(a) **(b)**

Figure 4.17: $\sigma_{sr} - \epsilon_{sm}$-curve under first loading and subsequent fatigue loading of specimen Dy3-Pm-w0: (a) ϵ_{sm} calculated based on strain gauges (SG), (b) ϵ_{sm} calculated based on displacement transducer (DT)

towards the middle location between cracks.

Only a selection of some test results is presented in this work. The detailed report with all test results is found in [4]. The most important parameter thereby is the average steel strain ϵ_{sm}. Its development gives information about the bond strength distribution, the changes of crack width, and the deformation capacity. The calculation of ϵ_{sm} may be performed either through integration of the strain values of the employed strain gauges (SG) and a subsequent averaging or through the use of displacement transducers (DT). The first method is more accurate, yet strain gauges, which are glued to the steel, may theoretically experience some sort of fatigue. Also a progressive weakening of the glue interface is theoretically possible. For this reason, both methods have been employed and compared. As a result, it may be observed that the determined values of ϵ_{sm} using

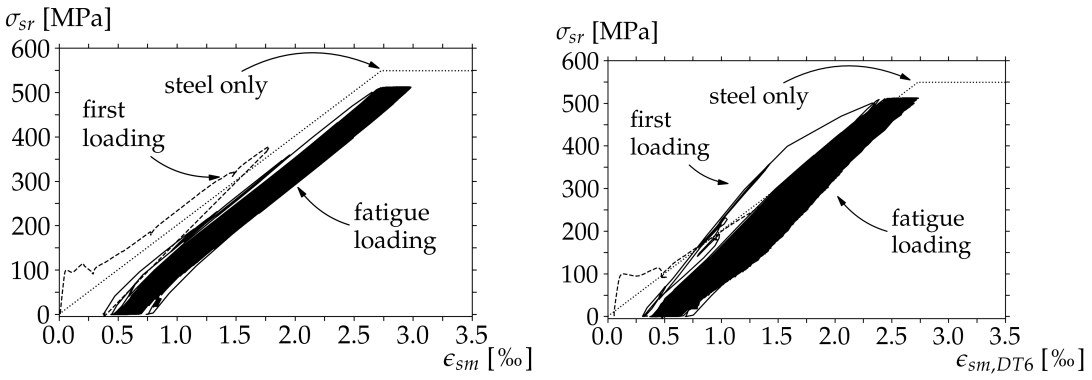

Figure 4.18: $\sigma_{sr} - \epsilon_{sm}$-curve under first loading and subsequent fatigue loading of specimen Dy7-Pb-w0.2: (a) ϵ_{sm} calculated based on strain gauges (SG), (b) ϵ_{sm} calculated based on displacement transducer (DT)

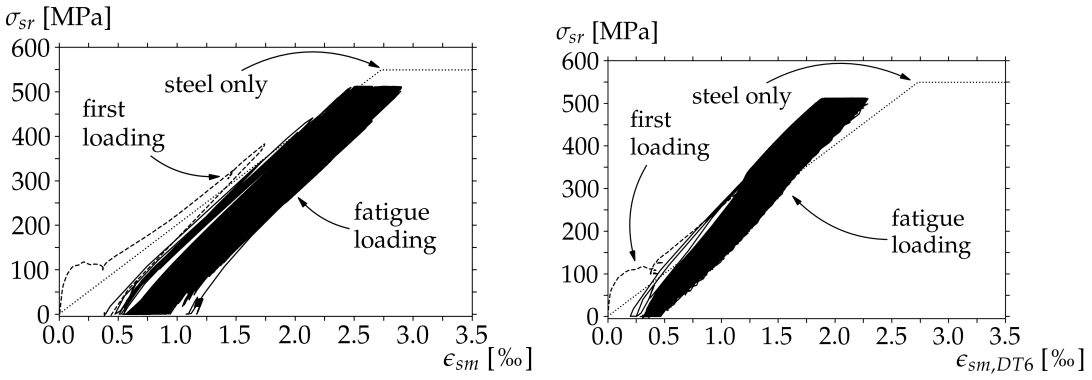

Figure 4.19: $\sigma_{sr} - \epsilon_{sm}$-curve under first loading and subsequent fatigue loading of specimen Dy8-Pb-w0.2: (a) ϵ_{sm} calculated based on strain gauges (SG), (b) ϵ_{sm} calculated based on displacement transducer (DT)

the strain gauges and displacement transducers are principally equal in the most tested specimens. Apart from variations owing to different locations, no significant discrepancies are notable. There are, however, test specimens which show great differences between the values of ϵ_{sm} calculated with strain gauges and with displacement transducers (cf. Fig. 4.19 and Fig. 4.21).

The results of the fatigue tests reveal steel deformations in the plastic range even though the applied loads were lower than the yield strength f_{sy}. The stress loads are to be understood as average values in relation to the undamaged reinforcement cross section. In specimens, where the ϵ_{sm}-values of the strain gauges and displacement transducers approximately coincide (cf. e.g. Fig. 4.16, 4.17, 4.18, 4.20), is the strain measurement probably correct. As mentioned before, some specimens apparently present contradictory

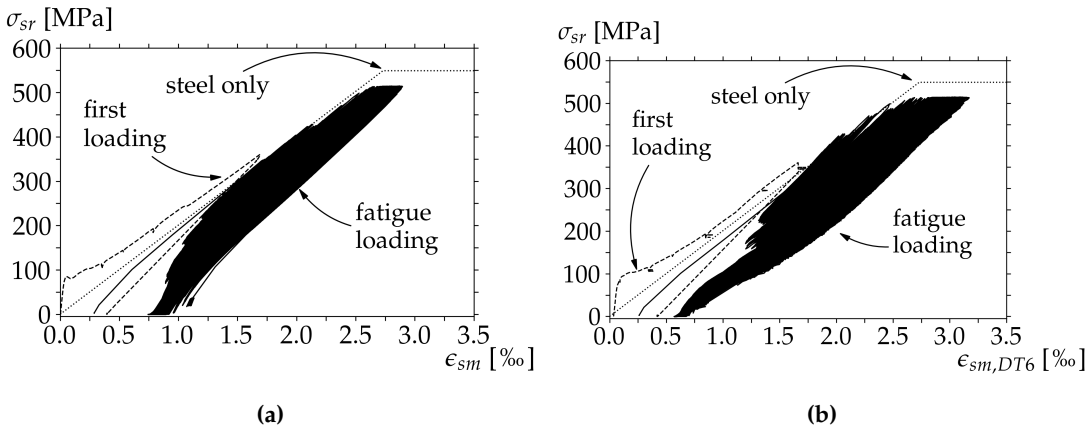

Figure 4.20: $\sigma_{sr} - \epsilon_{sm}$-curve under first loading and subsequent fatigue loading of specimen Dy10-Pm-w0.2: (a) ϵ_{sm} calculated based on strain gauges (SG), (b) ϵ_{sm} calculated based on displacement transducer (DT)

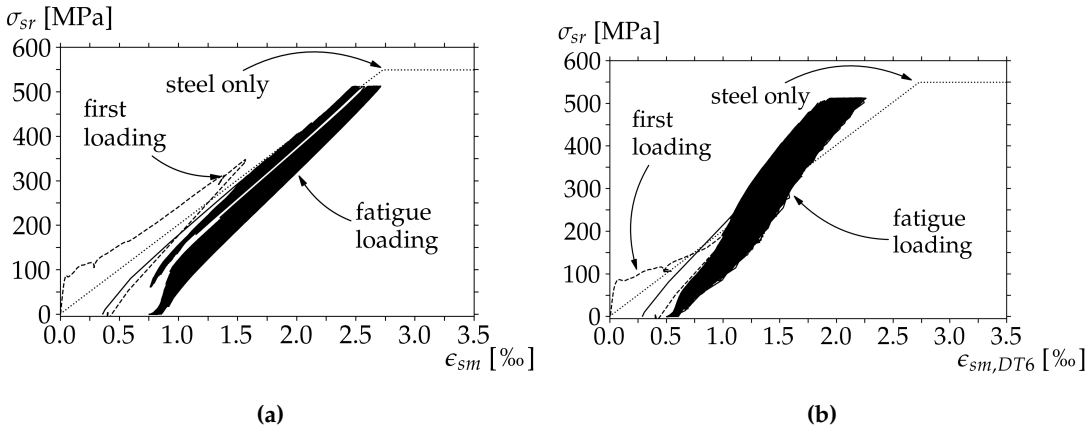

Figure 4.21: $\sigma_{sr} - \epsilon_{sm}$-curve under first loading and subsequent fatigue loading of specimen Dy12-Pe-w0.2: (a) ϵ_{sm} calculated based on strain gauges (SG), (b) ϵ_{sm} calculated based on displacement transducer (DT)

results (cf. e.g. 4.19, 4.21, 4.24).

In the limit case of a fully bond degradation, the tension chord behaves exactly as the "naked" reinforcement. In fact, the decrease of E_{sm} is an indicator of the bond deterioration. As mentioned before however, the results exhibit a continuous increase of (plastic) steel strains beyond the theoretical strains experienced by the "naked" reinforcement under the given loads. This plastic-strain-accumulation-process seems to be influenced by the load history. On the other hand, the applied transverse tension stress does not appear to be relevant. Nonetheless, the variation scatter is high and it is not possible to deduce more precise conclusions regarding the most important parameters. The value of remaining strains also grows progressively with increasing number of load peaks. By a theoretical fully bond degradation there are no remaining strains since the reinforcement

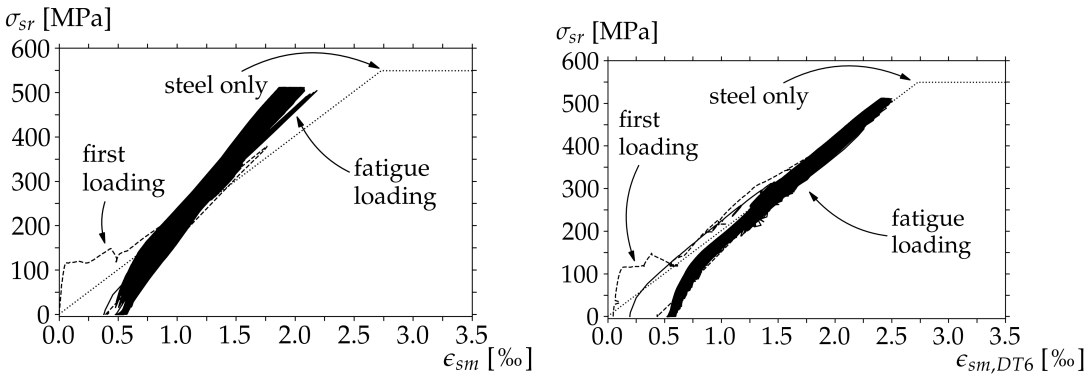

(a) **(b)**

Figure 4.22: $\sigma_{sr} - \epsilon_{sm}$-curve under first loading and subsequent fatigue loading of specimen Dy13-Pe-w0.3: (a) ϵ_{sm} calculated based on strain gauges (SG), (b) ϵ_{sm} calculated based on displacement transducer (DT)

may elongate freely without any resistance from the concrete. In this experimental case, though, the steel strains ϵ_s increase progressively at every location, where a strain gauge (SG) is placed, and may reach values higher than ϵ_{sy} despite of loads $\sigma_{sr} < f_{sy}$ – this even in the midpoint between principal cracks.

The (plastic) growth of ϵ_s may have several causes which are briefly analysed below.

- Steel creep: Creep is defined as a time- and stress-dependent deformation increase under constant loads and at a temperature $T > T_t \approx 0.3T_{mg}$ [89], where T_{mg} represents the melting temperature of reinforcement. T_t is called in the literature the transition temperature [89]. Creep effects lead to irreversible plastic deformations, crack formation and failure, and may occur even if the applied loads are lower than

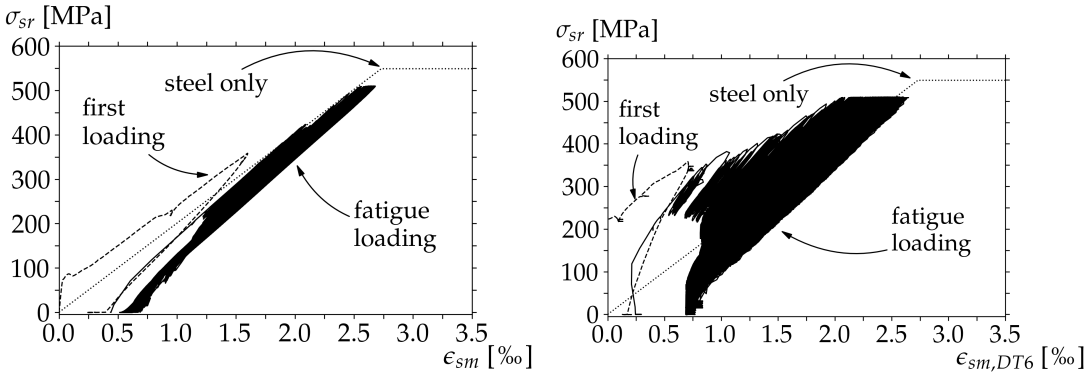

(a) **(b)**

Figure 4.23: $\sigma_{sr} - \epsilon_{sm}$-curve under first loading and subsequent fatigue loading of specimen Dy14-Pm-w0.3: (a) ϵ_{sm} calculated based on strain gauges (SG), (b) ϵ_{sm} calculated based on displacement transducer (DT)

f_{sy}. According to [26], creep effects may also be observed under dynamic loading. In the present case, the melting temperature strictly depends on the steel composition and may be estimated to $T_{mg} \approx 1450°C$ for ferritic steels; hence, $T_t \approx 435°C$. Such high temperatures have not been achieved in the experiments yet, otherwise the reinforcement would have glowed visibly. Dynamic loading causes indeed a temperature increase (Ch. 3.1.2). Additionally, the continuous slip variation between reinforcement and concrete leads to friction effects and thus to a heat growth. Yet, this temperature raise is not suitable to reach values higher than 435°C. In consequence, a creep of reinforcement cannot be considered as the cause for the observed plastic-strain-accumulation.

- Steel-ratcheting: The ratcheting-effect describes an incremental growth of plastic steel deformations under loading, unloading, and subsequent reloading with a constant load amplitude which exceeds the yield strength, i.e. $\sigma_{sr} > f_{sy}$ (Fig. 4.25a). In relation to applied loads in the macro-scale during testing, at least, this is not the case in the present experiments.

- Stress concentration at micro-crack tips: Micro-cracks in reinforcement may originate as a result of fatigue loading (Ch. 3.1.2). Due to the sharp direction change of the stress flow, a stress concentration may be observed in the vicinity of a crack tip (Fig. 4.25b). The local values of σ_s at the crack tip may exceed the yield strength f_{sy}, even if $\sigma_s < f_{sy}$ in the undamaged cross sections, producing – in this case locally – plastic deformations and steel-ratcheting. In consequence, the fatigue crack grows and the cross section A_s of the reinforcement decreases, leading this again to additional and higher stress concentrations and average stresses in A_s. The mentioned process occurs locally and only in cross sections which hold fatigue cracks. Through the strain measurements performed with strain gauges it becomes visible, yet, that the observed plastic-strain-accumulation occurs all over the length of the reinforcement

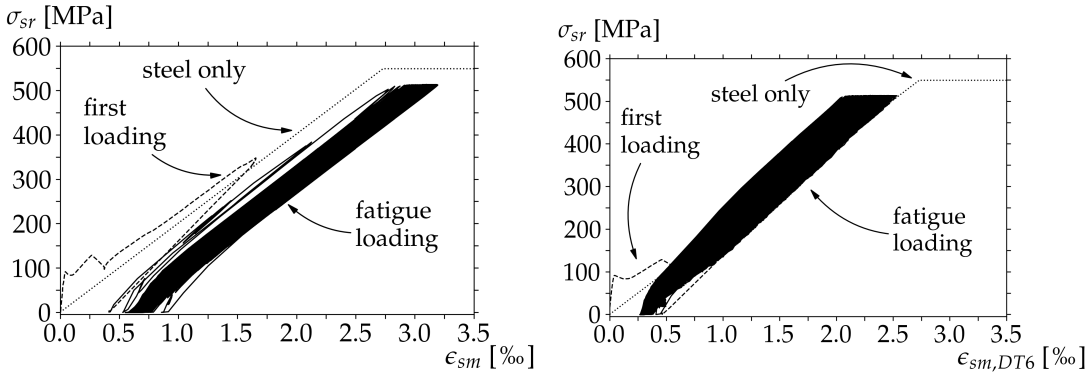

Figure 4.24: $\sigma_{sr} - \epsilon_{sm}$-curve under first loading and subsequent fatigue loading of specimen Dy15-Pb-w0.3: (a) ϵ_{sm} calculated based on strain gauges (SG), (b) ϵ_{sm} calculated based on displacement transducer (DT)

and not only in certain sections. Since it is improbable that fatigue cracks originate at every point, where strain gauges are located, another mechanism must be responsible for the reported results.

- Degradation of the Young's modulus of elasticity E_s: As in Ch. 3.2.4 described, the concrete secant-modulus E_c is reported to decrease under fatigue loads. Similar effects in steel have not been reported in the available literature; therefore, this variant will not be further considered. Nevertheless, due to fatigue cracks and the produced local increment of the average stress, larger deformations are possible, leading to a global stiffness reduction in structural members, i.e. at structural level.
- Finally, fatigue effects of the used strain gauges (grid, glue-interface) are theoretically possible. Also possible is a potential growing slip between test specimen and testing rig. However, the results delivered by the displacement transducers confirm in most cases similar results than by strain gauges. For this reason, data gained by the strain gauges may be considered as reliably. Test specimens with contradictory results point to some sort of irregularity and may be questionable. In this case, the values of the stress transducers do not show a plastic-strain-accumulation but only a bond degradation. Only in specimen Dy13-Pe-w0.3 there is an exception: The displacement transducer reports a plastic-strain-accumulation whereas the strain gauges do not.

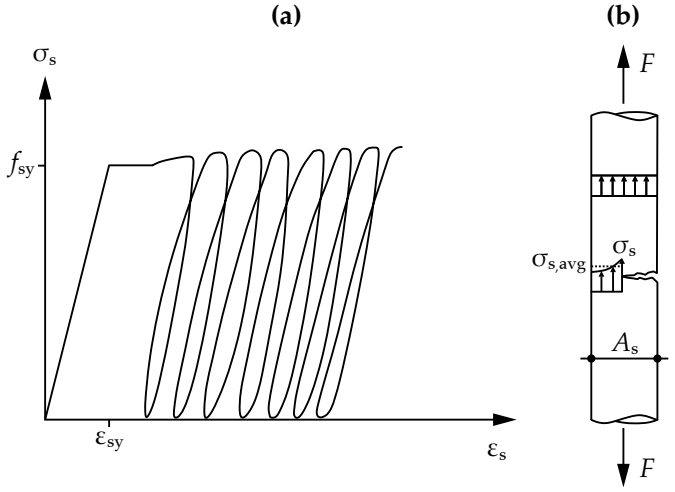

Figure 4.25: (a) Incremental growth of plastic strains under cyclic constant loading with $\sigma_s > f_{sy}$ (ratcheting), (b) Stress concentration at tip of fatigue crack

On the basis of these considerations it is concluded that the reinforcement may experience, in some cases, increasing plastic strains under fatigue loading with $\sigma_{sr} < f_{sy}$ (related to the undamaged cross section A_s). The strain increase is distributed all over the length of the reinforcement. This conclusion is met by means of the available results of the performed tests and may be questionable. In any case, further research is necessary in order to either confirm or contradict the conclusions and derived calculation models. It is suggested to monitor the deformation of reinforcement bars tested under fatigue loading

(stress-controlled) employing accurate displacement transducers in order to perceive any plastic deformation. A calculation model for the measured bond degradation and the supposed plastic-strain-accumulation is given on Ch. 4.2.4.

The deformation capacity was finally evaluated based only on the values of displacement transducers (cf. [4]). The figures Fig. 4.26, 4.27 present the $\epsilon_{sm}/\epsilon_{sr}$-coefficient as function of the steel strain ϵ_{sr} at the cracked cross section. Higher values of $\epsilon_{sm}/\epsilon_{sr}$ point to a higher deformation capacity [178], [5]. This so called bond-coefficient depends on the steel mechanical properties and, like in the present case, on the bond behaviour.

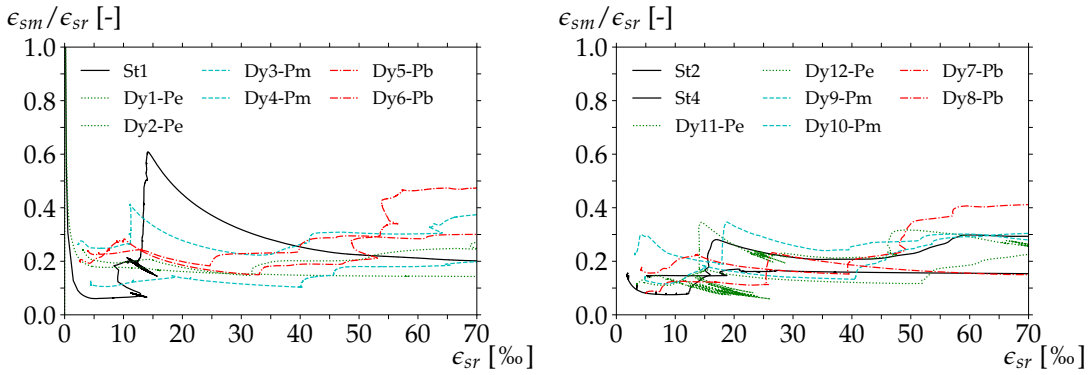

Figure 4.26: Deformation capacity of RC-members after fatigue loading: (a) Without a longitudinal crack and (b) For longitudinal crack of width w_{tr} = 0.2 mm

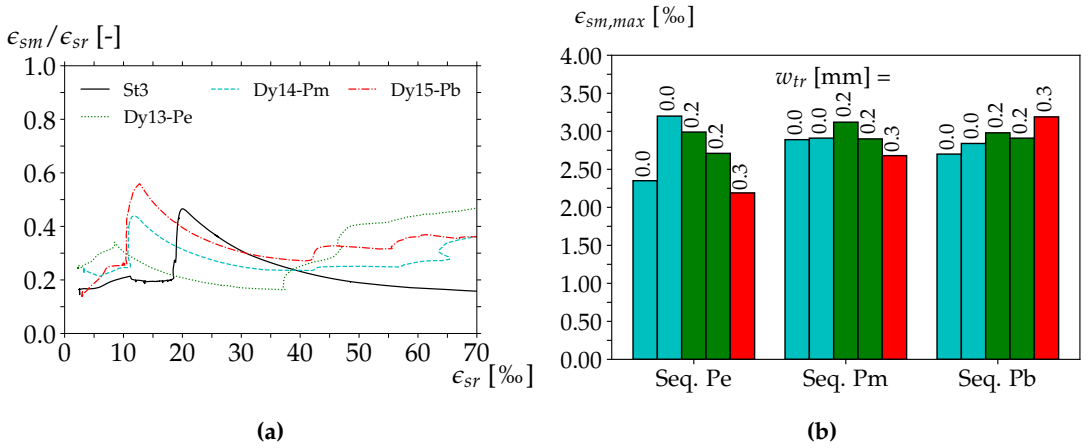

Figure 4.27: (a) Deformation capacity of RC-members after fatigue loading for longitudinal crack of width w_{tr} = 0.3 mm, (b) Maximal measured steel strains during fatigue

In Fig. 4.26, 4.27 the $\epsilon_{sm}/\epsilon_{sr}$-coefficient of the static tests are plotted together with those of the fatigue tests in the ultimate state. Since no fatigue failure was achieved in the tests, the specimens were tested later in the ultimate state (strain-controlled). As expected, the bond degradation and the plastic steel deformations prove to enhance the deformation capacity of structural members. This is in general a positive effect in the ultimate state,

though it may lead to changes in the structural response e.g. to shear forces of concrete beams. The different load sequences do not seem to influence the maximal measured strain ϵ_s. The ultimate strength f_{su} was not reduced in any experimental test.

4.2.2 Tension Chord Model for Static Loading

The first detailed derivation of mathematical expressions for the calculation of crack width after loading and unloading, the estimation of the required minimum reinforcement ratio as well as the elongation capacity of concrete chords using the Tension Chord Model is found in [2]. The force that leads to a first crack formation is subdivided into a force F_c applied on the concrete net area and a part F_s corresponding to the reinforcement:

$$F_{cr} = F_c + F_s = A_{c,ef}(1 - \rho_{s,ef}) f_{ct} + A_s n f_{ct}. \tag{4.15}$$

Setting $A_s = \rho_{s,ef} A_{c,ef}$ and dividing Eq. 4.15 through A_s one obtains the expression for the reinforcement stress σ_{sr0} at the cracked cross section area immediately after the first crack formation.

$$\sigma_{sr0} = \frac{f_{ct}}{\rho_{s,ef}} \left[1 + \rho_{s,ef}(n-1)\right]. \tag{4.16}$$

Assuming rigid-plastic values of bond stresses, the gradient of stresses and strains in the elastic state is linearly distributed (cf. Fig. 4.28). Since the concrete stress can not exceed the uniaxial tension strength f_{ct}, the maximal distance s_{r0} between cracks is determined under consideration of the derivation of the concrete stress σ_c after the length x (cf. Eq. 3.50).

$$-\frac{d\sigma_c}{dx} = \frac{4\rho_{s,ef}}{\varnothing_s(1 - \rho_{s,ef})} \tau_{b0} \equiv \frac{f_{ct}}{\frac{1}{2} s_{r0}}. \tag{4.17}$$

$$s_{r0} = \frac{\varnothing_s(1 - \rho_{s,ef})}{4\rho_{s,ef}\tau_{b0}} f_{ct}. \tag{4.18}$$

Based on a linear distribution of stresses in the elastic state, the calculation of the average strains ϵ_{sm} and ϵ_{cm} consists of the integration and averaging of σ_s as well as σ_c:

$$\epsilon_{sm} = \frac{\sigma_{sr0} + n f_{ct}}{2E_s}. \tag{4.19}$$

$$\epsilon_{cm} = \frac{n f_{ct}}{2E_s}. \tag{4.20}$$

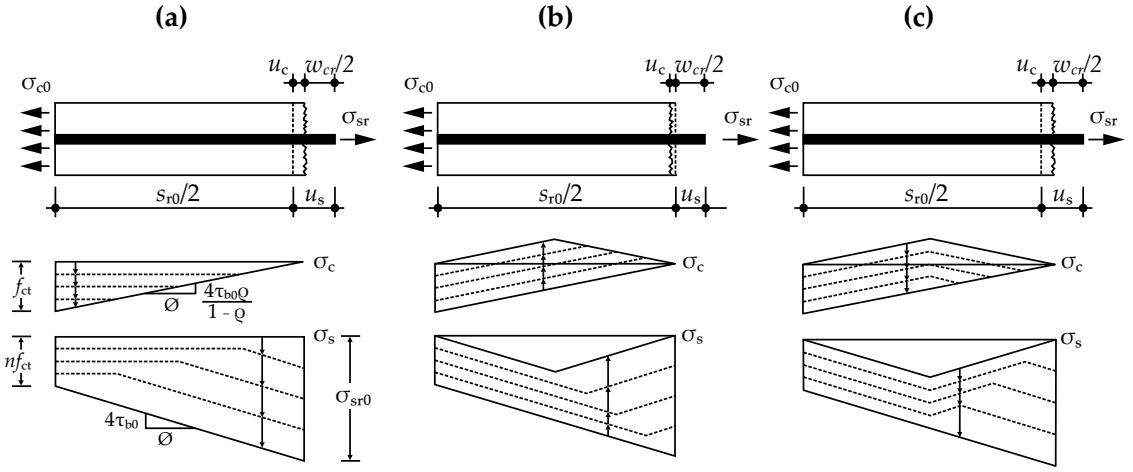

Figure 4.28: Stress distribution in concrete and reinforcement according to Tension Chrod Model [2]: (a) First loading, (b) Unloading, and (c) Reloading, redrawn from [2]

The crack width for load states beneath the yield stress of the reinforcement follows from

$$w_{cr} = (\epsilon_{sm} - \epsilon_{cm}) s_{r0} = \ldots = \frac{\text{Ø}_s (1 - \rho_{s,ef}) \left[1 + \rho_{s,ef}(n-1)\right] f_{ct}^2}{4 E_s \rho_{s,ef}^2 \tau_{b0}}. \tag{4.21}$$

The expressions for the minimal distance between cracks $s_{r,min} = 0.5 s_{r,max} = 0.5 s_{r0}$ may be derived similarly (see [116]). After unloading, both, reinforcement and concrete, tend to deform back. Yet, due to the existing slip δ_s and the fact that the reinforcement presents the largest absolute elongation value, negative bond stresses are activated while the slip δ_s is reduced. This causes the reinforcement to introduce compression stresses into the surrounding effective concrete area $A_{c,ef}$ and impeding the reinforcement to deform back completely. Alvarez [2] assumes implicitly that $A_{c,ef}$ remains constant. Additionally, he presumes that the steel strain maintains the same slope than at loading but with contrary algebraic sign, i.e. the bond stress at unloading precesses remains also constant with $\tau_b = -\tau_{b0}$. At reloading processes the activated bond stresses are also $\tau_b = \tau_{b0}$. At the same time, the concrete experiences, in the unloading process, compression stresses beginning at the cracked cross section and on this way the tension stresses in the concrete are progressively removed. The reinforcement experiences therefore a further (global) strain reduction equivalent in value to the reduction of the concrete strain; consequently, the steel strain ϵ_s as well as the concrete strain ϵ_c in the midpoint of cracks after unloading are zero – just as at the cracked cross section. Nevertheless, a state of restraint remains in the intermediate section (Fig. 4.28).

From the assumed linear distribution of strains at unloading (elastic state) follows, according to Alvarez [2], with $\tau_b = -\tau_{b0}$ for the stress σ_s in the intermediate point with

$x = 0.25 s_{r0}$:

$$-\frac{d\sigma_s}{dx} = -\frac{4\tau_{b0}}{\varnothing_s} \equiv \frac{\sigma_s}{\frac{1}{4}s_{r0}}. \tag{4.22}$$

$$\sigma_s\left(x = \frac{1}{4}s_{r0}\right) = -\frac{\tau_{b0}}{\varnothing_s}s_{r0}. \tag{4.23}$$

Similarly for the concrete stress at $x = 0.25 s_{r0}$:

$$\frac{d\sigma_c}{dx} = \frac{4\rho_{s,ef}\tau_{b0}}{\varnothing_s(1-\rho_{s,ef})} \equiv \frac{\sigma_c}{\frac{1}{4}s_{r0}}. \tag{4.24}$$

$$\sigma_c\left(x = \frac{1}{4}s_{r0}\right) = \frac{\rho_{s,ef}\tau_{b0}}{\varnothing_s(1-\rho_{s,ef})}s_{r0}. \tag{4.25}$$

By means of constitutive material equations and after deriving average values, the average strains and crack width after unloading ($\tau_b = -\tau_{b0}$) are, according to Alvarez [2]:

$$\epsilon_s\left(x = \frac{1}{4}s_{r0}\right) = -\frac{\tau_{b0}}{2\varnothing_s E_s}s_{r0}. \tag{4.26}$$

$$\epsilon_c\left(x = \frac{1}{4}s_{r0}\right) = \frac{\rho_{s,ef}\tau_{b0}}{2\varnothing_s(1-\rho_{s,ef})E_c}s_{r0}. \tag{4.27}$$

$$w_{cr} = (\epsilon_{sm} - \epsilon_{cm})s_{r0} = \ldots = -\frac{\varnothing_s(1-\rho_{s,ef})\left[1+\rho_{s,ef}(n-1)\right]f_{ct}^2}{8E_s\rho_{s,ef}^2\tau_{b0}}. \tag{4.28}$$

Eq. 4.28 is half the value of Eq. 4.21 at the crack formation phase. In case of a minimal distance between cracks, the crack width after unloading is half the value of Eq. 4.28 (cf. [116]):

$$w_{cr} = w_{cr} = (\epsilon_{sm} - \epsilon_{cm})s_{r0} = \ldots = -\frac{\varnothing_s(1-\rho_{s,ef})\left[1+\rho_{s,ef}(n-1)\right]f_{ct}^2}{16E_s\rho_{s,ef}^2\tau_{b0}}. \tag{4.29}$$

By reloading, Alvarez [2] assumes that the reinforced concrete chord behaves in the same way as before.

Fig. 4.29 describes the mechanical behaviour of reinforcement in a concrete chord under

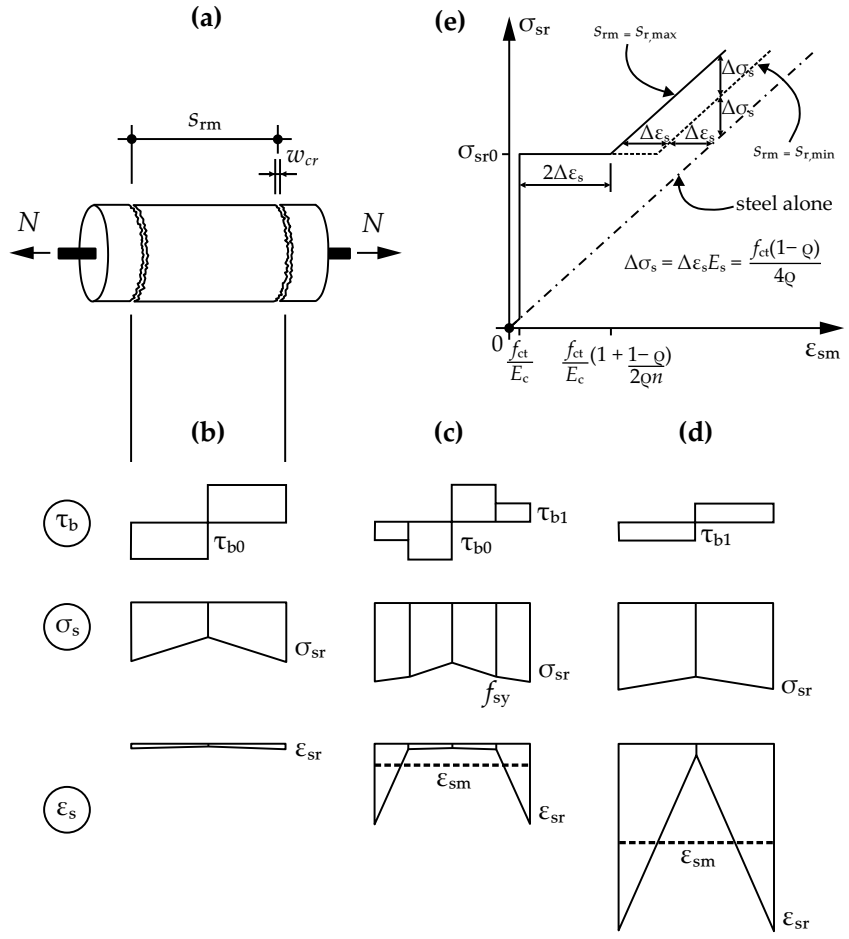

Figure 4.29: (a) Reinforced tension chord, (b) Stresses and strains in the elastic range, (c) after begin of yielding, (d) in the fully plastic range, and (e) $\sigma_{sr} - \epsilon_{sm}$-curve after the Tension Chord Model for the static-monotonic loading; relations for a bilinear constitutive material equation of the reinforcement, redrawn from [2]

loads larger than F_{cr}. When the tension stress in the concrete achieves the value $\sigma_c = f_{ct}$, the reinforcement stress is equal to $\sigma_s = n f_{ct}$. Due to the crack formation the value of the stress increases suddenly to $\sigma_s = \sigma_{sr0}$ according to Eq. 4.16. Simultaneously, the average steel strain increases abruptly. Considering the limit case of maximal distance between cracks, i.e. $s_{r,max} = s_{r0}$ (Eq. 4.18), the average steel strain ϵ_{sm} before cracking is

$$\epsilon_{sm}\left(\sigma_{sr} = \sigma_{sr0}\right) = \frac{1}{E_s}\frac{1}{2}\left(\sigma_{sr0} + n f_{ct}\right) = \ldots = \left(1 + \frac{1-\rho_{s,ef}}{2n\rho_{s,ef}}\right)\frac{f_{ct}}{E_c}. \tag{4.30}$$

The strain leap after cracking results from the difference between average steel strain

before and after cracking. Using Eq. 4.30 one obtains (cf. [2])

$$\Delta\epsilon_s = \frac{1}{2}\left[\epsilon_{sm}\left(\sigma_{sr} = \sigma_{sr0}\right) - \frac{f_{ct}}{E_c}\right] = \ldots = \frac{1-\rho_{s,ef}}{\rho_{s,ef}}\frac{f_{ct}}{4E_s}. \tag{4.31}$$

For the limit case of $s_{r,max} = s_{r0}$ the strain leap amounts $2\Delta\epsilon_s$ while it becomes $3\Delta\epsilon_s$ for $s_{r,min} = 0.5s_{r0}$. In the same way, using the Tension Chord Model it is possible to determine a strain difference between the "naked" reinforcement and the reinforced concrete of $2\Delta\epsilon_s$ for $s_{r,max} = s_{r0}$ and a strain difference of $\Delta\epsilon_s$ for $s_{r,min} = 0.5s_{r0}$.

The deformation capacity of a tension chord under static-monotonic loading depends highly on the constitutive material equation of the reinforcement. Alvarez [2] distinguishes three response regimes for a bilinear constitutive material equation of reinforcement. Beginning with the cracked cross section, at locations where the yield strength f_{sy} of reinforcement is reached, the bond strength is significantly reduced to $\tau_b = \tau_{b1}$ – mainly due to the produced damage in the concrete and the lateral contraction of reinforcement under tension [49] –, and the chord deformation concentrates there.

- Regime 1: $\sigma_{sr} < f_{sy}$. Linear distribution of steel strains. The distance between cracks is the average distance s_{rm}.

$$\epsilon_{sm} = \frac{\sigma_{sr}}{E_s} - \frac{s_{rm}\tau_{b0}}{\varnothing_s E_s}. \tag{4.32}$$

- Regime 2: $f_{sy} \leq \sigma_{sr} < \left(f_{sy} + \frac{2\tau_{b1}s_{rm}}{\varnothing_s}\right)$. Regime 2 begins with the yielding of reinforcement and ends before the reinforcement yields all over the chord length. This may be the case if the yielding transmission length l_{by} reaches the middle point between cracks. From the condition

$$\sigma_{sr} - \frac{4}{\varnothing_s}\tau_{b1}l_{by} = f_{sy}, \tag{4.33}$$

it follows

$$l_{by} = \frac{\varnothing_s}{4\tau_{b1}}\left(\sigma_{sr} - f_{sy}\right). \tag{4.34}$$

$$l_{by} = \frac{1}{2}s_{rm} \Leftrightarrow \sigma_{sr} = f_{sy} + \frac{2\tau_{b1}s_{rm}}{\varnothing_s}. \tag{4.35}$$

For regime 2 Alvarez [2] derives the average steel strain as follows:

$$\epsilon_{sm} = \frac{\left(\sigma_{sr} - f_{sy}\right)^2 \varnothing_s}{4E_{sh}\tau_{b1}s_{rm}}\left(1 - \frac{E_{sh}\tau_{b0}}{E_s\tau_{b1}}\right) + \frac{\left(\sigma_{sr} - f_{sy}\right)}{E_s}\frac{\tau_{b0}}{\tau_{b1}} + \left(\epsilon_{sy} - \frac{\tau_{b0}s_{rm}}{E_s\varnothing_s}\right). \tag{4.36}$$

- Regime 3: $\left(f_{sy} + \frac{2\tau_{b1}s_{rm}}{\varnothing_s}\right) \leq \sigma_{sr} < f_{su}$. In Regime 3 the reinforcement yields all over the tension chord. The bond strength is $\tau_b = \tau_{b1}$. According to [2]:

$$\epsilon_{sm} = \frac{\left(\sigma_{sr} - f_{sy}\right)}{E_{sh}} + \left(\epsilon_{sy} - \frac{s_{rm}\tau_{b1}}{\varnothing_s E_{sh}}\right). \tag{4.37}$$

Koppitz et al. [103] suggests a modification of the Tension Chord Model, which was postulated by Sigrist [178] and further derived by Alvarez [2], for cases of a single unloading and reloading process. On the basis of experimental data of Kenel [95] he observes a reduction of the bond properties and of the tension-stiffening effect. Following parameters are introduced:

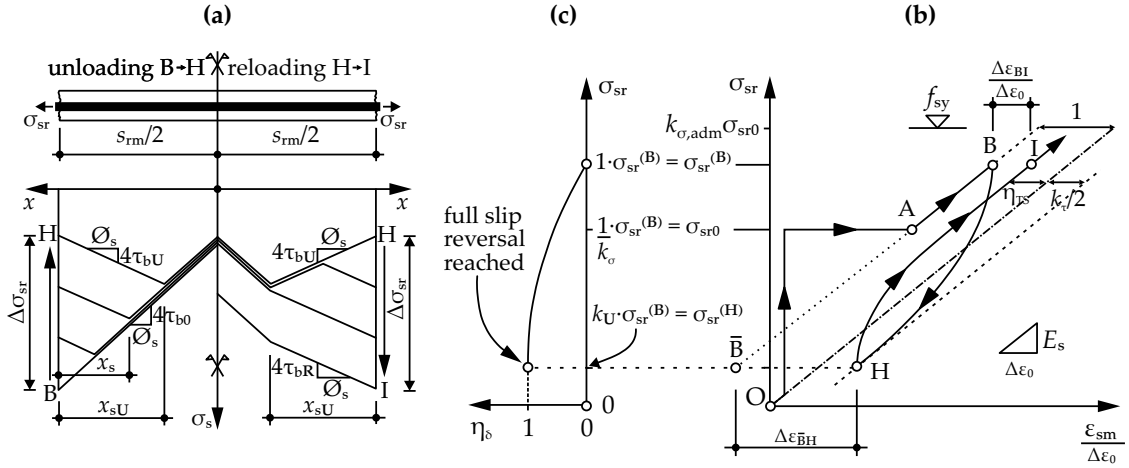

Figure 4.30: Modification of the Tension Chord Model according to Koppitz et al. [103]: (a) Reinforced tension chord under unloading from $\sigma_{sr}^{(B)}$ to $\sigma_{sr}^{(H)}$ (left) and reloading from $\sigma_{sr}^{(H)}$ to $\sigma_{sr}^{(I)}$ (right), (b) $\sigma_{sr} - \epsilon_{sm}$-curve for the unloading and reloading process with the tension-stiffening-number η_{TS}, (c) η_δ-parameter for the quantification of slip reversal, redrawn from [103]

$$1 \leq k_\sigma = \frac{\sigma_{sr}^{(B)}}{\sigma_{sr0}} \leq k_{\sigma,adm} = \frac{f_{sy}}{\sigma_{sr0}}, \tag{4.38}$$

$$0 \leq k_U = \frac{\sigma_{sr}^{(H)}}{\sigma_{sr0}}, \tag{4.39}$$

where σ_{sr0} corresponds to the stress in the reinforcement immediately after a crack formation (cf. Eq. 4.16). $\sigma_{sr}^{(B)} > \sigma_{sr0}$ represents the final achieved stress in the reinforcement in the first loading process, $\sigma_{sr}^{(H)} \leq \sigma_{sr}^{(B)}$ is the stress after unloading (it must not be necessarily zero). Loyal to the simplifications of the Tension Chord Model, the modification according to Koppitz et al. assumes constant bond stresses τ_b depending on whether the reinforcement yields or not. Additionally, for the unloading process $\tau_b = \tau_{bU}$, while $\tau_b = \tau_{bR}$ for the following reloading process. Koppitz et al. [103] assumes

$$\tau_{bU} = \tau_{bR} = k_\tau f_{ct} \leq \tau_{b0}, \tag{4.40}$$

being $k_\tau = 1.0$ and $\tau_{b0} = 2f_{ct}$. As comparison, König et al. suggests e.g. for an average constant bond stress for static monotonic loading $\tau_{bm} = 2f_{ct}$ and for repeated loading 70% of the static value, i.e. $\tau_{bm} = 1.4f_{ct}$.

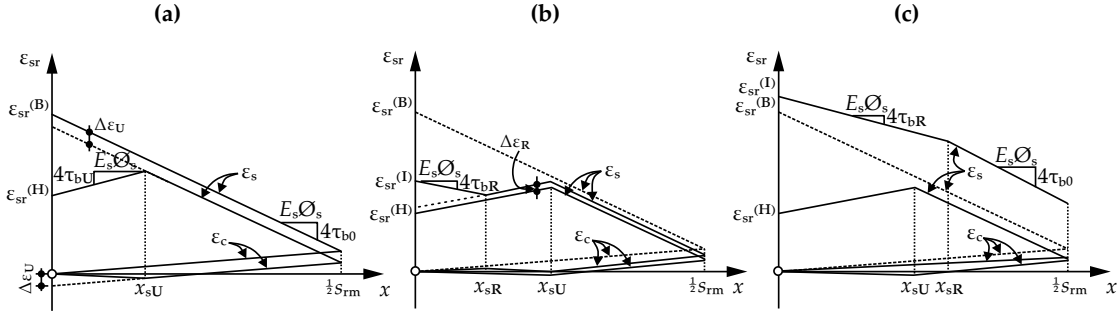

Figure 4.31: Strain distribution according to the modified Tension Chord Model of Koppitz et al. [103] in the cracked elastic range: (a) Reinforced tension chord under unloading from $\sigma_{sr}^{(B)}$ to $\sigma_{sr}^{(H)}$, (b) reloading from $\sigma_{sr}^{(H)}$ to $\sigma_{sr}^{(I)}$ with $\sigma_{sr}^{(I)} < \sigma_{sr}^{(B)}$, and (c) reloading from $\sigma_{sr}^{(H)}$ to $\sigma_{sr}^{(I)}$ with $\sigma_{sr}^{(I)} > \sigma_{sr}^{(B)}$

In the first loading process the relations given in Eq. 4.16 to 4.31 are valid. The load stress is $\sigma_{sr} = \sigma_{sr}^{(B)} > \sigma_{sr0}$ and the $\sigma_{sr} - \epsilon_{sm}$-curve follows the points OAB in Fig. 4.30b. The tension-stiffening-effect, defined as the distance to the $\sigma_s - \epsilon_s$-curve of the "naked" steel, is expressed by the tension-stiffening-number $\eta_{TS} = 2\lambda\Delta\epsilon_s$ [103], where $\Delta\epsilon_s$ is derived in Eq. 4.31 and $\lambda = 0.5...1.0$, depending on the crack spacing. In a second step the load stress is reduced to $\sigma_{sr} = \sigma_{sr}^{(H)} < \sigma_{sr}^{(B)}$ and both, ϵ_s and ϵ_c, decrease together all over the chord length by $\Delta\epsilon_U$ (Fig. 4.31). Beginning with $\epsilon_{sr}^{(H)}$ at the cracked cross section, the steel strain grows with the weakened slope resulting from $\tau_b = \tau_{bU}$ whereas compression stresses are induced in the surrounding concrete. The intersection point between unloading and loading curve is x_{sU}. Fig. 4.31 assumes in this case equal strains between steel and concrete

at $x = 1/2 s_{rm}$, i.e. $s_{rm} = s_{r,max}$. The concrete strain at $x = x_{sU}$ for the first-loading process amounts

$$\epsilon_c^{(B)}(x = x_{sU}) = \frac{4\tau_{b0}\rho_{s,ef}n}{(1-\rho_{s,ef})\varnothing_s E_s} x_{sU}, \tag{4.41}$$

and for the unloading process

$$\epsilon_c^{(H)}(x = x_{sU}) = \frac{-4\tau_{bU}\rho_{s,ef}n}{(1-\rho_{s,ef})\varnothing_s E_s} x_{sU}. \tag{4.42}$$

$\Delta\epsilon_U$ results from

$$\Delta\epsilon_U = \epsilon_c^{(B)}(x_{sU}) - \epsilon_c^{(H)}(x_{sU}) = \frac{4\rho_{s,ef}n}{(1-\rho_{s,ef})\varnothing_s E_s}(\tau_{b0} + \tau_{bU}) x_{sU}. \tag{4.43}$$

From the condition

$$\left(\epsilon_{sr}^{(B)} - \Delta\epsilon_U\right) - \frac{4\tau_{b0}}{\varnothing_s E_s} x_{sU} \equiv \epsilon_{sr}^{(H)} + \frac{4\tau_{bU}}{\varnothing_s E_s} x_{sU} \tag{4.44}$$

and taking Eq. 4.43 into account one obtains

$$x_{sU} = \frac{\varnothing_s}{4(\tau_{b0}+\tau_{bU})} \frac{1-\rho_{s,ef}}{1+\rho_{s,ef}(n-1)} E_s \left(\epsilon_{sr}^{(B)} - \epsilon_{sr}^{(H)}\right) = \frac{\varnothing_s}{4(\tau_{b0}+\tau_{bU})} \frac{1-\rho_{s,ef}}{1+\rho_{s,ef}(n-1)} \Delta\sigma_{sr}^{(BH)} \leq \frac{1}{2} s_{rm}. \tag{4.45}$$

η_δ quantifies the degree of slip reversal. As soon as $\eta_\delta = 1.0$, then $x_{sU} = 1/2 s_{rm}$. The distance $\Delta\epsilon_{\bar{B}H}$ is calculated from the difference of the average strains at the points (B) and (H) (Fig. 4.30b, 4.31a).

$$\epsilon_{sm}^{(B)} = \left(\epsilon_{sr}^{(B)} - \frac{\tau_{b0}}{\varnothing_s E_s} s_{rm}\right). \tag{4.46}$$

$$\epsilon_{sm}^{(H)} = \epsilon_{sr}^{(H)} + \frac{4(\tau_{b0}+\tau_{bU})}{\varnothing_s E_s} x_{sU}\left(1 - \frac{x_{sU}}{s_{rm}}\right) - \frac{\tau_{b0}}{\varnothing_s E_s} s_{rm}. \tag{4.47}$$

For the distance $\Delta\epsilon_{BH}$ one obtains

$$\Delta\epsilon_{BH} = \epsilon_{sm}^{(B)} - \epsilon_{sm}^{(H)} = \epsilon_{sr}^{(B)} - \epsilon_{sr}^{(H)} - \frac{4(\tau_{b0} + \tau_{bU})}{\varnothing_s E_s} x_{sU} \left(1 - \frac{x_{sU}}{s_{rm}}\right). \tag{4.48}$$

The sought distance $\Delta\epsilon_{\bar{B}H}$ results from

$$\Delta\epsilon_{\bar{B}H} = \Delta\epsilon_{\bar{B}B} - \Delta\epsilon_{BH} = \frac{4(\tau_{b0} + \tau_{bU})}{\varnothing_s E_s} x_{sU} \left(1 - \frac{x_{sU}}{s_{rm}}\right). \tag{4.49}$$

$\Delta\epsilon_{\bar{B}H}$ becomes maximal when $x_{sU} = 1/2 s_{rm}$. Using Eq. 4.40, 4.31, and setting $\Delta\epsilon_0 = 2\lambda\Delta\epsilon_s$ while $\tau_{b0} = 2 f_{ct}$, then

$$\Delta\epsilon_{\bar{B}H,max} = \left(1 + \frac{\tau_{bU}}{\tau_{bU}}\Delta\epsilon_0\right) = \left(1 + \frac{k_\tau}{2}\Delta\epsilon_0\right). \tag{4.50}$$

Finally the slip-reversal parameter $0 \le \eta_\delta \le 1.0$ corresponds to the relation

$$\eta_\delta = \frac{\Delta\epsilon_{\bar{B}H}}{\Delta\epsilon_{\bar{B}H,max}} = \ldots = 2\xi - \xi^2, \tag{4.51}$$

where ξ is introduced with the help of Eq. 4.38 and 4.39:

$$\xi = \frac{k_\sigma - k_U}{\lambda} \left(\frac{2}{2 + k_\tau}\right). \tag{4.52}$$

Eq. 4.52 is light different than the expression derived in [103].

The same characteristics are valid for the reloading process. Beginning with the cracked cross section, the bond strength is now $\tau_b = \tau_{bR}$ (cf. Fig. 4.31b). x_{sR} describes the place where there is a slip reversal between reloading and unloading. This is the case only if $x_{sR} < x_{sU}$, i.e. when $\sigma_{sr}^{(I)} < \sigma_{sr}^{(B)}$. The constant strain $\Delta\epsilon_R$ is similar to Eq. 4.43:

$$\Delta\epsilon_R = \frac{4\rho_{s,ef} n}{\varnothing_s(1 - \rho_{s,ef}) E_s} (\tau_{bU} + \tau_{bR}) x_{sR}. \tag{4.53}$$

Following condition leads to the determination of x_{sR}:

$$\left(\epsilon_{sr}^{(H)} + \Delta\epsilon_R\right) + \frac{4\tau_{bU}}{\varnothing_s E_s} \equiv \epsilon_{sr}^{(I)} - \frac{4\tau_{bR}}{\varnothing_s E_s} x_{sR} \tag{4.54}$$

$$x_{sR} = \frac{\varnothing_s}{4(\tau_{bU} + \tau_{bR})} \frac{1 - \rho_{s,ef}}{1 + \rho_{s,ef}(n-1)} E_s \left(\epsilon_{sr}^{(I)} - \epsilon_{sr}^{(H)} \right) \leq x_{sU}. \tag{4.55}$$

For cases where $\sigma_{sr}^{(I)} > \sigma_{sr}^{(H)}$, then x_{sU} is eliminated (cf. Fig. 4.31c). Consequently, the calculation of ϵ_{sm} and w_{cr} needs to differentiate whether $x_{sR} < x_{sU}$ or not. Anyway, the resulting mathematical expressions for ϵ_{sm} and w_{cr} are extensive and will not be presented in this work. By doing it however, the distance $\Delta\epsilon_{BI}$ (cf. Fig. 4.30b) may be determined and so the tension-stiffening-number η_{TS}:

$$0 \leq \eta_{TS} = 1 - \frac{\Delta\epsilon_{BI}}{\Delta\epsilon_0} \leq 1.0. \tag{4.56}$$

$\eta_{TS} = 1.0$ means no bond reduction due to an unloading and reloading process whereas $\eta_{TS} = 0$ points to a fully destruction of the bond properties so that no tension-stiffening acts and the tension chord behaves as if there were no surrounding concrete. In Fig. 4.31c it becomes visible that the chord elongation increases as a result of an unloading and reloading process. The modification of the Tension Chord Model of Koppitz et al. [103] is more accurate and will be used for describing the behaviour of a reinforced concrete chord under fatigue loading (Ch. 4.2.4).

For cases where the reinforced concrete chord is also prestressed or post-tensioned, Fürst [57] describes the loading, unloading, and reloading properties under fatigue, yet without quantifying the degree of bond degradation. Nonetheless, Fürst [57] demonstrates that a possible bond degradation of the reinforcement causes higher stress ranges in the prestressing steel. Therefore, a reliable fatigue design calculation for the reinforcement assumes intact bond properties whereas for the prestressing steel a complete bond destruction of the reinforcement leads to a more unfavourable fatigue design.

Note that, with the exception of the model of Zanuy [204], the calculation models for the tension-stiffening effect assume a constant value of the effective concrete area $A_{s,ef}$.

4.2.3 Effective Concrete Area $A_{c,ef}$

One parameter, which decisively influences the tension-stiffening, is the effective reinforcement ratio $\rho_{s,ef}$. A simplification of the force transfer in reinforced concrete members by means of tension and compression chords implies an effective concrete area $A_{c,ef}$ which actively takes part in the force transfer, and thus, in the deformation of structural members.

Actually, the calculation of $A_{c,ef}$ is carried out empirically based on geometrical considerations. An overview of numerous models may be found in [49]. Wasner [198] indicates that $A_{c,ef}$ depends on the applied load level. Under the action of fatigue loading the concrete around the reinforcement is subjected to alternating tension and compression stresses (Ch. 3.3) due to unloading and reloading processes. Since stiffness and strain of concrete are highly affected by fatigue loading (Ch. 3.2.4), it may be expected that $A_{c,ef}$ experiences some sort of changes. The only known author who tries to consider aspects of the concrete fatigue behaviour in the calculation of $A_{c,ef}$ is Zanuy [204]. In his model

he assumes a mechanical degradation of $A_{c,ef}$ equivalent to the ratio of Wöhler-curves of concrete under uniaxial tension-tension to uniaxial tension-compression stresses.

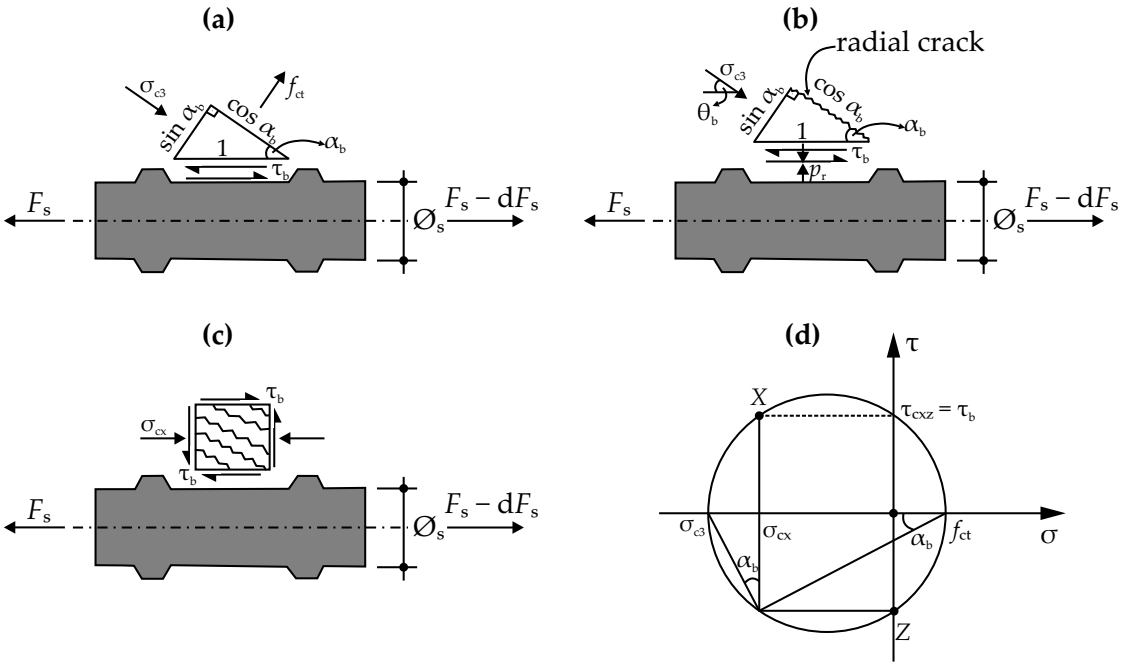

Figure 4.32: Equilibrium of forces around reinforcement bar: (a) Before radial cracking, (b) After radial cracking, (c) Stress state, and (d) Mohr-circle

The mechanism of force transfer between reinforcement and surrounding concrete may be considered as the principal factor that determines the size of $A_{c,ef}$ (cf. [162], [49]). Especially the angle α_b between reinforcement and principal compression stress is relevant. Similar to considerations of Will [200], equilibrium of forces in vertical and horizontal direction, before radial cracking (Fig. 4.32) occurs, leads to

$$\sigma_{c3} = \frac{f_{ct}^2}{\tan^2 \alpha_b}, \tag{4.57}$$

$$\sigma_{c3} = \frac{\tau_b}{\cos \alpha_b \sin \alpha_b} - f_{ct}. \tag{4.58}$$

The combination of Eq. 4.57 and 4.58 provides for α_b the expression

$$\tan \alpha_b = \frac{f_{ct}}{\tau_b}. \tag{4.59}$$

The same equation may be derived by means of a Mohr-stress-circle and the condition $\sigma_{c3} + f_{ct} = \sigma_{cx} + \sigma_{cz}$ with $\sigma_{cz} = 0$ (cf. Fig. 4.32d). In case that $\tau_b = \tau_{b0} = 2f_{ct}$, then $\alpha_b = 26.6°$,

whereas $\alpha_b = 45°$ if $\tau_b = f_{ct}$. Yet, higher loads may produce radial cracking. At this point the angle α_b changes its value and becomes steeper. By assuming that $\theta_c \approx \alpha_b$ (Fig. 4.32b) and that no shear force transfer is expected at the radial crack – a thinkable assumption at the ultimate state with large slip values δ_s –, the radial compression p_r depends only on the bond stress τ_b.

$$p_r = -\tau_b \tag{4.60}$$

Ritter [156] summarises the data of several authors concerning the value of the bond angle α_b and concludes that $\alpha_b = 27°...45°$. However, carefully performed strain measurements by Ritter reveal higher values of α_b in the ultimate state. On the basis of own test results she finds out that α_b remains practically constant when $\delta_s > \delta_{s,max}$, where $\delta_{s,max}$ corresponds to the slip value under $\tau_b = \tau_{b,max}$ (cf. Fig. 4.33). She suggests for α_b:

$$\alpha_b = \alpha_{b,max} \left(\frac{\delta_s}{\delta_{s,max}} \right)^{b_\tau}, \tag{4.61}$$

where b_τ depends on the concrete strength f_c and the bar diameter.

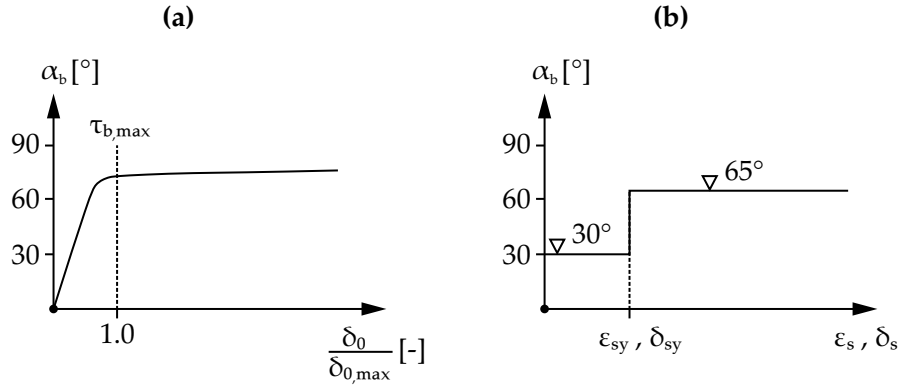

Figure 4.33: (a) Bond angle α_b according to Ritter [156], (b) Simplification

Schenkel [162] uses the geometric model of Schober [168] in order to describe the effective tension ring around the reinforcement bar which is assumed to be activated by circumferential stresses $\sigma_{b\Phi}$ (cf. 3.3.1). It appears also acceptable to assume in this work, considering the strut and tie model of the transfer of bond stresses into concrete according to Fig. 3.38, that $A_{c,ef}$ largely coincides with the geometry of the tension ring of $\sigma_{b\Phi}$. The outer radius r_o of the tension ring (cf. Fig. 3.36 and Fig. 4.34) is normally limited by the concrete cover c_{nom} whereas the inner radius r_i depends on the bar geometry as well as on the conical shell expansion ϕ_b of bond forces.

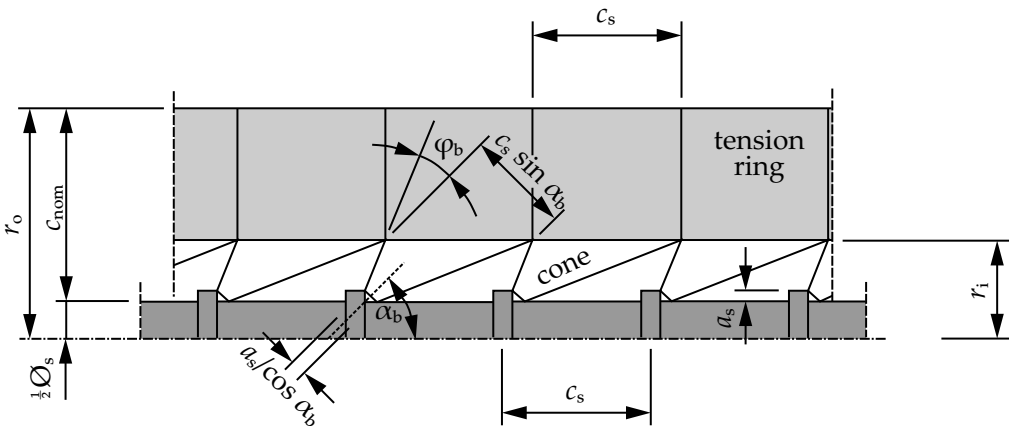

Figure 4.34: Tension ring around reinforcement bar, adapted from [162]

$$r_o = c_{nom} + \frac{1}{2}Ø_s. \tag{4.62}$$

$$r_i = \frac{\tan(\alpha_b - \phi_b)\left[\tan(\alpha_b + \phi_b)\left(c_s - a_s \tan(\alpha_b)\right) - a_s\right]}{\tan(\alpha_b + \phi_b) - \tan(\alpha_b - \phi_b)} + \frac{1}{2}Ø_s. \tag{4.63}$$

For the definition of c_s and a_s see Fig. 4.34. Schenkel assumes $\phi_b = 27°$ and the (simplified) effective concrete area $A_{c,ef}$ is turned into a function of bar geometry, concrete cover c_{nom} and bond angle α_b. In this way,

$$A_{c,ef} = \pi\left(r_o^2 - r_i^2\right). \tag{4.64}$$

As a consequence of fatigue loading, the slip δ_s tends to increase (cf. Ch. 3.3.2), leading to a steeper bond angle α_b according to Fig. 4.33. Thus, the inner radius r_i of the tension ring experiences a certain growth and $A_{c,ef}$ a progressive reduction according to Eq. 4.64, confirming the assumption made by Zanuy in [204]. This qualitative conclusion bases on a simple model which does not account for further effects like a concrete weakening due to fatigue, structural members with practically huge concrete cover c_{nom}, secondary cracks, and other effects. Further research on a quantification of $A_{c,ef}$ based on constitutive mechanical models is necessary, especially regarding the behaviour of $A_{c,ef}$ under fatigue loading. For this reason, in the present thesis $A_{c,ef}$ will be considered to remain constant and to obey the equations given in the Model Code 2010 [51].

4.2.4 Fatigue Tension Chord Model

In order to describe and quantify realistically the mechanical behaviour of concrete chords it becomes necessary to take into account the effects of fatigue loading in the serviceability

state. Principally, the progressive bond degradation leads to larger deformations under service loads. Yet, at the same time, the value of remaining deformations after unloading processes decreases since the restraint effect of the bond becomes weaker. The effective modulus of elasticity E_{sm} progressively decreases until the tension chord mechanically behaves like the "naked" reinforcement. At this point the bond is fully destroyed and the surrounding concrete highly damaged. A minimum remaining bond stress in form of friction bond stresses could not be confirmed in the performed tests since some specimens showed a practically complete bond destruction. The reduction of E_{sm} with increasing number of load cycles is notable and may be described mathematically.

The three used load sequential arrangements in this work are considered to be representative for the totality of loads experienced in the life time of a structural element (cf. Ch. 4.2.1). Hence, it seems reasonable to average the development of E_{sm} over the sequential load arrangements Pe, Pm, and Pb. A further parameter that was firstly assumed to play an important role in slab structures are cracks of a certain width along the reinforcing bars. A prominent influence of induced longitudinal cracks, as in [109] described, could not be distinguished, though. The variation scatter is high and a wide number of additional tests seems to be necessary.

A further modification of the Tension Chord Model is proposed in this chapter in order to account for the fatigue effects observed in [4] and briefly described in Ch. 4.2.1. Hereby yet, the effective concrete area $A_{c,ef}$ is assumed to be constant. Accordingly, the development of the average steel strain ϵ_{sm} is divided into two parts:

$$\epsilon_{sm} = \epsilon_{sm,\tau} + \epsilon_{sm,pl}. \tag{4.65}$$

The first term $\epsilon_{sm,\tau}$ corresponds to the cracked elastic behaviour of a tension concrete chord. Here, the bond development determines the stiffness E_{sm} of a tension chord and the achieved elongations do not exceed those of the "naked" reinforcement. The second term $\epsilon_{sm,pl}$ is introduced in order to quantify the observed plastic-strain-accumulation (cf. Ch. 4.2.1) which is assumed to occur independently of $\epsilon_{sm,\tau}$.

Following simple linear equations are suggested for a bond degradation of unloading and reloading processes depending on the relative load cycle number n/N of the averaged representative load sequential arrangements:

$$\tau_{bU}\left(\frac{n}{N}\right) = \tau_{bU1}\left[1 - \left(1 - \frac{\tau_{bU,rsd}}{\tau_{bU1}}\right)\frac{n}{N}\right], \tag{4.66}$$

$$\tau_{bR}\left(\frac{n}{N}\right) = \tau_{bR1}\left[1 - \left(1 - \frac{\tau_{bR,rsd}}{\tau_{bR1}}\right)\frac{n}{N}\right]. \tag{4.67}$$

The values of τ_{bU1} and τ_{bR1} represent the bond strength for unloading resp. reloading after a first load cycle and correspond to the relations described in [103]. They are determined unique on the basis of values of the displacement transducer DT6 according

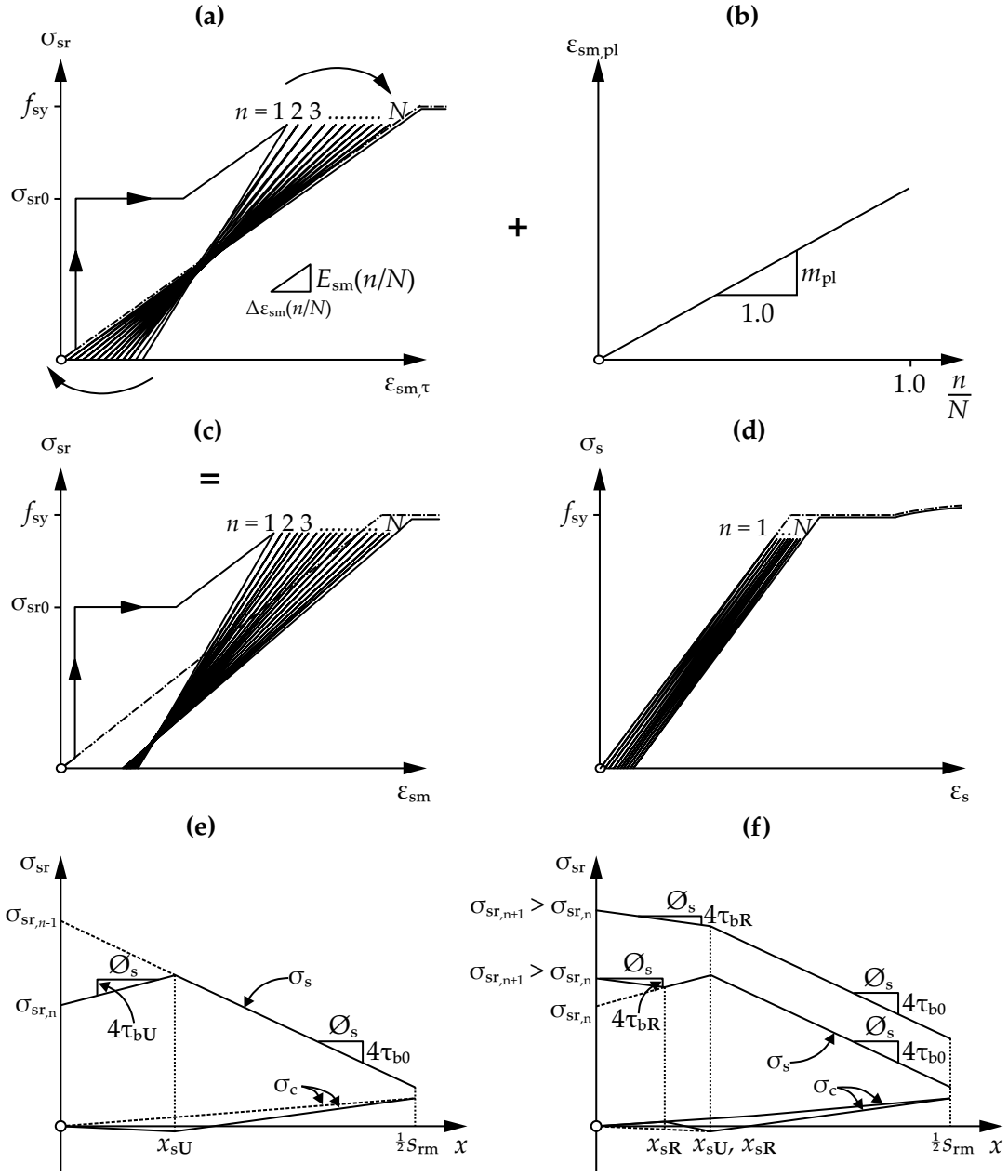

Figure 4.35: Modification of Tension Chord Model for fatigue loading: (a) Influence of bond degradation for $\epsilon_{sm,\tau}$, (b) Plastic-strain-accumulation $\epsilon_{sm,pl}$, (c) Combination of bond degradation and plastic-strain-accumulation $\epsilon_{sm} = \epsilon_{sm,\tau} + \epsilon_{sm,pl}$, (d) Supposed fatigue behaviour of the reinforcement (does not always occur) (e) Unloading after first load cycle, (f) First reloading process for the cases $x_{sR} < x_{sU}$ and $x_{sR} \geq x_{sU}$

to Fig. 4.9 since displacement transducers are more reliable than strain gauges. The static

value τ_{b0} of bond for the first loading results from reshaping Eq. 4.32:

$$\tau_{b0} = \frac{\sigma_{sr} \varnothing_s}{s_{rm}} - \frac{\epsilon_{sm} \varnothing_s E_s}{s_{rm}}. \tag{4.68}$$

σ_{sr} is given by the load sequential program while the distance between induced cracks $s_{rm} \approx 250$ mm is provided by notches in the test specimen. ϵ_{sm} is calculated as the average strain from values of the displacement transducer DT6 (cf. Fig. 4.9) following the relation $\epsilon_{sm} = \Delta l_{DT6}/L_{DT6}$, where Δl_{DT6} involves the recorded values of DT6 and L_{DT6} represents the initial length of DT6. τ_{b0}, however, is to be understood as average value since the distance of $\sigma_{sr} - \epsilon_{sm}$-curve from the "naked" steel after completed crack formation is not always constant.

τ_{bU1} describes the bond strength in the first unloading process. Similar to τ_{b0}, τ_{bU1} is calculated using values of the displacement transducer DT6. In a first step, a preferably low value of τ_{bU1} is estimated and subsequently the point of slip reversal x_{sU} is calculated according to the equation

$$x_{sU} = \frac{\varnothing_s}{4} \frac{\sigma_{sr1} - \sigma_{sr2}}{\tau_{b0} + \tau_{bU1}}. \tag{4.69}$$

σ_{sr1} and $\sigma_{sr2} = 0$ describe the stress values of the cracked cross section at the first loading and subsequent unloading stage respectively. Once x_{sU} is known, then the linear strain distribution according to the Tension Chord Model as well as the average strain ϵ_{sm} may be determined (cf. Fig. 4.35e). If the difference between calculated average strain $\epsilon_{sm,cal}$ and measured average strain $\epsilon_{sm,mess}$ is higher than a given tolerance, e.g. $|\epsilon_{sm,cal} - \epsilon_{sm,mess}| < 0.05‰$, the assumed value of τ_{bU1} is increased until the tolerance condition is fulfilled. For this purpose, an evaluation algorithm was implemented in python™ (see Appendix C).

τ_{bR1} follows the same muster. With the final value of τ_{bU1} the calculation of the initial bond strength τ_{bR1} for reloading is also iterative. Based on a stress value $\sigma_{sr3} > \sigma_{sr2}$ at a reloading stage, a new slip reversal point x_{sR} – this time for reloading processes – is to be calculated.

$$x_{sR} = \frac{\varnothing_s}{4} \frac{\sigma_{sr3} - \sigma_{sr2}}{\tau_{bU1} + \tau_{bR1}}. \tag{4.70}$$

τ_{bR1} is first to be estimated too. A better convergence of the iteration is achieved if a preferably high value is estimated, e.g. $\tau_{bR1} = 50.0$ MPa, on the basis of which the slip reversal point x_{sR} may be calculated following Eq. 4.70. The average strain ϵ_{sm} may be then calculated integrating the strain distribution of reinforcement and by a subsequent division of the result by s_{rm}. The cases $x_{sR} \leq x_{sU}$ and $x_{sR} > x_{sU}$ are to be distinguished in the iteration algorithm. For the case $x_{sR} > x_{sU}$, then $x_{sR} = x_{sU}$ is to be set. Another important boundary condition is $x_{sR} = 0.5 s_{rm}$ and $x_{sU} = 0.5 s_{rm}$ in case that $x_{sR} > 0.5 s_{rm}$

and $x_{sU} > 0.5 s_{rm}$ respectively. Finally, if $\epsilon_{sm,cal}$ and $\epsilon_{sm,mess}$ diverge considerably, a new value of τ_{bR1} is to be chosen and ϵ_{sm} is to be determined again until the desired tolerance $|\epsilon_{sm,cal} - \epsilon_{sm,mess}|$ is obtained.

$\tau_{bU,rsd}$ resp. $\tau_{bR,rsd}$ quantify a possible residual bond strength in case that no fully bond degradation is achieved. Fehlmann [48] and Spathelf [184] assume in this case e.g. a logarithmic decrement of the bond. They assume that the bond τ_b is fully destroyed after 10^6 load cycles.

Analogue to [103], the actual points of slip reversal for every load cycle for unloading x_{sU} and for reloading x_{sR} are determined by calculating the intersection point with the strain distribution of the load cycle before (cf. Fig. 4.35). An important difference compared to [103] is the neglect of the strain leap $\Delta\epsilon_U$ and $\Delta\epsilon_R$. This step simplifies the calculation algorithm and agrees better with the test results (Ch. 4.2.1).

The quantification of $\tau_{bU,rsd}$ and $\tau_{bR,rsd}$ is performed by means of the development of E_{sm} whereupon the value of E_{sm} is determined for every new loading peak n according to

$$E_{sm}(n) = \frac{\sigma_{sr,n} - \sigma_{sr,n+1}}{\epsilon_{sm,n} - \epsilon_{sm,n+1}}. \tag{4.71}$$

It has to be underlined that E_{sm} represents the slope of the $\sigma_{sr} - \epsilon_{sm}$-curve between every unloading point and the following reloading point and not between the zero point and every reloading point. E_{sm} may be considered as an average modulus of elasticity of the tested reinforced concrete element which depends on the tension-stiffening effect of the surrounding concrete and, hence, on the bond between reinforcement and concrete.

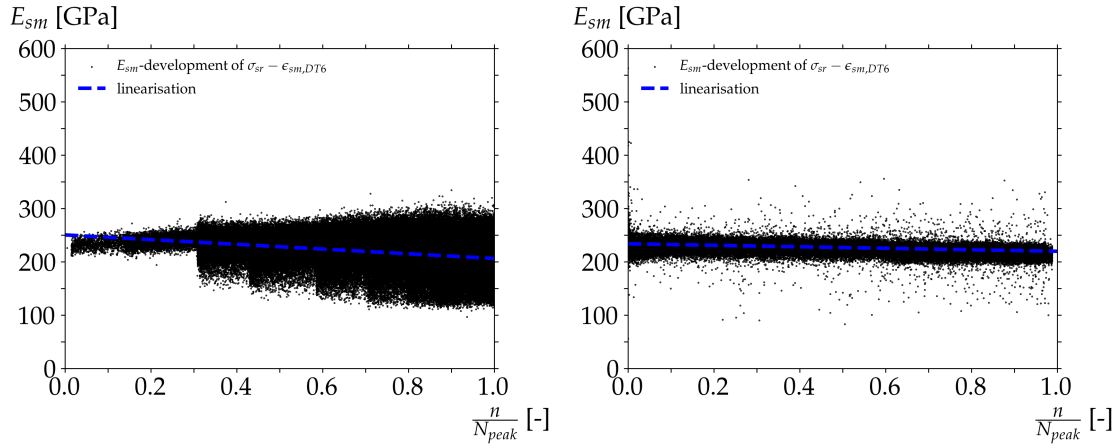

Figure 4.36: Linear regression of E_{sm} for (a) Test specimen Dy1-Pe-w0 and (b) Test specimen Dy6-Pb-w0

The development of E_{sm} of exemplary tests is presented in the Fig. 4.36 and 4.37. As soon as $E_{sm} \approx E_s$, then the bond τ_b all over the length may be considered as destroyed. The results base mostly on ϵ_{sm}-values calculated using data of the displacement transducer DT6 (cf. Fig. 4.9) since displacement transducers are more reliable than strain gauges.

Nevertheless, for some test specimens, E_{sm} had to be obtained from the average strain ϵ_{sm} of all strain gauges due to inconsistent values of the displacement transducer DT6. All values are listed on Tab. 4.5. A clear trend may be observed and a simple, linear curve fitting may be quickly found using the least square regression. A higher order regression is not meaningful due to the observed high variance. Similar to Koppitz et al. [103], τ_{bR} may be assumed to obey the same development as τ_{bU}. The linear approach follows the form

$$E_{sm}\left(\frac{n}{N}\right) = E_{sm0} + m_{sm}\frac{n}{N}. \tag{4.72}$$

With

$$\tau_{bU,rsd} = \kappa_{rsd}\tau_{bU1}, \tag{4.73}$$

$$\tau_{bR,rsd} = \kappa_{rsd}\tau_{bR1}, \tag{4.74}$$

the residual-bond parameter κ_{rsd} results from

$$\kappa_{rsd} = \frac{E_{sm,n=N} - E_s}{E_{sm,n=1} - E_s}. \tag{4.75}$$

$m_{sm} = 0.0$ means either practically no bond degradation; a value $m_{sm} > 0$ is physically

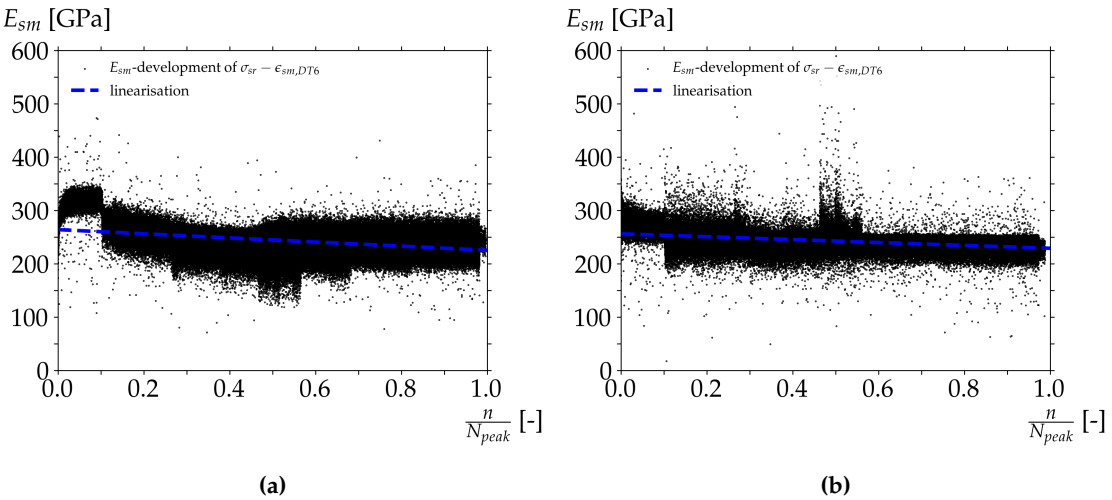

Figure 4.37: Linear regression of E_{sm} for (a) Test specimen Dy10-Pm-w0.2 and (b) Test specimen Dy14-Pm-w0.3

Table 4.5: Values of curve fitting of the bond development

Test specimen	E_{sm0} [GPa]	m_{sm} [GPa]	$E_{sm}(n = N)$ [GPa]	τ_{b0} [MPa]	τ_{bU1} [MPa]	τ_{bR1} [-]	κ_{rsd} [-]
St1-w0	-	-	-	$1.15 f_{ct}$	-	-	-
St2-w0.2	-	-	-	$0.72 f_{ct}$	$1.17 f_{ct}$	$0.66 f_{ct}$	-
St3-w0.3	-	-	-	$0.79 f_{ct}$	$1.19 f_{ct}$	$1.52 f_{ct}$	-
St4-w0.2	-	-	-	$2.61 f_{ct}$	$1.80 f_{ct}$	$2.07 f_{ct}$	-
St5-w0.3	-	-	-	-	-	-	-
Dy1-Pe-w0	250.00	-44.21	205.79	$0.38 f_{ct}$	$1.25 f_{ct}$	$0.67 f_{ct}$	0.10
Dy2-Pe-w0	217.67	-8.80	208.87	$1.73 f_{ct}$	$1.89 f_{ct}$	$0.50 f_{ct}$	0.47
Dy3-Pm-w0	227.94	-4.29	223.64	$2.28 f_{ct}$	$0.72 f_{ct}$	$1.90 f_{ct}$	0.84
Dy4-Pm-w0	$215.96^{(*)}$	$-13.21^{(*)}$	$202.75^{(*)}$	$0.95 f_{ct}$	$1.51 f_{ct}$	$0.27 f_{ct}$	0.12
Dy5-Pb-w0	238.85	-7.01	231.84	$0.60 f_{ct}$	$1.94 f_{ct}$	$0.63 f_{ct}$	0.81
Dy6-Pb-w0	233.34	-13.99	219.35	$2.50 f_{ct}$	$3.02 f_{ct}$	$2.42 f_{ct}$	0.57
Dy7-Pb-w0.2	$211.32^{(*)}$	$-0.74^{(*)}$	$210.58^{(*)}$	$0.74 f_{ct}$	$1.44 f_{ct}$	$0.64 f_{ct}$	0.93
Dy8-Pb-w0.2	$284.84^{(*)}$	$-36.92^{(*)}$	$247.92^{(*)}$	$1.15 f_{ct}$	$1.03 f_{ct}$	$1.79 f_{ct}$	0.56
Dy9-Pm-w0.2	$200.39^{(**)}$	$-2.93^{(**)}$	$197.45^{(**)}$	$1.20 f_{ct}$	$1.36 f_{ct}$	$1.28 f_{ct}$	0.00
Dy10-Pm-w0.2	263.65	-38.65	225.00	$0.69 f_{ct}$	$1.47 f_{ct}$	$0.58 f_{ct}$	0.38
Dy11-Pe-w0.2	$214.72^{(*)}$	$-5.84^{(*)}$	$208.88^{(*)}$	$1.28 f_{ct}$	$1.00 f_{ct}$	$2.24 f_{ct}$	0.57
Dy12-Pe-w0.2	427.31	-84.12	343.19	$0.77 f_{ct}$	$1.39 f_{ct}$	$1.18 f_{ct}$	0.63
Dy13-Pe-w0.3	207.06	0.00	207.06	$1.09 f_{ct}$	$1.51 f_{ct}$	$0.81 f_{ct}$	1.00
Dy14-Pm-w0.3	255.85	-27.14	228.70	$2.42 f_{ct}$	$1.94 f_{ct}$	$2.48 f_{ct}$	0.51
Dy15-Pb-w0.3	$203.94^{(*)}$	$-2.36^{(*)}$	$201.58^{(*)}$	$0.82 f_{ct}$	$1.65 f_{ct}$	$0.61 f_{ct}$	0.20
Gewi-Pb-w0	$201.67^{(**)}$	$-12.75^{(**)}$	$188.91^{(**)}$	$1.12 f_{ct}$	$1.54 f_{ct}$	$0.52 f_{ct}$	0.00

$^{(*)}$ Values base on strain gauges data
$^{(**)}$ Average values lower than E_s

inconsistent. Similarly, if the residual-bond parameter κ_{rsd} = 1.00, then there is practically no bond degradation while κ_{rsd} = 0.00 corresponds to a fully bond degradation. Values κ_{rsd} < 0.00 are physically no possible. Average values of κ_{rsd} for test specimens with no longitudinal crack (w = 0.0 mm – specimens Dy1, Dy2, Dy3, Dy4, Dy5, Dy6) are κ_{rsd} = 0.48. For the specimens Dy7, Dy8, Dy9, Dy10, Dy11, Dy12 with a longitudinal crack w = 0.2 mm the average value amounts κ_{rsd} = 0.51. Finally, κ_{rsd} = 0.57 for Dy13, Dy14, and Dy15 with w = 0.3 mm. The differences are therefore negligible and a clear influence of the implemented cracks along the reinforcement is no recognizable. For practical purposes,

an universal value of κ_{rsd} may be proposed as long as the load cycle number is no higher than 10^6:

$$\kappa_{rsd} = 0.50. \tag{4.76}$$

Likewise, following average values of the bond strength for the first loading action τ_{b0}, subsequent unloading τ_{bU1}, and reloading τ_{bR1} may be representative:

$$\tau_{b0} = 1.30 f_{ct} \qquad \tau_{bU1} = 1.50 f_{ct} \qquad \tau_{bR1} = 1.20 f_{ct}. \tag{4.77}$$

In contrast to [103], the found values of τ_{bU1} are higher than τ_{b0}. Also τ_{bR1} does not decrease in the rate reported in [103].

With the conditions

$$\sigma_{sr,n-1} - \frac{4}{\varnothing_s}\tau_{bR,n-1} x_{sU,n} \equiv \sigma_{sr,n} + \frac{4}{\varnothing_s}\tau_{bU,n} x_{sU,n}, \tag{4.78}$$

$$\sigma_{sr,n} + \frac{4}{\varnothing_s}\tau_{bU,n} x_{sR,n+1} \equiv \sigma_{sr,n+1} - \frac{4}{\varnothing_s}\tau_{bR,n+1} x_{sR,n+1}. \tag{4.79}$$

x_{sU} and x_{sR} may be estimated for every load cycle. At this point it is important to mention that several slip reversal points may be present at once depending e.g. whether $x_{sU,n-2} < x_{sU,n}$ and $x_{sR,n-1} < x_{sR,n}$ or not. Such a differentiation has to be accounted for in numerical calculations. An implemented algorithm is given in Appendix C.

For $\epsilon_{sr,n-1} > \epsilon_{sr,n}$:

$$x_{sU,n} = \frac{\varnothing_s E_s}{4} \frac{\epsilon_{sr,n-1} - \epsilon_{sr,n}}{\tau_{bR,n-1} + \tau_{bU,n}}. \tag{4.80}$$

For $\epsilon_{sr,n+1} > \epsilon_{sr,n}$:

$$x_{sR,n+1} = \frac{\varnothing_s E_s}{4} \frac{\epsilon_{sr,n+1} - \epsilon_{sr,n}}{\tau_{bR,n+1} + \tau_{bU,n}}. \tag{4.81}$$

The plastic-strain-accumulation $\epsilon_{sm,pl}$ exhibits an increment with every load cycle n. The load history shows here a pronounced influence, especially the load cycles with high amplitudes cause a non-linear "strain jump". With the use of a numerical filter programmed, e.g. in python™, it is possible to plot the development of ϵ_{sm} with every load cycle n and for any specified load stress σ_{sr}. Again, it is possible to use the least square regression and thus to estimate a linear fitting (cf. Fig. 4.38, 4.39, 4.40). As described before, in some test specimens there is a certain discrepancy between ϵ_{sm}-values calculated on the basis of strain gauges and those on displacement transducers. Strain gauges generally

deliver higher values of $\epsilon_{sm,pl}$ which may be caused by a possible deformation increase of the glue interface between strain gauge and reinforcement. For this cause, the evaluation of the plastic-strain-accumulation is performed taking only the values of ϵ_{sm} into account, that are derived from the displacement transducer DT6.

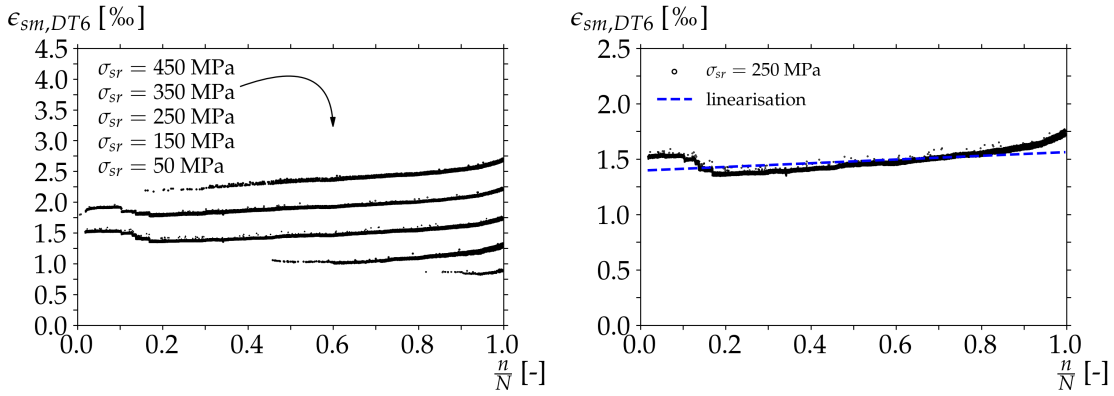

Figure 4.38: Measured plastic-strain-accumulation $\epsilon_{sm,pl}$ for different load stresses (a) Overview of Dy2-Pe-w0 and (b) Linear regression

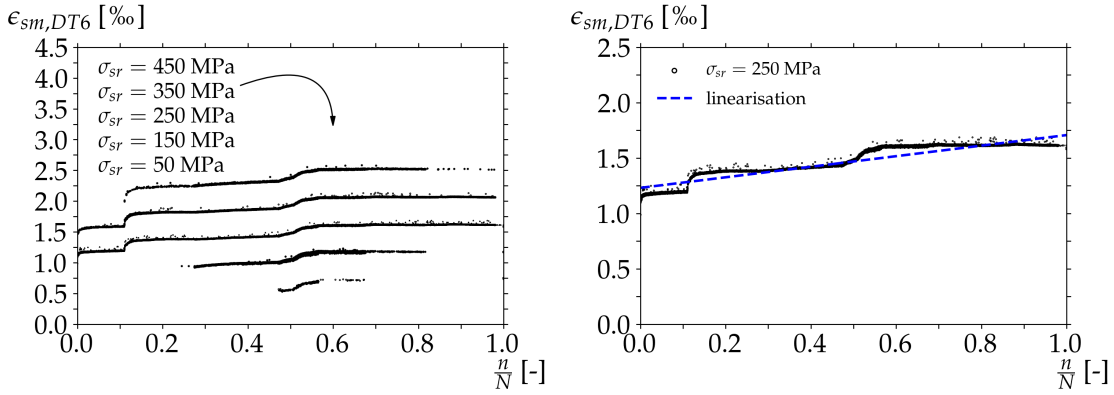

Figure 4.39: Measured plastic-strain-accumulation $\epsilon_{sm,pl}$ for different load stresses (a) Overview of Dy3-Pm-w0 and (b) Linear regression

It is important to put on record that the plastic-strain-accumulation does not seem to result in higher stresses, at least in the macroscopic scale (cf. Ch. 4.2.1). For cases where a plastic-strain-accumulation has been measured with both, strain gauges and displacement transducers, Eq. 4.82 is suggested for the estimation of $\epsilon_{sm,pl}$.

$$\epsilon_{sm,pl} = m_{pl} \frac{n}{N}. \tag{4.82}$$

m_{pl} describes the intensity of the plastic-strain increment with every load cycle. The

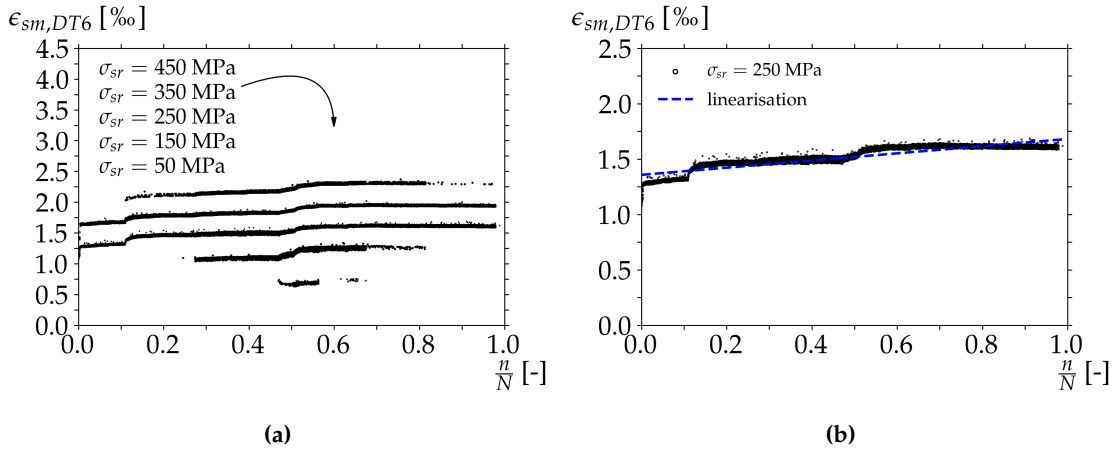

Figure 4.40: Measured plastic-strain-accumulation $\epsilon_{sm,pl}$ for different load stresses (a) Overview of Dy9-Pm-w0.2 and (b) Linear regression

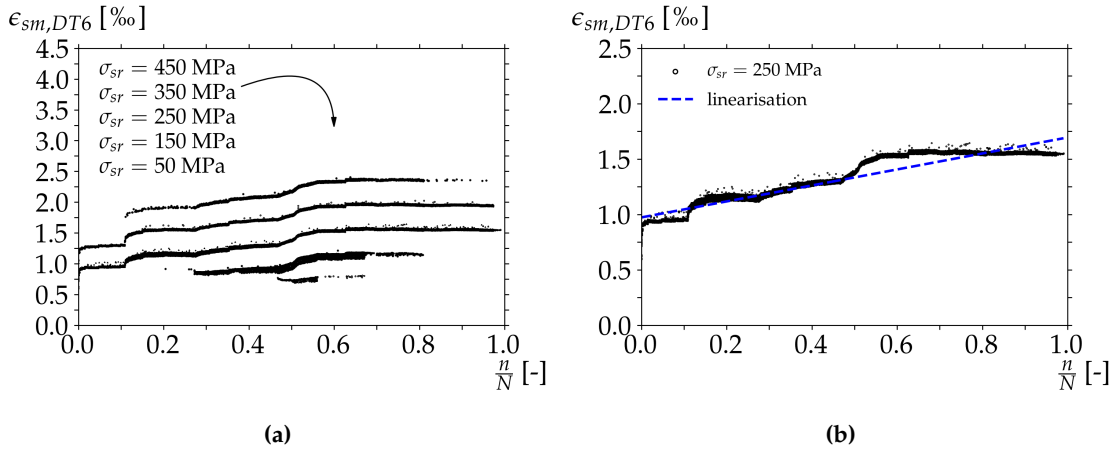

Figure 4.41: Measured plastic-strain-accumulation $\epsilon_{sm,pl}$ for different load stresses (a) Overview of Dy14-Pm-w0.3 and (b) Linear regression

value of m_{pl} proves to be constant, independently which load stress is plotted (cf. Fig. 4.38, 4.39, 4.40). The presence of a crack along the principal reinforcement does not seem to have a visible influence on $\epsilon_{sm,pl}$.

The average value of m_{pl} (without the Gewi-specimen and those test specimens with practically no recorded plastic-strain-accumulation) may be rounded to following value (in [‰/cycle]):

$$m_{pl} = 0.0003. \tag{4.83}$$

The generated load sequences Pe, Pm, and Pm have been recalculated in this work using the Fatigue Tension Chord Model. For the three mentioned load sequences, on the one

Table 4.6: Values of intensity-factor of plastic-strain-accumulation according to a linear regression. The values are based on results of the strain gauges and may not always coincide with the gained data from the displacement transducers.

Test specimen	m_{pl} [‰/cycle]	Comment	Test specimen	m_{pl} [‰/cycle]	Comment
Dy1-Pe-w0	0.00000	no p.s.a.$^{(*)}$	Dy9-Pm-w0.2	0.00032	
Dy2-Pe-w0	0.00017		Dy10-Pm-w0.2	0.00058	
Dy3-Pm-w0	0.00048		Dy11-Pe-w0.2	0.00012	
Dy4-Pm-w0	0.00017		Dy12-Pe-w0.2	0.00026	
Dy5-Pb-w0	0.00001	no p.s.a.$^{(*)}$	Dy13-Pe-w0.3	0.00001	no p.s.a.$^{(*)}$
Dy6-Pb-w0	0.00005		Dy14-Pm-w0.3	0.00072	
Dy7-Pb-w0.2	0.00000	no p.s.a.$^{(*)}$	Dy15-Pb-w0.2	0.00003	
Dy8-Pb-w0.2	0.00000	no p.s.a.$^{(*)}$	Gewi-Pb-w0	0.00001	no p.s.a.$^{(*)}$

$^{(*)}$ p.s.a. = plastic-strain-accumulation

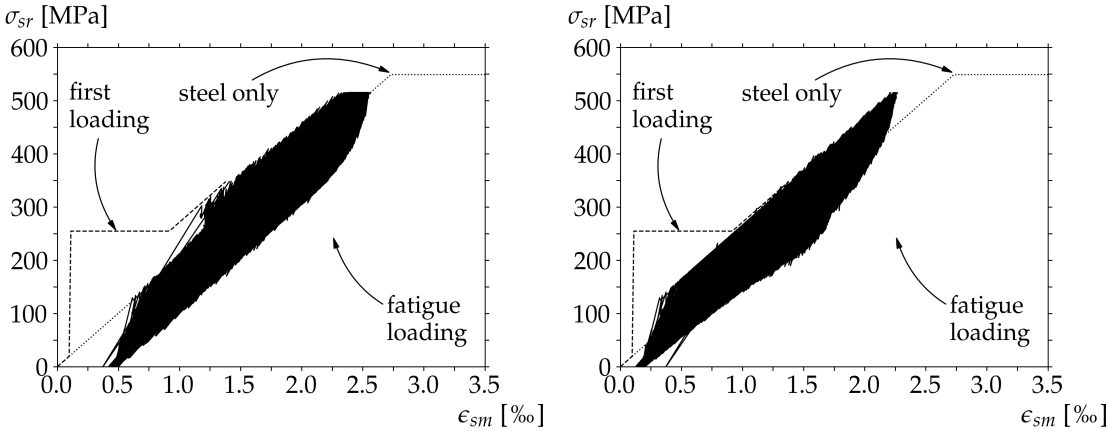

Figure 4.42: Recalculation of load sequences with Fatigue Tension Chord Model: (a) Load sequence Pe with plastic-strain-accumulation, (b) Load sequence Pe without plastic-strain-accumulation

hand, the plastic-strain-accumulation was accounted for; on the other hand, the three load sequences have also been recalculated without considering the plastic-strain-accumulation. Hereby, the proposed average values of τ_{b0}, τ_{bU1}, τ_{bR1}, κ_{rsd}, and m_{pl} (cf. Eq. 4.77, Eq. 4.82, Eq.4.83) were used. Restraint stresses due to shrinkage effects according to Model Code 2010 [51] have been taken into account in he first-crack-phase. The implemented code in python™ is reproduced in Appendix C, the corresponding program flow chart is on following Fig. 4.45.

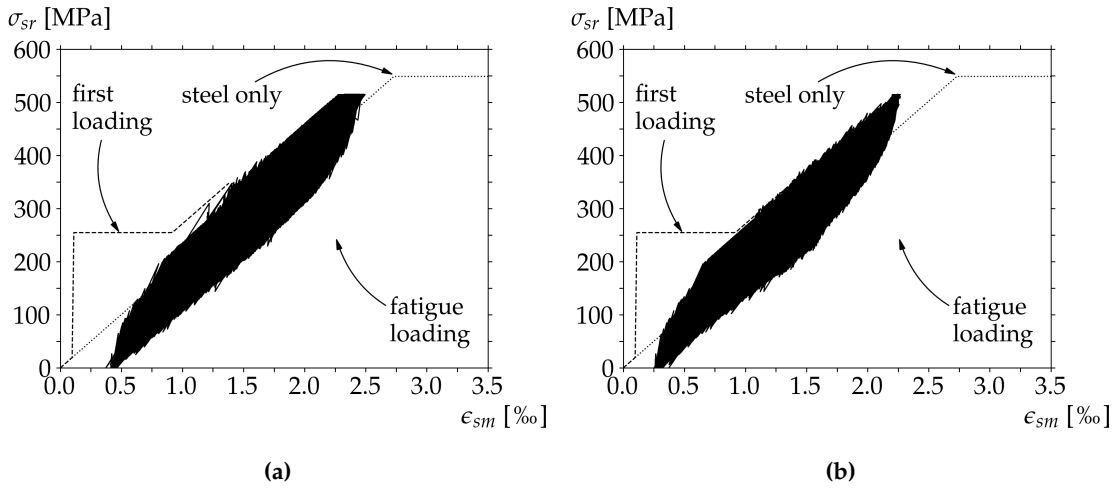

Figure 4.43: Recalculation of load sequences with Fatigue Tension Chord Model: (a) Load sequence Pm with plastic-strain-accumulation, (b) Load sequence Pm without plastic-strain-accumulation

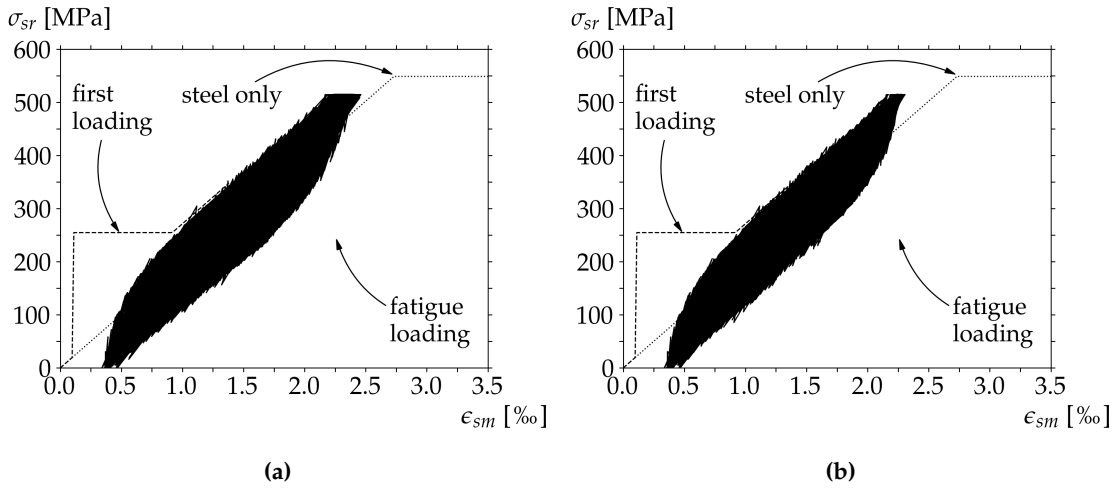

Figure 4.44: Recalculation of load sequences with Fatigue Tension Chord Model: (a) Load sequence Pb with plastic-strain-accumulation, (b) Load sequence Pb without plastic-strain-accumulation

The test results show an only little influence of the load sequential arrangement on ϵ_{sm}. Instead of using τ_{bU1} as well as τ_{bR1} – both for static-monoton cases – it may be convenient to use directly $\tau_{bU,rsd}$ and $\tau_{bR,rsd}$ for estimating the effects of a bond degradation. The tension-stiffening effect of bond in static-monotonic cases for $\sigma_{sr} \leq f_{sy}$ may be quantified calculating the distance $\epsilon_s - \epsilon_{sm} = \epsilon_0 = 2\lambda\Delta\epsilon$ (cf. Fig. 4.29e and Eq. 4.32) with $\lambda = 0.5...1.0$.

For a given crack distance s_{rm}, then

$$\epsilon_s - \epsilon_{sm} = \Delta\epsilon_0 = \frac{s_{rm}\tau_{b0}}{\varnothing_s E_s}. \tag{4.84}$$

As a result of a bond degradation the distance ϵ_0 is reduced by ϵ_{BI} (cf. Fig. 4.30b). In a simplified approach, a fatigue of the tension-stiffening effect may be quantified by considering only an unloading and a subsequent reloading process of the tension chord. However, as mentioned before, the values of τ_{bU1} as well as τ_{bR1} are to be employed. A possible plastic-strain-accumulation of the reinforcement is to be regarded separately. During the first loading with $\sigma_{sr0} < \sigma_{sr} = \sigma_{sr1} \leq f_{sy}$ and using the notation of Koppitz in [103], the average steel strain is

$$\epsilon_{sm}^{(B)} = \frac{\sigma_{sr1}}{E_s} - \frac{s_{rm}\tau_{b0}}{\varnothing_s E_s}. \tag{4.85}$$

An unloading to $\sigma_{sr} = \sigma_{sr2} < \sigma_{sr1}$ leads to an average steel strain of

$$\epsilon_{sm}^{(H)} = \frac{\sigma_{sr2}}{E_s} + \frac{4}{\varnothing_s E_s}\left(\tau_{b0} + \tau_{bU,rsd}\right)\left(1 - \frac{x_{sU}}{s_{rm}}\right)x_{sU} - \frac{s_{rm}\tau_{b0}}{\varnothing_s E_s} \tag{4.86}$$

with x_{sU} according to Eq. 4.69, whereupon $\tau_{bU,rsd}$ is to be set instead of τ_{bU1}. Reloading the tension chord to $\sigma_{sr} = \sigma_{sr3} > \sigma_{sr2}$ results in

$$\epsilon_{sm}^{(I)} = \frac{\sigma_{sr3}}{E_s} + \frac{4}{\varnothing_s E_s}\left(\tau_{b0} + \tau_{bR,rsd}\right)\frac{x_{sR}^2}{s_{rm}} - \frac{4}{\varnothing_s E_s}\tau_{bR,rsd}x_{sR} - \frac{s_{rm}\tau_{b0}}{\varnothing_s E_s}. \tag{4.87}$$

Similarly, $x_{sR} \geq x_{sU}$ according to Eq. 4.70 with $\tau_{bU,rsd}$ and $\tau_{bR,rsd}$. A degradation effect of the bond fatigue follows from

$$\Delta\epsilon_{BI} = \epsilon_{sm}^{(I)} - \epsilon_{sm}^{(B)} = \ldots = \frac{4}{\varnothing_s E_s}\left(\left[\tau_{b0} + \tau_{bR,rsd}\right]\frac{x_{sR}^2}{s_{rm}} - \tau_{bR,rsd}s_{rm}\right). \tag{4.88}$$

Finally, the tension-stiffening number η_{TS} according to Eq. 4.56 becomes

$$\eta_{TSfat} = 1 - 4\frac{x_{sR}}{s_{rm}}\left(\frac{x_{sR}}{s_{rm}} + \left[\frac{x_{sR}}{s_{rm}} - 1\right]\frac{\tau_{bR,rsd}}{\tau_{b0}}\right). \tag{4.89}$$

For the very probable case of $x_{sR} \approx \frac{1}{2}s_{rm}$ and $\tau_{bR1} \approx \tau_{b0}$ (cf. Eq. 4.77), then $\eta_{TSfat} = 0.5$, i.e. the tension-stiffening effect is reduced by 50%. In case of a plastic-strain-accumulation of the reinforcement under fatigue loading, then $\epsilon_{sm}^{(I)}$ and $\Delta\epsilon_{BI}$ are to be increased by $\epsilon_{sm,pl}$ according to Eq. 4.82 analogous, reducing this the value of η_{TSfat} additionally, which may

become negative. If $\eta_{TSfat} < 0$, then the deformation of a tension chord is larger than the elastic deformation of the "naked" reinforcement.

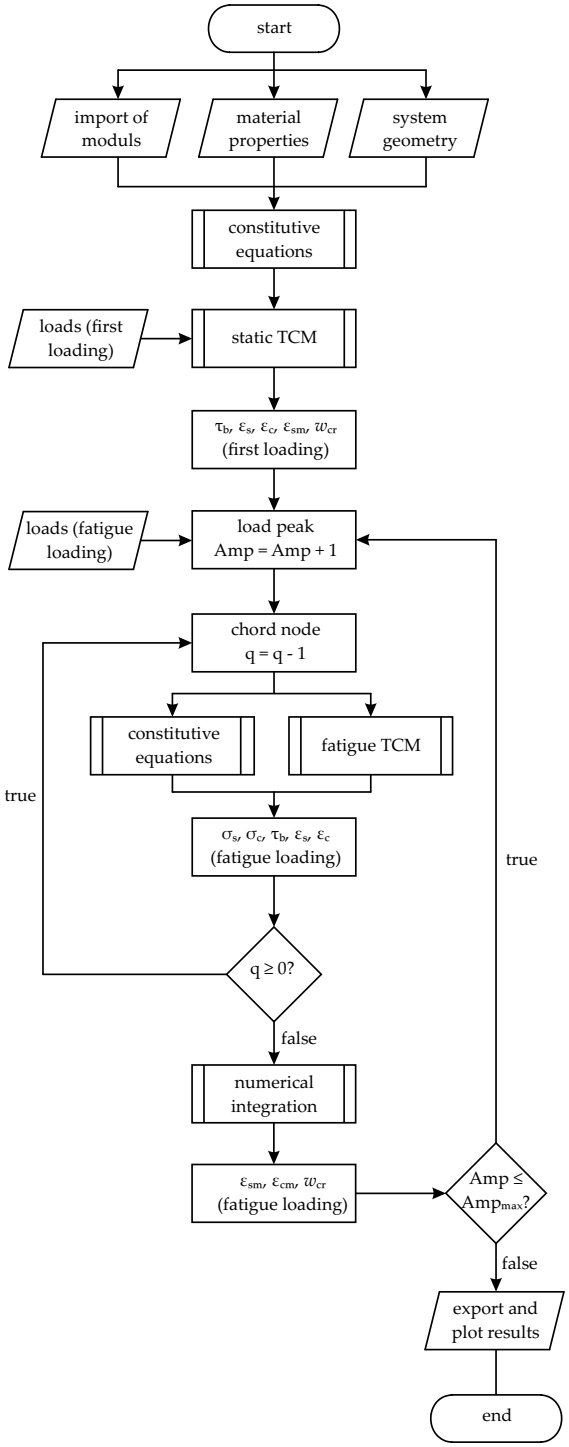

Figure 4.45: Flow chart of implemented code of Fatigue Tension Chord Model

CHAPTER 5

Fatigue Effects on the Structural Behaviour of Reinforced-Concrete Beams

5.1 Static Behaviour of Beams in Shear

The most accepted model for beams in shear is based on splitting the beam into a tension and a compression chords; further into a web [177]. The last one is idealised as a reinforced membrane element subjected to in-plane stresses σ_x, σ_z, τ_{xz}. Complex structures yet, which additionally experience a secondary load behaviour (e.g. bridges and offshore structures under transverse bending moments and local out-of-plane stresses), may require more detailed considerations. Nevertheless, a clever decomposition of beam structures into membranes and chords with simplified load configurations is a practical and proven tool for the structural design practice.

The structural design for the ultimate state has to be safe on a high level of reliability [64]. For reinforced membrane elements usually the quadratic yield criterion for concrete is used [112]. With the general Mohr-Coulomb yield criterion $Y = |\tau| + \sigma \tan \phi_c - c_c$ (Ch. 3.2.3) the following expression is derived (cf. Eq. 3.23):

$$Y_c = \sigma_{c1} (1 + \sin \phi_c) - \sigma_{c3} (1 - \sin \phi_c) - 2c_c \cos \phi_c = 0 \tag{5.1}$$

The quadratic yield criterion of concrete assumes $f_{ct} = 0$, no strength increase under multiaxial compression states, and an isotropic material behaviour. With the conditions $\sigma_{c1} = 0$ as well as $0 \geq \sigma_{c3} > -f_{ce}$ (tension failure) one obtains the first yield limit Y_{c1} of the concrete on the basis of the transformation equations of stresses. Note that the effective concrete compression strength f_{ce} depends highly on the surrounding strain state [105].

$$\sigma_{c1} = 0 = \frac{1}{2} (\sigma_{cx} + \sigma_{cz}) + \frac{1}{2} \sqrt{(\sigma_{cx} - \sigma_{cz})^2 + 4\tau_{cxz}^2} \tag{5.2}$$

$$Y_{c1} = \tau_{cxz}^2 - \sigma_{cx} \sigma_{cz} = 0 \tag{5.3}$$

The second yield limit Y_{c2} results from the restriction $0 > \sigma_{c1} \geq -f_c$ while $\sigma_{c3} = -f_{ce}$ for a

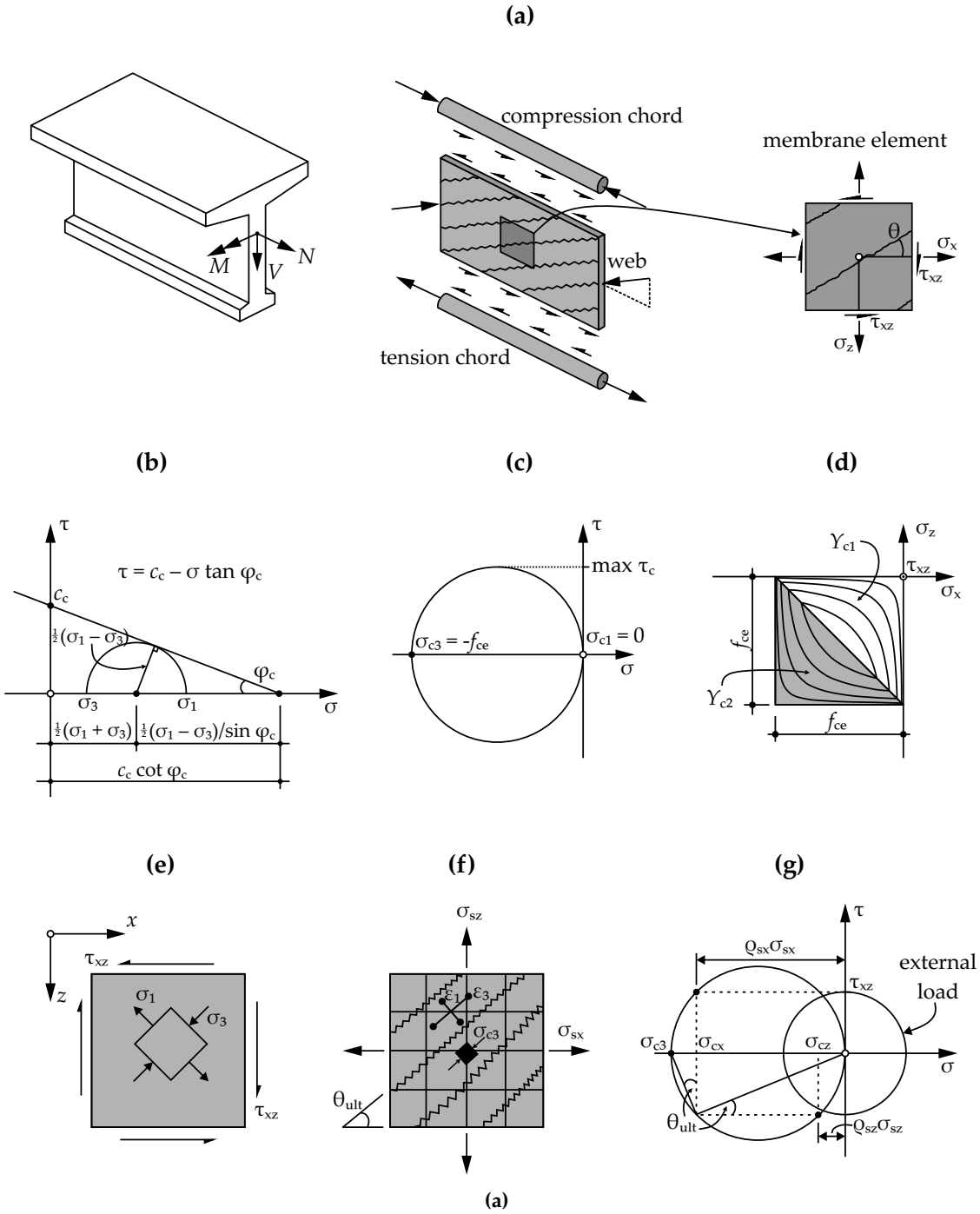

Figure 5.1: (a) Splitting of beam segment into tension chord, web, and compression chord, redrawn from [177], (b) Parameters for deriving the yield criterion of concrete, (c) Simplified yield limit of concrete, (d) Simplified yield surface of concrete in the $\sigma_x - \sigma_z$-plane with contour lines representing equal τ_{xz}-values, (e) Idealised shear load of web membrane element, (f) Idealised stresses and strains in orthogonally reinforced membrane element, (g) Relation between inclination angle Θ_{ult} and stress state in membrane.

failure under compression. Again, the stress transformation relation delivers

$$\sigma_{c3} = -f_{ce} = \frac{1}{2}\left(\sigma_{cx} + \sigma_{cz}\right) + \frac{1}{2}\sqrt{\left(\sigma_{cx} - \sigma_{cz}\right)^2 + 4\tau_{cxz}^2}, \tag{5.4}$$

$$Y_{c2} = \tau_{cxz}^2 - \left(\sigma_{cx} + f_{ce}\right)\left(\sigma_{cz} + f_{ce}\right) = 0. \tag{5.5}$$

At the same time the shear stresses in the concrete are limited to (cf. Fig. 5.1c)

$$\tau_{cxz} \leq \frac{1}{2}\left|\sigma_{c3} - \sigma_{c1}\right| = \frac{1}{2} f_{ce}, \tag{5.6}$$

and the concrete yield surface is composed of two elliptic cones (cf. Fig. 5.1d) [92], [175]. Assuming rigid bond conditions and shear stresses being carried only by the concrete (no dowel action of the reinforcement), then the ultimate load capacity of orthogonally reinforced membranes may be derived by means of the quadratic yielding criterion of the concrete. Axial stresses are carried by both, concrete and reinforcement [116]. After distributing the axial membrane forces $n_x = n_{cx} + a_{sx}\sigma_{sx}$ resp. $n_z = n_{cz} + a_{sz}\sigma_{sz}$ over the membrane breadth it follows.

$$\sigma_x = \sigma_{cx} + \rho_{sx}\sigma_{sx}, \qquad \sigma_z = \sigma_{cz} + \rho_{sz}\sigma_{sz}, \qquad \tau_{xz} = \tau_{cxz}. \tag{5.7}$$

A ductile failure mode is achieved through yielding of the reinforcement $\sigma_{sx} = \rho_{sx} f_{sy}$, $\sigma_{sz} = \rho_{sz} f_{sy}$, while the effective concrete strength f_{ce} is not reached. From Eq. 5.7 follows $\sigma_{cx} = \sigma_x - \rho_{sx} f_{sy}$ and $\sigma_{cz} = \sigma_z - \rho_{sz} f_{sy}$. The yield function $Y_{c1} = Y_1$ in Eq. 5.3 is reshaped, considering also Eq. 5.7, into

$$Y_1 = \tau_{xz}^2 - \left(\sigma_x - \rho_{sx} f_{sy}\right)\left(\sigma_z - \rho_{sz} f_{sy}\right) = 0. \tag{5.8}$$

For the case of a pure shear loading, i.e. $\tau_{xz} \neq 0$ and $\sigma_x = \sigma_z = 0$, as it is usually idealised for beam webs, Eq. 5.8 takes following form:

$$\tau_{xz} = f_{sy}\sqrt{\rho_{sx}\rho_{sz}}. \tag{5.9}$$

Eq. 5.9 describes the ultimate shear capacity of orthogonally reinforced membranes, though, it does not deliver any information about their deformation behaviour. The inclination Θ_{ult} of the compression strut results from the Mohr's circle in Fig. 5.1g:

$$\tan\Theta_{ult} = \frac{\tau_{xz}}{\sigma_{cx}} = \frac{f_{sy}\sqrt{\rho_{sx}\rho_{sz}}}{\rho_{sx} f_{sy}} = \sqrt{\frac{\rho_{sz}}{\rho_{sx}}}. \tag{5.10}$$

The applicability of Eq. 5.10 is limited since webs of beams in shear are reinforced mainly in the vertical direction ($\rho_{sx} = 0$). Therefore, more appropriate calculation models are necessary. The Generalised Stress Field Analysis (GSFA) of Sigrist [177], [73], for example, has proven to be an accurate model based on established physical relations. Accordingly, the axial force $F_{xV} = 1/2|V| \cot \Theta_{ult}$, caused by the stress field of shear forces, is not carried by the web but it is rather assumed to be distributed over the tension and the compression chords. This and other considerations will be discussed later in this chapter.

The analysis of the structural and deformation behaviour of reinforced membranes has been made possible with the so called Compression Field Theories. The work of Baumann [13] is worth mentioning; it derives important equations based on equilibrium conditions for reinforced membranes in the elastic state and is one of the first detailed study on this field. Also very known is the Modified Compression Field Theory of Vecchio and Collins [194], which was developed and is applied for reinforced membranes in the ultimate limit state. Yet, Kaufmann [92], [93] succeeded developing a more precise and accurate calculation model called Cracked Membrane Model for reinforced membranes employing the Tension Chord Model in order to estimate the average steel strain between the cracks. Seelhofer [175] refined and extended the Cracked Membrane Model. The main assumptions comprise fictive, rotable cracks with a neglectable crack spacing; also stress-free crack surfaces (this is the case for major crack widths), which leads to equal directions of principal stresses and principal strains. The principal compression stress is further also free to rotate in dependence of the magnitude of the applied loads.

The Mohr's circle of strains delivers the following elementary kinematic relation (cf. Fig. 5.2a) [177]:

$$\tan \Theta = \frac{\epsilon_x - \epsilon_3}{\frac{1}{2}\gamma_{xz}} = \frac{\frac{1}{2}\gamma_{xz}}{\epsilon_1 - \epsilon_x}. \tag{5.11}$$

From Eq. 5.11 follows $(1/2\gamma_{xz})^2 = (\epsilon_x - \epsilon_3)(\epsilon_1 - \epsilon_x)$. Using the first invariant of strains, ϵ_1 may be expressed as $\epsilon_1 = \epsilon_x + \epsilon_z - \epsilon_3$. Finally, Eq. 5.11 is brought in the known form

$$\tan^2 \Theta = \frac{(\epsilon_x - \epsilon_3)^2}{\left(\frac{1}{2}\gamma_{xz}\right)^2} = \frac{\epsilon_x - \epsilon_3}{\epsilon_z - \epsilon_3}. \tag{5.12}$$

Taking the above assumptions into account, the equilibrium equations for reinforced membrane elements (Fig. 5.2b) result in the following equations [116]. It is important to emphasize again that stresses at the crack surface are neglected.

$$\sigma_x = \rho_{sx}\sigma_{sx} + \sigma_{c3}\cos^2\Theta \quad \sigma_z = \rho_{sz}\sigma_{sz} + \sigma_{c3}\sin^2\Theta \quad \tau_{xz} = -\sigma_{c3}\sin\Theta\cos\Theta. \tag{5.13}$$

The relations expressed in Eq. 5.13 may be reshaped in order to find further useful

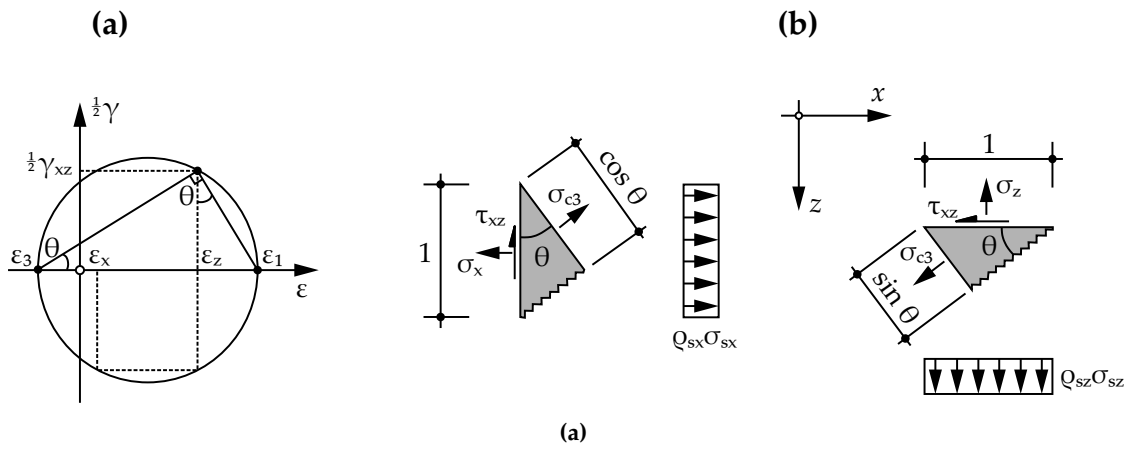

Figure 5.2: (a) Mohr's circle of strains, (b) Equilibrium of forces for derivation of elastic compression fields, adapted from [116].

expressions. The concrete stresses are equal to

$$\sigma_{c3} = \frac{\sigma_x - \rho_{sx}\sigma_{sx}}{\cos^2\Theta} = \frac{\sigma_z - \rho_{sz}\sigma_{sz}}{\sin^2\Theta} = \frac{-\tau_{xz}}{\sin\Theta\cos\Theta}, \tag{5.14}$$

which results in the following equations for the stresses in both, reinforcement and concrete:

$$\sigma_{sx} = \frac{\sigma_x + \tau_{xz}\cot\Theta}{\rho_{sx}} \qquad \sigma_{sz} = \frac{\sigma_z + \tau_{xz}\tan\Theta}{\rho_{sz}} \qquad \sigma_{c3} = -\tau_{xz}\left(\cot\Theta + \tan\Theta\right). \tag{5.15}$$

Eqs. 5.15 are employed for the structural design of reinforced membranes in the ultimate limit state according to [51], [42]. Consequently, the value of the inclination $\Theta = \Theta_{ult}$ is essential in the design of reinforced membranes, if the internal stresses of the membrane are known. On the other side, under serviceability conditions the reinforcement and (partially) the concrete are expected to remain linear-elastic. In this case, the simple linear material equations $\sigma_{sx} = E_s\epsilon_x$, $\sigma_{sz} = E_s\epsilon_z$, and $\sigma_{c3} = E_c\epsilon_3$ may be effectively used. In combination with the kinematic relation of Eq. 5.11 and Eq. 5.15, following relation is valid:

$$\sigma_{c3} = -\tau_{xz}\left(\cot\Theta + \tan\Theta\right) \equiv E_c\epsilon_3 = E_c\frac{\epsilon_z - \epsilon_x\cot^2\Theta}{1 - \cot^2\Theta}, \tag{5.16}$$

which leads to

$$E_c\left(\epsilon_z - \epsilon_x\cot^2\Theta\right) = \tau_{xz}\left(\cot^3\Theta - \tan\Theta\right). \tag{5.17}$$

Replacing $\epsilon_z = \sigma_{sz}/E_c$, $\epsilon_x = \sigma_{sx}/E_c$ (linear-elastic state), $n = E_s/E_c$, and employing Eq. 5.15 for the values of σ_{sz} resp. σ_{sx}, a nonlinear equation is obtained and the value of Θ in the linear-elastic state may be calculated with (cf. [13], [92]):

$$\tan^2\Theta\rho_{sx}\left(1+n\rho_{sz}\right)+\tan\Theta\rho_{sx}\frac{\sigma_z}{\tau_{xz}}=\cot^2\Theta\rho_{sz}\left(1+n\rho_{sx}\right)+\cot\Theta\rho_{sz}\frac{\sigma_x}{\tau_{xz}}. \tag{5.18}$$

Following Eq. 5.18, webs of reinforced concrete beams that experience no axial forces, i.e. $\sigma_x = \sigma_z \approx 0$ may exhibit an inclination angle Θ_{fat} in the serviceability and fatigue state of $\tan^2\Theta\rho_{sx}\left(1+n\rho_{sz}\right)+0=\cot^2\Theta\rho_{sz}\left(1+n\rho_{sx}\right)+0$. Compared to Eq. 5.10, the following expression may be derived if approximately equal reinforcement degrees in horizontal and vertical directions are assumed ($\rho_{sx} \approx \rho_{sz}$):

$$\tan^4\Theta_{fat}=\frac{\rho_{sz}\left(1+n\rho_{sx}\right)}{\rho_{sx}\left(1+n\rho_{sz}\right)}\approx\frac{\rho_{sz}}{\rho_{sx}}=\tan^2\Theta_{ult}. \tag{5.19}$$

Eq. 5.19 is given in the German version of Eurocode [132] and in the Model Code 2010 [51] for the calculation of Θ_{fat} with the aim of determining the stresses of the shear reinforcement on the basis of the strut and tie model used in the structural design at the ultimate limit state. The offshore standard DNV OS C502 [42] is more conservative and stipulates a value of $\Theta_{fat} = 45°$. According to the Model Code 2010, the concrete stress in the compression strut is to be estimated using Θ_{ult} instead of Θ_{fat}, though.

For reinforced beams the stress field analysis is more exact and for instance more appropriate. Accordingly, the ultimate shear load results from equilibrium equations (cf. [177], [209], [165]). The ultimate shear load of the shear reinforcement $V_{R,sy}$ and the ultimate shear load of the web concrete $V_{R,c}$ follow from

$$V_{R,sy}=b_w\rho_{sz}f_{sy}z\cot\Theta, \tag{5.20}$$

$$V_{R,c}=b_w f_{ce}z\sin\Theta\cos\Theta. \tag{5.21}$$

The limit analysis of the web corresponds to the case where the shear reinforcement (z-direction) yields, i.e. $\sigma_{sz} = f_{sy}$ and at the same time the effective concrete strength $\sigma_{c3} = -f_{ce}$ is reached. The so called regime 2 [93] of orthogonally reinforced concrete membranes describes the yielding criterion beginning with the requirement $\sigma_{c1} = 0$. From the stress transformation of Mohr's circle in Eq. 5.3, further from the condition $\sigma_{cm} = 1/2\left(\sigma_{cx}+\sigma_{cz}\right) = -1/2 f_{ce}$ (the effective concrete strength is reached), and considering $\sigma_z = \sigma_{cz} + \rho_{sz}f_{sy}$, then

$$\tau_{cxz}^2=\tau_{xz}^2=\sigma_{cx}\sigma_{cz}=\left(-f_{ce}-\sigma_{cz}\right)\sigma_{cz}=\left(-f_{ce}\left[\sigma_z-\rho_{sz}f_{sy}\right]\right)\left(\sigma_z-\rho_{sz}f_{sy}\right). \tag{5.22}$$

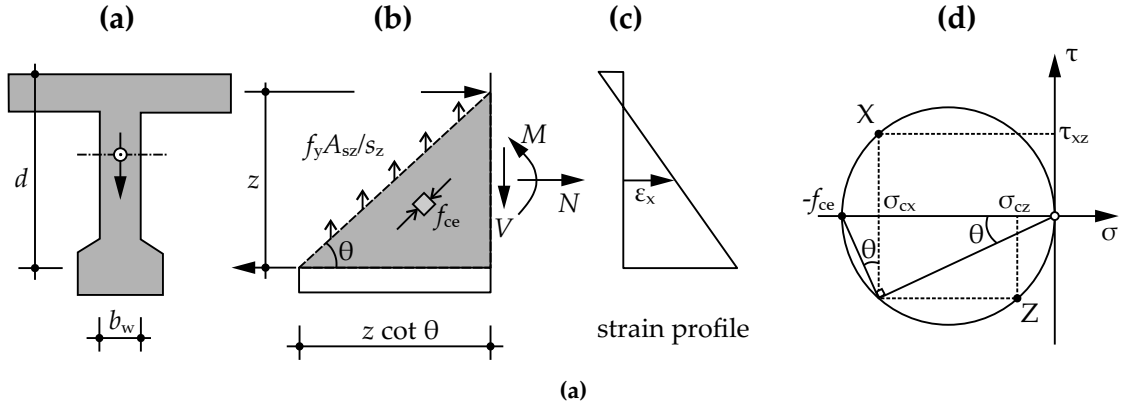

Figure 5.3: (a) Cross section, (b) Free-body diagram of stress field, c) Axial strain at mid depth of the web, d) Mohr's circle of stresses of concrete in web; adapted from [177].

With the known simplification of only shear stresses acting in the webs of beams ($\sigma_x = \sigma_z = 0$), Eq. 5.22 leads to

$$\tau_{xz} = \sqrt{\left(f_{ce} - \rho_{sz} f_{sy}\right) \rho_{sz} f_{sy}}. \tag{5.23}$$

The Mohr's circle of stresses in Fig. 5.3d delivers finally the inclination angle Θ of the compression strut according to the stress field analysis.

$$\tan\Theta = \frac{\tau_{cxz}}{\sigma_{cx}} = \frac{\tau_{cxz}}{-f_{ce} - \sigma_{cz}} = \frac{\sqrt{\left(f_{ce} - \rho_{sz} f_s\right) \rho_{sz} f_{sy}}}{-f_{ce} + \rho_{sz} f_{sy}} = \sqrt{\frac{\rho_{sz} f_{sy}}{f_{ce} - \rho_{sz} f_{sy}}}. \tag{5.24}$$

Eq. 5.24 may not be used without restriction since f_{ce} depends on the strain state of the web. Sigrist [180], [177] suggests the following constitutive material equation:

$$f_{ce} = \frac{1}{1.2 + 55\epsilon_1} f_c \left(\frac{30}{f_c}\right)^{\frac{1}{3}} \leq \frac{1}{1.2 + 55\epsilon_1} f_c. \tag{5.25}$$

ϵ_1 is calculated with the help of the first strain invariant ($\epsilon_1 + \epsilon_3 = \epsilon_x + \epsilon_z$) and the kinematic condition in Eq. 5.12:

$$\epsilon_1 = \epsilon_x + (\epsilon_x - \epsilon_3) \cot^2\Theta, \tag{5.26}$$

Sigrist [177] proposes to set $\epsilon_3 = -\epsilon_{c0} = -2.0‰$ as failure condition for the case of a static-monotonic loading. Additionally, ϵ_x is pragmatically chosen as the axial strain value at the mid-depth of the web, calculated by means of the acting forces in the compression

resp. tension chords

$$F = \pm\frac{M}{z} + \frac{|V|}{2}\cot\Theta + \frac{N}{2} \tag{5.27}$$

and their corresponding axial stiffness values EA. Applying Bernoulli's beam theory, then the distribution of ϵ_x over the beam cross section is linear. In the case where $F > F_{cr}$ and the sectional chord section hence turns into the elastic-cracked or even into the plastic-cracked state, ϵ_x may be estimated for a more general case employing the average steel strain ϵ_{smx} [73] derived from the Tension Chord Model. In order to simplify the calculation process, the minor compression strains of the concrete may be neglected. ϵ_x, on the other hand, may also be set equal to the value in the cracked section, i.e. $\epsilon_x = \epsilon_{srx}$ which leads to very conservative results. The resulting non-linear interaction between Θ and f_{ce} is to be solved iteratively.

The generalisation of the stress field analysis (GSFA) is performed by Sigrist [177] introducing limit values for the inclination of the compression struts Θ based on Eq. 5.12. Again, he assumes for a compression failure of the concrete the value $\epsilon_3 = \epsilon_{c0} = -2.0‰$. The vertical strain ϵ_z is set equal to the average strain ϵ_{smz} of the shear reinforcement in order to estimate more realistic values taking the tension-stiffening effect into account. For this purpose, the Tension Chord Model [115] is employed, leading to

$$\epsilon_z = \epsilon_{smz} = \kappa_\tau \epsilon_{s,max}. \tag{5.28}$$

The parameter $\kappa_\tau = \epsilon_{smz}/\epsilon_{s,max}$ describes the bond coefficient (cf. Ch. 4.2.1). Θ becomes a maximum, i.e. $\Theta = \Theta_{max}$, if $\epsilon_{s,max} = \epsilon_{su} \approx 50‰$ (high ductility steel B500B according to [36]). Sigrist derives $\kappa_\tau = 0.25$ with the Tension Chord Model (see Eq. 4.37). At this stage the failure due to concrete crushing becomes relevant, so that

$$\tau_{R,max} = f_{ce} \sin\Theta_{max} \cos\Theta_{max}. \tag{5.29}$$

As soon as the web reinforcement yields, i.e. $\epsilon_{s,max} = \epsilon_{sy} = 2.5‰$, the static failure of the reinforcement represents the relevant failure mode with $\Theta = \Theta_{min}$ and $\kappa_\tau = 0.8$ [177]:

$$\tau_{R,max} = \rho_{sz} f_{sy} \cot\Theta_{min}. \tag{5.30}$$

Sigrist also proposes a linearisation of the limits of Θ for practical purposes in [177]. With the afore mentioned conditions, then

$$20^\circ + 5000\epsilon_x \le \Theta \le 35^\circ + 5000\epsilon_x, \tag{5.31}$$

which is restricted for -0.5‰$\le \epsilon_x \le$ 1.5‰ and f_{sy} = 500 MPa.

5.2 Fatigue Behaviour of Beams in Shear

The mechanical behaviour of reinforced concrete beam elements under fatigue loading is complex. Both, concrete and bond, show a degradation process which, in case of the concrete, strongly depends on the surrounding stress state (cf. Ch. 3.2.3, Ch. 3.2.6). This dependency is not prominent for the bond (cf. Ch. 4.2.1). Because of the microcracking process caused by the fatigue loading in the concrete there is a stiffness loss that becomes noticeable through a measurable reduction of the secant modulus of elasticity E_{cm} (cf. Ch. 3.2.4); the bond is also weakened, leading to larger deformations. As a result, the stiffness E_{sm} of the tension chord decreases. Additionally, a part of the induced deformations persists after a complete unloading of the concrete (cf. Ch. 3.2.4). Negative bond stresses lead, on the other hand, to a restraint between reinforcement and surrounding concrete after unloading, causing irreversible deformations in the tension chord (cf. Ch. 3.3.1). A further important fact found in tests is the immutability of the uniaxial concrete strength f_c (cf. Ch. 3.2.4) and of the bond strength τ_b (cf. Ch. 3.3.2) in the ultimate limit state, even after being subjected to a fatigue loading.

Under fatigue loading, the reinforcement may also develop microcracks which act like notches, leading to stress concentrations on the crack tips and partially to local plastic deformations (cf. 3.1.2). Although its cross sectional area may be thereby reduced, structural reserves provided in a robust design may guarantee the structural reliability in the first two phases of the fatigue crack development. The global mechanical behaviour of the reinforcement under fatigue remains linear-elastic, yet a plastic-strain-accumulation process has been recorded in the tests described in Ch. 4.2.1.

For the design for shear under fatigue conditions the Model Code 2010 [51] uses a strut and tie model similar to the calculation model employed in the ultimate limit state (ULS). The design goal is principally the structural verification of the web reinforcement against fatigue failure; the concrete in the compression strut is also to be checked against a fatigue failure. The stress σ_{sw} in the web reinforcement results directly from the strut and tie model with

$$\sigma_{sw} = \frac{V_{fat}}{a_{sw} z \cot \Theta_{fat}}. \tag{5.32}$$

V_{fat} denominates the fatigue shear force exerted on a determined cross section of the beam element and a_{sw} indicates the existing web reinforcement area. The lever arm of internal forces z may be expected to be lower under fatigue conditions (service loads) than in the ultimate limit state. Both, concrete and reinforcement, have to be designed in terms of serviceability in such a way that they remain in the linear-elastic range. Based on the linear stress field analysis (cf. Ch. 5.1), the inclination $\Theta = \Theta_{fat}$ of the compression strut is derived in Eq. 5.19.

$$\tan \Theta_{fat} = \sqrt{\tan \Theta_{ULS}} \tag{5.33}$$

Eq. 5.33 implies that Θ_{fat} is higher than Θ_{ULS} [51]. An argument given in the literature

([191], [55]) for the steeper inclination of the compression strut under fatigue loading is the progressive deterioration of the concrete at the crack lips, leading to a reduced interlocking effect in the concrete. As a consequence, there is an internal load redistribution which partially relieves the concrete and increases the stress in the web reinforcement. However, Eq. 5.33 does not take into consideration additional degradation effects of the mechanical properties of concrete and bond under fatigue loading. A deeper analysis connected to the evaluation of experimental data is necessary in order to verify the applicability of Eq. 5.33.

Experiments performed by Frey [55] in order to study the fatigue behaviour of beams provided with shear reinforcement reveal a good agreement with Eq. 5.33 (cf. also [64]). The local strain distribution of the web reinforcement shows peak values being distributed over the whole height of the beam. Owing to the fatigue loading, the diagonal crack lips experience a successive deterioration process, permitting an almost free relative movement against each other. Thus, the existing transmission of shear stresses (parallel to the crack lips) and of normal stresses (orthogonal to the crack lips) is affected. A following static-monotonic loading in the ultimate load state shows, however, an unreckoned force transmission at the crack lips. The inclination of the compression strut becomes flatter and the beam reaches the static ultimate load. Hence, as long as there occurs no fatigue failure of the stirrups, the ultimate loading capacity of shear forces does not seem to be affected. This fact is fundamental when verifying the load-bearing capacity of old bridges. Since Eq. 5.33 is strictly valid only for membrane elements with a constant strain distribution over the element, Frey [55] derives the following equation for Θ_{fat} for beam elements which exhibit a linear distribution of the axial strain ϵ_x:

$$\tan^3\Theta_{fat}\left(1+\frac{1}{n\rho_{sz}}\right)-\cot\Theta_{fat}-\frac{\epsilon_x E_c}{\tau_{xz}}=0. \tag{5.34}$$

Here, $n = E_s/E_c$. Axial stresses resulting from post-tensioning lead to a modification of Eq. 5.33 which applies to reinforced concrete. According to Frey [55]

$$\tan\Theta_{fat}=\sqrt{\tan\Theta_{ULS}}\left[1+\lambda_x\left(\frac{1}{k}-1\right)^{-\frac{1}{4}}\right] \tag{5.35}$$

with the parameters $k = f_{py}/f_{sy}$ and $\lambda_x = \omega_{px}/\left(\omega_{sy}+\omega_{px}\right)$, where ω_{px} and ω_{sy} represent the mechanical reinforcement ratio of the post-tensioning steel and of the reinforcement respectively.

Teworte [191] performed fatigue tests with post-tensioned I-beams provided with different degrees of web reinforcement. His results deliver a valuable insight into the transfer mechanisms of the shear force under fatigue loading. A fatigue failure was reached only for the web reinforcement; thereby, the applied load peaks amounted approximately 91 ... 183% of the ultimate shear-load capacity calculated according to [41], which reveals that this calculation model is (too) conservative. Also the model of Frey [55] was found to be conservative in some cases, in others, however, not. During the tests, a gradual

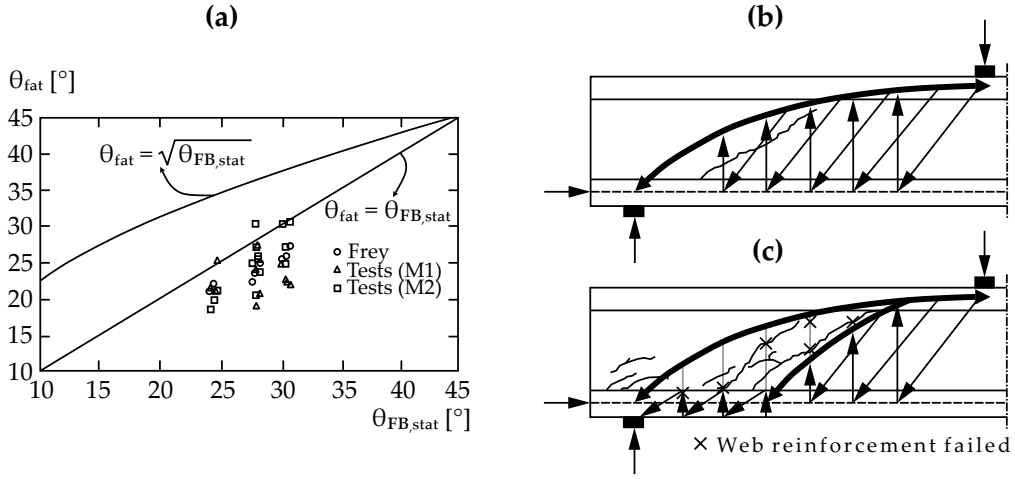

Figure 5.4: Shear-fatigue tests of Teworte [191] (a) Comparison of inclination angle Θ_{fat} of compression strut measured in tests and angle $\Theta_{FB,stat}$ calculated by [41] at the ultimate limit state, (b) Load transfer mechanism at the beginning of fatigue loading and (c) Load transfer mechanism after fatigue failure of web reinforcement. Redrawn from [191]

fatigue failure of the web reinforcement combined with a load redistribution into intact stirrups could be observed (cf. Fig. 5.4c). This was manifested through an abrupt increase of the strain of the intact stirrups as well as of the beam deformation and the crack width. At the same time, the measured diagonal strains in the web concrete progressively increased – abruptly in case of the fatigue failure of a stirrup –, pointing out to a further redistribution of stresses which is assumed to be also influenced by the degradation of the bond properties of the web reinforcement. Based on his results, Teworte presents in [191] two calculation models. The determined value of Θ_{fat} oscillates between $\Theta_{fat} = 18°...24°$ (model 1 of Teworte [191]) and $\Theta_{fat} = 20°...31°$ (model 2 of Teworte [191]) for high degrees of web reinforcement. The average value achieved with the model 2 in cases of a low degree of web reinforcement was $\Theta_{fat} = 20°$. He proposes to simply assume $\Theta_{fat} = \Theta_{FB,stat}$ (the last calculated with the approach of [41]) for the fatigue design of the stirrups.

The fatigue failure of the stirrups occurred mainly at the location of diagonal, shear-stress-induced cracks. In some cases the stirrups presented a fatigue failure in even two cross sections. According to Teworte [191], the fatigue failure of some stirrups definitely may lead to a subsequent reduced ultimate shear-load capacity if the web reinforcement degree is too low. Beams, which did not completely failed due to fatigue, were afterwards subjected to a static-monotonic, ultimate loading test. Although the test specimens already presented some failed stirrups, the achieved ultimate load was higher than the applied loads during the fatigue tests. Finally, the beam failed in the compression chord due to the growth of a diagonal crack.

The kinematic relation in Eq. 5.12 is universally valid and depends only on the strain state of the element. Its applicability on the web of beams, which show a linear distribution of the longitudinal strain ϵ_x, makes some adaptation necessary. The Generalised Stress Field Analysis (GSFA) [177] performs this step.

According to [177], the value of ϵ_x may be taken as the value ϵ_x of the web. In case of static-monotonic loading, ϵ_x may be calculated using Eq. 5.27 and appropriate stiffness values of the chords for the design in the ultimate limit state. A beam subjected to fatigue loading, though, presents differing values due to the stiffness loss in the compression chord and the bond weakening in the tension chord. An "exact" calculation is time-consuming and object of a large variability (cf. [48]). Effective but simple calculation models are still lacking. The structural standards do not provide usable expressions for estimating the fatigue-induced damage D of the concrete and, with it, its stiffness decrease.

For ϵ_3 Sigrist [177] suggests $\epsilon_3 = -\epsilon_{c0} = -2.0‰$, even though according to [105] strains $\epsilon_3 > -2.0‰$ may already lead to a failure under biaxial compression-tension (cf. Fig. 3.18b). For the strain development of the web concrete under fatigue loading and biaxial compression-tension there is almost no data available in the literature.

ϵ_z is set to $\epsilon_z = \epsilon_{smz}$, i.e. equal to the average strain of the web reinforcement.

For the estimation of Θ_{fat} and also Θ_{ULS} for states after an effective fatigue loading, the Generalised Stress Field Analysis has to be modified.

For ϵ_x, the strain at mid-depth of the web is proposed to be calculated assuming a cracked cross sectional area with $f_{ct} = 0$. This assumption seems to be justified although the uniaxial tension strength f_{ct} of the concrete under fatigue has not been reported to be effectively affected. However, its variation is high (cf. Ch. 3.2.5). In a simplified procedure, the static secant modulus of elasticity E_{cm} of the concrete in the compression chord is reduced by approximately 50% – similar to the bond strength decrease under fatigue expressed with $\kappa_{rsd} = 0.5$ in Ch. 4.2.4 – following the data of Haar [72] and Holmen [83]. The concrete failure is reached at the same strain value $-\epsilon_{cu} = -3.5‰$ as in the case of a static-monotonic loading (cf. Ch. 3.2.4). As a material constitutive equation, a simplified parabola-rectangular $\sigma_c - \epsilon_c$-diagram may be used with the reduced E_{cm}-value and $-\epsilon_{c0} = -\epsilon_{cu} = -3.5‰$(cf. Fig. 5.5a). The strain distribution in any cross section may be determined with help of a suitable calculation program like e.g. the freeware program INCA2 [145].

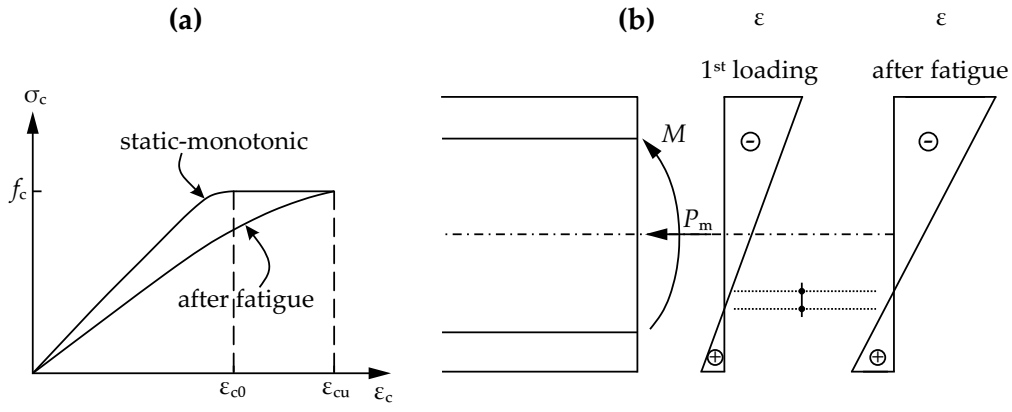

Figure 5.5: (a) Assumed uniaxial constitutive equation of concrete by a first, static-monotonic loading and after fatigue and (b) Axial strain distribution in a I-beam by a first, static-monotonic loading and fatigue

The strain ϵ_3 in the compression strut may be estimated on the basis of the measured strains in the tests of Teworte [191]. At the begin of the fatigue loading, $\epsilon_3 \approx -0.30 ... -0.20‰$ and at the end of the fatigue load program $\epsilon_3 \approx -1.10 ... -0.70‰$. An average, representative value for the beams tested by Teworte in [191] under fatigue loading may be suggested to $\epsilon_3 \approx -0.60‰$. This value is approximately the average of all values between ϵ_3 at the beginning and at the end of the fatigue tests and, hence, takes the development of ϵ_3 into account.

Subsequently, the proposed fatigue Tension Chord Model with $\kappa_{rsd} = 0.5$ may be used in order to estimate the average strain of the web reinforcement $\epsilon_z = \epsilon_{smz}$. Thereby, possible effects of a plastic-strain-accumulation of the web reinforcement may also be considered; for a subsequent ultimate limit state they may be neglected.

The tests performed by Teworte with beams with shear reinforcement in [191] have been analysed with the modified values of the Generalised Stress Field Analysis [177] in order to compare the calculated inclination $\Theta_{fat,cal}$ of the compression strut with the measured one $\Theta_{fat,mes}$ as well as with the inclination $\Theta_{fat,MC2010}$ prescribed by the Model Code 2010 [51]. As described above, the strain ϵ_x at mid-depth of the web has been calculated employing the software INCA2 [145] and a reduction of E_{cm} by 25% (an average value between the static-monotonic value and the value after fatigue loading) in the compression chord. Furthermore, the maximum values of shear force and bending moment (self-weight and test load) at the cross section at a distance of 1.0 m from the support have been evaluated. Due to the applied post-tensioning, the web of the beams is to a large extent under axial compression, i.e. $\epsilon_x < 0$.

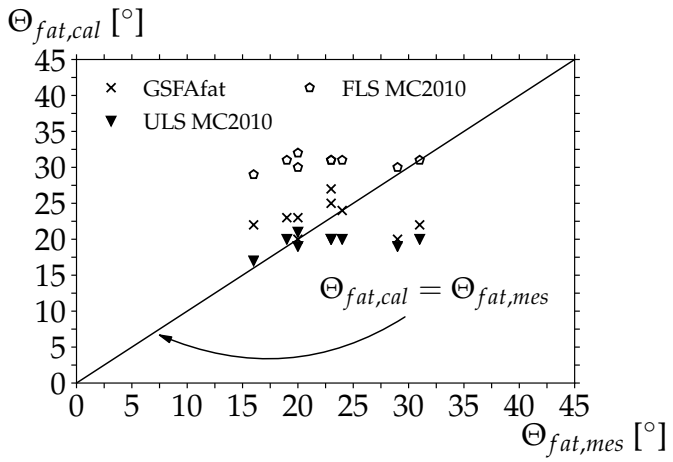

Figure 5.6: Comparison of values of $\Theta_{fat,cal}$ (calculated with the GSFA) with $\Theta_{ULS,MC2010}$ and $\Theta_{fat,MC2010}$, calculated according Model Code 2010 [51].

For the calculation of Θ_{fat}, in contrast to Θ_{ULS}, the web reinforcement does not yield. Therefore, the average strain ϵ_{smz} of the web reinforcement needs to be determined in an iterative calculation, starting with an estimated value of $\cot\Theta_{fat}$. Based on that, the stress in the web reinforcement σ_{sw} is calculated with Eq. 5.32; afterwards the average strain ϵ_{smz} may be determined. Using the corresponding values of ϵ_x and ϵ_3, respectively, a new

Table 5.1: Comparisson of $\Theta_{fat,cal}$ calculated with with the modified GSFA for fatigue with $\Theta_{fat,mes}$ of the tests published in [191] and $\Theta_{ULS,MC2010}$ and $\Theta_{fat,MC2010}$ according to the Model Code 2010 (MC10) [51]. The average strains ϵ_{smz} in the web reinforcement were calculated without plastic-strain-accumulation in the web reinforcement. The value $\Theta_{fat,mes}$ is assumed to be the equal to the measured inclination angle ϵ_3 of the principal stress. ϵ_x was calculated with the software INCA2 [145] after reducing the value of E_{cm} by 25%.

Test	P_m [kN]	V [kN]	M [kNm]	$E_{cm,stat}$ [GPa]	$E_{cm,fat}$ [GPa]	ϵ_x (cal) [‰]	ϵ_3 (mes) [‰]	ϵ_{smz} [‰]	Θ_{fat} (cal) [°]	Θ_{fat} (mes) [°]	Θ_{ULS} MC10 [°]	Θ_{fat} MC10 [°]
I-15-1	-636	177	179	23.3	11.6	-0.2	-0.6	2.6	20	20	19	30
I-15-2	-411	157	159	26.0	13.0	-0.1	-0.4	1.9	20	29	19	30
I-15-3	-320	167	169	26.2	13.1	-0.1	-0.7	2.8	23	20	21	32
I-22-1	-632	197	199	22.8	11.4	-0.2	-0.7	2.3	22	16	17	29
I-22-2	-432	192	194	25.6	12.8	-0.1	-0.6	2.2	22	31	20	31
I-22-3	-320	164	167	24.8	12.4	-0.1	-1.0	2.6	27	23	20	31
I-22-4	-314	138	141	23.6	11.8	-0.1	-0.6	1.8	24	24	20	31
I-22-5	-314	154	156	26.0	13.0	-0.1	-0.5	1.8	23	19	20	31
I-22-6	-314	177	179	22.7	11.4	-0.1	-0.5	2.1	22	-	21	32
I-22-7	-314	169	171	23.9	11.9	-0.1	-0.7	2.4	25	-	21	32
I-33-1	-314	155	157	25.7	12.9	-0.1	-0.4	1.2	23	-	20	31
I-33-2	-314	155	157	26.7	13.3	-0.1	-0.5	1.5	25	23	20	31
I-33-3	-314	169	172	23.7	11.8	-0.1	-0.6	1.7	25	-	21	32
I-33-4	-314	187	189	28.7	14.4	-0.0	-0.6	1.8	25	-	22	32

value of $\cot\Theta_{fat}$ may be calculated by means of the kinematic equation Eq. 5.12.

In the Level I of approximation of the Model Code 2010 [51], for members under significant axial compression, the minimum value of the inclination of the compression strut is $\Theta_{ULS} = 25°$. $\Theta_{ULS} = 30°$ is the minimum value for reinforced members without normal compression forces for such subjected to axial tension. In the Levels II and III, the strain state of the web is considered:

$$\min\Theta_{ULS} = 20° + 10000\epsilon_x, \tag{5.36}$$

with ϵ_x being evaluated at the mid-depth of the web. The limits of Θ_{ULS} are given with

$$\min\Theta_{ULS} \leq \Theta_{ULS} \leq 45°. \tag{5.37}$$

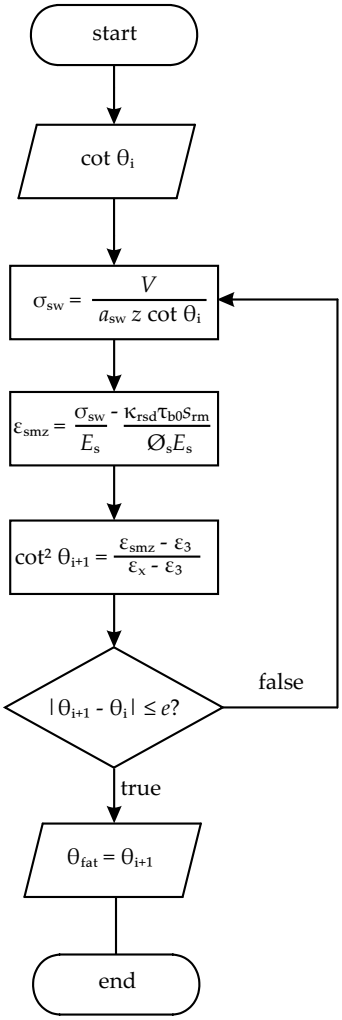

Figure 5.7: Flow chart of the iterative calculation of $\Theta_{fat,cal}$.

The results presented in Tab. 5.1 have been generated without taking the plastic-strain-accumulation of the web reinforcement into account. In general, the plastic-strain-accumulation effect leads to a reduction of the value of $\Theta_{fat,cal}$ of approximately 2° . Note that a possible yielding of the web reinforcement has not been taken into account here. As described in [191], another load-carrying-mechanism, namely the arch action (Fig. 5.4c) also contributes to the shear load-transfer, i.e. Eq. 5.32 is conservative. For the calculation of the values $\Theta_{ULS,MC2010}$ in the ultimate limit state according to the Model Code 2010, [51] the permanent actions resulting from self-weight have been multiplied with the safety factor γ_G = 1.35 while the variable actions of the fatigue loading program with γ_Q = 1.50.

The results in Tab. 5.1 also confirm the proposal of Teworte [191] for the calculation of the fatigue-induced stress in the web reinforcement. In [191], however, Θ_{ULS} is calculated using the formulas of the DIN Fachbericht 102 [41] which is a precursor of the German Eurocode 2 for concrete bridges [133]. The values $\Theta_{ULS,MC2010}$ in the Levels II and III of

the approximation are close to $\Theta_{fat,mes}$, i.e.

$$\Theta_{fat} \approx \Theta_{ULS}. \tag{5.38}$$

The modification of the Generalised Stress Field Analysis (GSFA) of Sigrist proves to deliver a good approximation of $\Theta_{fat,mes}$ (Tab. 5.1). The values $\Theta_{fat,MC2010}$ are clearly conservative. Using an average of $\epsilon_x = -0.10‰$, $\epsilon_3 = -0.60‰$, and $\epsilon_{smz} = 2.0‰$, Eq. 5.12 delivers $\Theta_{fat,cal} = 24°$, which lies between $\Theta_{fat,mes}$ and $\Theta_{fat,MC2010}$.

CHAPTER 6

Summary and Conclusions

The goal of the present work is a deep analysis of the bond between reinforcement and concrete under fatigue loading and its influence on the deformation capacity of tension chords. Furthermore, the impact of the fatigue-induced bond degradation on the transfer of shear forces in beam elements is investigated.

Chapter 2 presents a derivation of the reliability index β_{RC} of structures related to an acceptable low failure probability. Depending on their complexity and the consequences of a possible failure, structures are classified accordingly into consequence classes (CC) and on reliability classes (RC). The required reliability index determines the safety concept and consequently the load combinations.

Special attention is given to offshore concrete structures and to the calculation of fatigue loads by solving the linearised equation of motions and considering the different load types, including inertia and damping forces. The loads experienced under offshore conditions are highly irregular; however, a valuable statistical analysis becomes accessible using the spectral fatigue design. It consists of deriving transfer functions by means of unity loads (e.g. waves with the amplitude equal to one) for every relevant frequency and direction range. In a further step, the response spectra (motions, internal forces or stresses) may be calculated. Since the load spectra of waves is often narrow-banded, the response spectra are also narrow-banded and obey a Rayleigh-distribution which permits an extreme-value analysis. Through the calculation of the corresponding spectral moments of the response spectra one may obtain the zero-up crossing period $T_{z,\sigma}$ of the response. $T_{z,\sigma}$ may differ from the zero-up crossing period T_z of the wave and leads in adverse cases to a number of load cycles higher than the number of waves. After the determination of all response spectra in the long-term (scatter-diagram) a fatigue check may be conducted by transforming the response spectra into time-series and performing a classification and counting of the loads using an adequate counting procedure. An important condition of the spectral fatigue analysis is the linearity of loads and response; under fatigue (service) conditions this is usually the case. This procedure is also valid for other types of structures which are subjected to random loads (e.g. bridges).

Chapter 3 compiles most of the available information in literature regarding the fatigue behaviour of reinforcement and of concrete. The prevalent view is that the reinforcement remains in the linear-elastic range if it is subjected to fatigue (service) loads (high-cycle fatigue) does not reach the yield strength f_{sy}. However, plastic deformations – appearing principally locally – have been observed and reported in tests with various metallic specimens. Yet, there is no detailed information whether reinforcing bars exhibit such

effects which may be additionally enhanced by the ribs. A further question arises from the evidence in several publications regarding the influence of the sequence effect of the applied loads on the reinforcement fatigue behaviour. It is commonly accepted that the load history has no significant influence on the fatigue-induced damage. A systematic investigation and the proposal of representative load spectra for testing purposes are yet still lacking.

In addition, there is little information available on the ultimate loading capacity of reinforcement after having developed fatigue-induced cracks. It seems rather questionable that the static loading capacity is not negatively affected by such cracks. To clarify this issue, specific tests are necessary.

Due to fatigue loading irreversible strains may occur in concrete. It is reported in the literature that there is a quantifiable stiffness loss caused by a gradual, inner microcracking process which leads to growing strains. A limit for the gradual increase of fatigue-induced strains seems to be $-\epsilon_{cu} = -3.5‰$ for normal-strength concrete. The static, uniaxial strength f_c has not shown any alteration in the fatigue process – a very important fact for structures subjected to fatigue loading but which have been designed using static material properties. The secant modulus of elasticity E_c is reported to decrease to 50 ... 70% of its static value. As a consequence, a steady inner load redistribution takes place: Highly loaded regions are partially released, redirecting the inner force flow to less loaded regions. However, the eigenfrequency of concrete structures may decrease with time as a consequence of the stiffness reduction of the concrete. This effect has to be taken into account in the dynamic analysis of concrete structures.

The sequence effect plays an important role on the fatigue behaviour of concrete. Most investigations, though, do not focus on this parameter and the available data is scarce. Similarly, there is a high dependency on the load frequency. For this reason, more research is mandatory in order to develop adequate as well as representative load spectra for future tests.

Almost inexistent is research work which focuses on the biaxial concrete behaviour under fatigue loading. The German standard DIN EN 1992-1 [52] pragmatically suggests to reduce $f_{c,fat}$ by the same factor which f_c is reduced for cases with transverse tension. Since this issue is of great interest for the structural design of nodal zones and membrane elements under fatigue (like brides under alternating shear forces and torsional moments), more effort is required in order to understand better the biaxial fatigue behaviour of concrete.

Chapter 4 analyses the tension-stiffening effect in reinforced tension chords under static-monotonic and fatigue loading. A general overview of the state-of-the-art is given and the reported response behaviour is described. Similar to the concrete behaviour after suffering a fatigue process, the bond between reinforcement and concrete also undergoes a degradation which leads to a stiffness decrease of the tension chord and, for instance, to greater deformations of the reinforcement while the concrete withdraws from the load transfer. This becomes visible through a continuous rise of the slip δ_s between reinforcement and concrete until $\delta_s = \delta_{s,max}$, which seems to be a limit. On the other hand, the weakening of the bond reduces the restraint forces between reinforcement and concrete. As a result, the value of the remaining crack widths tends to decrease after

unloading. In the $\sigma_{sr} - \epsilon_{sm}$-diagram the average value of E_{sm} progressively decreases until theoretically $E_{sm} = E_s$. At this stage the bond, at least at a serviceability level, practically does not participate on the load transfer. A further essential finding is the fact that the ultimate bond strength $\tau_{b,max}$ is not altered by the fatigue-induced damage – comparable to the uniaxial concrete compressive strength f_c.

Experiments were carried out in the scope of this work [4] with reinforced tension chords using representative, random loads derived from different, realistic wave spectra of the North Sea and partially applying an unfavourable transverse tension. The results are presented and discussed. The load frequency was low (1.0 Hz) in accordance with the offshore load frequency. A load-dependant bond degradation, also known as bond fatigue, can be confirmed. The mechanical behaviour of the tension chord depends indeed on the load history, the influence of transverse tension but does not clearly show to be significant. However, the variability is high and more specimens should be tested in order to obtain more statistical validity. The steel and concrete strains were continuously measured via special strain gauges located on a groove; the deformations were monitored using displacement transducers. On the basis of these results, the average reinforcement strain ϵ_{sm} was derived and evaluated. As expected, the bond degradation causes a stiffness loss: The value of E_{sm}, defined as the curve slope between two load peaks and which is calculated based on the data from the displacement transducers, shows a tendency to decrease, though, with a great variability. Nevertheless, a linear regression of the results is satisfactory and the development of E_{sm} over the load cycles is directly connected to the bond degradation. After achieving 10^6 fictive load cycles the tests were stopped and static-monotonically loaded up to failure. Immediately before this stage, the residual bond strength at a serviceability level may be described through the residual-bond parameter κ_{rsd} which, in fact, simply reflects the reduction of τ_{b0} according to the Tension Chord Model. κ_{rsd} is derived from the development of E_{sm} and amounts, on average, $\kappa_{rsd} = 0.50$.

While the bond fatigue causes a gradual decrease of the inclination of the $\sigma_{sr} - \epsilon_{sm}$-curve until it follows the response behaviour of the naked steel, a further effect has been registered by both, displacement transducers and strain gauges: The reinforcement shows in half of the tests additional, irreversible strains which grow gradually and may even exceed the limit ϵ_{sy}. This plastic-strain-accumulation effect may be a material property which in any case needs more clarification. A linear regression of the results indicates sufficient accuracy.

The Tension Chord Model [115] for static-monotonic loading is modified and adapted for fatigue loading. As long as $\sigma_{sr} < f_{sy}$, the average strain ϵ_{sm} consists of a linear part $\epsilon_{sm,\tau}$ which depends on the bond properties and of a plastic part $\epsilon_{sm,pl}$ that is rather an inherent material property.

At the ultimate limit state, after being subjected to a fatigue loading, the tested specimens did not present any reduction of the load-bearing capacity. Yet, the tension-stiffening effect was lower and thus the deformation capacity higher.

Chapter 5 focuses on beams with shear reinforcement under fatigue loading. After an overview of actual calculation models, this work adapts the Generalised Stress Field Analysis [177], developed originally for cases of static-monotonic loading. The Generalised Stress Field Analysis is based on universal kinematic relations and therefore valid also

for cases with a fatigue-induced damage. Using the data of experiments reported in the literature, the Generalised Stress Field Analysis is modified for fatigue loading, achieving a good agreement with the experimental results. Accordingly, the inclination of the compression strut Θ_{fat} under high-cycle fatigue loading is practically the same as in the ultimate state Θ_{ULS} for static-monotonic loading. Thereupon, the code-based design of the web reinforcement for fatigue is conservative. During the fatigue loading, a permanent state of internal force redistribution takes place and the concrete strain in the web increases. Only if the web reinforcement ruptures, the ultimate load-bearing capacity is reduced; otherwise, it remains unaltered.

Bibliography

1. ALBRECHT, G., M. RUTNER, KURITA A., and O. OHYAMA: 'Modification des DIN-Fachberichtes 104 hinsichtlich der Berechnung des Langzeit-Tension Stiffening'. *Stahlbau* (9 2004), vol. (73): pp. 648–655 (cit. on p. 103).
2. ALVAREZ, MANUEL: *Einfluss des Verbundverhaltens auf das Verformungsvermögen von Stahlbeton*. Vol. 236. IBK-Berichte. Basel [u.a.]: Birkhäuser, 1998. ISBN: 3-7643-5993-5 (cit. on pp. 37, 38, 80–82, 98, 117, 126–131).
3. ANDRIANOV, A. I.: 'Hydroelastic Analysis of very Large Structures'. PhD thesis. Delft University of Technology, 2005. ISBN: 90-8559-081-7 (cit. on p. 20).
4. ARANA VILLAFÁN, T. and V. SIGRIST: *Experimental Results on Bond Degradation between Concrete and Reinforcement*. Tech. rep. Hamburg University of Technology, 2017 (cit. on pp. 107, 108, 110, 114, 119, 125, 139, 171).
5. BACHMANN, H.: 'Zur plastizitätstheoretischen Berechnung statisch unbestimmter Stahlbetonbalken'. PhD thesis. Eidgenössische Technische Hochschule Zürich, 1967. 188 pp. (cit. on p. 125).
6. BALÁZS, G. L.: 'Bond Behaviour under Repeated Loads'. *Studi e Ricerche. Corso di Perfezionamento per le Construzioni in Cemento Armato F.lli Pesenti Politecnico di Milano, Italia* (1986), vol. 8: pp. 395–430 (cit. on pp. 90–93).
7. BALÁZS, G. L.: 'Cracking Analysis Based on Slip and Bond Stresses'. *ACI Materials Journal* (1993), vol. 90(4): pp. 340–348 (cit. on p. 99).
8. BALÁZS, G. L.: 'Fatigue of Bond'. *ACI Materials Journal* (1991), vol. 88(6): pp. 623–630 (cit. on pp. 89–91, 93).
9. BALÁZS, G. L., C. U. GROSSE, R. KOCH, and H. W. REINHARDT: 'Damage Accumulation on Deformed Steel Bar to Concrete Interaction Detected by Acoustic Emission Technique'. *Magazine of Concrete Research* (1996), vol. 48(177): pp. 311–320 (cit. on pp. 83, 90, 92).
10. BALÁZS, G. L. and R. KOCH: 'Bond Behaviour under Random Cyclic Loading'. *Otto-Graf-Journal* (1994), vol. 5: pp. 52–67 (cit. on p. 93).
11. BANERJEE, H. K., T. HODGKIESS, and P. D. ARTHUR: 'Fatigue in Prestressed Concrete for Marine Applications. Proceedings of the 4th International Conference on Behaviour of Offshore Structures (BOSS'85)'. *Behaviour of Offshore Structures*. Ed. by BATTJES, J.A. Elsevier Science Publishers B.V., Amsterdam, 1985: pp. 499–506. ISBN: 0-444-42513-6 (cit. on p. 75).

12. BARGEL, HANS-JÜRGEN, HERMANN HILBRANS, KARL-HEINZ HÜBNER, OSWALD KRÜGER, and GÜNTER SCHULZE: *Werkstoffkunde*. Springer Berlin Heidelberg, Mar. 30, 2006 (cit. on pp. 34, 35).

13. BAUMANN, T.: *Tragwirkung orthogonaler Bewehrungsnetze beliebiger Richtung in Flächentragwerken aus Stahlbeton*. Tech. rep. Deutscher Ausschuss für Stahlbeton, 1972 (cit. on pp. 156, 158).

14. BENEKE, H.: *Lexikon der Korrosion und des Korrosionsschutzes*. Vulkan, 2000. ISBN: 3-8027-2918-8 (cit. on p. 44).

15. BERGMEISTER, K.: *Beton-Kalender 2004*. Ed. by BERGMEISTER, K.; WÖRNER J.-D. Ernst & Sohn, 2004. ISBN: 3-433-01668-2 (cit. on pp. 10, 43, 44, 62, 63, 67, 89, 90, 95, 96).

16. BERGMEISTER, K., F. FINGERLOOS, and J. D. WÖRNER: *Beton-Kalender 2010*. Ernst & Sohn, 2010. ISBN: 9783433029312 (cit. on pp. 49–52).

17. BÉTON (CEB), COMITÉ EURO-INTERNATIONAL du, ed.: *Fatigue of Concrete Structures - State of the Art Report, Bulletin D'Information N°188*. 1988 (cit. on p. 63).

18. BOLLRICH, G. and G. PREISSLER: *Technische Hydromechanik*. Vol. 1. Verlag für Bauwesen GmbH, 1992. ISBN: 3-345-00518-2 (cit. on p. 24).

19. BORKOWSKI, G.: 'Beitrag zur Rechnerischen Überpruüfung von Hohlkastenbrücken'. PhD thesis. Technische Universität Hamburg-Harburg, 2014. 224 pp. (cit. on pp. 99, 100).

20. BREITENBÜCHER, R., H. IBUK, and H. ALAWIEH: *Influence of Cyclic Loading on the Degradation of Mechanical Concrete Properties*. *Advances in Construction Materials 2007*. 2007: pp. 317–324. ISBN: 978-3-540-72448-3 (cit. on pp. 64–66).

21. BRÜHWILER, E., L. ESKOLA, R. HAJDIN, P. KUNZ, J.-J. REBER, and V. SIGRIST: *Dokumentation D 0133 - Ermüdung von Betonbauten*. Tech. rep. SIA - Schweizerischer Ingenieur- und Architekten-Verein, 1997 (cit. on p. 67).

22. BÜRGEL, RALF, HANS ALBERT RICHARD, and ANDRE RIEMER: *Werkstoffmechanik*. Vieweg+Teubner Verlag, July 31, 2014. ISBN: 3658039345 (cit. on p. 35).

23. BURNS, C.: 'Serviceability Analysis of Reinforced Concrete Based on the Tension Chord Model'. PhD thesis. Eidgenössische Technische Hochschule Zürich, 2011. 149 pp. (cit. on pp. 82, 98).

24. *CEB-FIP Model Code 1990: Design code*. 1993 (cit. on pp. 45, 73, 78, 94, 103).

25. CHRIST, H.-J.: *Ermüdungsverhalten metallischer Werkstoffe (German Edition)*. Wiley-VCH, 2009. ISBN: 978-3-527-31340-2 (cit. on pp. 38, 39, 48).

26. CHRIST, H.-J.: *Wechselverformung von Metallen - Zyklisches Spannungs-Dehnungs-Verhalten und Mikrostruktur*. Springer, 1991. ISBN: 3-540-53962-X (cit. on pp. 48, 123).

27. CLAUSS, G., E. LEHMANN, and C. ÖSTERGAARD: *Offshore Structures. Strength and Safety for Structural Design*. Vol. II. Springer Verlag London Heidelnerg New York Paris Tokyo Hong Kong Barcelona Budapest, 1994. ISBN: 3-540-19770-2 (cit. on p. 27).

28. COMMITTEE, SHIP STRUCTURE: *Survey of Experience Using Reinforced Concrete in Floating Marine Structures*. Tech. rep. SSC-321. Ship Structure Committee, 1984 (cit. on p. 29).
29. CORNELISSEN, H. A. W.: 'Fatigue Failure of Concrete in Tension'. *HERON* (1984), vol. 29(4) (cit. on pp. 75, 76).
30. CORNELISSEN, H. A. W. and A. J. M. SIEMES: 'Plain Concrete under Sustained Tensile or Tensile and Compressive Fatigue Loadings. Proceedings of the 4th International Conference on Behaviour of Offshore Structures (BOSS'85)'. *Behaviour of Offshore Structures*. Ed. by BATTJES, J.A. Elsevier Science Publishers B.V., Amsterdam, 1985: pp. 487–498. ISBN: 0-444-42513-6 (cit. on pp. 69, 70, 74, 76).
31. COURTNEY, T.H.: *Mechanical Behavior of Materials*. McGraw Hill, 1990. ISBN: 0-07-100680-X (cit. on pp. 39, 43, 46, 112).
32. DANIELEWICZ, D.: 'Zur Ermüdungsbemessung von Beton-Straßenbrücken'. PhD thesis. Technische Universität Darmstadt, 1994 (cit. on pp. 44, 45).
33. DEHN, F.: *Konstruktionswerkstoffe Im Bauwesen*. Wiley-VCH Verlag GmbH, 2003. ISBN: 3-433-01652-6 (cit. on pp. 35–37).
34. DIBT DEUTSCHES INSTITUT FÜR BAUTECHNIK: *Betonstabstahl B500B mit Gewinderippen - SAS500 Nenndurchmesser: 12 bis 50 mm*. 2015 (cit. on p. 107).
35. *DIN 1055-100: Einwirkungen auf Tragwerke - Teil 100: Grundlagen der Tragwerksplanung - Sicherheitskonzept und Bemessungsregeln*. Deutsches Institut für Normung, 2001 (cit. on p. 9).
36. *DIN 488-1: Betonstahl - Teil 1: Stahlsorten, Eigenschaften, Kennzeichnung*. Deutsches Institut für Normung, 2009 (cit. on pp. 36, 85, 107, 109, 160).
37. *DIN 50100: Beton - Festlegung, Eigenschaften, Herstellung und Konformität*. Deutsches Institut für Normung, 2017 (cit. on p. 43).
38. *DIN EN 10020: Begriffsbestimmung für die Einteilung der Stähle*. Deutsches Institut für Normung, 2000 (cit. on p. 35).
39. *DIN EN 1990: Eurocode: Grundlagen der Tragwerksplanung*. Deutsches Institut für Normung, 2010 (cit. on pp. 5, 6, 8, 9).
40. *DIN EN ISO 15630-1: Stähle für die Bewehrung und das Vorspannen von Beton - Prüfverfahren - Teil 1: Bewehrungsstäbe, -walzdraht und -draht*. Berlin: Deutsches Institut für Normung, Feb. 2011 (cit. on p. 47).
41. *DIN Fachbericht 102: Betonbrücken*. 2009 (cit. on pp. 162, 163, 167).
42. *DNV OS C502 - Offshore Concrete Structures*. Det Norske Veritas AS, 2012 (cit. on pp. 43, 74, 95, 112, 157, 158).
43. *DNV RP C205 - Environmental Conditions and Environmental Loads*. Det Norske Veritas AS, 2010 (cit. on pp. 15, 17, 20, 24, 25, 112, 113).
44. EIBL, J. and G. IVÁNYI: *Heft 260: Studie zum Trag- und Verformungsverhalten von Stahlbeton*. Tech. rep. Deutscher Ausschuss für Stahlbeton, 1976 (cit. on pp. 49, 50).

45. ELIGEHAUSEN, R., H. KRELLER, and P. LANGER: *Untersuchungen zum Verbundverhalten gerripter Bewehrungsstäbe mit praxisüblicher Betondeckung*. Tech. rep. Universitä Stuttgart, 1989 (cit. on p. 85).

46. ELIGEHAUSEN, R., E. P. POPOV, and V. V. BERTÉRO: 'Local Bond Stress-Slip Relationships of Deformed Bars under Generalized Excitations'. *Proceedings of the 7th European Conference on Earthquake Engineering*. Vol. 4. Athens: Techn. Chamber of Greece, 1982: pp. 69–80. DOI: http://dx.doi.org/10.18419/opus-415 (cit. on p. 91).

47. FALTINSEN, O.M.: *Sea Loads on Ships and Offshore Structures*. Ed. by PRESS, CAMBRIDGE UNIVERSITY. 1990. ISBN: 0-521-45870-6 (cit. on pp. 15, 20–22, 26, 30).

48. FEHLMANN, P.: 'Zur Ermüdung von Stahlbetonbrücken'. de. PhD thesis. ETH Zurich, 2012. DOI: 10.3929/ethz-a-007110386 (cit. on pp. 47, 48, 142, 164).

49. FEHSENFELD, C.: 'Zur Rissbildung und Mindestbewehrung in Stahlbetontragwerken'. PhD thesis. Technische Universität Hamburg-Harburg, 2007. 185 pp. (cit. on pp. 54, 79, 80, 83–88, 98, 99, 102, 115, 130, 135, 136).

50. FERNANDEZ CANTELI, A., V. ESSLINGER, and B. THÜRLIMANN: *Ermüdungsfestigkeit von Bewehrungs- und Spannstählen (Institut für Baustatik. Versuchsberichte)*. Birkhäuser, 1980. ISBN: 3764316136 (cit. on p. 48).

51. FIB: *FIB Model Code for Concrete Structures 2010*. [Berlin]: Ernst & Sohn, 2013. ISBN: 978-3-433-03061-5 (cit. on pp. 45, 67, 73, 74, 77, 102, 112, 138, 148, 157, 158, 161, 165–167, 201).

52. FINGERLOOS, FRANK, JOSEF HEGGER, and KONRAD ZILCH: *Der Eurocode 2 für Deutschland. Kommentierte und konsolidierte Fassung: DIN EN 1992-1-1 Bemessung und Konstruktion von Stahlbeton- und Spannbetontragwerken - Teil 1-1 Allgemeine Regeln für den Hochbau*. 1. Auflage. Bauwesen. Berlin: Ernst, Wilhelm & Sohn, 2011. ISBN: 978-3-410-20088-8 (cit. on pp. 95, 109, 170).

53. FLÜGGEN, E., M. NÜSSBAUMER, and K. REUTER: 'A Concrete Storage Barge – Results of a Large Scale Offshore Model Test'. *Gastech 84 LNG/LPG Conference*. 1985 (cit. on p. 29).

54. FORSTER, S., K. MAEKAWA, and F. VECCHIO: *Practitioners' Guide to Finite Element Modelling of Reinforced Concrete Sructures. State-of-art-report*. bulletin 45. Tech. rep. fib - fédération internationale du béton, 2008. 337 pp. (cit. on pp. 99, 100).

55. FREY, R.P.: 'Ermüdung von Stahlbetonbalken unter Biegung und Querkraft'. PhD thesis. Eidgenössische Technische Hochschule Zürich, 1984. 105 pp. ISBN: 3-7643-1710-8 (cit. on p. 162).

56. FROST, N.E., K.J. MARSH, and L.P. POOK: *Metal Fatigue*. Oxford University Press, 1974. 491 pp. ISBN: 0-19-856114-8 (cit. on pp. 40, 46, 49).

57. FÜRST, A.: 'Vorgespannte Betonzuggliedern im Brückenbau'. PhD thesis. Eidgenössische Technische Hochschule Zürich, 2001 (cit. on pp. 50, 98, 135).

58. GEISSLER, K.: *Handbuch Brückenbau*. Ernst, Wilhelm & Sohn, 2014. ISBN: 978-3-433-60345-1 (cit. on pp. 8, 9).

59. GMBH, GERMANISCHER LLOYD INDUSTRIAL SERVICES: *Guideline for the Certification of Offshore Wind Turbines. Rules and Guidelines Industrial Services*. 2012 (cit. on pp. 10, 20).

60. GÖHLMANN, J.: 'Zur Schädigungsberechnung an Betonkonstruktionen für Windenergieanlagen unter mehrstufiger und mehraxialer Ermüdungsbeanspruchung'. PhD thesis. Leibnitz Universität Hannover, 2009. ISBN: 978-3-8167-8210-0 (cit. on pp. 66, 72, 73, 78).

61. GÓMEZ NAVARRO, M. and J.-P. LEBET: 'Concrete Cracking in Composite Bridges: Tests, Models and Design Proposals'. *Structural Engineering International* (2001), vol. (3): pp. 184–190 (cit. on pp. 105, 106).

62. GOTO, Y.: 'Cracks Formed in Concrete Around Deformed Tension Bars'. *ACI Journal* (1971): *68-26*, vol.: pp. 244–251 (cit. on pp. 79, 83).

63. GRIM, O.: *Bewegungen und Belastungen des Schiffes im Seegang*. 1980 (cit. on pp. 11, 13, 20, 25).

64. GROB, J.: *Ermüdung von Stahlbeton und Spannbetontragwerken*. Eidgen"ossische Technische Hochschule Z"urich, 1977 (cit. on pp. 153, 162).

65. GRÜNBERG, J., J. GÖHLMANN, and S. MARX: 'Mechanische Modelle fü mehraxiales Festigkeits- und Ermüdungsversagen von Stahlbeton'. *Beton- und Stahlbetonbau* (2014), vol. 109(6): pp. 403–416. DOI: 10.1002/best.201400022 (cit. on p. 78).

66. GRÜNBERG, JÜRGEN, ed.: *Grundlagen der Tragwerksplanung - Sicherheitskonzept und Bemessungsregeln für den konstruktiven Ingenieurbau: Erläuterungen zu DIN 1055-100*. 1. Aufl. Praxis Bauwesen. Berlin: Beuth, 2004. ISBN: 3-410-15845-6 (cit. on pp. 5, 7, 9, 112).

67. *Guidance Notes on Spectral-based Fatigue Analysis for Vessels*. American Bureau of Shipping, 2012 (cit. on pp. 25, 27).

68. GÜNTHER, G.: 'Verbundverhalten zwischen Stahl und Beton unter Monoton Steigender, Schwellender und Lang Andauernder Belastung'. PhD thesis. Universität Kassel, 1989. 154 pp. (cit. on pp. 100, 101, 104–106, 109).

69. GÜNTHER, G. and G. MEHLHORN: 'Verbund-Modell für Stahlbetontragwerke'. *Beton- und Stahlbetonbau* (9 1991), vol. (86) (cit. on pp. 104, 106).

70. GÜNTHER, G. and G. MEHLHORN: 'Wirkungszone der Bewehrung sowie Rißabstände und Rißbreiten bei Stahlbetonbauteilen'. *Beton- und Stahlbetonbau* (5 1991), vol. (86) (cit. on pp. 99, 104, 106).

71. GÜNTHER, G. and G. MEHLHORN: 'Zentrische Zugversuche an Stahlbetonkörpern zur Ermittlung der Mitwirkung des Betons zwischen den Rissen'. *Beton- und Stahlbetonbau* (3 1991), vol. (86) (cit. on pp. 104, 106).

72. HAAR, C. von der and S. MARX: 'Development of stiffness and ultrasonic pulse velocity of fatigue loaded concrete'. *Structural Concrete* (2016), vol. 17(4): pp. 630–636. DOI: 10.1002/suco.201600007 (cit. on pp. 65, 66, 164).

73. HACKBARTH, B.: 'Zur Querkrafttragfähigkeit von Stahl- und Spannbetonträgern mit Bügelbewehrung'. PhD thesis. Technische Universität Hamburg-Harburg, 2014. 189 pp. ISBN: 978-3-8440-3417-2 (cit. on pp. 156, 160).

74. HAIBACH, E.: *Betriebsfestigkeit. Verfahren und Daten zur Bauteilberechnung*. Springer Berlin Heidelberg New York, 2006. ISBN: 3-540-29363-9 (cit. on pp. 5, 6, 9).

75. HEEK, P. and P. MARK: 'Zur Ermüdung von Beton und Stahlfaserbeton - Wöhlerlinien unter Berücksichtigung spannungs- und materialabhängiger Duktilität'. *Beton- und Stahlbetonbau* (4 2016), vol. 111: pp. 221–232 (cit. on pp. 63, 65, 72).

76. HEEKE, G.: 'Untersuchungen zur Ermüdungsfestigkeit von Betonstahl und Spannstahl im Zeit- und Dauerfestigkeitsbereich mit sehr hohen Lastwechselzahlen'. PhD thesis. Technische Universität Dortmund, 2016 (cit. on p. 44).

77. *Heft 525: Erläuterungen zu DIN 1045-1*. Tech. rep. Deutscher Ausschuss für Stahlbeton, 2003 (cit. on p. 45).

78. *Heft 600: Erläuterungen zu DIN EN 1992-1-1 und DIN EN 1992-1-1/NA (Eurocode 2)*. Tech. rep. Deutscher Ausschuss für Stahlbeton, 2012 (cit. on pp. 101, 102).

79. HILFSDORF, H. K. and C. E. KESLER: 'Fatigue Strength of Concrete Under Varying Flexural Stresses'. *Journal of the American Concrete Institute* (1966), vol. (cit. on p. 70).

80. HILLERBORG, A., M. MODÉER, and P.-E. PETERSSON: 'Analysis of Crack Formation and Crack Growth in Concrete by Means of Fracture Mechanics and Finite Elements'. *Cement and Concrete Research* (1976), vol. 6. Ed. by PERGAMON PRESS, INC.: pp. 773–782 (cit. on p. 53).

81. HODGKIESS, T. and P. D. ARTHUR: *Fatigue and Corrosion Effects in Reinforced Concrete Beams Partially Submerged in Seawater and Subjected to Reverse Bending. Concrete in the Oceans Technical Report No. 19*. Tech. rep. Her Majesty's Stationery Office, 1988. 91 pp. (cit. on pp. 47, 75).

82. HOHBERG, R.: 'Zum Ermüdungsverhalten von Beton'. Dissertation. Berlin: Technische Universität Berlin, Mar. 22, 2004 (cit. on pp. 62, 63, 65, 67, 70, 72, 114).

83. HOLMEN, J. O.: 'Fatigue of Concrete by Constant and Variable Amplitude Loading'. PhD thesis. University of Trondheim, 1979 (cit. on pp. 64–66, 68–72, 77, 164).

84. HSU, T. T. C.: 'Fatigue of Plain Concrete'. *ACI Journal* (1981), vol.: pp. 292–305 (cit. on p. 67).

85. HÜMME, J., C. von der HAAR, L. LOHAUS, and S. MARX: 'Fatigue Behaviour of a Normal-Strength Concrete - Number of Cycles to Failure and Strain Development'. *Structural Concrete* (2016), vol. 17(4): pp. 637–645. DOI: 10.1002/suco.201500139 (cit. on pp. 63–65, 67, 68).

86. IDDA, K.: 'Verbundverhalten von Betonrippenstählen bei Querzug'. PhD thesis. Karlsruhe: Universität Fridericiana zu Karlsruhe, 1999 (cit. on pp. 80, 89, 90).

87. INSTITUTE, AMERICAN CONCRETE: *Report on Floating an Float-In Concrete Structures. Reported by ACI Committee 357*. Tech. rep. ACI 357.2R-10, 2010 (cit. on p. 29).
88. INSTITUTE, AMERICAN CONCRETE: *State-of-the-Art Report: Bond under Cyclic Loads*. Tech. rep. ACI Committee 408, 1999 (cit. on pp. 90, 91).
89. *Internationaler Schweissfachingenieurlehrgang (SFI)*. GSI - Gesellschaft für Schweißtechnik International mbH, 2017 (cit. on pp. 33–39, 47, 48, 122).
90. JOURNÉE, J. M. J. and W. W. MASSIE: *Offshore Hydromechanics: First Edition*. 2001 (cit. on pp. 11, 14, 15, 18, 19).
91. KÄMPFE, HANSGERD: *Kleine Betonstahlkunde*. Vieweg+Teubner, 2010: pp. 23–44. DOI: 10.1007/978-3-8348-9920-0_3 (cit. on p. 36).
92. KAUFMANN, W.: 'Strength and Deformations of Structural Concrete Subjected to In-Plane Shear and Normal Forces'. PhD thesis. Institut für Baustatik und Konstruktion, Eidgenössische Technische Hochschule Zürich, 1998 (cit. on pp. 50, 51, 98, 155, 156, 158).
93. KAUFMANN, W.: 'Structural Concrete: Cracked Membrane Model'. *Journal of Structural Engineering* (1998), vol. 124(12): pp. 1467–1475 (cit. on pp. 156, 158).
94. KENEL, A.: 'Biegetragverhalten und Mindestbewehrung von Stalbetonbauteilen'. PhD thesis. Institut für Baustatik und Konstruktion, Eidgenössische Technische Hochschule Zürich, 2002 (cit. on pp. 52–54).
95. KENEL, A. and P. MARTI: *Faseroptische Dehnungsmessungen an einbetonierten Bewehrungsstäben*. Vol. Nr. 271. IBK-Bericht. Zürich: Vdf, Hochschulverl. an der ETH, 2002. ISBN: 3-7281-2835-X (cit. on p. 131).
96. KESSLER-KRAMER, C.: 'Zugtragverhalten von Beton unter Ermüdungsbeanspruchung'. PhD thesis. Universität Fridericiana zu Karlsruhe (TH), 2002 (cit. on pp. 76, 78).
97. KHABAKHPASHEVA, T. I. and KOROBKIN A. A.: 'Hydroelastic Behaviour of Compound Floating Plate in Waves'. *Journal of Engineering Mathematics* (44 2002), vol.: pp. 21–40 (cit. on p. 20).
98. KOHL, M.: 'Tragverhalten von Stahlbetontragwerken ohne Querkraftbewehrung unter Ermüdungsbeanspruchungen'. PhD thesis. Technische Universität Hamburg-Harburg, 2014: p. 319. ISBN: 9783844033427 (cit. on p. 72).
99. KÖHLER, M., S. JENNE, K. PÖTTER, and H. ZENNER: *Zählverfahren und Lastannahme in der Betriebsfestigkeit*. Springer Verlag, 2010. ISBN: 978-3-642-13163-9 (cit. on p. 29).
100. KOKKINOWRACHOS, K.: *Hydromechanik der Seebauwerke*. WENDEL, K. *Handbuch der Werften XV*. Ed. by HANSA, SCHIFFAHRTS-VERLAG. 1980 (cit. on pp. 12, 14, 18).
101. KOLLEGER, J.: 'Tension Stiffening bei schräg zum Riß angeordneten Bewehrungsstäben'. *Der Bauingenieur* (1992), vol. 67: pp. 35–38 (cit. on pp. 102, 103).
102. KÖNIG, G. and I. DANIELEWICZ: *Heft 439: Ermüdungsfestigkeit von Stahlbeton und Spannbetonbauteilen mit Erläuterungen zu den Nachweisen gemäß CEB-FIP Model Code 1990*. Tech. rep. Deutscher Ausschuss fü Stahlbeton, 1994 (cit. on pp. 39, 43, 44, 47, 48, 62, 73, 78).

103. KOPPITZ, R., A. KENEL, and T. KELLER: 'Tension Chord Modification for Uniaxial Unloading and Reloading in Elastic and Plastic States'. *ASCE Journal of Structural Engineering* (2014), vol. DOI: 10.1061/(ASCE)ST.1943-541X.0000999 (cit. on pp. 97, 98, 117, 118, 131, 132, 134, 135, 139, 142, 143, 145, 150).

104. KUPFER, H.: *Heft 229: Das Verhalten des Betons unter Mehrachsiger Kurzzeitbelastung unter Besonderer Berücksichtigung der Zweiachsigen Beanspruchung*. Tech. rep. Deutscher Ausschuss für Stahlbeton, 1973 (cit. on pp. 55, 56).

105. KUPFER, H. and H. K. HILSDORF: 'Behavior of Concrete under Biaxial Stresses'. *ACI Journal* (1969), vol.: pp. 656–666 (cit. on pp. 54–57, 153, 164).

106. LEEUWEN, J. van and A. J. M. SIEMES: 'Miner's Rule with Respect to Plain Concrete'. *Boss'79 - Second International Conference on Behaviour of Off-shore Structures*. 1979 (cit. on pp. 67, 68).

107. LEMNITZER, L., L. ECKFELDT, A. LINDORF, and M. CURBACH: *Tailor Made Concrete Structures: New Solutions for our Society. Biaxial Tensile Strength of Concrete - Answers from Statistics*. Ed. by WALRAVEN J.C.; Stoelhorst, D. CRC Press, 2008. ISBN: 978-0-415-47535-8 (cit. on pp. 54, 56).

108. LEONHARDT, F.: *Nachweis der Gebrauchsfähigkeit. Rissebeschränkung, Formänderungen, Momentenumlagerung und Bruchlinientheorie im Stahlbetonbau. Vorlesungen über Massivbau. Vierter Teil*. Springer-Verlag Berlin Heidelberg New York, 1978. 194 pp. ISBN: 3-540-08625-0 (cit. on pp. 101–103).

109. LINDORF, A.: 'Ermüdung des Verbundes von Stahlbeton unter Querzug'. PhD thesis. Technische Universität Dresden, 2011. 228 pp. (cit. on pp. 80, 83–85, 89, 96, 97, 139).

110. LINDORF, A. and M. CURBACH: 'Fatigue of Bond between Reinforcement and Concrete under Transverse Tension'. *fib Symposium PRAGUE 2011*. 2011. ISBN: 978-80-87158-29-6 (cit. on p. 96).

111. 'Long Term Random Dynamic Loading of Concrete Structures'. *Materials and Structures* (1984), vol. 17(97) (cit. on pp. 43, 47, 48, 62, 73, 74).

112. MARTI, P.: *Baustatik: Grundlagen, Stabtragwerke, Flächentragwerk*. Ernst & Sohn, 2012. ISBN: 9783433029909 (cit. on pp. 41–43, 59, 153).

113. MARTI, P.: 'Design of Concrete Slabs for Transverse Shear'. *ACI Structural Journal* (1990), vol. 2(87): pp. 180–190 (cit. on p. 99).

114. MARTI, P.: 'Zur Plastischen Berechnung von Stahlbeton'. PhD thesis. Institut für Baustatik und Konstruktion, Eidgenössische Technische Hochschule Zürich, 1980 (cit. on pp. 54, 57–59).

115. MARTI, P., M. ALVAREZ, W. KAUFMANN, and V. SIGRIST: 'Tension Chord Model for Structural Concrete'. *Structural Engineering International* (1998), vol. Volume 8(Number 4): pp. 287–298. DOI: 10.2749/101686698780488875 (cit. on pp. e, 2, 98, 104, 160, 171).

116. MARTI, P., M. ALVAREZ, W. KAUFMANN, and V. SIGRIST: *Tragverhalten von Stahlbeton - Fortbildungskurs für Bauingenieure*. Institut für Baustatik und Konstruktion, ETH Zürich-Hönggerberg, 1999 (cit. on pp. 37, 50, 99, 127, 128, 155–157).

117. MARTI, P., M. ALVAREZ, and S. VIKTOR: 'Rissbildung und Mindestbewehrung'. *Schweizer Ingenieur und Architekt* (1997), vol. 115(41). DOI: 10.5169/seals-79321 (cit. on p. 98).

118. MARTIN, H.: *Zusammenhang zwischen Oberflächenbeschaffenheit, Verbund und Sprengwirkung von Bewehrungsstählen unter Kurzzeitbelastung. Heft 228*. Tech. rep. Deutscher Ausschuss für Stahlbeton, 1973. 50 pp. (cit. on pp. 79, 82, 84–86).

119. MARTIN, H. and P. NOAKOWSKI: *Verbundverhalten von Betonstählen – Untersuchung auf Grundlage von Ausziehversuchen. Heft 319*. Tech. rep. Deutscher Ausschuss für Stahlbeton, 1981. 50 pp. (cit. on pp. 80, 84, 85).

120. MAURER, R.: 'Bestimmung der Ermüdungsfestigkeit von einbetoniertem Betonstahl mit dem Interaktiven Verfahren'. *DIBt Mitteilungen* (2010), vol. 41(1): pp. 35–35. DOI: 10.1002/dibt.201030007 (cit. on p. 44).

121. MEHLHORN, G.: *Der Ingenieurbau. Grundwissen. Rechnerorientierte Baumechanik*. Ernst & Sohn, 1995. ISBN: 3-433-01572-4 (cit. on pp. 99, 100).

122. MILELLA, P. P.: *Fatigue and Corrosion in Metals*. Springer Milan, 2013. DOI: 10.1007/978-88-470-2336-9 (cit. on pp. 39, 49).

123. MITZLAFF, A.: 'Meerestechnik. Vorlesunsmanuskript der Technischen Universität Hamburg-Harburg'. 2014 (cit. on pp. 15, 20, 22–24).

124. MÖBIUS, F.: 'Kraft-Verformungs-Verhalten von umschnürtem Stahlbeton'. PhD thesis. Institut für Massivbau, Technische Universität Hamburg-Harburg, 2009 (cit. on pp. 50, 52).

125. MOLINAS VEGA, I., M. A. BHATTI, and W. A. NIXON: 'A Non-Linear Fatigue Damage Model for Concrete in Tension'. *International Journal of Damage Mechanics* (1995), vol. 4(4): pp. 362–379. DOI: 10.1177/105678959500400404 (cit. on p. 76).

126. MUTTONI, A. and FERNÁNDEZ RUIZ M.: 'Concrete Cracking in Tension Members and Application to Deck Slabs of Bridges'. *ASCE Journal of Bridge Engineering* (2007), vol. 12(5): pp. 646–653. DOI: 10.1061/ASCE1084-0702200712:5646 (cit. on p. 117).

127. NAUDASCHER, E.: *Hydrodynamic Forces*. A. A. Balkema Publishers, 1991. ISBN: 9061919932 (cit. on p. 20).

128. NAUDASCHER, E. and D. ROCKWELL: *Flow-induced Vibrations. An Engineering Guide*. Dover Publications, 1994. ISBN: 9780486136134 (cit. on p. 20).

129. NEWMAN, J. N.: *Marine Hydrodynamics*. Ed. by TECHNOLOGY, THE MASSACHUSETTS INSTITUTE of. 1977. ISBN: 0-262-14026-8 (cit. on p. 15).

130. NIGEL BARLTROP, A. A.: *Floating Structures: a guide for design and analysis*. The Centre for Marine and Petroleum Technology, 1998. ISBN: 1-870553-357 (cit. on pp. 10, 16, 26).

131. NIGEL BARLTROP, ADRIAN ADAMS: *Dynamics of Fixed Marine Structures*. Butterworth-Heinemann, 1991. ISBN: 978-0750610469 (cit. on pp. 11, 15, 16, 18, 19, 21, 23, 24, 28).

132. NORMUNG, DEUTSCHES INSTITUT fü, ed.: *Eurocode 2: Bemessung und Konstruktion von Stahlbeton- und Spannbetontragwerken - Teil 2: Betonbrücken - Bemessungs- und Konstruktionsregeln*. 2010 (cit. on pp. 73, 77, 158).

133. NORMUNG, DEUTSCHES INSTITUT fü, ed.: *Nationaler Anhang - National festgelegte Parameter - Eurocode 2: Bemessung und Konstruktion von Stahlbeton- und Spannbetontragwerken - Teil 2: Betonbrücken - Bemessungs- und Konstruktionsregeln*. 2013 (cit. on pp. 43, 44, 167).

134. NUSSBAUMER, M. and J.H. RÖSSIG: 'The Seadeck Test Structure: Experiences and Results of a Large-scale Test Carried Out with a Floating Prestressed Concrete Structure in the Harsh North Sea Environment'. *Marine Concrete '86 - International Conference on Concrete in the Marine Environment*. The Concrete Society, 1986 (cit. on pp. 29, 31).

135. OH, B. H.: 'Cumulative Damage Theory of Concrete under Variable-Amplitude Fatigue Loadings'. *ACI Materials Journal* (1991), vol. 88(1): pp. 41–48 (cit. on pp. 70, 71, 78).

136. OH, B. H. and S. H. KIM: 'Realistic Models for Local Bond Stress-Slip of Reinforced Concrete under Repeated Loading'. *ASCE Journal of Structural Engineering* (2007), vol. 133(2): pp. 216–224. DOI: 10.1061/(ASCE)0733-9445(2007)133:2(216) (cit. on pp. 91, 93, 95).

137. ONESCHKOW, N.: 'Analyse des Ermüdungsverhaltens von Beton anhand der Dehnungsentwicklung'. PhD thesis. Institut für Baustoffe, Leibniz Universität Hannover, 2014 (cit. on pp. 62, 63, 67, 73, 79).

138. ONESCHKOW, N. and L. LOHAUS: 'Zum Ermüdungsnachweis von druckschwellbeanspruchtem Beton - Teil 1: Struktur des Ermüdungsnachweis'. *Beton- und Stahlbetonbau* (2017), vol. 112(8): pp. 530–540. DOI: 10.1002/best.201700024 (cit. on p. 73).

139. ONESCHKOW, N. and L. LOHAUS: 'Zum Ermüdungsnachweis von druckschwellbeanspruchtem Beton - Teil 2: Sicherheitsüberlegungen und Potenzial für Weiterentwicklungen'. *Beton- und Stahlbetonbau* (2017), vol. 112(9): pp. 611–622. DOI: 10.1002/best.201700026 (cit. on p. 74).

140. PARK, Y. J.: 'Fatigue of Concrete under Random Loadings'. *Journal of Structural Engineering* (1990), vol. 116(11): pp. 3228–3235 (cit. on pp. 72, 103).

141. PATERSON, W. S. and M. J. DILL: *Fatigue Strength of Reinforced Concrete in Seawater – Results from Phase II. Concrete in the Oceans Technical Report No. 20*. Tech. rep. Her Majesty's Stationery Office, 1988. 57 pp. (cit. on p. 75).

142. PÉREZ FERNÁNDEZ, R. and M. LAMAS PARDO: 'Offshore concrete structures'. *Ocean Engineering* (2013), vol. 58: pp. 304–316. ISSN: 0029-8018 (cit. on p. 29).

143. PETERSEN, C.: *Dynamik der Baukonstruktionen*. Ed. by MBH, FRIEDR. VIEWEG & SOHN VERLEGGESELLSCHAFT. 2000 (cit. on p. 17).

144. PFANNER, D.: 'Zur Degradation von Stahlbetonbauteilen unter Ermüdungsbeanspruchung'. PhD thesis. Ruhr-Universität Bochum, 2002. ISBN: 3-18-318904-6 (cit. on pp. 63, 72, 73, 78).

145. PFEIFFER, U.: *INCA 2 - Interactive Nonlinear Cross-Section Analysis Biaxial. Version 2.90*. 2019. URL: http://www.u-pfeiffer.de/inca2/inca2-09.html (cit. on pp. 164–166).

146. PLATE, ERICH J., ed.: *Statistik und angewandte Wahrscheinlichkeitslehre für Bauingenieure*. Berlin: Ernst, 1993. ISBN: 3-433-01073-0 (cit. on p. 6).

147. POCHANART, S. and T. HARMON: 'Bond-Slip Model for Generalized Excitations Including Fatigue'. *ACI Materials Journal* (1989), vol. 86(5): pp. 465–474 (cit. on p. 95).

148. POOK, L.: *Metal Fatigue: What It Is, Why It Matters: 145 (Solid Mechanics and Its Applications)*. Springer, 2007. ISBN: 978-1-4020-5597-3 (cit. on p. 48).

149. PRICE, W., E. C. HAMBLY, A. H. TRICKLEBANK, E. W. H. GIFFORD, and PARTNERS: *Review of Fatigue in Concrete Marine Structures. Concrete in the Oceans Technical Report No. 12*. Tech. rep. Her Majesty's Stationery Office, 1989. 106 pp. (cit. on pp. 43, 47, 75).

150. PRICE, W.I.J., A.H. TRICKLEBANK, and E.C. HAMBLY: 'Fatigue Considerations in the Design of Offhore Concrete Structures'. *IABSE International Association for Bridge and Structural Engineering* (1982), vol. 37 (cit. on p. 29).

151. REHM, G.: *Qualitätsstandard bei Betonstahl: Festschrift zum 60. Geburtstag von Harald Budelmann*. Ed. by REHM, GALLUS and HARTMUT WILHELM. Springer-Verlag Berlin Heidelberg, 2013. DOI: 10.1007/978-3-642-29573-7{\textunderscore}7 (cit. on pp. 43, 44).

152. REHM, G.: *Über die Grundlagen des Verbundes zwischen Stahl und Beton*. Tech. rep. Heft 138. Deutscher Ausschuss für Stahlbeton, 1961. 59 pp. (cit. on pp. 79, 81–83, 85).

153. REHM, G. and R. ELIGEHAUSEN: 'Einfluß einer nicht ruhenden Belastung auf das Verbundverhalten von Rippenstählen'. *Betonwerk + Fertigteil-Technik* (1977), vol. (6): pp. 295–299 (cit. on pp. 90–92).

154. REINHARDT, H.-W.: *Ingenieurbaustoffe*. Ernst W. + Sohn Verlag, Apr. 19, 2010. ISBN: 978-3-433-02920-6 (cit. on pp. 36, 37, 52).

155. REINHARDT, H.-W. and H. A. W. CORNELISSEN: 'Post-peak Cyclic Behaviour of Concrete in Uniaxial Tensile and Alternating Tensile and Compressive Loading'. *Cement and Concrete Research* (1984), vol. 14: pp. 263–270 (cit. on pp. 76, 77).

156. RITTER, L.: 'Der Einfluss von Querzug auf den Verbund zwischen Beton und Betonstahl'. PhD thesis. Technische Universität Dresden, 2013 (cit. on pp. 79, 83, 88, 89, 137).

157. ROGGE, A.: 'Materialverhalten von Beton unter mehrachsiger Beanspruchung'. PhD thesis. Technische Universität München, 2003 (cit. on pp. 49, 50, 55–61).

158. ROGGENDORF, T. and C. GORALSKI: 'Ermüdungsverhalten von Beton unter zyklischer Beanspruchung aus dem Betrieb von Windenergieanlagen'. *Beton- und Stahlbetonbau* (2014), vol. 109(11): pp. 824–828. DOI: 10.1002/best.201400064 (cit. on p. 65).

159. ROGNAAS, G., J. XU, S. LINDSETH, and F. ROSENDAHL: 'Mobile Offshore Base Concepts. Concrete Hull and Steel Topsides'. *Marine Structures* (2001), vol. (14): pp. 5–23 (cit. on p. 29).

160. ROMBACH, G.: *Anwendung der Finite-Elemente-Methode im Betonbau. Fehlerquellen und ihre Vermeidung*. 2nd ed. Ernst & Sohn, 2006. ISBN: 978-3-433-01701-2 (cit. on p. 99).

161. RTEIL, A., K. SOUDKI, and T. TOPPER: 'Mechanics of Bond under Repeated Loading'. *Construction and Building Materials* (2011), vol. (25): pp. 2822–2827 (cit. on pp. 95, 96).

162. SCHENKEL, M.: 'Zum Verbundverhalten von Bewehrung bei kleiner Betondeckung'. PhD thesis. Eidgenössische Technische Hochschule Zürich, 1998. 162 pp. (cit. on pp. 85–88, 136–138).

163. SCHIESSL, P.: *Heft 400: Grundlagen der Neuregelung zur Beschränkung der Rißbreite*. Tech. rep. 1989 (cit. on p. 82).

164. SCHIJVE, J.: *Fatigue of Structures and Materials*. Springer Netherlands, Dec. 22, 2008. 648 pp. ISBN: 1402068077 (cit. on pp. 39, 40, 43, 47, 48).

165. SCHLAICH, J. and K. SCHÄFER: *Konstruieren im Stahlbetonbau*. *Beton-Kalender 2001*. Ed. by EIBL, J. Wilhelm Ernst & Sohn Verlag fur Architektur und technische Wissenschaften, 2001 (cit. on p. 158).

166. SCHNEIDER, J. and SCHLATTER H. P.: *Sicherheit und Zuverlässigkeit im Bauwesen. Grundwissen für Ingenieure*. 2007 (cit. on pp. 6–8).

167. SCHNEIDER, S., D. VÖCKER, and M. MARX: 'Zum Einfluss der Belastungsfrequenz und der Spannungsgeschwindigkeit auf die Ermüdungsfestigkeit von Beton'. *Beton- und Stahlbetonbau* (2012), vol. 107(12): pp. 836–845. DOI: 10.1002/best.201200054 (cit. on p. 67).

168. SCHOBER, H.: 'Ein Modell zur Berechnung des Verbunds und der Risse im Stahl- und Spannbeton'. PhD thesis. Universität Stuttgart, 1984 (cit. on p. 137).

169. SCHOTT, G.: *Werkstoffermüdung - Ermüdungsfestigkeit*. 4. Edition. Stuttgart: Gesellschaft für Grundstoffindustrie, 1997. ISBN: 3342005114 (cit. on pp. 33, 34, 38–41, 43, 48).

170. SCHRÖDER, S.: 'Der Einfluss einer zweiachsialen Zugbelastung auf das Festigkeits- und Verformungsverhalten von Beton und gemischt bewehrten Bauteilen'. PhD thesis. Technische Universität Dresden, 2012 (cit. on p. 54).

171. SCHULTZ, H.-G. and E. von SCHULZ: *Zur Spannanungsanalyse von Schiffen im Seegang über die Methode finiter Elemente (FEMPA)*. Rheinisch Westfälische Technische Hochschule Aachen, 1976 (cit. on pp. 21–23).

172. SCHULZE, G.: *Die Metallurgie des Schweißens*. Springer Berlin Heidelberg, 2010. DOI: 10.1007/978-3-642-03183-0 (cit. on p. 33).

173. SCOTT, R. H. and P. A. T. GILL: 'Developments in the Measurement of Reinforcement Strain Distributions in Reinforced Concrete Members'. *Strain* (1982), vol.: pp. 61–63, 79 (cit. on p. 109).

174. SCOTT, R. H. and P. A. T. GILL: 'Reinforcement Strains in Reinforced Concrete Tension Members'. *IABSE congress report* (1984), vol. 12: pp. 919–925 (cit. on p. 109).

175. SEELHOFER, H.: 'Ebener Spannungszustand im Betonbau: Grundlagen und Anwendungen'. PhD thesis. Institut für Baustatik und Konstruktion, Eidgenössische Technische Hochschule Zürich, 2009 (cit. on pp. 51, 52, 155, 156).

176. SHARP, J. V., M. B. LEEMING, and R. K. VENABLES: *Concrete in the Oceans. Management Summary on the Whole Programme. Concrete in the Oceans Technical Report No. 26*. Tech. rep. Her Majesty's Stationery Office, 1989. 19 pp. (cit. on p. 75).

177. SIGRIST, V.: 'Generalized Stress Field Approach for Analysis of Beams in Shear'. *ACI Structural Journal* (2011), vol. 108(4): pp. 479–487 (cit. on pp. e, 3, 98, 153, 154, 156, 158–160, 163–165, 171).

178. SIGRIST, V.: 'Zum Verformungsvermögen von Stahlbetonträgern: Dissertation'. PhD thesis. Basel and Boston: Eidgenössische Technische Hochschule Zürich, 1995. ISBN: 3-7643-5279-5 (cit. on pp. 37–40, 50, 59, 73, 97, 98, 117, 125, 131).

179. SIGRIST, V. and T. ARANA VILLAFÁN: 'Long, Deep, Solid - Engineering Structures for Future Ports'. *Ports for Container Ships of Future Generations*. 2014 (cit. on p. 10).

180. SIGRIST, V. and B. HACKBARTH: 'Querkrafttragfähigkeit von Stahlbetonträgern'. *Beton- und Stahlbetonbau* (2010), vol. 105(11): pp. 686–694. DOI: 10.1002/best.201000052 (cit. on p. 159).

181. SIPPEL, T. M.: 'Zum Trag- und Verformungsverhalten von Stahlbetontragwerken unter Betriebsbelastung'. PhD thesis. Universität Stuttgart, 1996. 195 pp. (cit. on pp. 102–104, 106).

182. SLOWIK, V. and V. E. SAOUMA: 'Water Pressure in Propagating Concrete Cracks'. *Journal of Structural Engineering* (2000), vol. 126(2): pp. 235–242 (cit. on p. 74).

183. SPAETHE, GERHARD, ed.: *Die Sicherheit tragender Baukonstruktionen*. 2., neubearb. Aufl. Wien [u.a.]: Springer, 1992. ISBN: 3-211-82348-4 (cit. on p. 6).

184. SPATHELF, C.A.: 'Fatigue Performance of Orthogonally Reinforced Concrete Slabs'. PhD thesis. Eidgenössische Technische Hochschule Zürich, 2017: p. 214 (cit. on p. 142).

185. SPECK, K.: 'Beton unter Mehraxialer Beanspruchung. Ein Materialgesetz für Hochleistungsbetone unter Kurzzeitbelastung'. PhD thesis. Technische Universität Dresden, 2008 (cit. on pp. 57, 59, 61).

186. STARR, P. and D.A. WAINWRIGHT: 'Design and Construction of a Floating Concrete Berth'. *Engineering Structures* (1996), vol. 18(11): pp. 837–841 (cit. on p. 29).

187. STEMPNIEWSKI, L.: *Beton-Kalender 1996. Finite Elemente im Stahlbeton*. Ed. by EIBL, J. 1996. ISBN: 3433014167 (cit. on p. 100).

188. SUBRAMANIAM, K. V., J. S. POPOVICS, and S. P. SHAH: 'Fatigue Response of Concrete Subjected to Biaxial Stresses in the Compression-Tension Region'. *ACI Materials Journal* (1999), vol. 96(6): pp. 663–669 (cit. on pp. 77, 78).

189. TEPFERS, R.: 'Tensile Fatigue Strength of Plain Concrete'. *ACI Journal* (1979), vol.: pp. 919–933 (cit. on p. 76).

190. TEPFERS, R. ET AL.: *Bond of Reinforcement in Concrete. State-of-the-Art Report*. bulletin 10. Tech. rep. fib - fédération internationale du béton, 2000. 434 pp. (cit. on pp. 79, 82, 83, 89).

191. TEWORTE, F.: 'Zum Querkrafttragverhalten von Spannbetonträgern unter Ermüdungsbeanspruchung'. PhD thesis. Rheinisch-Westfälische Technische Hochschule, 2014. 211 pp. ISBN: 3-939051-18-7 (cit. on pp. 162, 163, 165–167).

192. TORRENTI, J.-M. ET. AL.: *Mechanical Behavior of Concrete*. Wiley-ISTE, 2010. ISBN: 9781848211780 (cit. on pp. 52–56, 74, 78).

193. U. H. CLORMANN and T. SEEGER: 'Rainflow - HCM: Ein Zählverfahren für Betriebsfestigkeitsnachweise auf werkstoffmechanischer Grundlage'. *Stahlbau* (1986), vol. 55(3): pp. 65–71 (cit. on pp. 29, 114, 195).

194. VECCHIO, F. J. and M. P. COLLINS: 'The Modified Compression-Field Theory for Reinforced Concrete Elements Subjected to Shear'. *ACI Structural Journal* (1986), vol. 83(2): pp. 219–231 (cit. on p. 156).

195. WAAGAARD, K.: 'Fatigue Strength Evaluation of Offshore Concrete Structures'. *IABSE proceedings* (1982), vol. 6(P-56): pp. 98–114 (cit. on pp. 70, 74).

196. WAGNER, H.: *Theorie der Wellenbewegung*. BOLLRICH, G. *Technische Hydromechanik, Band 2*. Ed. by BAUWESEN, VEB VERLAG für. 1st ed. 1989 (cit. on pp. 12, 14).

197. WAGNER, P.: *Meerestechnik. Eine Einführung für Bauingenieure*. Ernst W. + Sohn Verlag, 1990. ISBN: 3-433-01212-1 (cit. on p. 21).

198. WASNER, J.: 'Rissbildung in fugenlosen Kaianlagen - ein Berechnungsmodell für massige Bauteile aus Stahlbeton'. PhD thesis. Technische Universität Hamburg-Harburg, 2015. ISBN: 978-3-8440-3376-2. DOI: 10.15480/882.1327 (cit. on p. 135).

199. WEIRICH, T.: 'Ermüdungsverhalten des Betonstahls unter Berücksichtigung möglicher Korrosionseinflüsse'. PhD thesis. Universität Stuttgart, 2013 (cit. on pp. 36, 43, 47).

200. WILL, N.: 'Zum Verbundverhalten von Spanngliedern mit nachträglichem Verbund unter statischer und dynamischer Dauerbeanspruchung'. PhD thesis. RWTH Rhein Westfälische Technische Hochschule Aachen, 1997. ISBN: 3-9804729-4-9 (cit. on p. 136).

201. WILLAM, K. J. and E. P. WARNKE: 'Constitutive Model for the Triaxial Behaviour of Concrete'. *IABSE International Association for Bridge and Structural Engineering* (1974), vol. 19: pp. 1–30 (cit. on pp. 59–61, 78).

202. ZALESKI-ZAMENHOF, L.C., B.C. GERWICK, J. HELLESLAND, M. MATSUISHI, and X. ZHANG: 'Concrete Marine Structures: A State-of-the-Art Review'. *Marine Structures* (1990), vol. (3): pp. 199–235 (cit. on p. 29).

203. ZANUY, C.: 'Analytical Approach to Factors Affecting Long-Term Tension Stiffening'. *Magazine of Concrete Research* (2010), vol. 62(12): pp. 869–878. DOI: 10.1680/macr.2010.62.12.869 (cit. on p. 106).

204. ZANUY, C., L. ALBAJAR, and P. de la FUENTE: 'On the Cracking Behaviour of a Reinforced Concrete Tension Chord under Repeated Loading'. *Materials and Structures* (2010), vol. (43): pp. 611–632. DOI: 10.1617/s11527-009-9516-9 (cit. on pp. 106, 107, 135, 138).

205. ZANUY, C., L. ALBAJAR, and P. de la FUENTE: 'Tension Stiffening of Memebers under Highly Repeated Loads'. *3rd fib International Congress*. 2010 (cit. on p. 106).

206. ZANUY, C., P. de la FUENTE, and L. ALBAJAR: 'Estimation of Parameters Defining Negative Tension Stiffening'. *Engineering Structures* (2010), vol. (32): pp. 3355–3362. DOI: 10.1016/j.engstruct.2010.07.009 (cit. on p. 106).

207. ZHANG, B., D. V. PHILLIPS, and K. WU: 'Effects of Loading Frequency and Stress Reversal on Fatigue Life of Plain Concrete'. *Magazine of Concrete Research* (1996), vol. 48(177): pp. 361–375 (cit. on p. 62).

208. ZHANG, B., D. V. PHILLIPS, and K. WU: 'Further research on fatigue properties of plain concrete'. *Magazine of Concrete Research* (1997), vol. 49(180): pp. 241–252 (cit. on pp. 67, 74).

209. ZILCH, K. and G. ZEHETMAIER: *Bemessung im konstruktiven Betonbau*. Springer Berlin Heidelberg, 2010. DOI: 10.1007/978-3-540-70638-0 (cit. on pp. 9, 43, 44, 100–102, 158).

List of Figures

List of Tables

A Rainflow algorithm

The rainflow-algorithm implemented in FORTRAN in [193] has been rewritten in this appendix using python™, version 3.6.1. In a first step, the desired time-series is to be imported and then the load-classification classes are to be defined for the counting.

```
  ## Rain-Flow-Zählung according to U.H. Clormann (1986), Programm HCM
## ----------------------------------------------------------------
import numpy as np
import matplotlib as mpl
import matplotlib.pyplot as plt

  # ----------------------------------------------------------------
# Import of time series e.g.  of the force F(f)
# ----------------------------------------------------------------
t = [] # Time vector
x = [] # time-dependent parameter

  Zeit = open("Pm-ZeitOfFpeak.txt",'r')
for line in Zeit:
     l = line.rsplit()
     t.extend(l)
Zeit.close()
del t[0]
t = [float(i) for i in t]
t = np.array(t)

  stress = open("Pm-sigma_peaks.txt",'r')
for line in stress:
     l = line.rsplit()
     x.extend(l)
stress.close()
del x[0]
x = [float(i) for i in x]
x = np.array(x)

  # ----------------------------------------------------------------
# Further Inputs
# ----------------------------------------------------------------
# Please specify an even number of classes for the classification of x(t)
n = int(input('1) Even number of classes for x(t):  '))

  # ----------------------------------------------------------------
# Generation of classes of x(t)
# ----------------------------------------------------------------
OW = float(np.amax(x)) # Largest value of x(t) -> OW
UW = float(np.amin(x)) # Smalles value of x(t) -> UW
Range = 1/n*(np.abs(OW) + np.abs(UW)) # Magnitude of a class (= range/width)
xmean = np.mean(x) # mean value of x(t) serves as zero-point
```

```
  # Matrix with the numeration of the classes
# The class, where the zero-point is, has the number 0
# The classes underneath the zero-point are negative
# otherwise positive
# The distribution around the zero-point is symmetric
KlasseNr = np.arange(-1/2*n, 1/2*n + 1, 1, dtype=int)

  Nr = np.size(KlasseNr)
Grenzen = []
# -1/2*KlasseRange -> in order to increase the classes
# above extreme values by the half of the width of a class
for i in np.arange(-1/2*n, 1/2*n + 1, 1):
     Grenzen = Grenzen + [i*Range - 1/2*Range]

  # Add the last limit
Grenzen = Grenzen + [Range + Grenzen[Nr - 1]]

  # ------------------------------------------------------------------
# Transformation of x(t) in classes und t in k-points
# ------------------------------------------------------------------
x_Kl = np.array(np.round((x - xmean)/Range)) # Classification into class-numbers
xNr = np.size(x_Kl) # Number of values
K = np.array(np.arange(0, xNr)) # Matrix with the numbering of every value

  # ------------------------------------------------------------------------
# RFC-Algorithm (rainflow counting)
# ------------------------------------------------------------------------
# Maximal class (OK) and minimal class (UK)
OK = np.max(x_Kl)
UK = np.min(x_Kl)

  # Residuum vector
RES = np.zeros(Nr + 1) # Size of vector acc.  number of classes
# Markov-Matrix in the shape from-to-matrix
# The matrix is quadratic and has the size acc.  number of classes
HYMAT = np.zeros((Nr, Nr))

  # Pointer-parameter at the beginning of counting
IR = 1
IZ = 0

  # Counting-loop-algorithm of U.H. Clormann and T. Seeger
# (Rainflow HCM - Ein Zählverfahren für Betriebsfestigkeitsnachweise
# auf werkstoffmechanischer Grundlage
Source:  Stahlbau, Heft 3, 55.  Jahrgang, März 1986)
i = 0
while i < np.size(x_Kl):
     if IZ > IR:
          I = RES[IZ - 1]
          J = RES[IZ]
          if (x_Kl[i] - J)*(J - I) >= 0:
               IZ = IZ - 1
          elif abs(x_Kl[i] - J) >= abs(J - I):
```

```
                HYMAT[(J + abs(UK), I + abs(UK))] = HYMAT[(J + abs(UK), I + abs(UK))]
+ 1
                IZ = IZ - 2
           else:
                IZ = IZ + 1
                RES[IZ] = x_Kl[i]
                i = i + 1
     elif IZ == IR:
           J = RES[IZ]
           if (x_Kl[i] - J)*J >= 0:
                IZ = IZ - 1
           elif abs(x_Kl[i]) > abs(J):
                IR = IR + 1
           else:
                IZ = IZ + 1
                RES[IZ] = x_Kl[i]
                i = i + 1
     else:
           IZ = IZ + 1
           RES[IZ] = x_Kl[i]
           i = i + 1

  print('Residuum:  RES = ', RES)
print('Class-Nr.  From-to-Matrix:  HYMAT = ', '\n'
, HYMAT)

  # Transformation of the class-Nr.  of HYMAT-matrix
# into absolute values of from-to-Markov-matrix:
# From-Vector before from-to-Markov-matrix
VON = np.ndarray.tolist(Range*KlasseNr)
print('Vector from- of from-to-Markov-Matrix:  FROM = ', VON)
# From-Vector after from-to-Markov-matrix
NACH = np.ndarray.tolist(Range*KlasseNr)
print('Vector after- of from-to-Markov-Matrix:  TO = ', NACH)

  # ------------------------------------------------------
# Transformation of from-to-Matrix HYMAT into range-mean value-Markov-matrix
# ------------------------------------------------------
# Range vector m
delta = np.zeros(Nr) #
for i in np.arange(0, Nr, 1):
     delta[i] = Range*(i+1)*abs(KlasseNr[0] - KlasseNr[1])
delta = np.ndarray.tolist(delta)

  # Vector n of class mean value
mittl = np.zeros(Nr)
for i in np.arange(0, Nr, 1):
     if i <= Nr-2:
          mittl[i] = xmean + Range*1/2*(KlasseNr[i] + KlasseNr[i+1])
     elif i == Nr-1:
          mittl[i] = xmean + 1/2*Range*(i+1)
mittl = np.ndarray.tolist(mittl)

  # Transformation algorithm
```

```
pruef_delta = [] # Vector for finding shortest distance
pruef_mittl = [] # Vector for finding shortest distance
Markov = np.zeros((len(delta),len(mittl)))
for i in range(len(VON)):
     for j in range(len(NACH)):
          if HYMAT[(i, j)] != 0:
               dkl = abs(VON[i] - NACH[j]) # range 'roh'
               mkl = xmean + 1/2*(VON[i] + NACH[j]) # mean value 'roh'
               # Search of shortest distance in order to aplly 'dkl' and 'mkl'
               # to the generated classes in vector 'delta' and 'mittl',
               # i.e.  to round it up or down
               pruef_delta = np.abs(np.array(delta) - np.array(dkl)) # Calculate
distance
               pruef_mittl = np.abs(np.array(mittl) - np.array(mkl)) # Calculate
distance
               ort_delta = pruef_delta.argmin() # Index of items with shortest ditance
               ort_mittl = pruef_mittl.argmin() # Index of items with shortest ditance
               dkl = delta[ort_delta] # Round up or down
               mkl = mittl[ort_mittl] # Round up or down
               Markov[(delta.index(dkl), mittl.index(mkl))] = Markov[(delta.index(dkl),
mittl.index(mkl))] +
HYMAT[(i, j)]
          else:
               pass
print('Range-mean value-Matrix:  Markov = ', '\n'
, Markov)

  n_class = n + 1 # Real number of generated classes
## ----------------------------------------------------
## Output of Range-mean value-Markov-matrix as ASCII-file
## ----------------------------------------------------
# Range-mean value-Markov-matrix [MPa]
Output1 = [val for sublist in Markov for val in sublist] # Hängt alle Items von Markov
an Output1
Ntot = sum(Output1) # Total number of hysteresis

  print('Output =', Output1)
Matrix = open('MeanRangeMarkov.txt', 'w')
Matrix.write('Highest value' + ' ' + str('%.2f' % OW) + '[MPa]' + '\n'
'Lowest value' + ' ' + str('%.2f' % UW) + '[MPa]' + '\n'
'Number of classes' + ' ' + str('%d' % n_class) + '[-]' + '\n'
'Class range' + ' ' + str('%.2f' % Range) + '[MPa]' + '\n'
'Number of hystheresis' + ' ' + str('%d' % Ntot) + '[-]' + '\n')

  Matrix.write(' ')
for q in np.arange(1, len(mittl), 1):
     Matrix.write(str(q) + '.mean[MPa]' + ' ')
Matrix.write(str(len(mittl)) + '.mean[MPa]' + '\n')

  Matrix.write('range[MPa]' + ' ')
for q in range(len(mittl)):
     if q < len(mittl)- 1:
          Matrix.write(str('%.0f' % mittl[q]) + ' ')
     elif q == len(mittl) - 1:
```

```
          Matrix.write(str('%.0f' % mittl[q]) + \n")

  for r in range(len(delta)):
     Matrix.write(str('%.0f' % delta[r]) + ' ')
     for s in range(len(mittl) + 1):
          if s < len(mittl) - 1:
               Matrix.write(str('%d' % Markov[(r),(s)]) + ' ')
          elif s == len(mittl) - 1:
               Matrix.write(str('%d' % Markov[(r),(s)]) + "\n")

  Matrix.close()

  ## ------------------------------------------------------------
## Transformation of range-mean value-Markov-matrix
## into Markov-matrix with 3 columns:
## Mean value-range-number of issues
## ------------------------------------------------------------
# Calculation of number of rows in range-mean value-Markov-matrix with 3 columns
# (Number acc.  occupied cells in Markov-matrix)
Zeilen = 0
for m in range(len(mittl)):
     for d in range(len(delta)):
          if Markov[(d, m)] != 0:
               Zeilen = Zeilen + 1
          else:
               pass

  Markov3Spalten = np.zeros((Zeilen, 3))

  # Transformation
u = 0
Nhyst = 0
for m in range(len(mittl)):
     for d in range(len(delta)):
          if Markov[(d, m)] != 0:
               mkl3 = mittl[m]
               l dkl3 = delta[d]
               N = Markov[(d, m)]
               Markov3Spalten[(u, 0)] = mkl3
               Markov3Spalten[(u, 1)] = dkl3
               Markov3Spalten[(u, 2)] = N
               u = u + 1
               Nhyst = Nhyst + N
          else:
               pass

  print('Range-mean value-Markov-matrix with 3 columns:  Markov with 3 columns =
', '\n'
, Markov3Spalten)

  ## ------------------------------------------------
## Output of range-mean value-Markov-matrix with 3 columns as ASCII-file
## ------------------------------------------------
# Range-mean value-Markov-matrix with 3 columns [MPa]
```

```
Output2 = [val for sublist in Markov3Spalten for val in sublist]

  Matrix = open('3ColumnsMeanRangeMarkov.txt', 'w')
Matrix.write('Highest value' + ' ' + str('%.2f' % OW) + '[MPa]' + '\n'
'Lowest value' + ' ' + str('%.2f' % UW) + '[MPa]' + '\n'
'Number of classes' + ' ' + str('%d' % n_class) + '[-]' + '\n'
'Class range' + ' ' + str('%.2f' % Range) + '[MPa]' + '\n'
'Number of hystheresis' + ' ' + str('%d' % Nhyst) + '[-]' + '\n')
Matrix.write('mean[MPa]' + ' ' + 'range[MPa]' + ' ' + 'number[-]' + '\n')
for k in np.arange(0, np.size(Output2)-1, 3):
     Matrix.write(str('%.2f' % Output2[k]) + ' ' + str('%.2f' % Output2[k+1]) + '
' + str('%d' %
Output2[k+2]) + '\n')
Matrix.close()

  # ------------------------------------------------------------
# Figures
# ------------------------------------------------------------
plt.plot(K, x_Kl)
mpl.rcParams['agg.path.chunksize'] = 10000
plt.grid()
plt.title('Time-serie')
plt.xlabel("k-point [-]")
plt.ylabel("Class [-]")
plt.xlim(0, np.amax(K))
plt.ylim(np.amin(x_Kl-1), np.amax(x_Kl + 1))
plt.show()
```

B Numerical implementation of the bond-slip-relationship

Following code implemented in python™, version 3.6.1, describes the numerical iteration for calculating strains, stresses, bond-stresses, and the slip between reinforcement and concrete in a symmetric reinforced tension chord for any bond-slip constitutive equation. In this case, the bond-slip constitutive equation according to the Model Code 2010 [51] has been taken into account.

```
  # ------------------------------------------------
# Import of python modules
# ------------------------------------------------
import numpy as np
import math
from numpy import sign
import matplotlib.pyplot as plt
import matplotlib as mpl

  # ------------------------------------------------
# Dimensions of tension chord and nodes (discretisation)
# ------------------------------------------------
# Reinforcement
Ds = 0.020 # [m] Reinforcement diameter
As = 1/4*np.pi*(Ds)**2 # [m²] Reinforcement cross sectional area
# Concrete
Ac = 0.114*0.2 - As # [m²] Effective concrete area
# Geometrical reinforcement degree
ro = As/Ac # [-]

  print('--- System data ---')
print('Reinforcement diameter Ds [mm] = ', Ds*1000)
print('Reinforcement cross sectional area As [cm²] = ', As*10000)
print('Effective concrete area Ac [cm²] = ', Ac*10000 )
print('Geometrical reinforcement degree ro [%] = ', ro*100)

  # Length of tension chord between crack lip and midpoint of chord
L = 0.125 # [m]
print('Length of tension chord 1/2*L [cm] = ', L*100)
# Number of discretisation intervals in L
N = 10 # [-]
print('Number of discretisation intervals N [-] = ', N)
# Distance between nodes
dx = L/N # [m]
print('Distance between nodes dx [cm] = ', dx*100)
# Node vector with node coordinates beginning at the midpoint of chord
i = np.zeros(N+1)
for n in range(N+1):
i[n] = n*dx
print('Coordinates of generated nodes i in [mm] = ', i*1000)
print('Number of generated nodes i:  ', np.size(i))
```

```
  # ------------------------------------------------
# Load-input and load conditions
# ------------------------------------------------
# Load force
F = 0.15 # [MN] Load at the crack lip

  # ------------------------------------------------
# Input of constitutive equations
# ------------------------------------------------
# STEEL
# Reinforcemente constitutive equation
Es = 201000 # [MPa] Young's modulus of elasticity
eps_sy = 0.00273 # Strain at begin of yielding
eps_sh = 0.015 # Strain at begin of hardening
eps_su = 0.091 # Strain at maximal stress
fsy = 549 # Yielding stress
fsu = 645 # Ultimate stress
Esh = (fsu - fsy)/(eps_su - eps_sy) # Young's modulus at hardening
ka = 0.0245 # Parameter
kc = 1.038 # Parameter
kb = eps_sh - ka * np.log((kc - 1)/kc) # Parameter
a = ka * (eps_sh - eps_su)/(eps_sh - kb) # Parameter

  # EQUATION
# Steel stress - the strain is the input-parameter
def sigma_s(epsilon_s):  # in [MPa]
     if 0 <= epsilon_s <= eps_sy:
          return Es * epsilon_s
     elif eps_sy < epsilon_s <= eps_sh:
          return fsy
     elif eps_sh < epsilon_s <= eps_su:
          return fsy + (fsu - fsy) * kc * (1 - np.exp((eps_sh - epsilon_s)/a))
     elif epsilon_s > eps_su:
          return 0
          print('Reinforcement fails!')
     elif -eps_sy < epsilon_s:
          return Es * epsilon_s

  # EQUATION
# Steel strain - the stress is the input-parameter
def epsilon_s(sigma_s):
     if 0 <= sigma_s <= fsy:
          return sigma_s/Es
     elif fsy < sigma_s:# <= fsu:
          return eps_sy + 1/Esh*(sigma_s - fsy)
     elif sigma_s > fsu:
          return 0
          print('Rinforcement fails!')
     elif -fsy < sigma_s < 0:
          return sigma_s/Es
          print('Reinforcement under compression stress!')
     else:
          return -fsy
```

```
          print('Reinforcement yields under compression stress!')

  # ------------------------------------------------
# CONCRETE
# Concrete constitutive equation (linear part only)
fc = 55.0 # [MPa] average concrete compression strength
fct = 4.0 # [MPa] average concrete tension strength
Ec = 38000 # [MPa] Young's Modulus of elasticity of concrete

  # EQUATION
# Concrete stress - the strain is the input-parameter
def sigma_c(epsilon_c):  # in [MPa]
     if 0 <= epsilon_c <= fct/Ec:
          return Ec * epsilon_c
     elif epsilon_c > fct/Ec:
          return 0
          print('Concrete fails under tension!')
     else:
          print('Concrete fails under compression!')
          return Ec * epsilon_c

  # EQUATION
# Concrete strain - the stress is the input parameter
def epsilon_c(sigma_c):
     if 0 <= sigma_c <= fct:
          return sigma_c/Ec
     elif sigma_c > fct:
          return 0
          print('Concrete fails under tension!')
     else:
          return sigma_c/Ec
          print('Concrete fails under compression!')

  # ------------------------------------------------
# Quotient between Young's Moduli of elasticity of steel and concrete

  n = Es/Ec
print('n = Es/Ec = ', n)

  # ------------------------------------------------
# BOND - ACCORDING TO MODEL CODE 2010
# Parameters according to MC2010:
tau_bmax = 2.5*fc**0.5 # [MPa] Max.  bond stress
tau_bf = 0.4*tau_bmax # [MPa] Residual stress after failure
alpha = 0.4 # [-] Exponent
s1 = 0.001 # [m] Slip by tau_bmax
s2 = 0.002 # [m] Slip at decline start
s3 = 0.2 # [m] Assump.:  clear distance between ribs
print('--------------------')
print('tau_bmax acc.  MC2010 [MPa]:  ', tau_bmax)
print('tau_bf acc.  MC2010 [MPa]:  ', tau_bf)
print('--------------------')

  # EQUATION
```

```
# Bond-slip-equation acc.  MC2010:
def tau(delta):
     if 0 <= delta <= s1:
          return tau_bmax * (delta/s1)**alpha
     elif s1 < delta <= s2:
          return tau_bmax
     elif s2 < delta <= s3:
          return tau_bmax - (tau_bmax - tau_bf) * (delta - s2)/(s3 - s2)
     elif delta > s3:
          return tau_bf
     else:
          return -tau_bf
          print('tau_b[j,k] negativ!')

  # ---------------------------------------------------
# Functions for choosing numerical increments
# ---------------------------------------------------
# Steel strain definition on node j
# Definitions:  eps_s_lastj = eps_s[j-1], Steel strain of previous node
# deps_s_j = deps_s[j], Increment for present node
def strain(eps_s_last_j, deps_s_j):
     return eps_s_last_j + deps_s_j

  # Slip-function definition on node j
# Definitions:  dj = delta[j], Slip of previous node
# eps_s_j = eps_s[j], Steel strain of previous node
# eps_s_jplus = eps_s[j+1], Steel strain of present node
def delta_next_j(dj, eps_s_next_j, eps_s_j):
     return dj + dx/2 * (eps_s_next_j + eps_s_j)

  # ---------------------------------------------------
# ---------------------------------------------------
# DEFINITIONS: ROWS j CORRESPOND TO NODES
# COLUMNS k CORRESPOND TO ITERATIONS
# ---------------------------------------------------
# ---------------------------------------------------
# Zero-point-functions
# From Equilibrium conditions:  Force variation in reinforcement
# and in concrete must correspond to variation of bond-force

  # Zero-point-function for reinforcement
# Definitions:  s_sj = sigma_s[j,k], Steel strain on node j by iteration k
# s_s_last_j = sigma_s[j-1,k], Steel strain on node j-1 by iteration k
# tau_j = tau[j,k], Bond stress on node j by iteration k
# tau_last_j = tau[j-1,k], Bond stress on node j-1 by iteration k
def f(s_sj, s_s_last_j, tau_j, tau_last_j):
     return s_sj - s_s_last_j - 1/2 * dx * (tau_j + tau_last_j) * 4/Ds

  # ---------------------------------------------------
# Algorithm for BISECTION METHOD (INTERN ITERATION)
# ---------------------------------------------------
# Bisection method - Intern iteration
# From:  'Numerical Methods for Engineering' (2014) of Jaan Kiusalaas
     "' root = bisection(f,x1,x2,switch=0,tol=1.0e-9).
```

```
     Finds a root of f(x) = 0 by bisection with tolerance 'tol'.
     The root must be bracketed in (x1,x2).
     Setting switch = 1 returns root = None if
     f(x) increases upon bisection."'
# Tolerance of 0.01 mm/m
def bisection_nodes(f, deps_s1, deps_s2, switch=1, tol=0.01e-3):
     delta[0,k] = 0
     tau_b[0,k] = tau(delta[0,k])
     strain1 = strain(eps_s[j-1,k], deps_s1)
     strain2 = strain(eps_s[j-1,k], deps_s2)
     stress1 = sigma_s(strain1)
     stress2 = sigma_s(strain2)
     delta1 = delta_next_j(delta[j-1,k], strain1, eps_s[j-1,k])
     delta2 = delta_next_j(delta[j-1,k], strain2, eps_s[j-1,k])
     tau1 = tau(delta1)
     tau2 = tau(delta2)
     f1 = f(stress1, sig_s[j-1,k], tau1, tau_b[j-1,k])
     if f1 == 0.0:
          deps_s[j,k] = deps_s1
          return deps_s[j,k]
     f2 = f(stress2, sig_s[j-1,k], tau2, tau_b[j-1,k])
     if f2 == 0.0:
          deps_s[j,k] = deps_s2
          return deps_s[j,k]
     if sign(f1) == sign(f2):
          print('Zero-point not in given interval!')
     n = int(math.ceil(math.log(abs(deps_s2 - deps_s1)/tol)/math.log(2.0)))
     for i in range(n):
          deps_s3 = 0.5*(deps_s1 + deps_s2)
          strain3 = strain(eps_s[j-1,k], deps_s3)
          stress3 = sigma_s(strain3)
          delta3 = delta_next_j(delta[j-1,k], strain3, eps_s[j-1,k])
          tau3 = tau(delta3)
          f3 = f1 = f(stress3, sig_s[j-1,k], tau3, tau_b[j-1,k])
          if (switch == 1) and (abs(f3) > abs(f1)) and (abs(f3) > abs(f2)):
               return None
          if f3 == 0.0:
               deps_s[j,k] = deps_s3
               return deps_s[j,k]
          if sign(f2)!= sign(f3):
               deps_s1 = deps_s3
               f1 = f3
          else:
               deps_s2 = deps_s3
               f2 = f3
     deps_s[j,k] = (deps_s1 + deps_s2)/2.0
     return deps_s[j,k]

  #---------------------------------------------------
# Matrix definition:  Rows correspond to nodes,
# column number describes iteration number
# ---------------------------------------------------
# Number of nodes is N+1; N is only number of intervals
deps_s = np.zeros((N+1,1)) # Increments of eps_s
```

```
# (N+1, first value = 0, since start-node; 2.  value is for 1.  interval)
eps_s = np.zeros((N+1,1))
sig_s = np.zeros((N+1,1))
delta = np.zeros((N+1,1))
tau_b = np.zeros((N+1,1))
saeule = np.zeros((N+1,1)) # New column for additional iteration
rest_sig = np.zeros((1,1)) # Rest = sig_s_max - sig_s[j,k]
zelle = np.zeros((1,1)) # New element for addtional iteration
# ------------------------------------------------

  # ------------------------------------------------
# ITERATION
# ------------------------------------------------
# Start at crack lip
# (by j=0 -> Boundary conditions!  Provision later under 'j+1')
j = 1 # Node number
k = 0 # Iteration number

  # ------------------------------------------------
# Iteration:  Strains, stresses, bond-stress, deformations
# ------------------------------------------------
# Values at crack lip (i = N+1)
sig_s_max = F/As # [MPa] Reinforcement stress at crack lip
eps_s_max = epsilon_s(sig_s_max)
print('Max.  aufnehmbare Kraft:  Fmax [kN] = ', fsu*As*1000)
print('sig_s_max [MPa] = ', sig_s_max)
print('--------------------')

  # ------------------------------------------------
# Iterations with the bisection method
# ------------------------------------------------
eps_s[0,0] = 0.01/1000
sig_s[0,0] = sigma_s(eps_s[0,0])
while np.abs(sig_s_max - sig_s[N,k]) > 10:
     if k >= 10:  # chosen:  k.max = 10
          print('deps_s [Ž030] = ', deps_s*1000)
          print('eps_s [Ž030] = ', eps_s*1000)
          print('delta [mm] = ', delta*1000)
          print('tau_b [MPa] = ', tau_b)
          print('sigma_s [MPa] = ', sig_s)
          print('rest_sig [MPa] = ', rest_sig)
          print('--------------------')
          print('Note j = ',j,' Iteration k =', k)
          print("NO CONVERGENCE after k.max = 10 iterations!")
          print('--------------------')
          break
     while j <= N:
          # Iteration of deps_s[j,k], to fullfill equilibrium
          bisection_nodes(f, -0.00, 0.05, switch=1, tol=0.01e-3)
          # Values of strain, slip, bond-stress and stress (steel)
          eps_s[j,k] = eps_s[j-1,k] + deps_s[j,k]
          delta[j,k] = delta_next_j(delta[j-1,k], eps_s[j,k], eps_s[j-1,k])
          tau_b[j,k] = tau(delta[j,k])
          sig_s[j,k] = sigma_s(eps_s[j,k])
```

```
          # Next node
          j = j + 1
          # After iteration over all nodes:
          if (j > N):
               rest_sig[0,k] = sig_s_max - sig_s[N,k]
               break
     if (np.abs(sig_s_max - sig_s[N,k]) <= 10):
          break
     elif (np.abs(sig_s_max - sig_s[N,k]) > 10) and k == 0:
          # Value-matrix is increased by a column
          deps_s = np.concatenate((deps_s, deps_s[:, k:]),axis=1)
          eps_s = np.array(np.concatenate((eps_s, saeule),axis=1))
          sig_s = np.array(np.concatenate((sig_s, saeule),axis=1))
          delta = np.array(np.concatenate((delta, saeule),axis=1))
          tau_b = np.array(np.concatenate((tau_b, saeule),axis=1))
          rest_sig = np.concatenate((rest_sig, zelle),axis=1)

            eps_s[0,k+1] = 2/1000
          sig_s[0,k+1] = sigma_s(eps_s[0,k+1])

            k = k + 1
          j = 1

       elif (np.abs(sig_s_max - sig_s[N,k]) > 10) and k > 0:
          # Value-matrix is increased by a column
          deps_s = np.concatenate((deps_s, deps_s[:, k:]),axis=1)
          eps_s = np.array(np.concatenate((eps_s, saeule),axis=1))
          sig_s = np.array(np.concatenate((sig_s, saeule),axis=1))
          delta = np.array(np.concatenate((delta, saeule),axis=1))
          tau_b = np.array(np.concatenate((tau_b, saeule),axis=1))
          rest_sig = np.concatenate((rest_sig, zelle),axis=1)
          # Better increment value
          eps_s[0,k+1] = eps_s[0,k] - (eps_s[0,k] -
          eps_s[0,k-1])*rest_sig[0,k]/(rest_sig[0,k] - rest_sig[0,k-1])
          sig_s[0,k+1] = sigma_s(eps_s[0,k+1])

            k = k + 1
          j = 1
     else:
          print('ERROR')
          break

  ## ------------------------------------------------
## Ergebnis
## ------------------------------------------------
deps_s_fin = deps_s[:, k:]
eps_s_fin = eps_s[:, k:]
sig_s_fin = sig_s[:, k:]
delta_fin = delta[:, k:]
tau_b_fin = tau_b[:, k:]
print('- RESULTS -')
print('deps_s_fin [‰] = ', deps_s_fin*1000)
print('eps_s_fin [‰] = ', eps_s_fin*1000)
print('sig_s_fin [MPa] = ', sig_s_fin)
```

```
print('delta_fin [mm] = ', delta_fin*1000)
print('tau_b_fin [MPa] = ', tau_b_fin)

  # ------------------------------------------------
# Plotten
# ------------------------------------------------
fig, x1 = plt.subplots()
Dehnung1 = plt.plot(i*1000, eps_s_fin*1000)
plt.rc('text', usetex=True)
plt.rc('font', **'family':  'serif', 'serif':['Palatino'])
plt.grid()
plt.title('Strains')
plt.setp(Dehnung1, lw=2.0,color='k', ls='solid')
x1.set_xlabel("Distance x from crack lip [mm]", fontsize=12)
x1.set_ylabel(r'ε_s [Ž030]', fontsize=12)
x1.set_xlim(0,L*1000)
x1.set_ylim(0, 1000*np.max((eps_s_fin)))
x1.set_xticks(np.linspace(0,L*1000,10))
x1.set_yticks(np.linspace(0, 1000*np.max(eps_s_fin)), 12)
legend = plt.legend(loc='upper left')
plt.show()

  fig, x1 = plt.subplots()
Spann1 = plt.plot(i*1000, sig_s_fin)
plt.rc('text', usetex=True)
plt.rc('font', **'family':  'serif', 'serif':['Palatino'])
plt.grid()
plt.title('Stresses')
plt.setp(Spann1, lw=2.0, color='k', ls='solid')
x1.set_xlabel("Distance x from crack lip [mm]", fontsize=12)
x1.set_ylabel(r'σ_s [MPa]', fontsize=12)
x1.set_xlim(0,L*1000)
x1.set_ylim(0, fsu)
x1.set_xticks(np.linspace(0,L*1000,15))
x1.set_yticks(np.linspace(0, fsu, 12))
legend = plt.legend(loc='upper left')
plt.show()

  Schlupf1 = plt.plot(i*1000, delta_fin*1000)
plt.rc('text', usetex=True)
plt.rc('font', **'family':  'serif', 'serif':['Palatino'])
plt.grid()
plt.title('Slip')
plt.setp(Schlupf1, lw=2.0, color='k', ls='solid')
legend = plt.legend(loc='upper right')
plt.xlabel("Distance x from crack lip [mm]")
plt.ylabel(r'δ_b [mm]')
plt.xlim(0,L*1000)
plt.ylim(0,1000*np.max(delta_fin))
plt.xticks(np.linspace(0,L*1000,10))
plt.yticks(np.linspace(0,1000*np.max(delta_fin),10))
plt.show()
```

```
  Verb1 = plt.plot(i*1000, tau_b_fin)
plt.rc('text', usetex=True)
plt.rc('font', **'family':  'serif', 'serif':['Palatino'])
plt.grid()
plt.title('Bond stresses')
plt.setp(Verb1, lw=2.0, color='k', ls='solid')
legend = plt.legend(loc='upper right')
plt.xlabel("Distance x from crack lip [mm]")
plt.ylabel(r'τ_b [MPa]')
plt.xlim(0,L*1000)
plt.ylim(0, tau_bmax)
plt.xticks(np.linspace(0,L*1000,10))
plt.yticks(np.linspace(0,tau_bmax,10))
plt.show()
```

C Numerical implementation of the fatigue Tension Chord Model

The fatigue Tension Chord Model (TCMfat) has been implemented in python™, version 3.6.1, in following code (cf. Ch. 4.2.4).

```
  # ------- FATIGUE TENSION CHORD MODEL ---------
#########################################################
# Numerical calculation of the stress-strain-behaviour
# of a symmetrical loaded tension chord

  # ------------- CONDITIONS ---------------
# 1.  After a local maxima there is a local minima,
# then again a local maxima and a local minima, etc.
# 2.  Effective concrete area is constant.
# 3.  After complete unloading the steel strain at the
# crack surface is zero.
# 4.  Load stresses are only peaks.

  # ---------------------------------------------------
# Import of python modules
# ---------------------------------------------------
import numpy as np
import matplotlib.pyplot as plt
import matplotlib as mpl
from matplotlib.ticker import FormatStrFormatter

  # ---------------------------------------------------
# Dimensions of tension chord and nodes (discretisation)
# ---------------------------------------------------
# Reinforcement
Ds = 0.020    # [m] Reinforcement diameter
As = 1/4*np.pi*(Ds)**2    # [m²] Reinforcement cross sectional area
# Concrete
Ac = 0.114*0.2 - As    # [m²] Effective concrete area
# Geometrical reinforcement degree
ro = As/Ac    # [-]

  print('--- System data ---')
print('Reinforcement diameter Ds [mm] = ', Ds*1000)
print('Reinforcement cross sectional area As [cm²] = ', As*10000)
print('Effective concrete area Ac [cm²] = ', Ac*10000 )
print('Geometrical reinforcement degree ro [%] = ', ro*100)

  # Length of tension chord between crack lip and midpoint of chord
L = 0.125    # [m]
print('Length of tension chord 1/2*L [cm] = ', L*100)
# Number of discretisation intervals in L
N = 10    # [-]
print('Number of discretisation intervals N [-] = ', N)
```

```
# Distance between nodes
dx = L/N     # [m]
print('Distance between nodes dx [cm] = ', dx*100)
# Node vector with node coordinates beginning at the midpoint of chord
i = np.zeros(N+1)
for n in range(N+1):
     i[n] = n*dx
print('Coordinates of generated nodes i in [mm] = ', i*1000)
print('Number of generated nodes i:  ', np.size(i))
# ------------------------------------------------
# Load-input and load conditions
# ------------------------------------------------
# FIRST LOADING
# First loading in tests usually until sigma.sr = 350 MPa
sigma_sfirst = np.arange(0, 350, 2)

  # FATIGUE LOADING
sigma_sfat = [] # Vector definition

  # Import of stresses
# NUR PEAKS!
stress = open(r'C:\XXXXXX\Pe-sigma_peaks.txt','r')
for line in stress:  # Every line in file is readed
l = line.rsplit() # Elements in line are separated in different vectors according
to space character
sigma_sfat.extend(l) # List 'l' is assigned to 'sigma_sfat'
stress.close()
del sigma_sfat[0] # First elemet (vector name) is deleted
sigma_sfat = [float(i) for i in sigma_sfat] # List content is floated
sigma_sfat = np.array(sigma_sfat)
# Fatigue loading starts after first loading
sigma_sfat = np.insert(sigma_sfat, 0, [max(sigma_sfirst), 0])
print('Number of load-peaks:  ', len(sigma_sfat))

  # Relative number of load cycles n_rel = n/N
# Important:  1.  Value of sigma_sfat corresponds to static first loading.
# Bond degradation is activated with the 2.  load value (first reloading),
# therefore "len(sigma_sfat)-1" als denominator in the equation of n_rel
# n_rel = 1/(len(sigma_sfat)-1) * np.arange(0, len(sigma_sfat), 1)

  print('Relative number of load peaks n_rel = ', n_rel)

  # ------------------------------------------------
# Input of constitutive equations
# ------------------------------------------------
# STEEL
# Reinforcemente constitutive equation
Es = 201000 # [MPa] Young's modulus of elasticity
eps_sy = 0.00273 # Strain at begin of yielding
eps_sh = 0.015 # Strain at begin of hardening
eps_su = 0.091 # Strain at maximal stress
fsy = 549 # Yielding stress
fsu = 645 # Ultimate stress
Esh = (fsu - fsy)/(eps_su - eps_sy) # Young's modulus at hardening
```

```
ka = 0.0245 # Parameter
kc = 1.038 # Parameter
kb = eps_sh - ka * np.log((kc - 1)/kc) # Parameter
a = ka * (eps_sh - eps_su)/(eps_sh - kb) # Parameter

  # EQUATION
# Steel stress - the strain is the input-parameter
def sigma_s(epsilon_s):  # in [MPa]
     if 0 <= epsilon_s <= eps_sy:
          return Es * epsilon_s
     elif eps_sy < epsilon_s <= eps_sh:
          return fsy
     elif eps_sh < epsilon_s <= eps_su:
          return fsy + (fsu - fsy) * kc * (1 - np.exp((eps_sh - epsilon_s)/a))
     elif epsilon_s > eps_su:
          return 0
          print('Reinforcement fails!')
     elif -eps_sy < epsilon_s:
          return Es * epsilon_s

  # EQUATION
# Steel strain - the stress is the input-parameter
def epsilon_s(sigma_s):
     if 0 <= sigma_s <= fsy:
          return sigma_s/Es
     elif fsy < sigma_s:# <= fsu:
          return eps_sy + 1/Esh*(sigma_s - fsy)
     elif sigma_s > fsu:
          return 0
          print('Rinforcement fails!')
     elif -fsy < sigma_s < 0:
          return sigma_s/Es
          print('Reinforcement under compression stress!')
     else:
          return -fsy
          print('Reinforcement yields under compression stress!')

  # ------------------------------------------------
# CONCRETE
# Concrete constitutive equation (linear part only)
fc = 55.0 # [MPa] average concrete compression strength
fct = 4.0 # [MPa] average concrete tension strength
Ec = 38000 # [MPa] Young's Modulus of elasticity of concrete

  # EQUATION
# Concrete stress - the strain is the input-parameter
def sigma_c(epsilon_c):  # in [MPa]
     if 0 <= epsilon_c <= fct/Ec:
          return Ec * epsilon_c
     elif epsilon_c > fct/Ec:
          return 0
          print('Concrete fails under tension!')
     else:
          print('Concrete fails under compression!')
```

```
          return Ec * epsilon_c

  # EQUATION
# Concrete strain - the stress is the input parameter
def epsilon_c(sigma_c):
     if 0 <= sigma_c <= fct:
          return sigma_c/Ec
     elif sigma_c > fct:
          return 0
          print('Concrete fails under tension!')
     else:
          return sigma_c/Ec
          print('Concrete fails under compression!')

  # ------------------------------------------------
# Quotient between Young's Moduli of elasticity of steel and concrete

  n = Es/Ec
print('n = Es/Ec = ', n)

  # ------------------------------------------------
# BOND - TENSION CHORD MODEL (TCM)
# Values according to the TCM (static-monotonic)
tau_b0 = 1.3*fct # Rigid-plastic bond strength for sigma.s <= f.sy
tau_b1 = 0.7*fct # Rigid-plastic bond strength for sigma.s > f.sy
sig_sr0 = (fct - 0.65)*(1/ro + n - 1) # Steel stress at crack lip acc.  TCM
# Tension stress in concrete due to shrinkage effects according
# to Model Code 2010 amounts appr.  0.65 MPa

  print('tau_b0 according to TCM [MPa] = ', tau_b0)
print('tau_b1 according to TCM [MPa] = ', tau_b1)

  # EQUATION
# Rigid-plastic bond-slip relationship (static-monotonic loading)
def tau_ZG(sigma_s):
     if 0 <= sigma_s <= fsy:
          return tau_b0
     elif sigma_s > fsy:
          return tau_b1
     else:
          return -tau_b1

  # EQUATION
# Fatigue model of the bond (degradationn of the bond strength)
# UNLOADING
def tau_bU(n_N):
     tau_bU1 = 1.5 * fct # Average value of tests
     tau_bUrest = 0.50 * tau_bU1 # Average value of tests
     return tau_bU1 * (1 - (1 - tau_bUrest/tau_bU1)*n_N)

  # EQUATION
# Fatigue model of the bond (degradationn of the bond strength)
# RELOADING
def tau_bR(n_N):
```

```
      tau_bR1 = 1.2 * fct # Average value of tests
      tau_bRrest = 0.50 * tau_bR1 # Average value of tests
      return tau_bR1 * (1 - (1 - tau_bRrest/tau_bR1)*n_N)

  # EQUATION
# Calculation of displacements beginning at the crack lip
# Definition of displacement equation on node j (for both:  steel and concrete)
# Definitions:
# u_j = u[j] Displacement of the previous node
# eps_j_plus = eps[j] Strain of the previous node
# eps_j = eps[j+1] Strain of the actual node
def u_jZG(u_j, eps_j_plus, eps_j):
      return u_j - dx/2 * (eps_j_plus + eps_j)

  # ------------------------------------------------
# Calculation model of the plastic strain accumulation
# ------------------------------------------------
def PlastDehnAkku(relNr):
      # relNr = n/N relative number of load peaks
      # m = slope of linearised equation
      # Equation calculates plastic strain increase with every load peak
      m = 0.0003 # Average value of all tests
      return m * relNr

  # ------------------------------------------------
# Static-monotonic Tension Chord Model (TCM) - only first loading
# ------------------------------------------------
# EQUATION
# Input-parameter is the strain, the result is a stress
def ZGMstat(epsilon):
      if 0 <= epsilon <= fct/Ec:
            return Es*epsilon
      # Crack space between maximal and minimal crack space
      elif fct/Ec <= epsilon <= (1 + 2.3*(1-ro)/(4*ro*n))*fct/Ec:
            return sig_sr0
      else:
            return Es*epsilon + (1.0*(1-ro)/(4*ro)*fct)

  # EQUATION
# Inversely:  Input-parameter is the stress, the result is a strain
# Only after concluded crack formation phase;
# the section between first ans concluded crack formation
# is not explicitly definable
def ZGMstat_Spannung(stress):
      return 1/Es * (stress - 1.0 * (1-ro)/(4*ro)*fct) # Minimal crack space

  # ------------------------------------------------
# Equation for finding the nearest element-index from specified value
# ------------------------------------------------
def closest_index(matrix, item):
      return np.argmin(np.abs(matrix - item))

  # ------------------------------------------------
# Calculation of the sigma.s-strain.sm-curve of the first static-monotonic load
```

```
# ------------------------------------------------
max_epsilon_srfirst = ZGMstat_Spannung(max(sigma_sfirst))
eps_smfirst = np.linspace(0, max_epsilon_srfirst,100, endpoint=True)
sigma_srfirst = np.zeros(len(eps_smfirst))
for y in range(len(eps_smfirst)):
     sigma_srfirst[y] = ZGMstat(eps_smfirst[y])
print('eps_smfirst [Ž030] = ', eps_smfirst*1000)

  # ------------------------------------------------
# Definition of parameters
# ------------------------------------------------
eps_sZG = np.zeros((N+1)) # Steel strain
eps_cZG = np.zeros((N+1)) # Concrete strain
sig_sZG = np.zeros((N+1)) # Steel stress
sig_cZG = np.zeros((N+1)) # Concrete stress
u_sZG = np.zeros((N+1)) # Steel displacement
u_cZG = np.zeros((N+1)) # Concrete displacement
deltaZG = np.zeros((N+1)) # Slip = u_sZG - u_cZG
tau_bZG = np.zeros((N+1)) # Bond stress

  x_sU = np.zeros(1) # Matrix of slip-reversal-values for unloading
x_sR = np.zeros(1) # Matrix of slip-reversal-values for reloading

  # ------------------------------------------------
# LOOP for fatigue Tension Chord Model (TCMfat)
# ------------------------------------------------
# With every new load peak the stress-, strain-, bond-stress-, and displacement-
# matrices are added a new row.  The row-number corresponds to the number of the
# load peak, the values of the row correspond to the node-position at the tension
# chord under the specific load peak.
# At the beginning of every loop a zero-row is added, the values are calculated
# during the loop and updated.

  # Zero-row:
Nullzeile = np.zeros((N+1))

  # Number of peaks:  Amp = Number of peak values in stress-matrix
Amp = 0 # First load amplitude

  ############ FIRST LOADING ################ FIRST LOADING ####################
# 1.  Iteration for first load peak according to static-monotonic TCM
# Boundary conditions at the crack lip
print('Calculation-Nr.:  ', Amp)
print('First loading')
sig_sZG[N] = sigma_sfat[0] # Steel stress at crack lip = given load stress peak
sig_cZG[N] = 0 # Concrete stress at crack lip = 0
# Steel strain at crack lip acc.  to constitutive equation
eps_sZG[N] = epsilon_s(sig_sZG[N])
eps_cZG[N] = 0 # Concrete strain at crack lip = 0
tau_bZG[N] = tau_ZG(sig_sZG[N]) # Bond-stress acc.  to static-monotonic TCM
u_sZG[0] = 0 # No displacement in the midpoint (symmetric loading)
u_cZG[0] = 0 # No displacement in the midpoint (symmetric loading)
deltaZG[0] = u_sZG[0] - u_cZG[0]
```

```
  # Values are put on the 1.  row of matrices
q = N-1
while q >= 0:
     sig_sZG[q] = sig_sZG[q+1] - dx * tau_bZG[q+1] * 4/Ds
     sig_cZG[q] = sig_cZG[q+1] + dx * tau_bZG[q+1] * 4/Ds * ro/(1 - ro)
     eps_sZG[q] = epsilon_s(sig_sZG[q])
     eps_cZG[q] = epsilon_c(sig_cZG[q])
     tau_bZG[q] = tau_ZG(sig_sZG[q])
     q = q - 1
     # Slip and displacement calculated through numerical integration
     for r in range(1, N+1 ,1):
          u_sZG[r] = dx * 1/2 * (eps_sZG[r] + eps_sZG[r-1])
          u_cZG[r] = dx * 1/2 * (eps_cZG[r] + eps_cZG[r-1])
          deltaZG[r] = u_sZG[r] - u_cZG[r]

  ############ FATIGUE-LOADING ################ FATIGUE-LOADING #################
# Further calculation steps for next load peaks
# Number of calculations corresponds to number of load peaks

  Amp = 1
print('Total number of loops:  ', len(sigma_sfat))
while Amp < len(sigma_sfat):
     print('Calculation-Nr.:  ', Amp,'/',len(sigma_sfat)-1)
     # Zero-row is added for next loop
     sig_sZG = np.vstack((sig_sZG, Nullzeile))
     sig_cZG = np.vstack((sig_cZG, Nullzeile))
     eps_sZG = np.vstack((eps_sZG, Nullzeile))
     eps_cZG = np.vstack((eps_cZG, Nullzeile))
     tau_bZG = np.vstack((tau_bZG, Nullzeile))
     u_sZG = np.vstack((u_sZG, Nullzeile))
     u_cZG = np.vstack((u_cZG, Nullzeile))
     deltaZG = np.vstack((deltaZG, Nullzeile))
     x_sU = np.vstack((x_sU, 0))
     x_sR = np.vstack((x_sR, 0))
# ------------------------------------------------------------
     # Differentiation, whether UNLOADING or RELOADING present

       ############ UNLOADING ############## UNLOADING ###################
     if sigma_sfat[Amp] <= sigma_sfat[Amp-1]:
          print('UNLOADING')
          # Boundary condition for next load peak
          # Steel stress at crack lip = given load stress
          sig_sZG[Amp,N] = sigma_sfat[Amp]
          sig_cZG[Amp,N] = 0 # Concrete stress at crack lip = 0
          # New plastic-strain-increase only for RELOADING;
          # for UNLOADING is the plastic-strain-
          # increase equal to the one of the previous load peak Amp-1
          # Steel strain acc.  to constitutive equation
          eps_sZG[Amp,N] = epsilon_s(sig_sZG[Amp,N]) + PlastDehnAkku(n_rel[Amp-1])
          eps_cZG[Amp,N] = 0 # Concrete strain at crack lip = 0
          # Bond-stress acc.  to static-monotonic TCM
          tau_bZG[Amp,N] = tau_bU(n_rel[Amp])
          u_sZG[Amp,0] = 0 # No displacement in the midpoint (symmetric loading)
          u_cZG[Amp,0] = 0 # No displacement in the midpoint (symmetric loading)
```

```
            deltaZG[Amp,0] = u_sZG[Amp,0] - u_cZG[Amp,0]

              # Start with 2.  node
            q = N-1

              while q >= 0:
                 # Steel stress increases from crack lip until x_sU (unloading)
                 sig_sZG[Amp,q] = sig_sZG[Amp,q+1] + dx * tau_bZG[Amp,q+1] * 4/Ds
                 sig_cZG[Amp,q] = sig_cZG[Amp,q+1] - dx * tau_bZG[Amp,q+1] * 4/Ds
* ro/(1 - ro)
                 # New plastic-strain-increase only for RELOADING;
                 # for UNLOADING is the plastic-strain-
                 # increase equal to the one of the previous load peak Amp-1
                 eps_sZG[Amp,q] = epsilon_s(sig_sZG[Amp,q]) + PlastDehnAkku(n_rel[Amp-1])
                 eps_cZG[Amp,q] = epsilon_c(sig_cZG[Amp,q])
                 tau_bZG[Amp,q] = tau_bU(n_rel[Amp])
                 q = q - 1 # Next node

              # Calculation of intersection point with curves of previous values,
            # beginning with nearest previous load peak.  Search is stopped
            # as soon as an intersection point is founded
            if Amp > 1:
                 for w in range(1, Amp, 1):
                      idx = np.argwhere(np.diff(np.sign(
                      sig_sZG[Amp,:]  - sig_sZG[Amp-w,:]))).ravel()
                      if idx.size:
                           Schnittpkt = i[min(idx)]
                           # Index begins from midpoint of tension chord
                           index_Schnittpkt = closest_index(i, Schnittpkt)
                           # New allocation of slip-reversal-point
                           x_sU[Amp] = i[index_Schnittpkt]
                           q = index_Schnittpkt - 1
                           # Correction starting from intersection point
                           while q >=0:
                                # Previous loop:
                                sig_sZG[Amp,q] = sig_sZG[Amp-w,q]
                                sig_cZG[Amp,q] = sig_cZG[Amp-w,q]
                                eps_sZG[Amp,q] = eps_sZG[Amp-w,q]
                                eps_cZG[Amp,q] = epsilon_c(sig_cZG[Amp-w,q])
                                tau_bZG[Amp,q] = tau_bU(n_rel[Amp-w])
                                q = q - 1 # Next node
                           break
                      else:
                           x_sU[Amp] = L

              elif Amp == 1:
                 idx = np.argwhere(np.diff(np.sign(sig_sZG[Amp,:]
                 - sig_sZG[Amp-1,:]))).ravel()
                 if idx.size:
                      Schnittpkt = i[min(idx)]
                      # Index begins from midpoint of tension chord
                      index_Schnittpkt = closest_index(i, Schnittpkt)
                      # New allocation of slip-reversal-point
                      x_sU[Amp] = i[index_Schnittpkt]
```

```
                    q = index_Schnittpkt - 1
                    while q >=0:  # Correction beginning from intersection point
                         # Previous loop
                         sig_sZG[Amp,q] = sig_sZG[Amp-1,q]
                         sig_cZG[Amp,q] = sig_cZG[Amp-1,q]
                         eps_sZG[Amp,q] = eps_sZG[Amp-1,q]
                         eps_cZG[Amp,q] = epsilon_c(sig_cZG[Amp-1,q])
                         tau_bZG[Amp,q] = tau_bU(n_rel[Amp-1])
                         q = q - 1 # Next node
               else:
                    x_sU[Amp] = L

          # Calculation of slip and displacement through numerical integration
          for r in range(1, N+1 ,1):
               u_sZG[Amp,r] = dx * 1/2 * (eps_sZG[Amp,r] + eps_sZG[Amp,r-1])
               u_cZG[Amp,r] = dx * 1/2 * (eps_cZG[Amp,r] + eps_cZG[Amp,r-1])
               deltaZG[Amp,r] = deltaZG[Amp,r-1] + u_sZG[Amp,r] - u_cZG[Amp,r]

     ################ RELOADING ################ RELOADING ###################
    elif sigma_sfat[Amp] > sigma_sfat[Amp-1]:
          print('RELOADING')
          # Boundary condition for next load peak
          # Steel stress at crack lip = given load stress
          sig_sZG[Amp,N] = sigma_sfat[Amp]
          sig_cZG[Amp,N] = 0 # Concrete stress at crack lip = 0
          # New plastic-strain-increase only for RELOADING;
          for UNLOADING is the plastic-strain-
          # increase equal to the one of the previous load peak Amp-1
          # Steel strain acc.  to constitutive equation
          eps_sZG[Amp,N] = epsilon_s(sig_sZG[Amp,N]) + PlastDehnAkku(n_rel[Amp])
          eps_cZG[Amp,N] = 0 # Concrete strain at crack lip = 0
          # Bond-stress acc.  to static-monotonic TCM
          tau_bZG[Amp,N] = tau_bR(n_rel[Amp])
          u_sZG[Amp,0] = 0 # No displacement in the midpoint (symmetric loading)
          u_cZG[Amp,0] = 0 # No displacement in the midpoint (symmetric loading)
          deltaZG[Amp,0] = u_sZG[Amp,0] - u_cZG[Amp,0]

            # Start with 2.  node
          q = N-1

            while q >= 0:
               sig_sZG[Amp,q] = sig_sZG[Amp,q+1] - dx * tau_bZG[Amp,q+1] * 4/Ds
               sig_cZG[Amp,q] = sig_cZG[Amp,q+1] + dx * tau_bZG[Amp,q+1] * 4/Ds
* ro/(1 - ro)
               eps_sZG[Amp,q] = epsilon_s(sig_sZG[Amp,q]) + PlastDehnAkku(n_rel[Amp])
               eps_cZG[Amp,q] = epsilon_c(sig_cZG[Amp,q])
               tau_bZG[Amp,q] = tau_bR(n_rel[Amp])
               q = q - 1 # Next node

            # Calculation of intersection point with curves of previous values,
          # Intersection point with curve distribution of previuos load peak
          idx = np.argwhere(np.diff(np.sign(sig_sZG[Amp,:]
          - sig_sZG[Amp-1,:]))).ravel()
          if idx.size:
```

```
                Schnittpkt = i[min(idx)]
                index_Schnittpkt = closest_index(i, Schnittpkt)
                x_sR[Amp] = i[index_Schnittpkt]
                q = index_Schnittpkt - 1
                while q >=0:  # Correction beginning from intersection point
                     sig_sZG[Amp,q] = sig_sZG[Amp-1,q] # Previous loop
                     sig_cZG[Amp,q] = sig_cZG[Amp-1,q] # Previous loop
                     eps_sZG[Amp,q] = eps_sZG[Amp-1,q] # Previous loop
                     eps_cZG[Amp,q] = epsilon_c(sig_cZG[Amp-1,q])# Previous loop
                     tau_bZG[Amp,q] = tau_bU(n_rel[Amp-1]) # Previous loop
                     q = q - 1 # Next node

             else:
                x_sR[Amp] = np.amin([np.amin(x_sU), L, Ds/4 * (sigma_sfat[Amp] -
                sigma_sfat[Amp-1])/(tau_bU(n_rel[Amp-1]) + tau_bR(n_rel[Amp]))])
                # Index begins from midpoint of tension chord
                index_sR = closest_index(i, x_sR[Amp])
                x_sR[Amp] = i[index_sR]# New allocation of slip-reversal-point
                if np.amin(x_sU) < Ds/4 * (sigma_sfat[Amp] -
                sigma_sfat[Amp-1])/(tau_bU(n_rel[Amp-1]) + tau_bR(n_rel[Amp])) and
                np.amin(x_sU) < L:
                     idx_min = np.argmin(x_sU)
                     q = (N - 1) - index_sR
                     # From slip-reversal-point are the values of prev.  loop valid
                     while q >= 0:
                          sig_sZG[Amp,q] = sig_sZG[Amp,q+1] -
                          dx * tau_bZG[idx_min,q+1] * 4/Ds
                          sig_cZG[Amp,q] = sig_cZG[Amp,q+1] +
                          dx * tau_bZG[idx_min,q+1] * 4/Ds * ro/(1 - ro)
                          eps_sZG[Amp,q] = epsilon_s(sig_sZG[Amp,q]) +
                          PlastDehnAkku(n_rel[Amp])
                          eps_cZG[Amp,q] = epsilon_c(sig_cZG[Amp,q])
                          tau_bZG[Amp,q] = tau_bR(n_rel[Amp])
                          q = q - 1 # Next node
                else:
                     pass

           # Calculation of slip and displacement through numerical integration
          for r in range(1, N+1 ,1):
                u_sZG[Amp,r] = dx * 1/2 * (eps_sZG[Amp,r] + eps_sZG[Amp,r-1])
                u_cZG[Amp,r] = dx * 1/2 * (eps_cZG[Amp,r] + eps_cZG[Amp,r-1])
                deltaZG[Amp,r] = deltaZG[Amp,r-1] + u_sZG[Amp,r] - u_cZG[Amp,r]

      # Next load peak
     Amp = int(Amp + 1)

  # ------------------------------------------------
# Calculation of the average steel strain for every load peak
# ------------------------------------------------
eps_smfat = np.zeros((Amp,1))
print('eps_smfat [Ž030] = ', eps_smfat*1000)
j = 0
k = 0
while j < Amp:
```

```
     while k < N:
          eps_smfat[j] = eps_smfat[j] + 1/L * 1/2 * (eps_sZG[j,k] +
          eps_sZG[j,k+1]) * dx
          k = k + 1
     j = j + 1
     k = 0
print('eps_smfat [‰] = ', eps_smfat*1000)

  # ------------------------------------------------
# Stress-strain-curve of the reinforcement
# ------------------------------------------------
strain_s = np.arange(0, 0.090, 0.00001)
stress_s = np.zeros(len(strain_s))
for z in range(len(strain_s)):
     stress_s[z] = sigma_s(strain_s[z])

  # ------------------------------------------------
# Calculation of the crack width
# ------------------------------------------------
crack_width = []
for z in range(len(sigma_sfat)):
     # deltaZG amounts only half of the length of tension chord
     crack_width = np.append(crack_width, 2*deltaZG[z,N])

  # ------------------------------------------------
# Output of values
# ------------------------------------------------
# Output of average steel strains
Koeffizienten = open(r'C:\XXXXXXX\eps_sm-Nachrechnung-Pe.txt', 'w')
Koeffizienten.write('epsilon_sm-Nachrechnung[mm/m)' + '\n')
for r in range(len(eps_smfat)):
     Koeffizienten.write(str('%.4f' % (eps_smfat[r]*1000)) + '\n')
Koeffizienten.close()

  # ------------------------------------------------
# Plotten
# ------------------------------------------------
# Average stress-strain-diagram of the reinforcement
# ------------------------------------------------
mpl.rcParams['agg.path.chunksize'] = 20000
ax1 = plt.subplot()
SigEpsFat = ax1.plot(eps_smfat*1000, sigma_sfat) # Concrete chord, fatigue
# Concrete chord, 1th cracking
SigEpsFirst = ax1.plot(eps_smfirst*1000, sigma_srfirst)
steel = ax1.plot(1000*strain_s, stress_s) # Steel only
# Latex-Format übernommen
plt.rc('text', usetex=True)
plt.rc('font', **'family':  'serif', 'serif':['Palatino'])
plt.setp(SigEpsFat, lw=1.0, color='k', ls='-')
plt.setp(SigEpsFirst, lw=1.0, color='k', ls='-')
```

```
plt.setp(steel, lw=1.0, color='k', ls=':')
# Axes
plt.xlabel(r'ε_sm [‰]',fontsize=21.0)
plt.ylabel(r'σ_sr [MPa]',fontsize=21.0,rotation='horizontal')
ax1.xaxis.set_label_coords(1.04, -0.13) # Xlabel to the right
ax1.yaxis.set_label_coords(0.0, 1.04) # Ylabel at the top
ax1.xaxis.set_major_formatter(FormatStrFormatter('%0.1f'))
ax1.yaxis.set_major_formatter(FormatStrFormatter('%0.f'))
plt.xlim(0, 3.5)
plt.ylim(0.0, 600.0)
plt.xticks(np.arange(0, 3.75, 0.25))
plt.yticks(np.arange(0, 650, 50))
ax1.xaxis.set_ticks_position('both') # Ticks on both sides of axis
ax1.yaxis.set_ticks_position('both') # Ticks on both sides of axis
for label in ax1.get_xticklabels()[1::2]:  # Numeration only every second tick
     label.set_visible(False)
for label in ax1.get_yticklabels()[1::2]:  # Numeration only every second tick
     label.set_visible(False)
ax1.xaxis.set_tick_params(labelsize=21.0) # Font size x-axis
ax1.yaxis.set_tick_params(labelsize=21.0) # Font size y-axis
textstr1 = 'fatigue\nloading'
textstr2 = 'steel only'
textstr3 = 'first\nloading'
ax1.annotate(textstr1,xy=(2.25,250),xytext=(2.7,50),fontsize=20,color='k',
arrowprops=dict(arrowstyle='-|>,head_length=0.4,head_width=0.1',
connectionstyle='arc3,rad=-0.3',edgecolor='k',facecolor='k'))
ax1.annotate(textstr2,xy=(2.75,550),xytext=(1.0,500),fontsize=20,color='k',
arrowprops=dict(arrowstyle='-|>,head_length=0.4,head_width=0.1',
connectionstyle='arc3,rad=-0.3',edgecolor='k',facecolor='k'))
ax1.annotate(textstr3,xy=(0.5,250),xytext=(0.1,450),fontsize=20,color='k',
arrowprops=dict(arrowstyle='-|>,head_length=0.4,head_width=0.1',
connectionstyle='arc3,rad=0.3',edgecolor='k',facecolor='k'))
mpl.rcParams['agg.path.chunksize'] = 20000
plt.savefig(r'C:\XXXXXXXX\Nachrechn-Seq_Pe-mpl.png', format='png', dpi=250, bbox_-
inches='tight')
#plt.show()
plt.cla()
plt.close('all')
```